



Universidad de Oviedo
Universidá d'Uviéu
University of Oviedo

**Electrical, Electronic, Computers and Systems
Engineering Department**

PhD Program in Energy and Process Control

PhD Thesis

**Control and monitoring of
Variable-Leakage-Flux IPMSM**

by

Diego Fernández Laborda

Gijón, February 2022



Universidad de Oviedo
Universidá d'Uviéu
University of Oviedo

**Departamento de Ingeniería Eléctrica, Electrónica, de
Computadores y Sistemas**

Programa de Doctorado en Energía y Control de Procesos

Tesis doctoral

**Control y monitorización de máquinas
síncronas de imanes permanentes
enterrados de flujo variable**

por

Diego Fernández Laborda

Gijón, Febrero 2022



Universidad de Oviedo
Universidá d'Uviéu
University of Oviedo

**Electrical, Electronic, Computers and Systems
Engineering Department**

PhD Program in Energy and Process Control

Control and monitoring of Variable-Leakage-Flux IPMSM

by

Diego Fernández Laborda

**Dissertation submitted in fulfillment of the requirements for the
degree of Doctor of Philosophy in Electrical Engineering with
International Mention**

Advisors

David Díaz Reigosa. Full Professor. Dept. of Elec., Computer, & Systems
Engineering, University of Oviedo
Daniel Fernández Alonso. Assistant Professor. Dept. of Elec., Computer, &
Systems Engineering, University of Oviedo

Gijón, February 2022



Universidad de Oviedo
Universidá d'Uviéu
University of Oviedo

**Departamento de Ingeniería Eléctrica, Electrónica, de
Computadores y Sistemas**

Programa de Doctorado en Energía y Control de Procesos

Control y monitorización de máquinas síncronas de imanes permanentes enterrados de flujo variable

por

Diego Fernández Laborda

**Tesis presentada en cumplimiento de los requisitos para el grado de
Doctor en Filosofía en Ingeniería Eléctrica con Mención Internacional**

Tutores

David Díaz Reigosa. Profesor catedrático. Dpto. de Ing. Eléctrica, Electrónica,
de Computadores y Sistemas, Universidad de Oviedo

Daniel Fernández Alonso. Profesor ayudante doctor. Dpto. de Ing. Eléctrica,
Electrónica, de Computadores y Sistemas, Universidad de Oviedo

Gijón, Febrero 2022

A mi familia.

Acknowledgements

En primer lugar, me gustaría agradecer a mis directores de tesis, David Díaz Reigosa y Daniel Fernández Alonso, su constante ayuda, tiempo y, sobre todo, paciencia durante la realización de esta tesis. He aprendido mucho durante estos años trabajando con vosotros, y sé que lo seguiré haciendo. También querría agradecer a Fernando Briz y a Juan Manuel Guerrero por su ayuda, tiempo y por estar siempre disponibles cuando os necesitaba.

I would like to express my gratitude to all the members from EV system Laboratory at Nissan Advanced Technology Center that help me during the development of this thesis, especially to Kato-san, Sasaki-san and Okada-san.

Me gustaría agradecer a mis compañeros de grupo, que compartieron laboratorio conmigo y me ayudaron siempre de forma desinteresada. Muchas gracias, María, Cristina, Marcos y Lidia, por haber hecho de estos cuatro últimos años una de las etapas más bonitas de mi vida.

Me gustaría agradecer a toda mi familia su incondicional cariño y apoyo a pesar de mi prácticamente completa desaparición durante estos últimos años. Esta tesis os la dedico a vosotros, sobre todo a los más jóvenes, para demostraros que, con esfuerzo, podemos lograr las metas que nos proponemos. Me gustaría agradecer especialmente el apoyo y cariño de mis padres.

Por último, quiero agradecer y dedicar esta tesis a Rosana, no hay palabras que pueda escribir para transmitir todo lo que significa para mí tu apoyo y cariño durante estos años.

Resumen

El interés en vehículos eléctricos (EVs) y vehículos híbridos (HEVs) ha aumentado sustancialmente durante las últimas dos décadas debido a la introducción de nuevas regulaciones motivadas por el cambio climático. Los EVs y HEVs fueron usados en los inicios del siglo 20, pero fueron derrotados por los vehículos de motor de combustión interna (ICEVs) que eran más baratos, más ligeros y de recarga más rápida.

Hoy en día, la tecnología actual ha permitido a los EVs y HEVs competir justamente con los ICEVs. Sin embargo, el precio de los EVs sigue siendo alto, su rango relativamente corto, comparado con los ICEVs, y son más lentos de recargar. Durante los últimos años, los EVs han conseguido rangos de funcionamiento mayores gracias a una mayor densidad de energía de sus baterías y sistemas de tracción más eficientes. El uso de máquinas síncronas de imanes permanentes (PMSMs) ha aumentado la eficiencia a costa de usar imanes permanentes (PMs) basados en tierras-raras como el neodimio, y consecuentemente aumentar su coste.

Las PMSMs son muy eficientes a bajas velocidades, sin embargo, a altas velocidades necesitan la inyección continua de corriente de debilitamiento de flujo para contrarrestar el enlace de flujo de los PMs e igualar la fuerza contraelectromotriz (Back-EMF) con la tensión de bus DC disponible. Este modo de operación está caracterizado por unas pérdidas en el cobre y núcleo inherentes a causa de la aplicación continua de una corriente negativa en el eje-d y los armónicos extra producidos en el flujo del entrehierro.

Las máquinas de flujo variable (VF-PMSMs) y las máquinas de flujo de dispersión variable (VLF-PMSMs) son diseñadas para reducir o incluso eliminar la inyección de corriente de debilitamiento de flujo y sus efectos adversos. Las VF-PMSMs son capaces de cambiar el estado de magnetización de sus PMs du-

rante su funcionamiento, pero este proceso necesita de la inyección de corrientes de muy alta magnitud y el control preciso del estado de magnetización sigue bajo investigación. Por otro lado, las VLF-PMSMs son capaces de reducir la inyección de corrientes de debilitamiento de flujo usando un diseño de rotor especial, manteniendo el estado de magnetización de los PMs constante y evitando las desventajas del proceso de magnetización y desmagnetización.

La introducción de este tipo de máquinas en la industria reducirá las pérdidas de potencia a altas velocidades, aumentando la eficiencia y el rango de funcionamiento de los EVs y HEVs. Pero antes de que estas máquinas puedan ser introducidas en el mercado, métodos de estimación de la temperatura de los PMs y el par producido deben de ser desarrolladas para aumentar la fiabilidad del sistema de tracción. Los métodos disponibles no pueden ser extrapolados fácilmente a este tipo de máquinas debido a la variación del enlace de flujo de sus PMs, obteniéndose errores de estimación demasiado altos.

En esta tesis se muestra un método para la estimación de temperatura de los PMs basada en el enlace de flujo de los PMs y un método de estimación de par basado en la combinación de inyección de señales de baja y alta frecuencia para VLF-PMSMs. Estas técnicas han sido profundamente analizadas en una VLF-PMSM real bajo diferentes condiciones de operación.

Abstract

The interest in electric vehicles (EVs) and hybrid electric vehicles (HEVs) have increased substantially during the last two decades due to the new regulations motivated by climate change. EVs and HEVs were used in the early 20th century, but they were beaten by the cheaper, lighter, faster rechargeable internal combustion engine vehicles (ICEVs).

Nowadays, the current technology has allowed the EVs and HEVs to fairly compete with ICEVs. However, EVs price is still high, the driving range is relatively small compared to ICEVs and they are slower to recharge. During the last years, larger driving range is being achieved by EVs due to higher energy density batteries and more efficient drives. The use of Permanent magnet synchronous machines (PMSMs) has increased the efficiency at the cost of using rare-earth PMs such as neodymium, and consequently increasing their cost.

PMSMs are very efficient at low speeds, however at high speeds they need the continuous injection of flux-weakening current to counteract PM flux linkage to match the back electromotive force (Back-EMF) with the available DC voltage. This operating mode is characterized by an inherent copper and core loss increase due to the continuous application of negative d-axis current and the extra harmonics produced in the airgap field.

Variable flux PMSMs (VF-PMSMs) and variable leakage flux PMSMs (VLF-PMSMs) designs are aimed to reduce or even avoid the injection of flux weakening current and its subsequent adverse effects. VF-PMSMs are able to change their magnetization in-situ, during normal machine operation, but this process involves the injection of very large magnitude currents and precise PM magnetization control is still under development. On the other hand, VLF-PMSMs are able to reduce the injection of flux weakening currents by using a special rotor design, keeping the PM magnetization constant and avoiding the drawbacks of

magnetization and demagnetization process.

The introduction of these type of machines in the industry will reduce the losses at high speeds, increasing efficiency and driving range of the EVs and HEVs. Before these machines can be introduced to the market, PM temperature and produced torque estimation techniques should be available in order to increase their reliability. Already available methods are not easily extrapolated to these types of machines due to their variable PM flux linkage, leading to large estimation errors.

This thesis addresses a PM temperature estimation method based on PM flux linkage and a torque estimation method enhanced by a combination of high and low frequency signal injection for VLF-PMSMs. These techniques have been deeply analysed in a real VLF-PMSM under different operating conditions.

List of Figures

1.1	Human influence in observed surface temperature change.	2
1.2	EVs and HEVs timeline.	2
1.3	PM energy product evolution.	4
1.4	Energy and power density of different battery technologies.	5
1.5	Comparison of conventional IPMSM, VF-PMSM and VLF-PMSM designs.	8
2.1	VLF-PMSM d- and q-axes.	14
2.2	VLF-PMSM variables vs. stator current at $T_r = 20$ °C.	15
3.1	Variation of coercitivity and remanence of a N42-type NdFeB magnet of SH thermal grade (150°C).	18
3.2	WLTC class 3 driving cycle speed profile.	20
3.3	Graphical approximation for PM flux linkage estimation.	25
3.4	Temperature estimation system scheme.	26
3.5	Schematic representation of voltage, current and Gopinath type flux observers.	28
3.6	Voltage model flux observer in stationary reference frame.	29
3.7	Schematic representation of the injected stator d-axis current, fundamental and small-amplitude, low frequency, square-wave currents, (i_{sd}^r) and resulting stator d-axis flux (λ_{sd}^r).	30
3.8	FEA results. PM flux linkage vs. stator current and PM temperature LUTs. $\omega_r=3750$ r/min, $T_r=20, 50, 80, 110$ and 140 °C.	32

3.9	FEA results. 3000 r/min, $T = 50$ Nm, $T_r = 20, 50, 80, 110$ and 140 °C.	33
3.10	Comparison of linear interpolation, cubic spline interpolation and quadratic regression for $I_{sdq}^r = 0$	34
3.11	FEA results. Introduced temperature estimation error by PM flux interpolations vs. stator current at $T_r = 80$ °C and $\omega_r = 3750$ r/min. 34	34
3.12	FEA results. Temperature estimation error. $\omega_r = 3750$ r/min, $T_r = 20, 50, 80, 110$ and 140 °C.	35
3.13	Experimental results. $\omega_r = 3000$ r/min, $T = 50$ Nm.	36
3.14	Experimental results. Estimated PM flux linkage and FEA results vs. q-axis stator current. $\omega_r = 3000$ r/min, $T_r = 20, 50, 80$ and 110 °C.	37
3.15	Experimental results. $\omega_r = 3000$ r/min, $T = 50$ Nm.	38
3.16	Experimental results in the torque vs. speed region. “*”: operating point shown in Fig. 3.15.	39
3.17	Experimental results. $\omega_r = 3000$ r/min, $T = 50$ Nm.	40
4.1	Torque transducer sectional view from Magtrol Inc.	45
4.2	Wireless torque pulsations measurement system.	46
4.3	PM flux linkage variation with q-axis current at different PM temperatures for the VLF-PMSM at $I_{sd}^r = 0$ A.	47
4.4	VLF-PMSM variables vs. stator current for different temperatures. 48	48
4.5	Block diagram of the fundamental torque control and torque estimation strategy for a VLF-PMSM.	50
4.6	Gopinath type flux observer scheme.	51
4.7	Schematic representation of the injected stator d-axis current, fundamental and small-amplitude, low frequency, square-wave currents, (i_{sd}^r) and resulting stator d-axis flux (λ_{sd}^r)	52
4.8	Experimental results. Measured by the microcontroller at 10 kHz. $I_{sdq}^r = 0$, $I_{HF} = 0.05$ pu, $\omega_{HF} = 2\pi 500$ rad/s, $\omega_r = 500$ r/min and $T_r = 20$ °C	57
4.9	Experimental results. Measured by the microcontroller at 10 kHz. $I_{sdq}^r = 0$, $I_{HF} = 0.05$ pu, $\omega_{HF} = 2\pi 500$ rad/s, $\omega_r = 500$ r/min and $T_r = 20$ °C	58

4.10 FEA and experimental estimated inductance results. $I_{HF} = 0.05$ pu, $\omega_{HF}=2\pi 500\text{rad/s}$, $\Delta I_{sd}^r = 0.02$ pu, $\omega_r = 500$ r/min and $T_r = 20$ °C	59
4.11 FEA results. Cross-coupling inductances vs. stator current at $T_r=20$ °C.	61
4.12 Schematic representation of DC or linearized inductance and HF or incremental inductance.	62
4.13 FEA and experimental results. $I_{HF} = 0.05$ pu, $\omega_{HF}=2\pi 500\text{rad/s}$, $\omega_r = 500$ r/min and $T_r = 20$ °C	63
4.14 FEA and experimental results. $I_{HF} = 0.05$ pu, $\omega_{HF}=2\pi 500\text{rad/s}$, $\omega_r = 500$ r/min and $T_r = 20$ °C	64
4.15 Estimated PM flux linkage vs. stator current. $\Delta I_{sd}^r=0.02$ pu, $\omega_r=500$ r/min and $T_r=20$ °C.	65
4.16 FEA and experimental results. $I_{HF} = 0.05$ pu, $\omega_{HF}=2\pi 500\text{rad/s}$, $\omega_r = 500$ r/min and $T_r = 20$ °C	66
4.17 FEA and experimental results. $I_{HF} = 0.05$ pu, $\omega_{HF}=2\pi 500\text{rad/s}$, $\omega_r = 500$ r/min and $T_r = 20$ °C	68
5.1 VLF-PMSM developed torque vs voltage angle under six-step operation.	70
5.2 Definition of the injected voltage angle under six-step operation.	70
5.3 Six-step open loop control scheme.	71
5.4 FEA results. d-axis inductance vs stator current and PM temperature	73
5.5 FEA results. PM flux linkage vs. injected voltage angle and speed for different PM temperatures.	73
5.6 FEA results. PM flux linkage variation with temperature using the 20 °C case as reference for different PM temperatures	74
5.7 FEA Results. Inductance signature for different PM temperatures.	75
5.8 FEA Results. Inductance signature variations from 20 °C case for different PM temperatures.	76
5.9 FEA results. d-axis fundamental current for different PM temperatures.	77

5.10	FEA results. d-axis current variations using the 20 °C case as reference for different PM temperatures.	77
5.11	PM temperature estimation signal processing from measured d-axis current.	78
5.12	Experimental results. d-axis fundamental current for different PM temperatures.	79
5.13	Experimental results. Estimated PM temperature using the fundamental d-axis current for different PM temperatures.	80
5.14	Experimental results. PM temperature estimation error using the fundamental d-axis current for different PM temperatures.	80
5.15	Experimental results. Voltage angle transient from 95° to 105°. . .	81
5.16	Experimental results. Measured and fundamental d-axis current during voltage angle transient. Measured at 10 kHz by the microcontroller.	81
5.17	Experimental results. Estimated PM temperature during voltage angle transient.	82
5.18	Experimental results. PM temperature estimation error during voltage angle transient.	82
5.19	Experimental results. Speed transient during six-step operation. .	83
5.20	Experimental results. Measured and fundamental d-axis current during speed transient. Measured at 10 kHz by the microcontroller.	83
5.21	Experimental results. Estimated PM temperature during speed transient.	84
5.22	Experimental results. PM temperature estimation error during speed transient.	84
A.1	Test bench.	105
A.2	Power system connection scheme.	106
A.3	Power system of the experimental setup.	107
A.4	Test bench attachment to the floor and a rubber shock absorber. .	107
A.5	120 mm ² shielded power cable used to connect machines and inverters.	108
A.6	Three phase diode rectifier VUO62-12NO7.	108

A.7	Control box with the control card and auxiliary systems.	109
A.8	Control PCB.	109
A.9	TC-08 from Pico Technology.	110
A.10	Wireless PM temperature measurement system along with the aluminum case attached to the rear part of the rotor.	110
A.11	Schematic representation of the temperature measurement system and desktop application.	112
A.12	Torque transducer of Interface Inc.	113
A.13	Machine phase current distortion due to inverter deadzone.	115
A.14	Current ripple in machine phase current due to PWM switching.	116
A.15	Magnitude and angle of the voltage distortion due to inverter deadzone.	117
A.16	Comparison between commanded and measured inverter output voltage, before and after compensation for $I_{sd}^r = 0$ A and $I_{sq}^r = 100$ A.	117

List of Tables

1.1	EV/HEV and their electric machines	6
2.1	VLF-PMSM parameters	15
3.1	Maximum operating temperature of different electric machine parts.	18
3.2	PM temperature estimation based on PM flux linkage methods . .	24
3.3	Advantages and drawbacks of flux models	27
4.1	Advantages and drawbacks of flux models	51
A.1	Main characteristics of the PM temperature measurement system .	111
A.2	Main characteristics of the torque sensor	113

Contents

1	Introduction	1
1.1	Background	1
1.2	Research motivation and overview	8
1.3	Outline of the document	11
2	VLF-PMSM Model	13
3	PM Temperature Estimation based on PM flux linkage in VLF-PMSMs	17
3.1	Introduction	17
3.1.1	The importance of PM temperature in PMSMs drives . . .	17
3.1.2	Measurement and estimation techniques for PMSM drives .	20
3.1.2.1	PM temperature measurement systems for PMSM drives	20
3.1.2.2	PM temperature estimation methods for conventional PMSM drives	21
3.1.3	PM temperature estimation methods for VLF-PMSM drives	24
3.2	PM temperature estimation based on PM flux linkage variation . .	24
3.2.1	Flux observer	26
3.2.2	PM flux linkage estimator	29
3.2.3	PM Temperature estimation	31
3.3	Simulation results	31

3.4	Experimental results	35
3.5	Conclusions	40
4	Torque Estimation	43
4.1	Introduction	43
4.1.1	Torque measurement techniques	44
4.1.2	Torque estimation techniques	46
4.2	Torque estimation based on flux observer enhanced with on-line parameters estimation	49
4.2.1	Stator flux linkage estimation	49
4.2.2	PM flux linkage estimation	51
4.2.3	Resistance and inductances estimation using high frequency signal injection	53
4.3	FEA and experimental verification	56
4.3.1	Inductance estimation	57
4.3.1.1	Cross-coupling inductance effect	59
4.3.1.2	DC inductance estimation from HF inductance	61
4.3.2	PM flux linkage estimation	64
4.4	Torque estimation	65
4.5	Conclusions	66
5	PM Temperature estimation under six-step operation	69
5.1	Introduction	69
5.2	PM Temperature estimation under six-step operation	71
5.2.1	PM flux linkage	72
5.2.2	Sixth harmonic inductance	74
5.2.3	D-axis current	76
5.3	Experimental verification	78
5.3.1	Steady state	79
5.3.2	Injection angle transient	81
5.3.3	Speed transient	82
5.4	Conclusions	84

B Publications	119
B.1 Peer-reviewed journal publications	119
B.1.1 SynRM Sensorless Torque Estimation Using High Frequency Signal Injection	119
B.1.2 Permanent Magnet Synchronous Machine Torque Estima- tion Using Low Cost Hall-Effect Sensors	130
B.1.3 Battery Internal Resistance Estimation Using a Battery Balancing System Based on Switched Capacitors	140
B.1.4 Resolver Emulation for PMSMs Using Low Cost Hall-Effect Sensors	153
B.2 Conference papers	163
B.2.1 Magnet Temperature Estimation in Variable Leakage Flux Permanent Magnet Synchronous Machines Using the Mag- net Flux Linkage	163
B.2.2 Enhanced Torque Estimation in Variable Leakage Flux PMSM Combining High and Low Frequency Signal Injection	171
B.2.3 Online PI Current Controller Tuning Based on Machine High-Frequency Parameters	180
B.2.4 Comparative Analysis of Torque Pulsations Measurement Methods for PMSM Drives	188
B.2.5 Use HF Signal Injection for Simultaneous Rotor Angle, Torque and Temperature Estimation in PMSMs	196
B.2.6 Comparison Of Anti-Windup Alternatives For Parallel Con- trollers	205
B.2.7 Magnetic Resolver Using Hall-Effect Sensors	212

6	Conclusions and future work	85
6.1	Conclusions	85
6.2	Contributions	86
6.2.1	Contributions of the dissertation published in international journals	87
6.2.2	Contributions of the dissertation published in international conferences	87
6.2.3	Other contributions published in international journals	88
6.2.4	Other contributions published in international conferences	88
6.3	Future work	90
6.4	Dissertation funding	90
6	Conclusiones y trabajo futuro	91
6.1	Conclusiones	91
6.2	Contribuciones	92
6.2.1	Contribuciones de la tesis doctoral publicadas revistas internacionales	93
6.2.2	Contribuciones de la tesis doctoral publicadas en congresos internacionales	94
6.2.3	Otras contribuciones publicadas en revistas internacionales	94
6.2.4	Otras contribuciones en conferencias internacionales	95
6.3	Trabajo Futuro	96
6.4	Financiación	96
A	Experimental setup	105
A.1	Power system	105
A.2	PM temperature measurement system	108
A.3	Torque sensor	112
A.4	Inverter nonlinearities evaluation	113
A.4.1	Introduction	113
A.4.2	Current Waveform Distortion	114
A.4.3	Compensation	116

Chapter 1

Introduction

1.1 Background

New regulations motivated by climate change have increased the interest in transportation electrification during the last decade. The Intergovernmental Panel on Climate Change (IPCC) has stated that human influence has unequivocally warmed the atmosphere, oceans, and land (see Fig. 1.1) [1]. Furthermore, it has been shown that CO_2 accounts for 77% of total accumulative greenhouse gas (GHG) emissions, transportation being among the top contributors [2].

The use of electric vehicles (EVs) and hybrid electric vehicles (HEVs) has raised as an alternative to conventional internal combustion engine vehicles (ICEVs) to reduce GHG emissions. However, transportation electrification will not eliminate CO_2 emissions until electric energy used by EVs is generated from CO_2 -free renewable energy sources.

Although the rise of interest in EVs and HEVs is recent, they were invented and used in the late 19th century and early 20th century [3, 4]. A timeline of the most relevant EVs and HEVs, as well as key technological advances is shown in Fig. 1.2.

The considered first commercial electric vehicle, the “William Morrison Electric wagon” appeared in 1891. It was designed for twelve passengers with a 3 kW electric direct current (DC) machine. This was the base design for the Electrobat

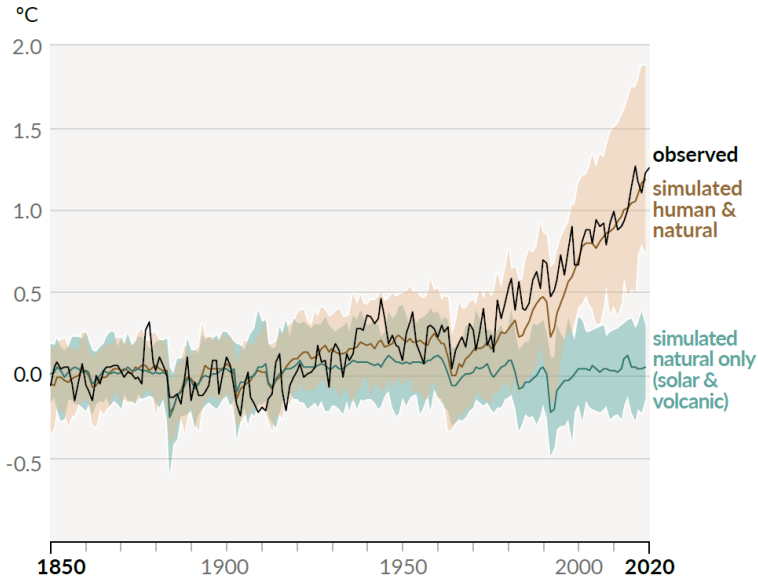


Figure 1.1: Human influence in observed surface temperature change [1].

taxicabs which operated in New York from 1896. They were propelled by two 1.1 kW DC motors, reaching a maximum range of 40 km per charge. One year later, an electric taxicab service, using the taxicabs designed by W. Bersey, was inaugurated by W.H. Preece in London.

By the end of the 19th century, EVs were fairly competing with ICEVs and steam vehicles, each type of vehicle with a 30% market share. The tough market competition led to new interesting designs including hybrid vehicles that combined two of these technologies, such as the Lohner-Porsche HEV in 1900, which

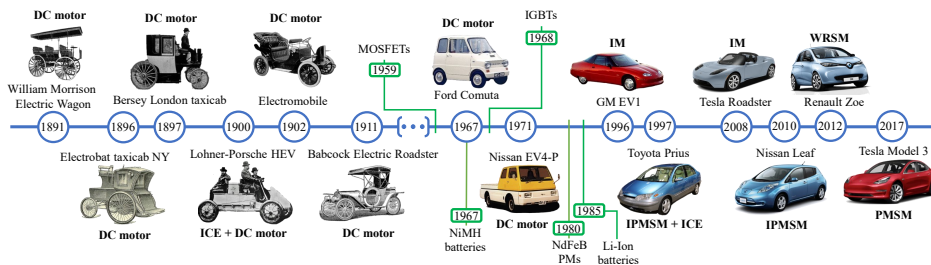


Figure 1.2: EVs and HEVs timeline.

combined an ICE and a DC motor. All these EVs and HEVs used DC electric machines and batteries, which allowed a simple electrical design such as manual rheostatic control. At that time, induction machines (IMs) and the technology to create alternating current (AC) from DC batteries was available by means of rotary converters. However, the added weight, reduction in efficiency and increase in complexity made the use of AC machines in EVs and HEVs unpractical.

In the first decade of the 20th century, car manufacturers kept improving their EVs and HEVs designs, battery exchange systems being offered and more battery charging stations being available in the cities. All this made EVs a well established and healthy technology market that thrived during this period of time. After 1910, the quality of the roads between cities improved increasing the interest in touring and larger driving range vehicles, but charging facilities or battery exchange services were usually located inside the cities and the short range of EVs (up to 80 km) made impossible to consider EVs for long distance touring. Additionally, in the EEUU market, fuel availability for ICEVs was not an issue anymore due to increasing discoveries of oil in Texas, dropping the fuel price to historic minimums. The invention of the electric starter in 1912 made ICEVs start faster, reliably and safely. All these new discoveries and changes made ICEVs much more interesting than EVs. By 1920, most of the EV manufacturers had closed their business or moved to ICEVs production. The market crisis of 1929 also impacted EV technology by preventing any possible research investment.

From 1920 to 1970, EVs were out of the market and ICEVs were the preferred choice for transportation. The interest on EVs only appeared under some special circumstances such as fuel shortages during World War II (WWII) and early 1970s. For instance, during WWII, the milk delivery service in UK was accomplished by EVs due to the high price and low availability of gasoline that became an strategical resource.

Despite the fall of EVs market from 1920 to 1970, important technological advancements were made during this period. Electric machines used in these first EVs did not include permanent magnets (PMs) because of the low strength of the only available PM material, magnetite, electromagnets were used instead. The use of PMs in electric machines was not practical until the invention of AlNiCo in the 1930s. With the later discovery of ferrite magnets in the 1950s, samarium in the 1960s, and neodymium-iron-boron PMs in the 1980s, what stimulated the development of electric machines based on PMs. Each new PM technology allowed to increase the power density and efficiency of PM-based electric machines, this can be seen by the evolution of the maximum energy product BH_{max} in

Fig. 1.3.

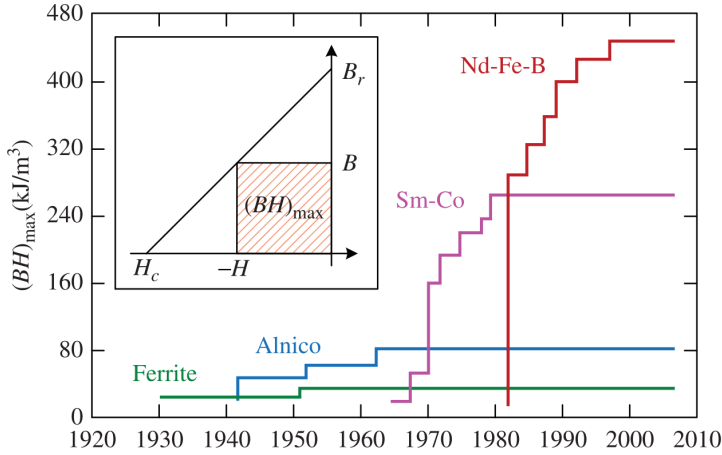


Figure 1.3: PM energy product evolution [4].

Machine control during the early 20th century was accomplished by rheostatic control that was simple but inefficient. This system allowed the control of the machine speed by varying the value of a series resistance (rheostat), consequently modifying the machine applied voltage. The use of power electronics was not possible until the invention of selenium rectifiers in 1933, bipolar transistors in 1948, MOSFETs in 1959 and IGBTs in 1968. The use of these power switches allowed an efficient power conversion and the possibility of creating AC currents from the DC batteries while maintaining the overall system relatively light weight, small size and high efficiency.

During this period of time, batteries kept improving with better designs of lead-acid batteries. Other battery technologies were also developed such as the invention of the nickel-cadmium (NiCd) battery in 1899 in Sweden, being commercialized in 1910 and reaching US in 1946. Nickel metal hydride battery (NiMH) was invented in 1967 significantly increasing the energy density of NiCd batteries. Commercial lithium batteries were available in the 1970s, but they were not rechargeable, the first prototype of rechargeable lithium-ion batteries was made in 1985 in Japan. Lithium-ion (Li-Ion) batteries have much higher energy density than NiCd and NiMH batteries allowing significantly larger vehicle driving range. The improvements in energy density that these new technologies provided can be seen in Fig. 1.4.

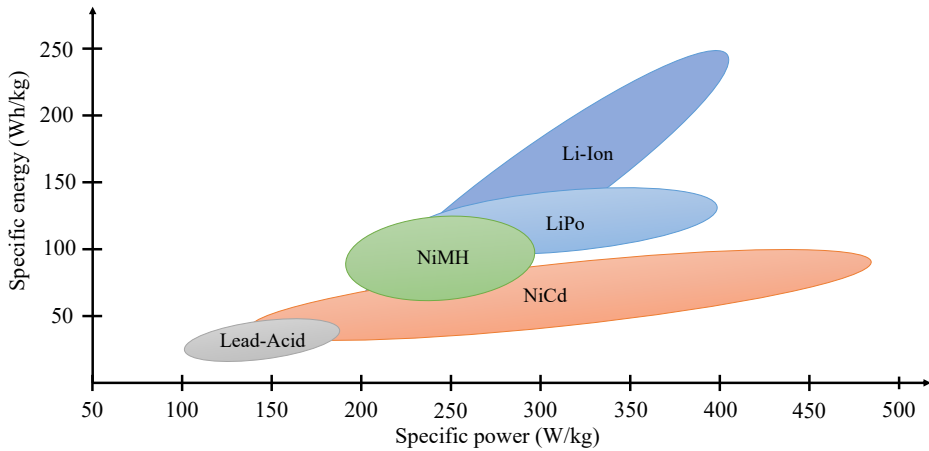


Figure 1.4: Energy and power density of different battery technologies.

These technological advancements arranged a good environment for new EV designs that overcome the limitations present in the early 20th century. The oil shortages around 1970 were the perfect push that EV development needed. In 1967, Ford released an experimental EV named Ford Comuta with two DC motors powered by four lead-acid batteries and with 60 km range. In 1971, the Lunar Roving Vehicle landed in the moon during Apollo 15 mission. It equipped four DC motors, one in each wheel, powered by two silver-zinc batteries. In the same year, Nissan designed the EV4-P, a pick-up truck powered by a lead-acid battery and a DC motor, achieving a range of 300 km. Many other companies started experimenting and developing their own EVs and HEVs from 1970 to 1990.

The development of EV1 by General Motors in 1996 established the base design of modern EVs. They used a 102 kW three-phase IM driven by an IGBT-based power inverter. The first EV1 version used a lead-acid battery with a range of 126 km, the second version (produced in 1999) with NiMH batteries, extended the previous range to 228 km.

The first mass-produced HEV was the Toyota Prius in 1997, produced in Japan and limited to the Japanese market. It equipped a 30 kW interior PMSM (IPMSM) with neodymium magnets, an IGBT-based power inverter and NiMH batteries.

In 2008, Tesla presented their first EV: the Tesla Roadster. It was equipped with a 185 kW three-phase IM and Lithium-ion batteries, reaching a maximum

range of 400 km. Two years later, in 2010, General Motors developed the Chevrolet Volt/Opel Ampera, the first plug-in HEV. This kind of vehicle can be used as a pure EV charging the battery from an electric supply or use the ICE capable to extend the range of the vehicle. It was equipped with a 111 kW PMSM and lithium-ion batteries, reaching a range (in pure EV mode) of 56 km. The additional space and weight constrains introduced by the addition of the ICE, reduced the capacity of the battery and its pure EV range. The same year, Nissan presented the Nissan Leaf, an EV powered by an 80 kW IPMSM, lithium-ion batteries and a range of 117 km. In 2011 Renault presented the Fluence ZE equipped with a 70 kW wound rotor synchronous machine (WRSM), 22 kW·h lithium-ion batteries, achieving a range of 185 km. These EV/HEV and their electric machines are shown in Table 1.1.

Table 1.1: EV/HEV and their electric machines

Vehicle	Year	Electric Machine And Power	Range
W. M. Electric Wagon	1891	3 kW DC machine	80 km
Electrobat	1896	2x 1.1 kW DC machines	40 km
Bersey London taxicab	1897	2.2 kW DC machine	50 km
Lohner-Porsche HEV	1900	2x 1.8 kW DC machines	-
Electromobile	1902	6 kW DC machine	-
Babcock Electric Roadster	1911	11 kW DC machine	160 km
Ford Comuta	1967	2x DC machines	60 km
Nissan EV4-P	1971	27 kW DC machine	300 km
General Motors EV1	1996	102 kW IM	126/228 km
Toyota Prius	1997	30 kW IPMSM	-
Tesla Roadster	2008	185 kW IM	400 km
Opel Ampera	2010	111 kW PMSM	56 km
Nissan Leaf	2010	80 kW IPMSM	117 km
Renault Fluence ZE	2011	70 kW WRSM	185 km
Renault Zoe	2012	66 kW WRSM	160 km
BMW i3	2013	125 kW PMSM	130 km
Tesla Model 3	2017	225 kW PMSM	354 km
Audi e-Tron	2018	2x 140 kW IM	357 km
Hyundai Kona EV	2018	150 kW PMSM	300 km

Nowadays, PMSMs are the preferred option for EVs and HEVs due to their

high torque and power density, wide speed capability, and higher efficiency compared to DC machines, IMs, WRSMs and synchronous reluctance machines (Syn-RMs). On the other hand, the use of rare-earth magnets, such as neodymium, make them one of the most expensive choices. Additionally, neodymium PMs can suffer from permanent demagnetization at relatively low temperatures compared to other PM types, losing their remanent flux completely if they reach their Curie temperature. Inverters based on solid-state switching devices are used to drive the AC electric machines from the DC voltage provided by batteries. PMSMs have PMs in their rotor which create a rotor field without the need of injecting any magnetizing current, which has allowed PMSMs to be reduced in size and weight, increasing their torque density. At low speeds, torque production of PMSMs can be optimized to reduce copper losses by using maximum torque per ampere (MTPA) techniques, being very efficient. However, at high speeds, the injection of negative direct (d-) axis (aligned with rotor PMs) current is needed to counteract PM flux linkage and match the back electromotive force (Back-EMF) with the available DC voltage [5]. This operating mode is known as flux-weakening and is characterized by an inherent copper and core loss increase due to the continuous application of negative d-axis current and the extra harmonics produced in the airgap field [5].

Variable flux PMSMs (VF-PMSMs) [6] and variable leakage flux PMSMs (VLF-PMSMs) designs [7] are aimed to reduce or even avoid the injection of flux weakening current and its subsequent adverse effects. VF-PMSMs use low coercive force (H_c) PMs (or a combination of high and low H_c) what allows to change their magnetization in-situ, during normal machine operation [6]. The magnetization and demagnetization process involve the injection of large d-axis currents (from 3 to 20 times the nominal value), and precise PM magnetization control is still a research challenge [6, 8]. On the other hand, VLF-PMSMs are able to reduce the injection of flux weakening currents by using a special rotor design, keeping the PM magnetization state constant and avoiding the drawbacks of magnetization and demagnetization process. In Fig. 1.5, a comparison of conventional PMSM, VF-PMSM and VLF-PMSM designs is shown. The typical flux barriers present in conventional PMSM rotor are partially removed in VLF-PMSMs, allowing some of the PM flux to flow through the quadrature (q-) axis region (PM leakage flux) when no current or low magnitude current is injected in the q-axis. When large q-axis current is injected (high load conditions) the rotor q-axis region gets saturated and the PM flux can no longer flow through that rotor region (due to higher reluctance), linking with the stator coils and consequently increasing the PM flux linkage (PM leakage flux being reduced).

At low speeds, when higher torque is required (large q-axis current) the larger PM flux linkage allows the machine to meet the high torque density standards of PMSMs. However, at high speeds, the magnitude of the q-axis current is usually lower, reducing the PM flux linkage of VLF-PMSMs and the magnitude of flux-weakening currents, increasing the efficiency [7,9].

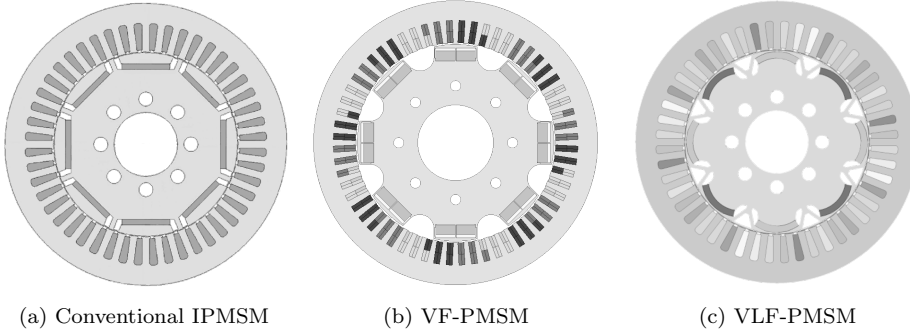


Figure 1.5: Comparison of conventional IPMSM, VF-PMSM and VLF-PMSM designs.

The introduction of these type of machines in the industry will reduce the losses at high speeds, increasing efficiency and driving range of the EVs and HEVs. Machine reliability is a major concern in the industry, PM temperature and torque production measurement or estimation being among the most important topics for PMSMs. Standard PMSMs, along with IMs and SynRMs, have been studied and reliable methods to estimate rotor temperature and produced torque are already present in the literature. However the extension of these techniques to VLF-PMSMs and VF-PMSMs is not straight forward due to their variable PM flux linkage and they are still under research. Their variable PM flux linkage leads to large inductance variations and, in the case of VLF-PMSMs, large cross-coupling inductances and parameter variations with stator current due to their rotor design. This thesis aims to extend these techniques to VLF-PMSMs.

1.2 Research motivation and overview

Independent to the PMSM design, PM thermal monitoring is a major concern since its strength decreases with temperature, which impacts the torque production capability. Additionally, excessive temperature can lead to irreversible demagnetization and even complete demagnetization if Curie Temperature is

reached. In the case of VF-PMSMs, the variation of PM magnetization places additional concerns, affecting the magnetization/demagnetization process and torque control [8]. In VLF-PMSMs, PM temperature affects the variable leakage flux property and reduces the accuracy controlling torque [9]. From the previous discussion, it can be concluded that knowledge of PM temperature is required for monitoring and control purposes.

This thesis addresses PM temperature and torque estimation methods in VLF-PMSMs. Several PM temperature and torque estimation methods can be found in literature for conventional PMSMs and they can be roughly classified into:

- **Thermal models:** consist of power sources that represent the power losses of the machine, thermal nodes that represent uniform temperature regions, thermal resistances that model the heat transfer between thermal nodes and heat capacitors that represent the heat storage characteristic (heat capacity) of the different machine parts [10–14]. To accurately model the thermal behaviour of the machine, all these elements require precise knowledge of stator and rotor geometry, materials and cooling system, as well as the environmental conditions, which makes them highly dependent on the machine design and application.
- **Back-EMF based methods:** estimate the magnet temperature from the PM flux linkage, typically by a linear relationship [14–18]. The PM flux linkage is obtained from the machine terminal voltages and currents, inductance maps and/or stator resistance being needed for non-zero current conditions. These methods do not require previous knowledge of the geometry and cooling system of the machine, but they are affected by the stator resistance variation with temperature and they cannot be used at very low speed or standstill due to the diminishing magnitude of the back-EMF.
- **Signal injection methods:** estimate the PM temperature by the machine electrical response to an injected, voltage or current, signal. This response is used to estimate an electrical variable that is supposed to vary with PM temperature, such as high frequency (HF) inductance, HF resistance or phase angle of HF phase harmonic. Several types of HF signal have been used to estimate these machine parameters, the most common being HF sinusoidal current or voltage signals [19–23]. These methods can work in the entire speed range of the machine as long as enough voltage is available to inject the signal. However they are sensitive to stator resistance variation with temperature, saturation and magnetoresistive effect [24]. They require

the injection of an additional signal, which places concerns from the losses, noise, vibration and torque ripple point of view.

PM temperature monitoring is important to prevent irreversible PM demagnetization, in addition the PM flux decreases as temperature increases before reaching the irreversible PM demagnetization. This PM flux reduction affects the torque production capability of the machine, reducing the maximum output torque achieved per injected ampere. The PM flux linkage reduction due to PM temperature can be compensated by appropriate machine torque control if the PM flux linkage is known. This is specially important in EV and HEV because they require precise control of the torque produced by the machine [25–27], torque measurement/estimation being therefore needed.

Precise torque measurement is expensive, requires room and extra cables, and introduces reliability concerns, torque estimation being therefore preferred [28–39]. Torque estimation methods present in the literature can be roughly classified into:

- **Torque equation-based methods:** constant machine parameters, such as PM flux linkage and inductances, are often used to estimate machine output torque. However, saturation and variable PM flux linkage effect would lead to large estimation errors. Look-up tables (LUTs) can be used to address the variation of these parameters with operating conditions. As a drawback, they need large memory storage, while they are not able to predict the effect of machine degradation due to aging
- **Indirect estimation methods:** use machine variables to indirectly estimate the output torque of the machine. Proposed indirect estimation methods can be roughly classified into:
 - ◇ *Torque estimation based on electric power and shaft speed.* This method uses stator current and voltages to calculate the electric power [31]. The accuracy of this method relies on the resolution of the rotor speed sensor and it cannot work at standstill.
 - ◇ *Torque estimation based on intelligent control.* Several approaches based on machine learning have been proposed in the literature: fuzzy neural networks [40], wavelet neural networks [39] and iterative learning methods [32]. All these methods require a previous training processes, which is specific for each machine, and the computational burden could involve the use of more costly and complex control units.

However, accurate estimation of PM temperature and produced torque in VLF-PMSM involve the use of machine parameters such as inductances, resistances and PM flux linkage. Due to the large variation of these parameters with stator current and temperature in VLF-PMSMs, the extension of the methods already present in the literature for classical PMSMs would lead to large estimation errors. This dissertation addresses PM temperature and output torque estimation in VLF-PMSMs, overcoming these limitations. The PM temperature estimation method that is presented in this thesis will be based on the machine PM flux linkage estimation, which will be obtained from the Back-EMF of the machine, while the torque estimation method that is presented in this thesis will be based on the general torque equation combined with a flux observer enhanced by the use of combined high and low frequency signal injection to estimate the machine parameters such as PM flux linkage, inductances and stator resistance. Finally, an online PM temperature measurement system has been specially designed to check the accuracy of PM temperature estimation methods. Accuracy of torque estimation methods will be obtained by means of a high-speed torque transducer. In all cases, simulation will be provided by means of FEA software and a VLF-PMSM prototype of an EV will be used to experimentally demonstrate the viability of the proposed methods.

1.3 Outline of the document

- **Chapter 1:** introduces the research line of this dissertation. This chapter includes an overview of the evolution of electric machines used in EVs and HEVs from DC machines in early 20th century to the new VF-PMSMs and VLF-PMSMs designs.
- **Chapter 2:** presents the VLF-PMSM model that will be used in this dissertation and its main differences compared to conventional PMSMs.
- **Chapter 3:** presents a PM temperature estimation method for VLF-PMSMs based on the PM flux linkage estimation. It overcomes the limitations of already available methods by considering the variation of the PM flux linkage with stator current.
- **Chapter 4:** presents a torque estimation method for VLF-PMSMs based on a Gopinath flux observer enhanced by a novel high and low frequency signal injection combination to estimate the relevant machine parameters for torque estimation.

- **Chapter 5:** presents a PM temperature estimation method for VLF-PMSMs working under six-step operation.
- **Chapter 6:** summarizes the main conclusions and contributions derived from this dissertation. Finally, future research lines aimed to improve the accuracy of proposed methods are also presented.
- **Appendix A:** presents the experimental setup used in this dissertation to provide experimental results, including a VLF-PMSM and a conventional PMSM. In order to verify the accuracy of the proposed estimation methods, the test bench will be equipped with a wireless thermocouple-based PM temperature measurement system and a torque sensor.

Chapter 2

VLF-PMSM Model

As previously introduced, the main difference of VLF-PMSMs with conventional PMSMs is their variable PM flux linkage capabilities. Their variable PM flux linkage capability is achieved by a special rotor design that partially removes the flux barriers present in conventional PMSM rotors. In conventional PMSMs, these flux barriers maximize the PM flux that links with stator coils and, therefore, minimize the PM leakage flux. On the other hand, VLF-PMSM rotor designs intentionally allow some of the PM flux to flow through the rotor increasing the PM leakage flux. This leakage flux flows through the rotor region between north and south poles, i.e. rotor q-axis region, allowing the PM flux linkage to be varied by q-axis current. When low magnitude q-axis current is injected, the flux bridges are not saturated allowing some part of the PM flux to flow through the rotor without linking with the stator, i.e. PM leakage flux. If the flux bridges get saturated by large q-axis flux (due to q-axis current) the PM flux is not longer allowed to flow through that path, linking with the stator and increasing the PM flux linkage and produced electromagnetic torque per injected ampere.

In Fig. 2.1, the VLF-PMSM that will be used in this dissertation is shown. This rotor design uses the “Y” shaped flux bridges between PMs to create the PM variable leakage flux characteristic. Its stator design consist of a distributed three-phase windings and it has no significant differences with the stator of other electric machines such as IMs, SynRMs and conventional PMSMs.

The VLF-PMSM model is similar to the PMSM model [41] but including

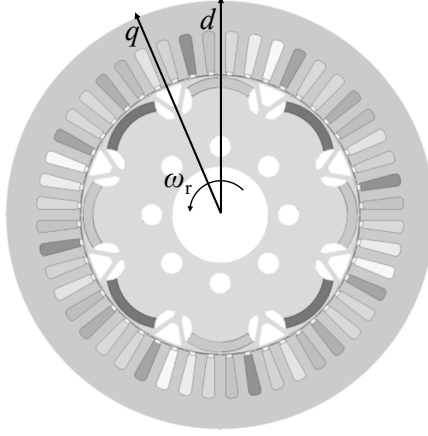


Figure 2.1: VLF-PMSM d- and q-axes.

a variable PM flux linkage. The voltage equations of the VLF-PMSM electric model can be expressed as (2.1) in the rotor synchronous reference frame, where v_{sd}^r and v_{sq}^r are the d- and q-axis stator voltages, i_{sd}^r and i_{sq}^r are the d- and q-axis stator currents, R_s is the stator resistance, λ_{sd}^r and λ_{sq}^r are the d- and q-axis flux linkages and ω_r is the rotor electrical speed.

$$\begin{aligned} v_{sd}^r(t) &= R_s i_{sd}^r(t) + \frac{d\lambda_{sd}^r(t)}{dt} + \omega_r \lambda_{sq}^r(t) \\ v_{sq}^r(t) &= R_s i_{sq}^r(t) + \frac{d\lambda_{sq}^r(t)}{dt} + \omega_r \lambda_{sd}^r(t) \end{aligned} \quad (2.1)$$

The d- and q-axis flux linkages can be expressed as a function of the d- and q- axis inductances (L_d and L_q) and the PM flux linkage (λ_{pm}) as in (2.2). As has been stated before, the main difference of a VLF-PMSM with conventional PMSMs is their variation of PM flux linkage with stator current. Therefore the variation of PM flux linkage should be considered in the d-axis flux linkage model. Additionally, the variation of both inductances due to both d and q-axis currents should be considered due to the relatively high cross-coupling between axes of VLF-PMSMs compared to conventional PMSMs [42].

$$\begin{aligned} \lambda_{sd}^r(t) &= L_d(i_{sd}^r, i_{sq}^r) i_{sd}^r(t) + \lambda_{pm}(i_d^r, i_q^r) \\ \lambda_{sq}^r(t) &= L_q(i_{sd}^r, i_{sq}^r) i_{sq}^r(t) \end{aligned} \quad (2.2)$$

In Figs. 2.2a and 2.2b, the d- and q-axis inductances of the VLF-PMSM that will be used in this dissertation are shown. Fig. 2.2c shows the PM flux linkage

vs. stator current, where the variable leakage flux property of the VLF-PMSMs can be observed. Additional parameters of the VLF-PMSM are shown in Table 2.1.

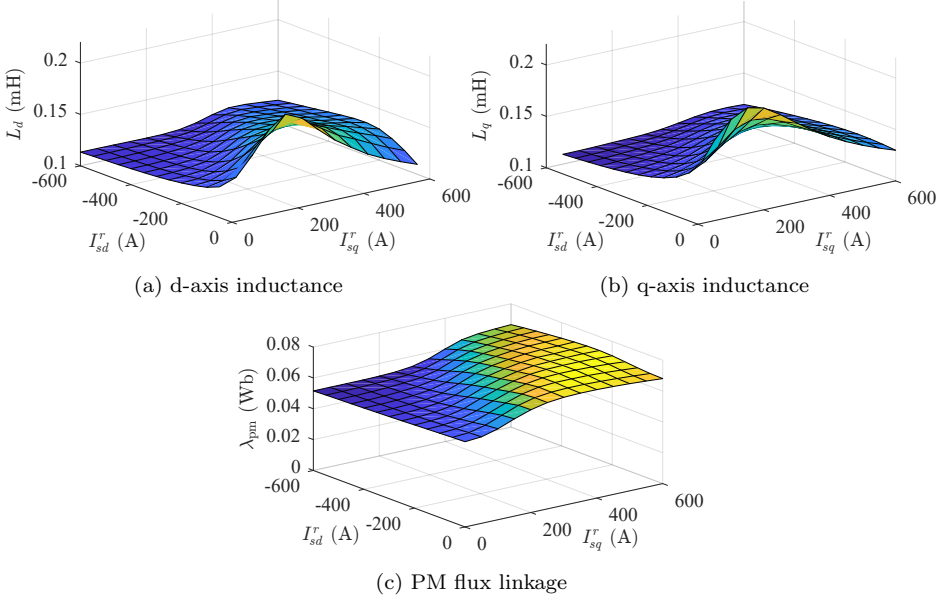


Figure 2.2: VLF-PMSM variables vs. stator current at $T_r = 20$ °C.

Table 2.1: VLF-PMSM parameters

P_{Rated} [kW]	I_{Rated} [A]	ω_r max. [r/min]	T_{Rated} [Nm]	$Poles$
110	640	10000	250	8

Finally, the electromagnetic torque of a VLF-PMSM can be expressed by (2.3) as function of stator flux linkages and currents [41], where P is the number of poles of the machine. This equation is valid for both conventional PMSMs and VLF-PMSMs. The d- and q-axis flux linkages include the variable PM flux linkage and inductance variations with stator current.

$$T(t) = \frac{3P}{2} [\lambda_{sd}^r(t) i_{sq}^r(t) - \lambda_{sq}^r(t) i_{sd}^r(t)] \quad (2.3)$$

Chapter 3

PM Temperature Estimation based on PM flux linkage in VLF-PMSMs

3.1 Introduction

3.1.1 The importance of PM temperature in PMSMs drives

PM thermal monitoring is a major concern in PMSMs, specially in EV & HEV applications as PMs typically set the thermal operating limit of a PMSM. Since the maximum operating temperature of the commonly used PMs is relatively low compared to other components, i.e. copper insulation, bearings, magnetic cores, etc. (see Table 3.1), having information of the current PM temperature of a given PMSMs drive, provides the following advantages:

- Prevents PM irreversible demagnetization of the machine: Coercitivity of a PM is reduced as the PM temperature increases (see Fig. 3.1), leading to a potential irreversible demagnetization due to the field produced by stator coils. Some regions of the PMs can also be partially demagnetized for operating temperatures near the PM thermal grade. If this occurs, the initial

Table 3.1: Maximum operating temperature of different electric machine parts.

Copper insulation	Bearings	Magnetic cores	Neodymium PM
120-650 °C	90-350 °C	200-500 °C	60-220 °C

magnetization state can only be restored when the PM is fully saturated again (i.e. re-magnetization process), what typically implies a disassembly of the machine. In industry, PMSMs manufacturers typically set a safety margin between the maximum operating temperature of the PMs and the PMs thermal grade in order to prevent partial demagnetization. When the PM temperature is an available variable in the drive, the thermal safety margin can be reduced, safely adjusting the peak power of the machine or the total time that the peak power can be applied, leading to a better utilization of the machine capabilities.

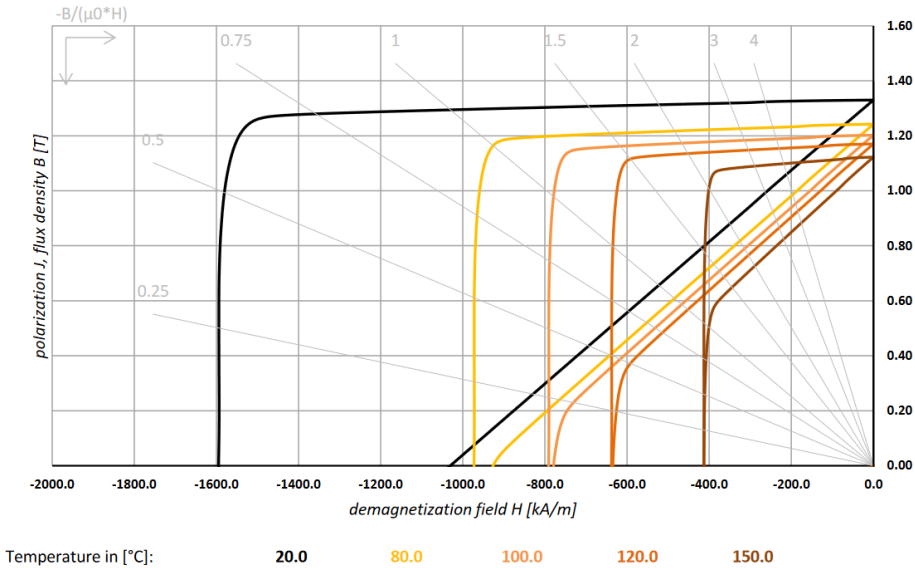


Figure 3.1: Variation of coercivity and remanence of a N42-type NdFeB magnet of SH thermal grade (150°C) [43].

- Enhances torque estimation techniques: As the PM temperature increases, the PM flux density is reduced. In PMSMs, this is reflected in a PM flux linkage reduction and therefore, the total developed torque of the machine

is lower for a given applied current. Additionally, the PM flux density variation produce changes in the saturation and, therefore, modify the inductance values. This change in the inductance values affects the reluctance torque, further modifying the MTPA trajectory. Torque estimation techniques based on estimated parameters may become inaccurate when the PM flux linkage drop due to temperature variations is not compensated. When the PM temperature is a known variable in the drive, the actual PM flux linkage can be directly calculated and the total developed torque of the machine can be estimated with higher accuracy.

- Controls overload capability of the machine: maximum power of the machine is typically provided by manufacturers along with a maximum time of application. If these two values are met during PMSM operation, the temperature limit of the weakest component of the drive should not be surpassed. However, these values are calculated experimentally for some given conditions and using the machine for high room temperatures may lead to the machine operating above limit conditions. On the other hand, if the PM temperature is available in the drive, the maximum overload capability of the machine can be updated dynamically, according to the operating conditions of the machine at any time. A dynamic update of the overload capability of the machine is specially important for traction applications, when the maximum power is only applied during the acceleration process for relatively short periods of time. This can be easily observed in Fig 3.2 where the standard World harmonized Light-duty vehicles Test Procedure (WLTC) class 3 driving cycle is used to test the range of EVs and HEVs.
- Provides information of abnormal operation, aging effects of the PMs and helps predictive maintenance: Constant monitoring of PM temperature can be further used to define operating patterns i.e. having the PM thermal time constant, temperature rise for a given torque applied can be predicted. Periodic comparison between predicted and expected temperature rise can help identifying abnormal operation. On the other hand, aging effects in PMs occur at a lower temperature than the $B(H)$ curve of the material might indicate [44] leading to higher PM eddy current losses under the same operating conditions [45]. However, if PM temperature is a known variable in the drive, aging effects could be monitored, thus helping to protect the machine against severe failures.

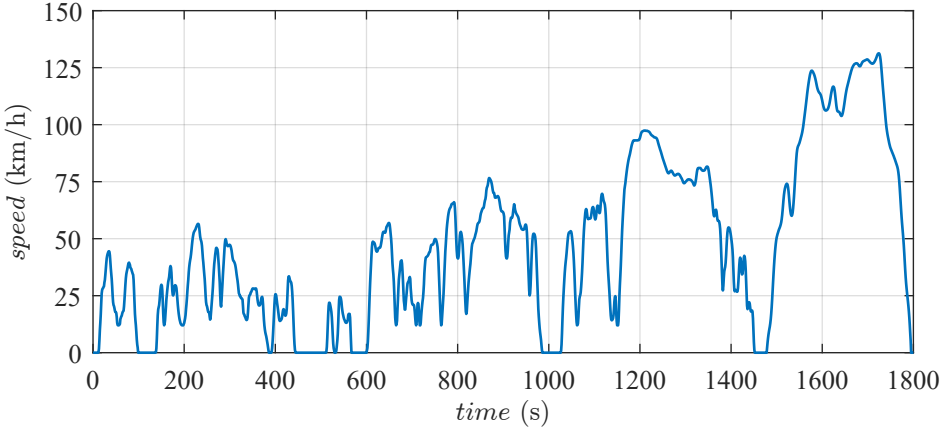


Figure 3.2: WLTC class 3 driving cycle speed profile.

3.1.2 Measurement and estimation techniques for PMSM drives

PM temperature can be measured, using temperature sensors or can be alternatively estimated by analyzing the electrical signals of the drive, the model of the plant, etc.

3.1.2.1 PM temperature measurement systems for PMSM drives

Depending on the type of temperature sensor, PM temperature measurement methods can be classified in non-contact and contact type sensors.

Non-contact type sensors are based on light reflection and/or emission, typically infrared (IR) light. These measurement systems require the PM surface to be visible, this being affordable for surface PMSMs but not feasible for interior PMSMs. In any case, for radial-flux-type PMSMs, only the side edges of the magnets can be observed in the rotor of assembled machines. Further concerns for this type of sensors include price, accuracy, mounting issues and reduced robustness.

Contact type sensors, such as thermistors, RTDs or thermocouples, can be mounted in the rotor of the machine using slip rings or wireless transmission devices to extract PM temperature information.

Nonetheless, equipping the machine with temperature sensors in the rotor implies a physical modification of its geometry, what complicates its design and

manufacturing process adding the task of inserting the sensing devices. Besides, due to the weak electrical signals that these kind of sensors offer at its terminals, an auxiliary electronic device is often required for conditioning and filtering purposes, what again penalizes the robustness and increases the cost of the whole drive system. As contact-type sensors are placed on the PMs surface in the rotor and the signal acquisition device is in the stationary part, slip rings or wireless transmission devices are often needed.

In [46, 47] a rotor temperature measurement system using thermocouples attached to the rotor of the machine and slip rings is proposed. These systems involve several issues including limitation in the number of slip rings, limited operating speed, electrical noise and material compatibility. For low power machines, this is a bulky device that extend the shaft length and consequently, the total volume of the machine.

Wireless transmission systems overcome these limitations [48, 49], but are susceptible to electromagnetic interference due to the strong magnetic fields in the machine and electromagnetic noise produced by the machine, converter and wires. Light based transmission [50] can mitigate the issues of electromagnetic interference at the cost of using a hollow shaft encoder since the light emitter has to be centered on a free end of the motor shaft.

In [49] a wireless transmission device is used to extract the PM temperature distribution of a 6 pole IPMSM machine. The temperature sensors are IC-type and every pole contains 15 temperature measurement points. In parallel, 15 hall-effect sensors are integrated in the same measurement system to provide a flux density map of each pole. It achieves high PM temperature measurement accuracy, 0.5°C and can be used at any operating point of the machine. The information is transmitted to a computer using a WiFi link and the whole system is battery-fed what limits the total operation time of the machine.

Despite the PM temperature measurement accuracy that the previous systems provides, they are obviously limited to laboratory applications: they are bulky, costly and represents the mechanically weakest component of the drive.

3.1.2.2 PM temperature estimation methods for conventional PMSM drives

PM temperature estimation methods can be roughly classified into thermal models based methods, [10–14], back-EMF based methods [14–18], and high frequency signal injection based methods [19–23].

Thermal models consist of power sources that represent power losses of the machine (i.e. eddy current losses in magnets and magnetic cores, hysteresis losses in magnetic cores, joule losses in coils, etc.), thermal nodes that represent uniform temperature regions (i.e. ambient, any of the parts of the machine), thermal resistances that model the heat transfer between thermal nodes and heat capacitors that represent the heat storage characteristic (heat capacity) of the different machine parts [10–14]. Lumped thermal models [10, 12, 14] estimate the PM temperature without providing information about the temperature distribution. However, these thermal models can be extended to 3D to provide temperature distribution estimation [13] at the cost of higher computational burden, limiting the applicability for online estimation. FEA simulations can also be used to estimate the PM temperature [11] but their applicability is limited to offline estimation. In all these cases, to accurately model the thermal behaviour of the machine, precise knowledge of stator and rotor geometry, materials and cooling system is required, as well as the environmental conditions, which makes them highly dependent on the machine design and application.

On the contrary, Back-EMF based and signal injection based methods do not require previous knowledge of the geometry or cooling system of the machine. They do require, however, the stator temperature knowledge to compensate for the stator resistance variation with temperature. However, this is not a major drawback in many cases, as the stator winding temperature is normally measured in standard PMSMs by means of RTDs or thermocouple sensors.

Signal injection based methods estimate the PM temperature by the machine electrical response to an injected, voltage or current, signal. This response is used to estimate an electrical variable that is supposed to vary with PM temperature, such as high frequency (HF) inductance, HF resistance or phase angle of a given HF harmonic component. Several types of HF signal have been used to estimate these machine parameters e.g. pulse signals, sinusoidal signal; the most common being HF sinusoidal current or voltage signals [19–23].

Rotatory HF voltage signals can be used to obtain the HF resistance of the machine and estimate the PM temperature [20]. The HF stator resistance and its variation with stator temperature must be known previously, but this is not a major issue since stator temperature sensors are usually installed in the stator coils. However, this method suffers from increased parameter sensitivity due to saturation and machine speed dependence. The use of a pulsating HF current in the d-axis of the machine while cancelling the HF current in the q-axis overcome these limitations [19]. The use of the injection of a voltage pulse in the d-axis

was also proposed in [21], but this method is sensitive to the machine operating point. Nevertheless, these methods are sensitive to stator resistance variation with temperature, and the magnetoresistive effect that shows up in machines equipped with NdFeB magnets under deep flux weakening operation [24]. An alternative has been proposed in [22,23] that studies the machine response of the speed HF component from the injection of a HF signal, this method being highly dependent on the speed/position sensor accuracy and its resolution. The main drawback of all these methods, however, is the need of an additional injected signal, which induces additional losses, noise, vibration and torque ripple in the drive.

Back-EMF based methods estimate the magnet temperature from the PM flux linkage, typically by a linear relationship in the whole current range [14–18] being a safe assumption in case of PMSMs since the changes in PM flux linkage with stator current is small in these type of machines. PM flux linkage is obtained from the machine terminal voltages and currents, inductance maps and/or stator resistance being needed for non-zero current conditions. These methods do not require previous knowledge of the geometry and cooling system of the machine, but they cannot be used at very low speed or standstill due to the inherent diminishing magnitude of the back-EMF.

In [15], a PM temperature observer based on current and voltage measurements, with the need of look-up tables (LUTs) to correlate stator current and flux, is presented. While current sensors are commonly available in industrial drive systems, voltage sensors are not usually present increasing the drive system cost. In [16], the current controller command is used instead of voltage sensors, additionally the effect of airgap length variation due to stator and rotor thermal expansion is addressed. In [17], an estimation method based on a Kalman filter with a linear state-space model and LUTs is proposed. In [14], the estimation range is extended to low speeds and standstill by including a thermal model based on a particle swarm optimization commissioning process. In [51], the use of high bandwidth measurements of PWM voltage and current waveforms for PM flux linkage and temperature estimation is presented, this method is sensitive to machine inductance when the d-axis current is non-zero, making this method less interesting for interior PMSMs. Major advantages/limitations of back-EMF based estimation methods are summarized in Table 3.2.

Table 3.2: PM temperature estimation based on PM flux linkage methods

	No need of voltage sensors	No PM flux linkage behaviour	No need of LUTs
[14]	-	✗	✗
[15]	✗	✗	✗
[16]	✓	✗	✗
[17]	✓	✗	✗
[18]	✓	✗	✗
[51]	✗	✗	✓
Proposed method	✓	✓	✗

3.1.3 PM temperature estimation methods for VLF-PMSM drives

The extrapolation of the available PM temperature estimation methods, listed in the previous subsections, to VLF-PMSMs leads to large estimation errors due to its inherent inductances variation and PM flux linkage variation with stator current [7]. This dissertation proposes the use of a small-amplitude, low frequency, square-wave current signal to estimate the PM flux linkage. The PM temperature will be estimated using a PM flux linkage LUT overcoming the mentioned limitations. This method uses a voltage model flux observer, presenting the typical speed range constrains of back-EMF based methods.

3.2 PM temperature estimation based on PM flux linkage variation

This section describes the principles and implementation of the proposed temperature estimation method.

As already stated in the preceding discussion, PM flux linkage decreases as PM temperature increases [19–23, 52]. Consequently, PM flux linkage is a reliable metric for PM temperature estimation.

It can be seen from (3.1) that the d-axis inductance L_d and PM flux linkage λ_{pm} can be estimated from λ_{sd}^r by producing small variations in the d-axis current

I_{sd}^r . These variations should be small enough to produce a linear response. PM flux linkage (3.1)-(3.2) will be estimated using the method proposed in [9], the principle of operation of this method is schematically shown in Fig. 3.3. Stator flux linkage is obtained using a flux observer based on (3.3)-(3.4), where λ_{sd}^s and λ_{sq}^s are d- and q-axis flux linkages in the stationary reference frame, I_{sd}^s and I_{sq}^s are the d- and q-axis stator currents in the stationary reference frame, R_s is the stator resistance, and V_{sd}^s and V_{sq}^s are the d- and q-axis stator voltages in the stationary reference frame.

$$\lambda_{sd}^r = L_d I_{sd}^r + \lambda_{pm} \quad (3.1)$$

$$\lambda_{sq}^r = L_q I_{sq}^r \quad (3.2)$$

$$\lambda_{sd}^s = \int (V_{sd}^s - R_s I_{sd}^s) dt \quad (3.3)$$

$$\lambda_{sq}^s = \int (V_{sq}^s - R_s I_{sq}^s) dt \quad (3.4)$$

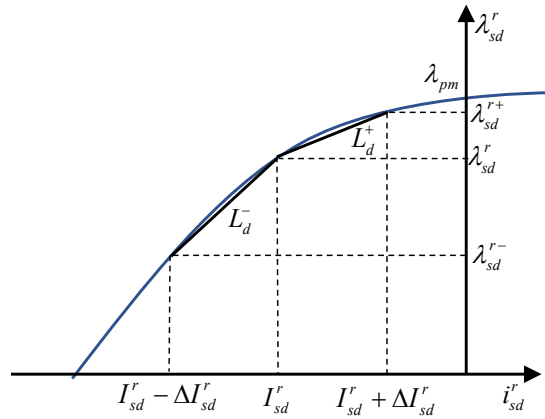


Figure 3.3: Graphical approximation for PM flux linkage estimation.

In order to estimate the PM temperature from the measured currents and the voltages commanded by the current regulators, the block diagram shown in Fig. 3.4 is developed. Fig. 3.4 also shows the torque/current control block diagram of a VLF-PMSMs. The main blocks of the PM temperature estimation block diagram being:

- **Flux observer:** estimates the stator flux linkage ($\hat{\lambda}_{sdq}^r$) from the measured stator current (i_{sdq}^r) and the commanded stator voltage (i.e. the output of the fundamental current regulator, v_{sdq}^{r*}).
- **PM flux linkage estimator:** estimates the PM flux linkage, $\hat{\lambda}_{pm}$, from the stator flux linkage provided by the flux observer, $\hat{\lambda}_{sdq}^r$, in combination with the response of the machine to a small-amplitude, low frequency, quasi-square-wave current that will be injected on top of the fundamental current (Δi_{sdq}^{r*}) [9]. A logical signal “Trig” is used to synchronize the injection of this signal with the estimation algorithm, since this signal will not be injected continuously.
- **Look-up table (LUT):** it links the estimated PM flux linkage and the PM temperature.

All these blocks are described in detail in the following subsections:

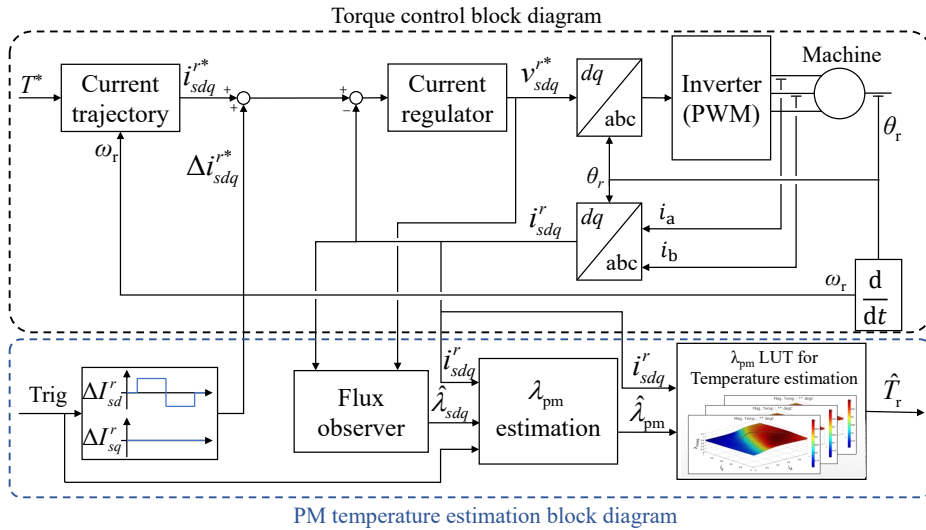


Figure 3.4: Temperature estimation system scheme.

3.2.1 Flux observer

Different stator flux observers have been proposed in the literature, the main types being voltage model based (3.3)-(3.4) [53, 54], current model based (3.1)-(3.2) [55] and Gopinath type [53]. The current model (3.1)-(3.2) can be used to

estimate stator flux in the whole speed range of the machine, but parameters, such as PM flux linkage and inductances, must be previously known, therefore not being feasible for PM flux linkage estimation. On the other hand, voltage model (3.3)-(3.4) can be used to estimate machine stator flux at high speeds [54], at low speeds it becomes inaccurate due to the diminishing magnitude of the Back-EMF with the speed and it cannot be used at standstill. In addition, as a pure integrator is required to estimate the flux, there is an initial estimation error (integration constant) which needs to be compensated [53, 56]. Voltage (at high speed) and current (at low speed including standstill) models can be combined in a Gopinath type flux observer [53], a PI controller being used to make a smooth transition between models. These three observer types are shown in Fig. 3.5.

The controller bandwidth will set the transition frequency from current to voltage model. This type of flux observer provides reliable estimation in the whole speed range of the machine, including standstill, being more sensitive to machine parameters (such as PM flux, inductances and stator resistance) at low speeds due to the current model parameter dependency and small magnitude of the Back-EMF. The advantages and drawbacks of the three models are summarized in Table 3.3.

Table 3.3: Advantages and drawbacks of flux models

	Current model	Voltage model	Gopinath
Low parameter sensitivity at high speed	✗	✓	✓
Estimation in the whole speed range, including standstill	✓	✗	✓

From the previous discussion, it is concluded that, although the current model and Gopinath type flux observers can be used in the whole speed range of the machine, they do not provide additional information about the PM flux linkage since the PM flux linkage is an input parameter in the current model (3.1)-(3.2), i.e. they cannot be used for PM flux linkage estimation. Despite the fact that voltage model flux observer cannot work in the entire speed range of the machine, it can be used at medium to high speeds where EVs, and HEVs are more susceptible of working under overload conditions. Therefore, a voltage model (3.3)-(3.4) flux observer in the stationary reference frame will be used for PM temperature estimation in this dissertation.

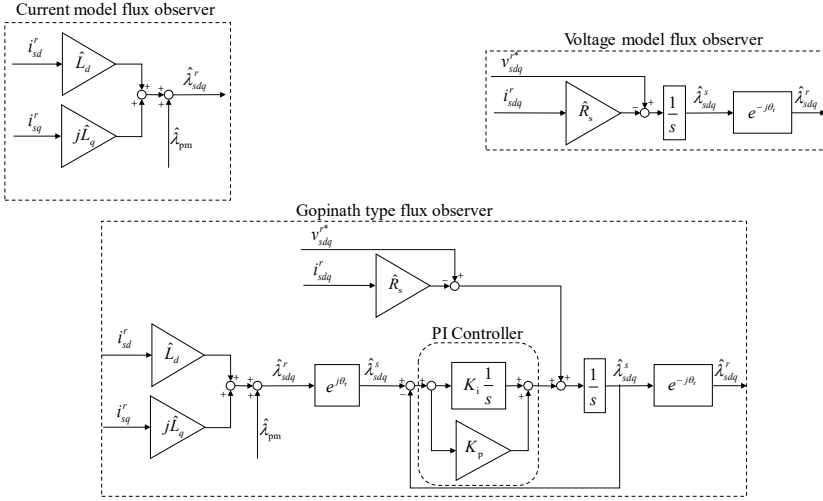


Figure 3.5: Schematic representation of voltage, current and Gopinath type flux observers.

Fig. 3.6 shows the implementation of the flux observer based on the voltage model (3.3)-(3.4). Current regulator voltage command is used instead of voltage measurements, inverter nonlinearities caused by dead-time being considered [57], see Appendix A. The resistive term is decoupled by means of the measured resistance at 20 °C and stator temperature sensors. The estimated stator flux linkage in the stationary reference frame, $\hat{\lambda}_{sdq}^s$, is obtained from (3.3)-(3.4) after applying a first order high pass filter (HPF) to avoid the infinite DC gain of the pure integrator [58]. The cutoff frequency of the HPF was selected as a trade-off between settling time and the negative effects of the gain and phase shift introduced by the HPF. In order to minimize the effects of gain and phase shift, the cutoff frequency could be reduced at the cost of higher settling times. Additionally, adaptive (electrical speed dependent) phase and magnitude compensation of HPF effects have been implemented. This gain and phase shift introduced by the HPF can be easily compensated due to its digital implementation and known response, see (3.5), where s is the Laplace variable and ω_{HPF} is the filter cutoff frequency in rad/s.

$$HPF(s) = \frac{s}{s + \omega_{HPF}} \quad (3.5)$$

The estimated stator flux linkage in the rotor reference frame, $\hat{\lambda}_{sdq}^r$, is ob-

tained by applying Park's transformation to the estimated stator flux linkage; a first order low pass filter (LPF) is finally used to eliminate high frequency harmonics of the stator flux linkage; i.e. only the fundamental component of the stator flux linkage will be used for temperature estimation. However, the cutoff frequency of the LPF should be high enough to allow a precise flux estimation during transients and varying conditions. This is specially relevant for the PM flux linkage estimation method that will be used in section 4.2.1, where a small variation of the operating point (low-frequency low-magnitude quasi-square wave current injection) is used to estimate the PM flux linkage. In this case, lower cutoff frequencies of the LPF could lead to estimation delays due to the larger settling time.

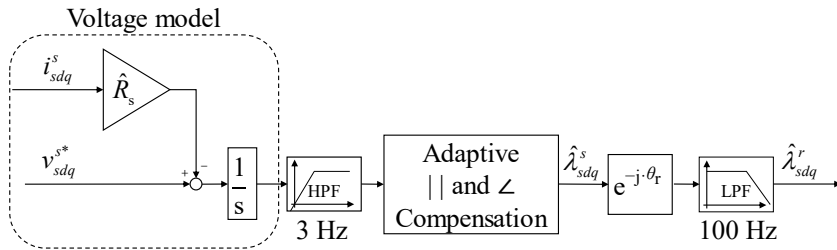


Figure 3.6: Voltage model flux observer in stationary reference frame.

3.2.2 PM flux linkage estimator

Since PM flux linkage has a large variation with stator currents in VLF-PMSMs, it should be estimated considering the saturation effect. In this dissertation, it is estimated from the stator flux linkage when a small-amplitude, low frequency, quasi-square wave current is superimposed on top to the fundamental current [9]. The stator d-axis flux linkage response from the injected d-axis current will be used to estimate the PM flux linkage, as shown in Fig. 3.7. The frequency of the injected signal should be small enough to ensure the correct reference tracking of current regulators. However, the dynamic response is not important since the evaluation is performed with the steady-state values of d-axis current and flux linkage. This signal does not need to be injected continuously, instead it can be injected at a fixed time rate (seconds or minutes, since rotor temperature time constant is usually quite large), or after the operating conditions of the machine have changed (i.e. going from high saturation to low saturation region). The specific values will depend on the machine design.

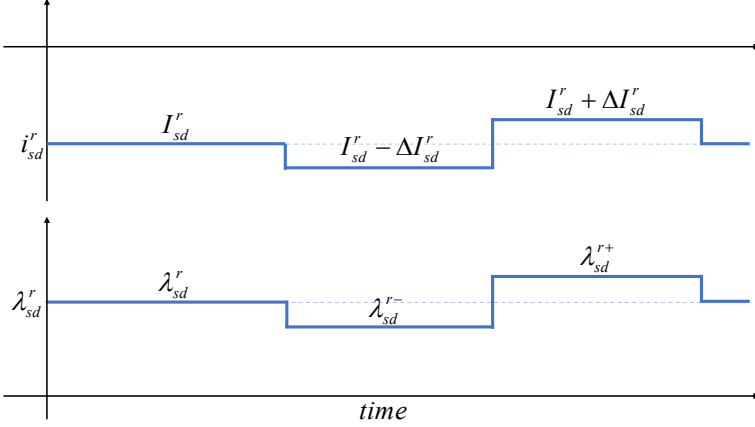


Figure 3.7: Schematic representation of the injected stator d-axis current, fundamental and small-amplitude, low frequency, square-wave currents, (i_{sd}^r) and resulting stator d-axis flux (λ_{sd}^r).

The d-axis stator flux linkage, λ_{sd}^r , is represented by (3.6) where the PM flux linkage and d-axis inductance are assumed to change with d-axis current. The magnitude of the d-axis current step should be as small as possible to minimize these variations, while keeping an acceptable signal-to-noise ratio. λ_{sd}^{r+} is the d-axis flux linkage when positive d-axis current step, i.e. $+\Delta I_{sd}^r$, is applied (3.7), while λ_{sd}^{r-} is the d-axis flux linkage when negative d-axis current step, i.e. $-\Delta I_{sd}^r$, is applied (3.8). The stator flux linkages, $\hat{\lambda}_{sd}^r$, $\hat{\lambda}_{sd}^{r+}$ and $\hat{\lambda}_{sd}^{r-}$, are estimated using the flux observer discussed in the previous subsection. The inductances L_d^+ and L_d^- are expressed in (3.9) and (3.10) by assuming a linear inductance behaviour during the injection of the positive and negative ΔI_{sd}^r . $\hat{\lambda}_{pm}^+$ (estimated PM flux linkage when applying positive $+\Delta I_{sd}^r$) and $\hat{\lambda}_{pm}^-$ (estimated PM flux linkage when applying negative $-\Delta I_{sd}^r$) are estimated from (3.11) and (3.12) respectively. (3.11) and (3.12) are obtained by substituting (3.9) and (3.10) into (3.7) and (3.8). Finally, $\hat{\lambda}_{pm}$ is obtained as the average of $\hat{\lambda}_{pm}^+$ and $\hat{\lambda}_{pm}^-$ in (3.13) [9].

$$\lambda_{sd}^r = \lambda_{pm} + L_d I_{sd}^r \quad (3.6)$$

$$\lambda_{sd}^{r+} = \lambda_{pm}^+ + L_d^+ (I_{sd}^r + \Delta I_{sd}^r) \quad (3.7)$$

$$\lambda_{sd}^{r-} = \lambda_{pm}^- + L_d^- (I_{sd}^r - \Delta I_{sd}^r) \quad (3.8)$$

$$L_d^+ = \frac{\lambda_{sd}^{r+} - \lambda_{sd}^r}{\Delta I_{sd}^r} \quad (3.9)$$

$$L_d^- = \frac{\lambda_{sd}^{r-} - \lambda_{sd}^r}{-\Delta I_{sd}^r} \quad (3.10)$$

$$\hat{\lambda}_{pm}^+ = \frac{1}{\Delta I_{sd}^r} \left[(I_{sd}^r + \Delta I_{sd}^r) \hat{\lambda}_{sd}^r - I_{sd}^r \hat{\lambda}_{sd}^{r+} \right] \quad (3.11)$$

$$\hat{\lambda}_{pm}^- = \frac{1}{\Delta I_{sd}^r} \left[I_{sd}^r \hat{\lambda}_{sd}^r - (I_{sd}^r - \Delta I_{sd}^r) \hat{\lambda}_{sd}^{r-} \right] \quad (3.12)$$

$$\hat{\lambda}_{pm} = \frac{\hat{\lambda}_{pm}^+ + \hat{\lambda}_{pm}^-}{2} \quad (3.13)$$

3.2.3 PM Temperature estimation

PM temperature estimation using PM flux linkage is especially challenging in VLF-PMSMs due to the variation of PM flux linkage with the stator current. LUTs will be used to compensate for this effect [9]. LUTs are built storing the estimated PM flux linkage ($\hat{\lambda}_{pm}$) values for different currents and PM temperatures. Fig. 3.8 shows an example of LUT obtained with FEA from (3.7)-(3.13) after injecting a quasi-square-wave current signal which provides the PM flux linkage vs. stator current and PM temperature for the VLF-PMSMs test machine that will be used for the experimental verification of the method. The VLF-PMSM and injected signal characteristics are detailed in the next section. It can be observed from Fig. 3.8 that the PM flux linkage decreases as the PM temperature (T_r) increases; this variation will be used for temperature estimation. It can be also observed that the PM flux linkage is heavily affected by stator current, which was an expected result due to the inherent variable leakage flux property of VLF-PMSMs [9].

3.3 Simulation results

Fig. 2.1 shows the schematic representation of the VLF-PMSMs that will be used both for simulation and experimental verification of the proposed method, the parameters being shown in Table 2.1. The machine is a 110kW, 8 poles VLF-PMSM.

■ $T_r = 20$ °C, ■ $T_r = 50$ °C, ■ $T_r = 80$ °C, ■ $T_r = 110$ °C, ■ $T_r = 140$ °C

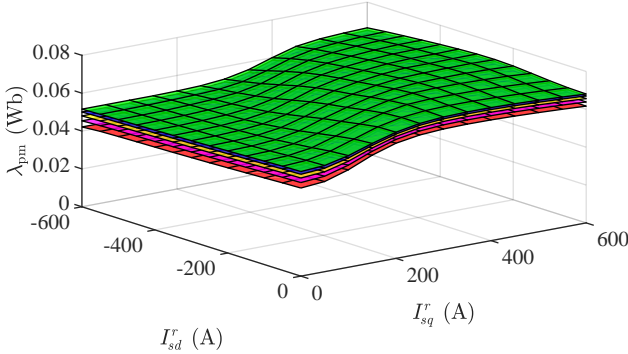
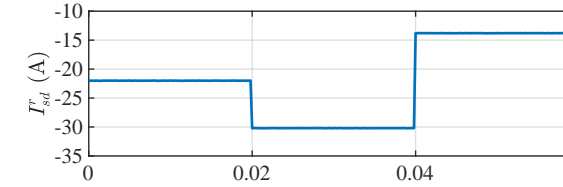


Figure 3.8: FEA results. PM flux linkage vs. stator current and PM temperature LUTs. $\omega_r=3750$ r/min, $T_r=20, 50, 80, 110$ and 140 °C.

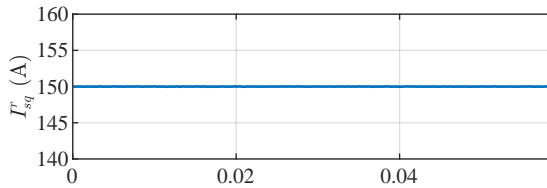
Fig. 3.9a and 3.9b show the d- and q-axis currents, respectively. A quasi-square-wave current of $|\Delta I_{sd}^r|=8.2$ A (0.013 pu) is seen to be superposed on top of the fundamental d-axis current. Fig. 3.9c and 3.9d show the estimated stator d- and q-axis flux linkages using the flux observer described in section 3.2.1, for five different PM temperatures. After the PM flux linkage is estimated from (3.7)-(3.13), it is used as an input to LUTs, from which temperature is estimated. During normal operation of the machine, the current operating point and estimated PM flux linkage does not necessarily match with the stored values, in that case, a 3D interpolation must be performed.

The 3D interpolation is performed in three steps: (i) interpolation along the d-axis current; (ii) interpolation along the q-axis current; (iii) interpolation along the PM flux linkage axis. The first two interpolations are used to predict the PM flux linkage at stored temperatures (i.e. 20, 50, 80, 110, 140 °C) at the actual current. Then, the PM temperature can be estimated by interpolation of predicted PM flux linkage (result from steps (i) and (ii)) and the estimated PM flux linkage (see Fig. 3.6). Three different interpolation methods have been evaluated: linear interpolation, cubic spline interpolation and, finally, a combination of linear interpolation for d- and q-axis with quadratic regression for PM flux linkage axis. These interpolations and regression are shown in Fig. 3.10 for one operating point ($I_{sdq}^r = 0$). The linear interpolation have lower computational burden than cubic spline interpolation and quadratic regression. Cubic spline interpolations have the largest computational burden and memory cost but usually provide high

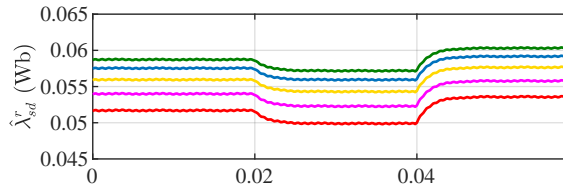
■ $T_r = 20$ °C, ■ $T_r = 50$ °C, ■ $T_r = 80$ °C, ■ $T_r = 110$ °C, ■ $T_r = 140$ °C



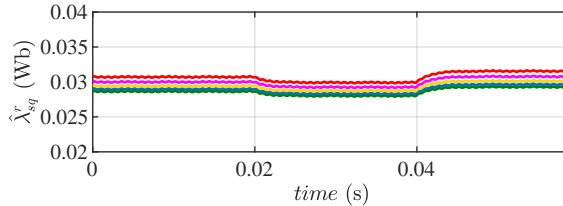
(a) d-axis current



(b) q-axis current



(c) Estimated d-axis stator flux linkage



(d) Estimated q-axis stator flux linkage

Figure 3.9: FEA results. 3000 r/min, $T = 50$ Nm, $T_r = 20, 50, 80, 110$ and 140 °C.

interpolation accuracy. The quadratic regression have a computational burden and memory use between linear interpolation and cubic spline interpolation. It provides a reasonable fit accuracy as can be seen in Fig. 3.10.

Fig. 3.11 shows the temperature estimation error resulting from steps (i)-(iii) for the three interpolation methods that have been evaluated. It is observed that cubic spline interpolation shows the best performance in terms of temperature error, while the linear interpolation method exhibits larger error. Quadratic re-

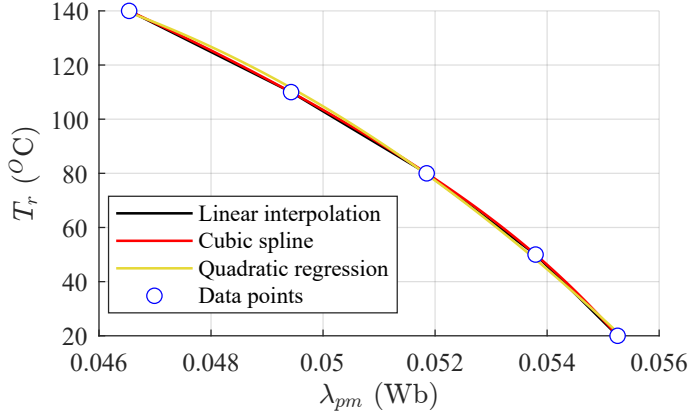


Figure 3.10: Comparison of linear interpolation, cubic spline interpolation and quadratic regression for $I_{sd}^r = 0$.

gression shows slightly worse results than cubic spline interpolation but at a lower computational cost. For final temperature estimation results, linear interpolation will be used in this dissertation as it shows the lowest computational burden and low memory size. In other applications where the computational burden and memory requirements are not a limiting factor, spline interpolations could be used instead. Finally, Fig. 3.12 shows the PM temperature estimation error of the proposed method using linear interpolations of LUTs. Estimation error is seen to be within 10°C .

■ Linear Interpolation, ■ Spline Interpolation, ■ Quadratic Regression

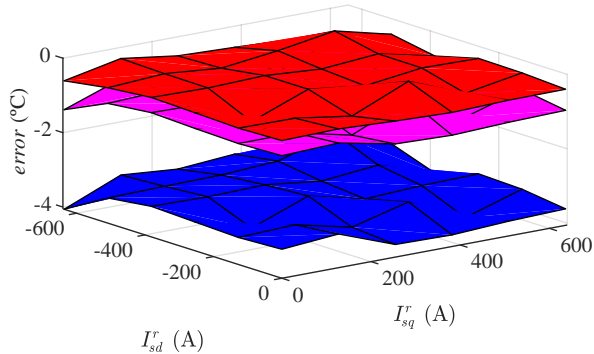


Figure 3.11: FEA results. Introduced temperature estimation error by PM flux interpolations vs. stator current at $T_r = 80^\circ\text{C}$ and $\omega_r = 3750$ r/min.

■ $T_r = 20$ °C, ■ $T_r = 50$ °C, ■ $T_r = 80$ °C, ■ $T_r = 110$ °C, ■ $T_r = 140$ °C

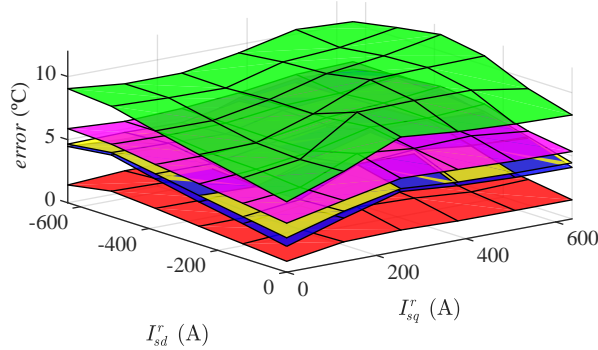


Figure 3.12: FEA results. Temperature estimation error. $\omega_r = 3750$ r/min, $T_r = 20, 50, 80, 110$ and 140 °C.

3.4 Experimental results

The test bench used for the experimental verification and the wireless PM temperature measurement system used to verify the accuracy of the proposed method can be seen in Appendix A. In order to estimate the PM flux linkage the previously described small-amplitude quasi-square wave current signal is injected on top of the fundamental current wave. Fig. 3.13a and 3.13b show the measured d- and q-axis stator currents, similar to Fig. 3.9 and for the same operating conditions of the machine, $T = 50$ Nm and $\omega_r = 3000$ r/min. Fig. 3.13c and 3.13d show the estimated d- and q-axis stator flux linkage, respectively. In Fig. 3.13c the response of the stator flux to the injected square-wave can be readily observed, from which the PM flux linkage is obtained, see section 3.2.2. A small cross coupling between d- and q-axis can be observed in Fig. 3.13d. This observed cross coupling is an expected result due to the inherent coupling between d- and q-axes in VLF-PMSMs produced by the rotor flux bridges, which are used to create the variable PM leakage flux, as previously described.

The PM flux linkage is obtained for different temperatures ($T_r = 20, 50, 80$ and 110 °C) using the PM flux linkage estimation method presented in section 3.2.2. Fig. 3.14 shows the estimated PM flux linkage, extracted from micro-controller, during a commissioning process along with the FEA results at 20°C for comparison. It can be observed that the experimental results exhibit lower PM flux linkage than FEA results, due to a lower PM magnetization level in the

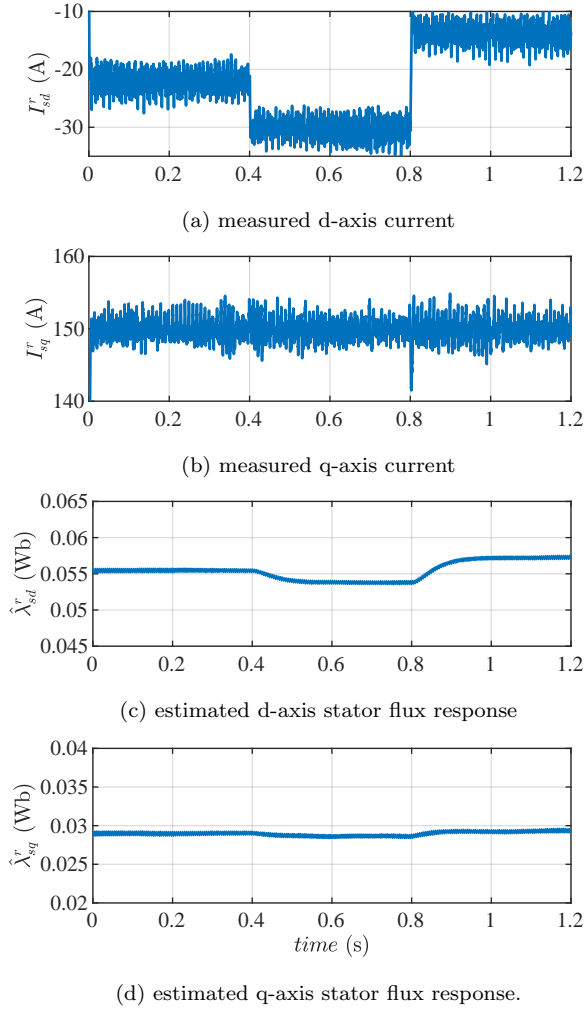


Figure 3.13: Experimental results. $\omega_r = 3000$ r/min, $T = 50$ Nm.

actual machine. It is also noted that the experimental results have been limited to 450 A due to inverter maximum current limitations, see Fig. 3.14. The results shown in Fig. 3.14 will be used as commissioning process and they will be stored in the LUTs to be later used for PM temperature estimation during machine normal operation. Using these results, the FEA model can be adjusted to take into account the actual PM magnetization present in the test machine, potentially reducing the commissioning process.

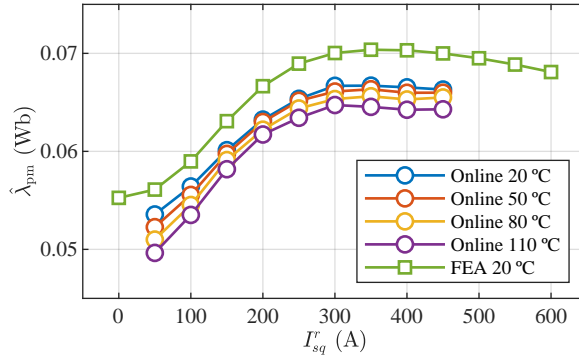


Figure 3.14: Experimental results. Estimated PM flux linkage and FEA results vs. q-axis stator current. $\omega_r = 3000$ r/min, $T_r = 20, 50, 80$ and 110 °C.

Using the LUTs and the PM flux linkage, the PM temperature is estimated online with the machine working in steady-state. Fig. 3.15a and 3.15b show the estimated PM flux linkage and estimated PM temperature, respectively; the measured PM temperature (using the wireless PM temperature measurement system) is also shown in Fig. 3.15b. Fig. 3.15c shows the estimation error which is seen to be within ± 4 °C.

In order to verify the accuracy of the proposed method in the whole torque vs. speed characteristic of the machine, analogous experiments to the one shown in Fig. 3.15 have been performed. Due to the large number of operating points to be tested and the large duration of each experiment (around 1 hour), the method performance will be analyzed in terms of mean estimation error (3.14) and the maximum absolute error (3.15) during the whole experiment duration; the operating point shown in Fig. 3.15 is marked “*” in Fig. 3.16.

$$\text{Mean}(\text{error}) = \text{mean}(\hat{T}_r - T_r) \quad (3.14)$$

$$\text{Max}|\text{error}| = \text{max}(|\hat{T}_r - T_r|) \quad (3.15)$$

Torque has been limited to 100 Nm due to the inverter current limit of 450 A; the proposed method has been verified for a minimal speed of 500 revolutions per minute (r/min) due to the intrinsic limitations of the voltage-model based flux observer at low speed. This speed is rather low compared to the speed range of the machine (10000 r/min). Furthermore, the power losses and temperature

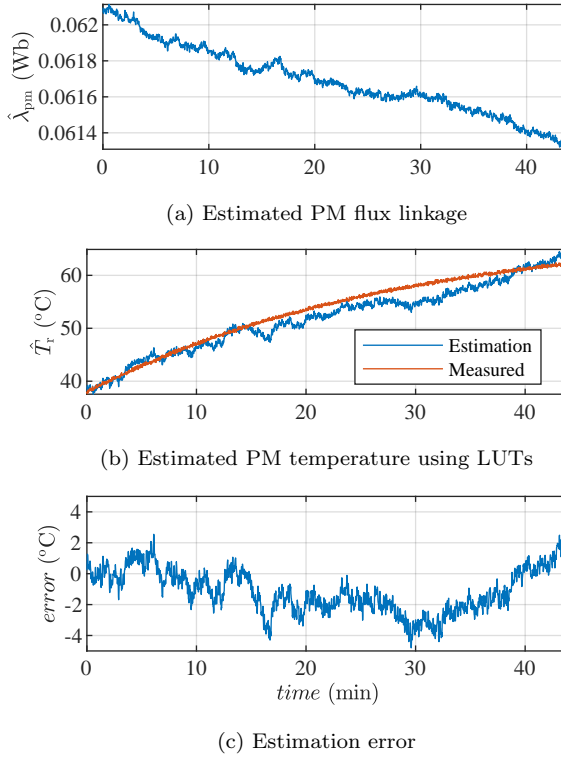
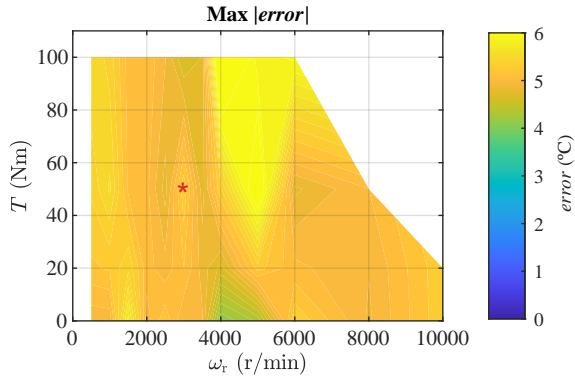


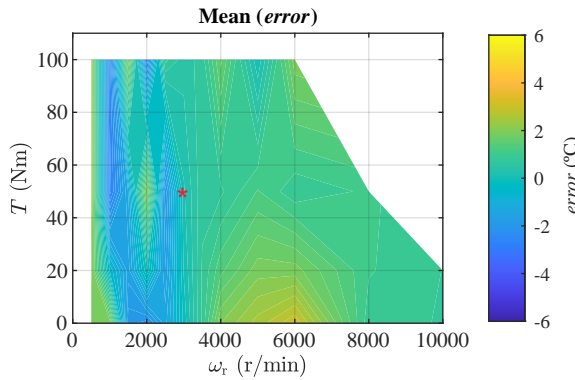
Figure 3.15: Experimental results. $\omega_r = 3000$ r/min, $T = 50$ Nm.

increase in the PM and rotor at low speeds is lower than at high speeds, where the hysteresis and Eddy current losses are not negligible. This method can be extended to lower speeds, but increased error might be expected due to the stator resistance sensitivity increase. Fig. 3.16a shows the absolute maximum error obtained during the experiment for each operation point, while Fig. 3.16b shows the mean error during the experiment for each operating condition. It can be observed that the peak temperature estimation error is $<6^{\circ}\text{C}$, while the mean estimation error for the entire experiment is within $\pm 3^{\circ}\text{C}$. These results are considered precise enough for PM temperature monitoring purposes and could be used for torque control compensation to counteract the PM flux linkage variation due temperature. The precision is lower than some of the PM measurement devices previously described but the proposed method does not affect the reliability of the drive system. Therefore, this estimation method can be used to overcome the mentioned limitations of operating the drive without PM temperature knowl-

edge such as preventing irreversible demagnetization and dynamically update the overload capability of the machine.



(a) Maximum absolute error during the experiments

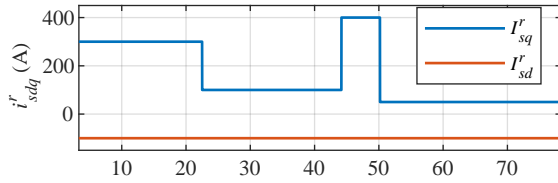


(b) Mean error during the experiments

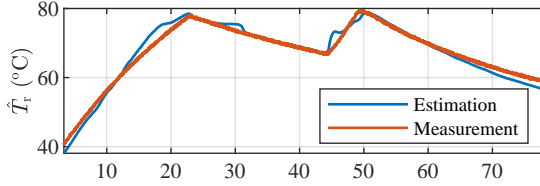
Figure 3.16: Experimental results in the torque vs. speed region. “*”: operating point shown in Fig. 3.15.

Finally, Fig. 3.17 shows experimental results during load transients: in the first 22 minutes, a 0.5 pu current is injected in the q-axis and the rotor temperature reaches almost 80 °C; at minute 22, the machine load varies and the q-axis current decreases to 0.16 pu; from minute 22 to minute 44, the rotor decreases its temperature to 65 °C; at minute 44, the load is increased again and the q-axis current reaches 0.63 pu; this operating point is kept only during the next 6 minutes due to the stator temperature limit, during this time the rotor reaches 80 °C; at minute 50, the load is decreased to 0.08 pu q-axis current and the rotor cools

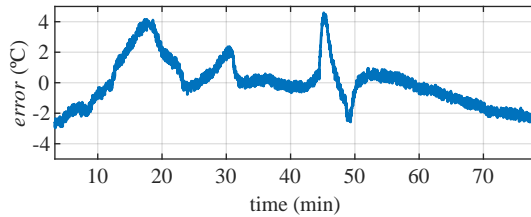
down until the end of the experiment, reaching 60 °C. Fig. 3.17a shows the d- and q-axis currents, Fig. 3.17b shows the estimated and measured temperatures and Fig. 3.17c shows the temperature estimation error. It can be observed from Fig. 3.17c that the peak error is <math><5^{\circ}\text{C}</math>, but most of the time it is within a 2 °C window. The performance of the method during standard driving cycles is out of the scope of this dissertation, but the presented results during transients shows that the method performance is not compromised by transient operation, exhibiting similar estimation errors than in the steady state experiments.



(a) d and q-axis current used during the experiment



(b) Estimated and measured rotor PM temperature



(c) Estimation error

Figure 3.17: Experimental results. $\omega_r = 3000$ r/min, $T = 50$ Nm.

3.5 Conclusions

A method for PM temperature estimation in VLF-PMSMs based on the PM flux linkage variation with temperature has been proposed. PM flux linkage

is obtained from the stator flux linkage of the machine after applying a small-amplitude, low frequency, quasi-square-wave current signal, which is superposed on top of the fundamental current excitation. The method requires LUTs linking the PM flux linkage vs. stator current and PM temperature. Simulation and experimental results have been provided to demonstrate the validity of the proposed technique. The performance of the proposed method has been verified by means of simulation and experimentally.

Chapter 4

Torque Estimation

4.1 Introduction

Electric traction systems are generally based on torque-controlled electric drives as this is the way of controlling the acceleration of the entire mobility system. Having the torque variable available for the drive, enables the application of techniques to reduce torque pulsations, that are naturally produced in the machine by current and flux harmonics, cogging torque or magnetization state asymmetries. The availability of the total developed torque can also help verifying the performance of PMSMs under the MTPA trajectory [59], implement early fault detection strategies [60], or use it as a redundant parameter for improving safety [61]. Adequate use of this variable confers reliability, safety and high efficiency to the drive. However, the electromagnetic torque developed by the electric machine depends on the load current (q-axis current), the field current (d-axis current), the PM flux linkage and inductances, being not linear due to magnetic saturation of ferromagnetic materials. In addition, modeling the torque becomes challenging as it depends on factors like PM temperature.

EVs & HEVs require precise control of the torque produced by the machine [25–27] for several reasons. Positive torque is used to accelerate the vehicle using the reference provided by the accelerator pedal. A precise torque control is reflected in a smooth and easy controllability of the vehicle speed. The torque

control is even more important and complex for the vehicle during the braking process. In order to improve the efficiency and driving range of the EVs & HEVs, regenerative braking is commonly used and the electrical power generated by this process should be absorbed by the vehicle battery. In some applications like railway or race cars, where the delivered regenerative power is larger than the battery can absorb, auxiliary energy storage systems (such as super-capacitors or small flywheels) are used as short-term energy buffers. Therefore, the torque (and power) applied by the electric machine should be dynamically limited considering the peak power that these energy storage systems are able to withstand. Furthermore, mechanical breaks are also included in EVs & HEVs in order to increase the total braking capability, redundancy and safety reasons. In these applications, the maximum and instantaneous applied torque should be precisely calculated in order to make a correct distribution of braking forces among mechanical and electrical subsystems. Additionally, for vehicles that have more than one electric machine, such as in-wheel-machines [25], precise torque control and its distribution among the different wheels impacts the vehicle stability during acceleration and deceleration and its efficiency.

From the previous discussion, it can be concluded that precise control of torque developed in EVs & HEVs is of utmost importance for achieving the maximum efficiency and therefore, the longest possible ranges. Effective mechanical output torque can be measured, using sensors, or can be alternatively estimated based on the torque equation of the machine, observers or indirect estimation methods. In conventional PMSMs, the torque is composed of an electromagnetic term, due to the PM flux linkage, and a reluctance component, due to the rotor anisotropy. However, both the electromagnetic and reluctance terms depend on the machine parameters, like flux linkage or the inductances. Therefore, torque calculation is specially challenging as these parameters vary with the operating point of the machine i.e. temperature, load current, saturation level, etc. In VLF-PMSMs, parameters L_d , L_q and λ_{pm} suffer larger variations compared with conventional PMSMs due to their special rotor design and variable PM flux linkage characteristic.

4.1.1 Torque measurement techniques

Mechanical output torque developed by a machine can be measured using torque transducers. Torque transducers based on strain gauges (see Fig. 4.1) are likely the preferred option and widely available in the market. These measurement systems use strain gauges to measure the force inside a mechanical coupling

system at a given distance from the shaft center. In Fig. 4.1, a sectional view of a torque transducer is shown. It can be observed that the shaft cross sectional area is reduced in order to increase the sensitivity of the strain gauge. The main differences among commercially available devices are in the system to feed the sensors and extract the measurements from the moving part to the stationary part. Capacitive or inductive coupling and slip rings being among the most common coupling systems. Less popular alternatives are systems based on torsional displacement methods [62].

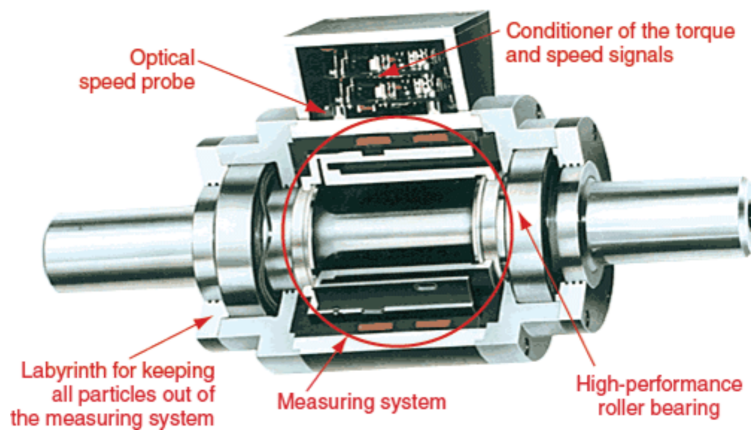


Figure 4.1: Torque transducer sectional view from Magtrol Inc.

Recently, wireless transmission devices based on accelerometers have also been proposed [63], which does not need mechanical coupling between the machine and the load and are presented in reduced size. These systems use transducers based on micro-electro-mechanical systems (MEMS) to acquire changes in acceleration. However, they are battery-fed, with a limit operation time, and are intended for high frequency torque pulsation measurements, needing to use integration-based methods to measure the fundamental torque. Due to this, they can only be found in a prototype or experimental development stage for laboratory use and are not commercialized. The prototype developed in [63] is shown in Fig. 4.2

Regardless of the method being used, precise torque measurement is expensive, requires room and extra cables, and introduces reliability concerns. For all these reasons, torque estimation techniques are the preferred option [28–39].

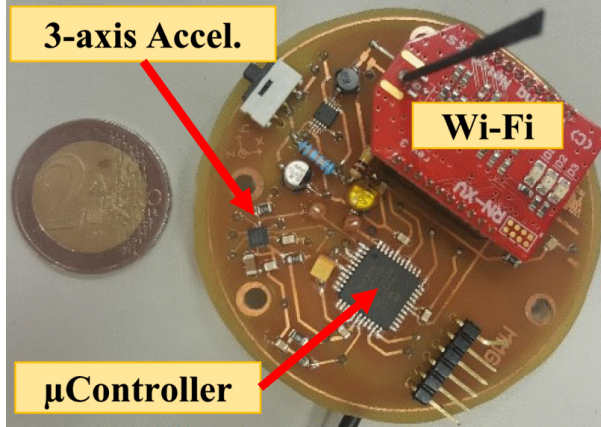


Figure 4.2: Wireless torque pulsations measurement system [63].

4.1.2 Torque estimation techniques

Torque estimation techniques are the preferred option for industry applications since as they do not require additional sensors, cabling or modification in the mechanical coupling. The robustness of the drive is not affected and the accuracy of the estimated variable is sufficiently high for many applications. Torque estimation methods can be roughly classified into torque equation-based methods [28–30] and indirect estimation methods [31–39].

Torque equation-based estimation methods often use constant machine parameters, such as PM flux linkage and inductances, to estimate machine output torque. However, saturation and variable PM flux linkage would lead to large estimation errors. Look-up tables (LUTs) can be used to address the variation of these parameters with operating conditions. As a drawback, they need larger storage memory, while they are not adaptive, i.e. unable to predict aging effects in the machine. On the other hand, these parameters can be estimated online by injecting HF signals and using the machine response [30, 64, 65]. However, the use of HF signals require enough voltage at the DC bus to be available for the injection and lead to an increment in machine losses, vibration and noise.

Indirect estimation methods use machine variables to obtain the mechanical torque of the machine. Torque estimation based on electric power and shaft speed uses stator current and voltages to calculate the electrical power [31]. From the electrical power of the machine, using the measured rotor speed and a coefficient to take into account the machine efficiency, the output torque is calculated. The

accuracy of this method relies on the resolution of the rotor speed sensor and it cannot work at standstill. Additionally, several torque estimation methods based on machine learning have been proposed in literature, such as fuzzy neural networks [40], wavelet neural networks [39] and iterative learning methods [32]. All of them rely on the previous training processes, which is specific for each machine and the computational burden could involve the use of more costly and complex control units. Typically, estimation methods based on intelligent algorithms are processed offline using a computer. Otherwise, the learning process is only performed at the initial commissioning stage and the method cannot be adapted to parameters changes due to aging.

All torque estimation methods cited [28–39] require precise knowledge of machine parameters (resistances, inductances or magnet flux) which can vary with the operating conditions of the machine (e.g. torque and field currents, magnet temperature or saturation level).

The PM flux linkage variation with q-axis current at different PM temperatures for the VLF-PMSM is shown in Fig. 4.3. It can be seen from Fig. 4.3 that the PM flux linkage suffers variations with stator current (variable leakage flux property) and with PM temperature. These variations lead to nonlinearities in the developed torque and they should be considered for torque estimation.

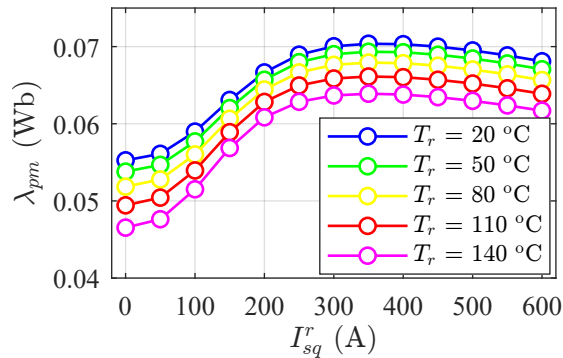


Figure 4.3: PM flux linkage variation with q-axis current at different PM temperatures for the VLF-PMSM at $I_{sd}^r = 0$ A.

The variation of torque developed by the VLF-PMSMs with stator current and temperature can be summarized and seen in Fig. 4.4. These results are obtained from the FEA model of the VLF-PMSM which will be used for experimental verification for different PM temperatures.

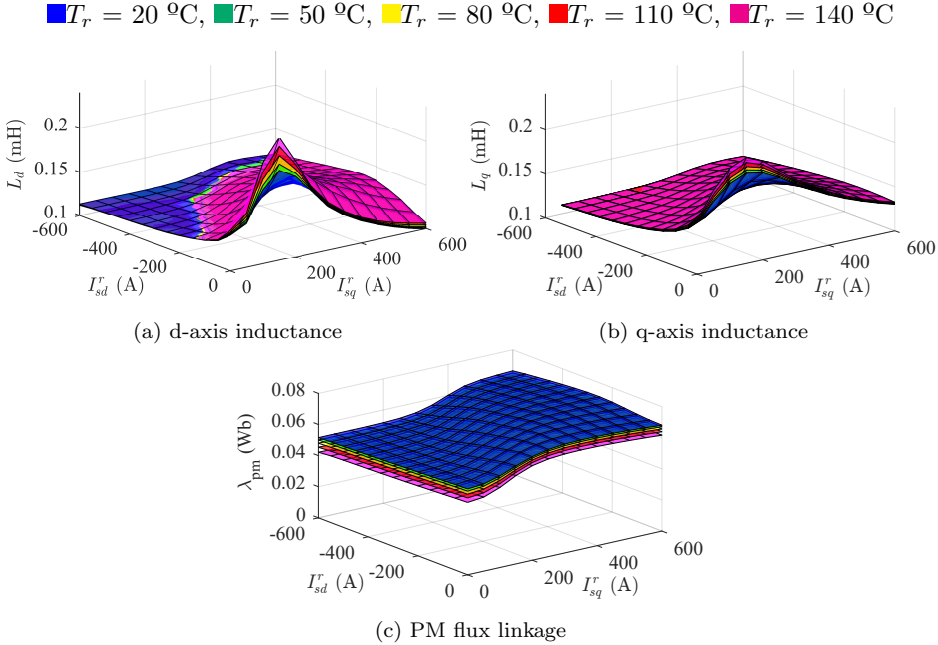


Figure 4.4: VLF-PMSM variables vs. stator current for different temperatures.

Torque estimation in VLF-PMSM is specially challenging due to its PM flux linkage and inductance variations with stator current and temperature. The PM flux linkage has a variation range of $\approx 40\%$ in the whole current and temperature operating region. The d and q-axis inductances are expected to vary a $\approx 35\%$ in the whole current and temperature operation regions. While LUTs can be used to account for the inductance and flux linkage variations with stator current and temperature, PM temperature sensors are not usually available and their use leads to reliability issues in the machine, as discussed in Chapter 3. Additional drawbacks derived from the use of LUTs, like large memory usage and not accounting for aging effects, are still present. Since torque equation based methods need precise information of PM flux linkage and inductances, and these parameters suffer large variations during normal operation of the VLF-PMSM, they should be estimated.

In this dissertation, a method to improve the accuracy of torque estimation in VLF-PMSMs, overcoming the discussed limitations, is presented. D and q-axes inductances and stator resistance will be estimated from the response of the machine to a pulsating HF current signal, while the PM flux linkage will

be estimated from the response of the machine to a low frequency square-wave current signal. Both signals are low magnitude and are injected on top of the fundamental excitation.

As it was shown in Chapter 2, the output torque of a VLF-PMSM is function of dq-axes stator flux linkages, which depend on the dq-axes inductances and PM flux linkage [41]. Additionally, the dq-axis flux linkages can be expressed as function of stator voltage and currents (3.3)-(3.4), in this case being dependent on the stator resistance. These parameters vary during normal machine operation, e.g. due to temperature or saturation. Fig. 4.4a-c shows the dq-axis inductances and PM flux linkage vs. dq-axis currents and different magnet temperatures (T_r) of the VLF-PMSMs that will be used for the experimental verification of the proposed method. It is observed from Fig. 4.4 that the variation of these parameters (L_d , L_q , and λ_{pm}) with the machine operating condition cannot be ignored, machine parameters estimation being therefore needed. Results shown in Fig. 4.4 will be used for the experimental verification of the proposed method.

4.2 Torque estimation based on flux observer enhanced with on-line parameters estimation

This section presents the proposed torque estimation method based on a flux observer enhanced with on-line parameters estimation. Fig. 4.5 shows the proposed torque estimation method as well as its integration with the fundamental control of the machine. It can be observed from (2.1) and Fig. 4.5 that torque estimation requires: a) stator flux linkage estimation, λ_{sdq} , b) PM flux linkage estimation, λ_{pm} , and c) stator resistance, R_s , and inductances estimation, L_d , L_q . The procedure to obtain these parameters is described in the following subsections.

4.2.1 Stator flux linkage estimation

As it was stated in the previous section, different stator flux observers have been proposed in the literature, the voltage model (3.3)-(3.4) and the current model (3.1)-(3.2) based being the most extended options [53, 54]. The Gopinath type flux observer was proposed in [53], combining the voltage and current models. The advantages and drawbacks of both models can be seen in Table 3.3.

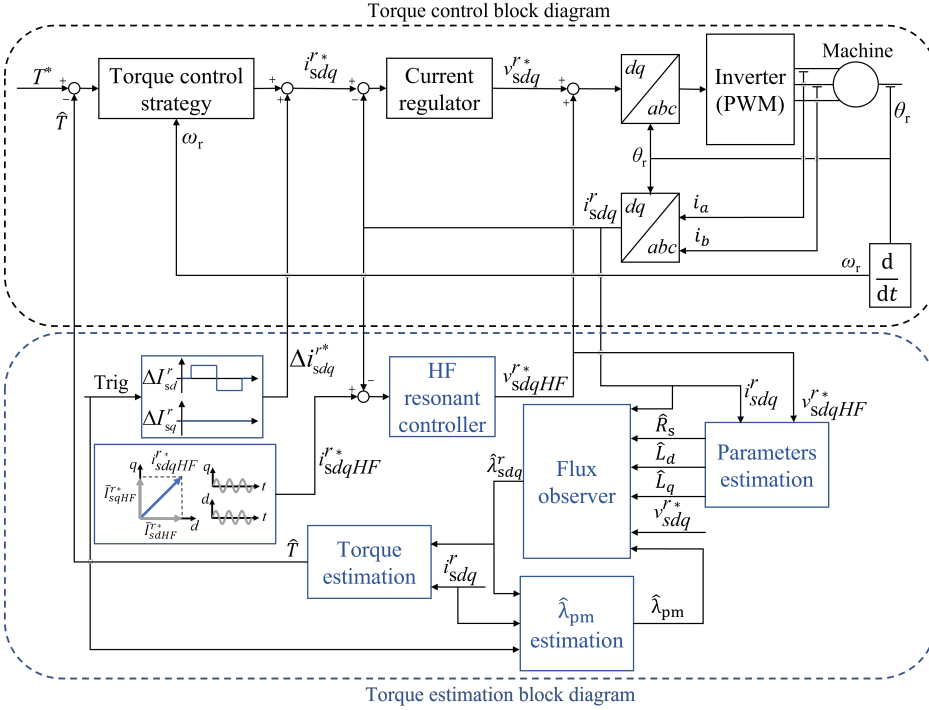


Figure 4.5: Block diagram of the fundamental torque control and torque estimation strategy for a VLF-PMSM.

The current model can be used to estimate the stator flux in the whole speed range of the machine but requires the magnet flux linkage to be available, as well as d- and q-axes inductances and stator current (see (3.1)-(3.2)). On the other hand, voltage model can be used to estimate machine flux in the mid-to-high speed [54]. However, it becomes inaccurate at low speeds due to the diminishing magnitude of the Back-EMF and it cannot be used at standstill. In addition, as a pure integrator is required to estimate the stator flux, an initial estimation error exists (integration constant) which needs to be compensated [53, 56]. Furthermore, small bias usually present in the measured signals will result in unacceptable drifts of integrator output.

The Gopinath type flux observer combining voltage and current models was proposed in [53]. It combines a voltage model for high speed operation and a current model for low and standstill operation, a PI controller being used to make a smooth transition between models. The controller bandwidth will determine

the transition frequency from current to voltage model. This type of flux observer provides reliable estimation in the whole speed range of the machine, including standstill, being more sensitive to machine parameters at low speeds than at high speeds due to the parameter dependency of the current based model. Advantages and drawbacks of the discussed observers are summarized in Table 4.1.

Table 4.1: Advantages and drawbacks of flux models

	Current model	Voltage model	Gopinath
Low parameter sensitivity at high speed	✗	✓	✓
Estimation in the whole speed range, including standstill	✓	✗	✓

The Gopinath type flux observer shown in Fig. 4.6 will be used in this dissertation to estimate the stator flux linkage [53]. The parameters of the observer (L_d , L_q , R_s and λ_{pm}) will be estimated using a combination of HF and LF signal injection.

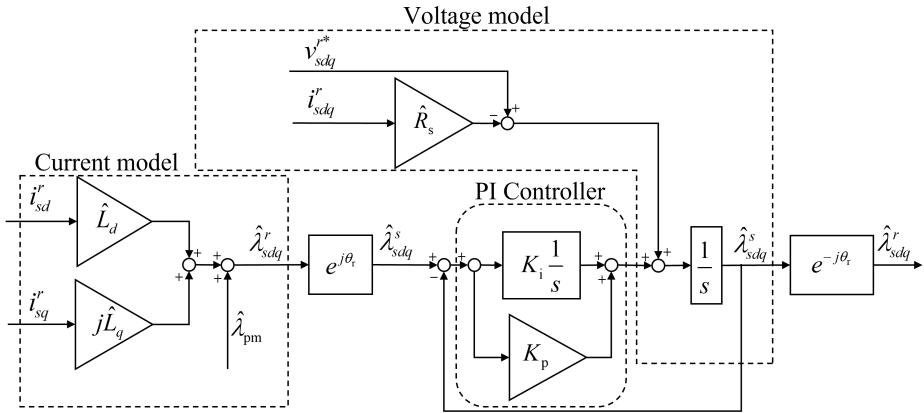


Figure 4.6: Gopinath type flux observer scheme.

4.2.2 PM flux linkage estimation

PM flux linkage is relatively easy to estimate from the back-EMF at no load but is difficult to estimate when the machine is loaded [9, 66]. The method

proposed in [9] provides PM flux linkage estimation under load conditions and considering saturation effects. Therefore, the method proposed in [9] will be used in this dissertation.

The PM flux linkage is estimated from the response of the machine to a low frequency, small magnitude, quasi-square-wave current signal of magnitude ΔI_{sd}^r injected on top of the fundamental current [9], this is schematically represented in Fig. 4.7. The d-axis stator flux linkage, λ_{sd}^r is represented by (4.1), λ_{sd}^{r+} is the d-axis flux linkage when positive d-axis current step, $+\Delta I_{sd}^r$, is applied (4.2), while λ_{sd}^{r-} is the d-axis flux linkage when negative d-axis current step, $-\Delta I_{sd}^r$, is applied (4.3). The stator flux linkages, $\hat{\lambda}_{sd}^r$, $\hat{\lambda}_{sd}^{r+}$ and $\hat{\lambda}_{sd}^{r-}$, are not obtained using (4.1)-(4.3), instead, they are estimated by the Gopinath type flux observer shown in the previous subsection. $\hat{\lambda}_{pm}^+$ and $\hat{\lambda}_{pm}^-$ are estimated from (4.4) and (4.5), respectively. $\hat{\lambda}_{pm}$ (PM flux linkage when no applying ΔI_{sd}^r) is finally obtained as the average of $\hat{\lambda}_{pm}^+$ and $\hat{\lambda}_{pm}^-$, (4.6).

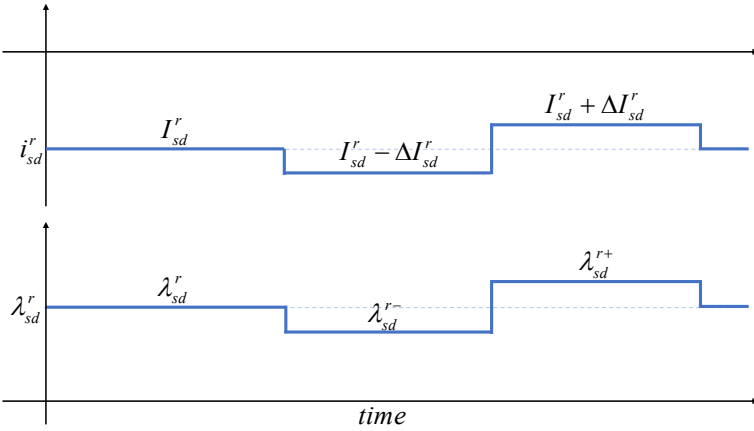


Figure 4.7: Schematic representation of the injected stator d-axis current, fundamental and small-amplitude, low frequency, square-wave currents, (i_{sd}^r) and resulting stator d-axis flux (λ_{sd}^r).

$$\lambda_{sd}^r = \lambda_{pm} + L_d I_{sd}^r \quad (4.1)$$

$$\lambda_{sd}^{r+} = \lambda_{pm}^+ + L_d^+ (I_{sd}^r + \Delta I_{sd}^r) \quad (4.2)$$

$$\lambda_{sd}^{r-} = \lambda_{pm}^- + (I_{sd}^r - \Delta I_{sd}^r) \quad (4.3)$$

$$\hat{\lambda}_{pm}^+ = \frac{1}{\Delta I_{sd}^r} \left[(I_{sd}^r + \Delta I_{sd}^r) \hat{\lambda}_{sd}^r - I_{sd}^r \hat{\lambda}_{sd}^{r+} \right] \quad (4.4)$$

$$\hat{\lambda}_{pm}^- = \frac{1}{\Delta I_{sd}^r} \left[I_{sd}^r \hat{\lambda}_{sd}^r - (I_{sd}^r - \Delta I_{sd}^r) \hat{\lambda}_{sd}^{r-} \right] \quad (4.5)$$

$$\hat{\lambda}_{pm} = \frac{\hat{\lambda}_{pm}^+ + \hat{\lambda}_{pm}^-}{2} \quad (4.6)$$

The magnitude of the square-wave signal should be selected to minimize inductance and PM flux linkage variations in order to produce a linear d-axis flux response, i.e. the magnitude should be as small as possible while keeping acceptable signal to noise ratio. The selection of the frequency of this signal is not a major issue since the bandwidth of current regulators is usually high enough (100-1000 Hz) for EVs and HEVs applications. For lower bandwidths of the current regulator, the estimation must be delayed accordingly, taking more time and interfering longer with the machine operation. The injection of the quasi-square signal only affects the reluctance torque and, given the small magnitude of the signal, its effect in the reluctance torque can be negligible.

4.2.3 Resistance and inductances estimation using high frequency signal injection

Injection of a high frequency signal has been shown to be a reliable method for resistance and inductance estimation [30, 64, 65] in conventional PMSMs. In this dissertation, the injection of a high frequency pulsating current will be used to estimate stator resistance and inductances, as these parameters need to be updated in the flux observer (see Fig. 4.6) for any operating point of the machine. The HF current is injected in closed loop control using resonant controllers [30]. The proposed method shares some similarities with [30]. However, the method in [30] required two pulsating HF currents while only one HF signal is required in the proposed method, which reduces the adverse effects of HF signal injection, simplifies the implementation, the signal processing and the computational burden.

If a PMSM is fed with a HF voltage/current, the magnet flux dependent term in (2.1) can be safely neglected, as it does not contain any HF component, the HF model shown in (4.7) is therefore obtained, where R_{dHF} , R_{qHF} , L_{dHF} and L_{qHF} are the d- and q-axes high frequency resistances and inductances, respectively;

i_{sdHF}^r and i_{sqHF}^r are the d and q-axes high frequency currents; v_{sdHF}^r and v_{sqHF}^r are the d and q-axes high frequency voltages.

d and q-axis HF inductances and resistances can be obtained by injecting a pulsating HF at 45° from the d-axis, (4.8) of magnitude I_{HF}^* and frequency ω_{HF} (see Fig. 2.2). The HF voltages that will be commanded by the resonant controller will be of the form shown in (4.9).

$$\begin{bmatrix} v_{sdHF}^r \\ v_{sqHF}^r \end{bmatrix} = \begin{bmatrix} R_{dHF} & -\omega_r L_{qHF} \\ \omega_r L_{dHF} & R_{qHF} \end{bmatrix} \begin{bmatrix} i_{sdHF}^r \\ i_{sqHF}^r \end{bmatrix} + p \begin{bmatrix} L_{dHF} & 0 \\ 0 & L_{qHF} \end{bmatrix} \begin{bmatrix} i_{sdHF}^r \\ i_{sqHF}^r \end{bmatrix} \quad (4.7)$$

$$i_{sdqHF}^{r*} = \begin{bmatrix} \bar{I}_{sdHF}^{r*} \\ \bar{I}_{sqHF}^{r*} \end{bmatrix} = \begin{bmatrix} I_{HF}^* \cos(\omega_{HF} t) \\ I_{HF}^* \cos(\omega_{HF} t) \end{bmatrix} \quad (4.8)$$

$$v_{sdqHF}^{r*} = \begin{bmatrix} \bar{V}_{sdHF}^{r*} \\ \bar{V}_{sqHF}^{r*} \end{bmatrix} = \begin{bmatrix} (R_{dHF} + j\omega_{HF} L_{dHF}) \bar{I}_{sdHF}^r - \omega_r L_{qHF} \bar{I}_{sqHF}^r \\ (R_{qHF} + j\omega_{HF} L_{qHF}) \bar{I}_{sqHF}^r + \omega_r L_{dHF} \bar{I}_{sdHF}^r \end{bmatrix} \quad (4.9)$$

L_{dHF} can be estimated from the measured d-axis HF current, $i_{sdqHF}^{r'}$ (4.10), and the commanded d-axis HF voltage, $v_{sdqHF}^{r'}$ (4.11). Both (4.10) and (4.11) can be separated into positive sequence ($i_{sdqHFpc}^{r'}$ and $v_{sdqHFpc}^{r'}$) and negative sequence ($i_{sdqHFnc}^{r'}$ and $v_{sdqHFnc}^{r'}$) components, (4.12) and (4.13). The d-axis HF impedance, (4.14) can be obtained either from the positive or negative sequence component, the d-axis HF inductance being its imaginary part (4.15).

$$i_{sdqHF}^{r'} = \begin{bmatrix} \bar{I}_{sdHF}^{r*} \\ 0 \end{bmatrix} = \begin{bmatrix} I_{HF}^* \cos(\omega_{HF} t) \\ 0 \end{bmatrix} \quad (4.10)$$

$$v_{sdqHF}^{r'} = \begin{bmatrix} \bar{V}_{sdHF}^{r*} \\ 0 \end{bmatrix} = \begin{bmatrix} (R_{dHF} + j\omega_{HF} L_{dHF}) \bar{I}_{sdHF}^r - \omega_r L_{qHF} \bar{I}_{sqHF}^r \\ 0 \end{bmatrix} \quad (4.11)$$

$$i_{sdqHF}^{r'} = \frac{|i_{sdqHF}^{r'}|}{2} e^{j\omega_{HF} t} + \frac{|i_{sdqHF}^{r'}|}{2} e^{-j\omega_{HF} t} = i_{sdqHFpc}^{r'} + i_{sdqHFnc}^{r'} \quad (4.12)$$

$$v_{sdqHF}^{r'} = \frac{|v_{sdqHF}^{r'}|}{2} e^{j(\omega_{HF} t - \varphi_{zd})} + \frac{|v_{sdqHF}^{r'}|}{2} e^{-j(\omega_{HF} t + \varphi_{zd})} = v_{sdqHFpc}^{r'} + v_{sdqHFnc}^{r'} \quad (4.13)$$

$$Z_{dHF} = R_{dHF} - \omega_r L_{qHF} + j\omega_{HF} L_{dHF} = \frac{v_{sdqHFpc}^{r'}}{i_{sdqHFpc}^{r'}} = \frac{v_{sdqHFnc}^{r'}}{i_{sdqHFnc}^{r'}} \quad (4.14)$$

$$L_{dHF} = \Im[Z_{dHF}]/\omega_{HF} \quad (4.15)$$

L_{qHF} can be estimated from the measured q-axis HF current, $i_{sdqHF}^{r''}$ (4.16), and the commanded q-axis HF voltage, $v_{sdqHF}^{r''}$ (4.17), using (4.18)-(4.21) similarly as for d-axis HF inductance estimation.

$$i_{sdqHF}^{r''} = \begin{bmatrix} 0 \\ \bar{I}_{sqHF}^{r*} \end{bmatrix} = \begin{bmatrix} 0 \\ I_{HF}^* \cos(\omega_{HF} t) \end{bmatrix} \quad (4.16)$$

$$v_{sdqHF}^{r''} = \begin{bmatrix} 0 \\ \bar{V}_{sqHF}^{r*} \end{bmatrix} = \begin{bmatrix} 0 \\ (R_{qHF} + j\omega_{HF} L_{qHF}) \bar{I}_{sqHF}^r + \omega_r L_{dHF} \bar{I}_{sdHF}^r \end{bmatrix} \quad (4.17)$$

$$i_{sdqHF}^{r''} = \frac{|i_{sdqHF}^{r''}|}{2} e^{j\omega_{HF} t} + \frac{|i_{sdqHF}^{r''}|}{2} e^{-j\omega_{HF} t} = i_{sdqHFpc}^{r''} + i_{sdqHFnc}^{r''} \quad (4.18)$$

$$v_{sdqHF}^{r''} = \frac{|v_{sdqHF}^{r''}|}{2} e^{j(\omega_{HF} t - \varphi_{zq})} + \frac{|v_{sdqHF}^{r''}|}{2} e^{-j(\omega_{HF} t + \varphi_{zq})} = v_{sdqHFpc}^{r''} + v_{sdqHFnc}^{r''} \quad (4.19)$$

$$Z_{qHF} = R_{qHF} - \omega_r L_{dHF} + j\omega_{HF} L_{qHF} = \frac{v_{sdqHFpc}^{r''}}{i_{sdqHFpc}^{r''}} = \frac{v_{sdqHFnc}^{r''}}{i_{sdqHFnc}^{r''}} \quad (4.20)$$

$$L_{qHF} = \Im[Z_{qHF}]/\omega_{HF} \quad (4.21)$$

dq-axis HF resistance can be obtained from (4.22) and (4.23), the stator HF resistance R_{sHF} (4.24) being obtained as the average of the d and q-axis resistances.

$$R_{dHF} = \Re[Z_{dHF}] + \omega_r L_{qHF} \quad (4.22)$$

$$R_{qHF} = \Re[Z_{qHF}] - \omega_r L_{dHF} \quad (4.23)$$

$$R_{sHF} = \frac{R_{dHF} + R_{qHF}}{2} \quad (4.24)$$

Selection of the pulsating HF current signal magnitude is a tradeoff between the adverse effects of HF injection (i.e. losses, vibration, noise, etc.) and the signal to noise ratio. The HF signal frequency should be high enough to ensure the spectral separation with fundamental frequency. Note that this signal is injected synchronously with the rotor, therefore, the spectral separation does not depend on the speed of the machine. For the FEA and experimental results that will be shown in the following section, the magnitude of the injected signal will be 0.05 pu and the frequency will be 500Hz.

4.3 FEA and experimental verification

Parameters estimation using the proposed method is presented in this section. Fig. 2.1 shows the schematic representation of the test machine that will be used for both FEA and experiments. The parameters of the VLF-PMSM test machine are shown in Table 2.1.

Simulations and experimental results are performed at three different speeds:

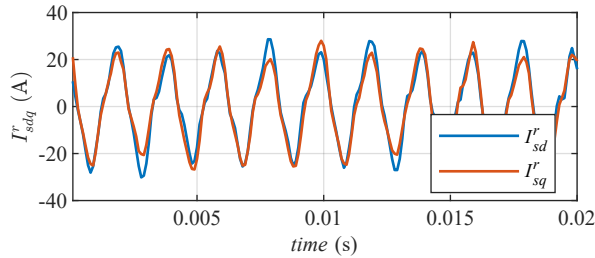
- 0 r/min (standstill), where only the current model contributes to the flux observer estimation.
- 500 r/min where both, current model and voltage model, contribute to the flux observer estimation
- 3000 r/min where only the voltage model model contributes to the flux observer estimation.

The test bench used for the experimental verification of the method is described in detail in Appendix A. The test bench is composed of a conventional IPMSM used as a load, the VLF-PMSM under test, each machine being driven by a three-phase inverter; experimental results been limited to 450 A due to the maximum inverter current limit. The two inverters share the DC-link and are controlled using a TMS320F28335 microcontroller.

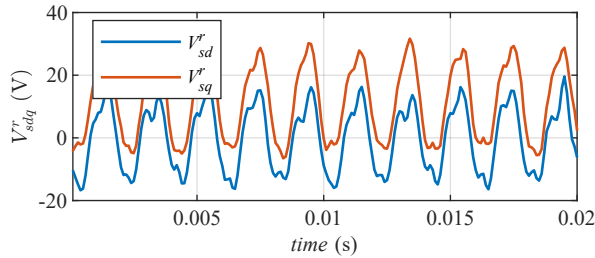
As already stated, implementation of the proposed method requires the injection of two signals, a pulsating HF current signal for d and q-axis inductances and stator resistance estimation and a low frequency square-wave current signal for PM flux linkage estimation.

4.3.1 Inductance estimation

Fig. 4.8a and 4.8b show the measured currents and the commanded voltages for one operating point ($I_{sdq}^r = 0$) during the injection of the HF signal, respectively. These signals have been sampled at 10 kHz by the microcontroller using synchronous sampling to eliminate the PWM switching harmonics. The 500 Hz component can be readily observed in both currents and voltages. The d- and q-axis current waveforms are nearly overlapping since the HF signal is injected at 45° , see (4.8).



(a) d and q-axis current



(b) d and q-axis voltage

Figure 4.8: Experimental results. Measured by the microcontroller at 10 kHz.

$I_{sdq}^r = 0$, $I_{HF} = 0.05$ pu, $\omega_{HF} = 2\pi 500$ rad/s, $\omega_r = 500$ r/min and $T_r = 20$ °C

The HF inductances and resistance are obtained as shown in Section 4.2.3 (see (4.15), (4.21) and (4.24)), the estimated d and q-axis HF inductances are shown in Fig. 4.9a and the estimated HF resistance is shown in Fig. 4.9b. During

this experiment the stator temperature (T_s) and PM temperature (T_r) were both 20°C. The estimated HF resistance is in good agreement with the measured total stator resistance of $\approx 15 \text{ m}\Omega$ including cable resistance.

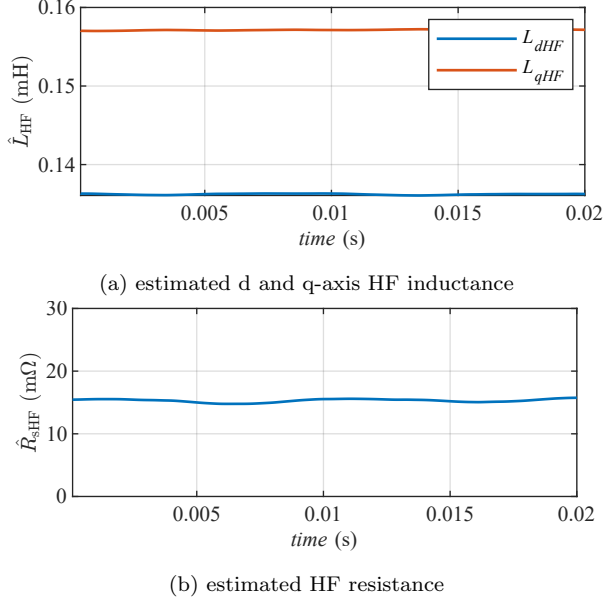


Figure 4.9: Experimental results. Measured by the microcontroller at 10 kHz.

$$I_{sdq}^r = 0, I_{HF} = 0.05 \text{ pu}, \omega_{HF} = 2\pi 500 \text{ rad/s}, \omega_r = 500 \text{ r/min and } T_r = 20 \text{ }^\circ\text{C}$$

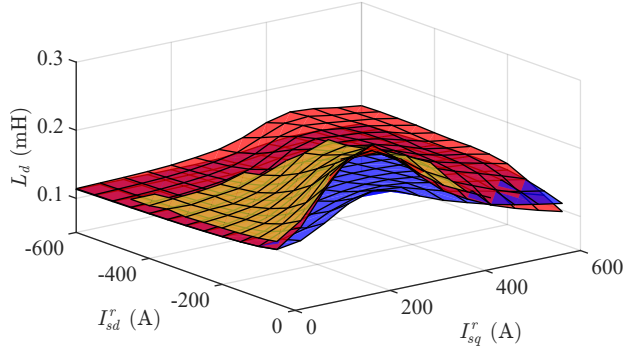
Fig. 4.10a and 4.10b shows the estimated d and q-axes HF inductances, both using FEA and experimentally. FEA results are obtained as described in Section 4.2.3. For the sake of comparison DC inductances obtained using (4.25) and (4.26) are also shown. The d and q-axis flux linkages are directly provided by the FEA software while the PM flux linkage, λ_{pm} , is obtained from (4.6) by the method described in Section 4.2.2. Experimental results shown in 4.10a and 4.10b are also obtained as described in Section 4.2.2.

$$L_d = \frac{\lambda_{sd}^r - \lambda_{pm}}{I_{sd}^r} \quad (4.25)$$

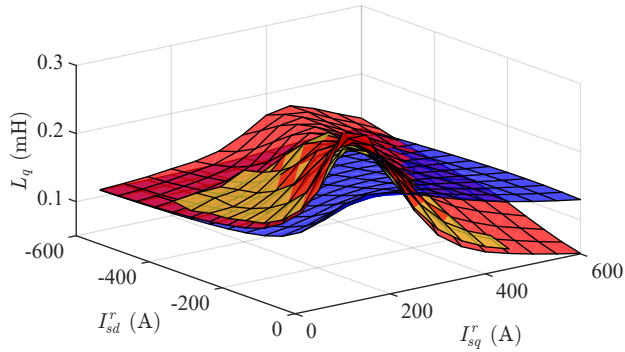
$$L_q = \frac{\lambda_{sq}^r}{I_{sq}^r} \quad (4.26)$$

It is observed that the estimated HF (FEA and experimentally) and DC inductances are not matching, which was expected due to: (i) the inherent high

■ DC inductance ■ FEA HF inductance ■ Experimental HF inductance



(a) d-axis HF (FEA and experimental) and DC inductance vs. stator current



(b) q-axis HF (FEA and experimental) and DC inductance vs. stator current

Figure 4.10: FEA and experimental estimated inductance results. $I_{HF} = 0.05$ pu, $\omega_{HF} = 2\pi 500$ rad/s, $\Delta I_{sd}^r = 0.02$ pu, $\omega_r = 500$ r/min and $T_r = 20$ °C

cross-coupling of VLF-PMSMs; (ii) the relationship between HF (or dynamic) and DC (or linearized) inductances [42, 67], showing that saturation effects are not negligible, see Fig. 4.12. These issues are discussed in the follow subsections:

4.3.1.1 Cross-coupling inductance effect

In Section 4.2.3, the cross-coupling inductance effect was not taken into account, because the impact of this phenomenon could be neglected, depending on the application and the PMSM used. However, cross-coupling inductance in VLF-PMSMs can be significant and may affect the parameter estimation technique accuracy. The resulting HF model of a PMSM considering this effect is shown in (4.27), which is obtained from (4.7) after including the cross-coupling

inductances [42, 67].

$$\begin{aligned} \begin{bmatrix} v_{sdHF}^r \\ v_{sqHF}^r \end{bmatrix} &= \begin{bmatrix} R_{dHF} & 0 \\ 0 & R_{qHF} \end{bmatrix} \begin{bmatrix} i_{sdHF}^r \\ i_{sqHF}^r \end{bmatrix} + p \begin{bmatrix} L_{dHF} & L_{dqHF} \\ L_{qdHF} & L_{qHF} \end{bmatrix} \begin{bmatrix} i_{sdHF}^r \\ i_{sqHF}^r \end{bmatrix} + \\ &+ \omega_r \begin{bmatrix} -L_{dqHF} & -L_{qHF} \\ L_{dHF} & L_{dqHF} \end{bmatrix} \begin{bmatrix} i_{sdHF}^r \\ i_{sqHF}^r \end{bmatrix} \end{aligned} \quad (4.27)$$

Following the procedure described in section 4.2.3 but for the model including the cross-coupling (4.27), the estimated HF inductances in (4.15) and (4.21) becomes (4.28) and (4.29), respectively. It is observed from (4.28) and (4.29) that the d and q-axis HF inductances can be obtained by subtracting the cross-coupling high frequency inductances (L_{dqHF} and L_{qdHF}), which are defined by (4.30) and (4.31), being $L_{qdHF} = L_{dqHF}$ [67]. Fig. 4.11 shows the cross-coupling inductances obtained from FEA using (4.30) and (4.31).

$$\hat{L}_{dHF} = \Im[Z_{qHF}]/\omega_{HF} = L_{dHF} + L_{dqHF} \quad (4.28)$$

$$L_{qHF} = \Im[Z_{dHF}]/\omega_{HF} = L_{qHF} + L_{qdHF} \quad (4.29)$$

$$L_{dqHF} = \frac{\partial \lambda_{sd}}{\partial i_{sq}^r} \quad (4.30)$$

$$L_{qdHF} = \frac{\partial \lambda_{sq}}{\partial i_{sd}^r} \quad (4.31)$$

Cross-coupling inductances can also be estimated by using the q-axis stator flux response to a quasi-squarewave, small-amplitude, low frequency current signal, which was already used for PM flux linkage estimation as shown in Section 4.2.1. The cross-coupling inductance can be obtained from (4.32), being λ_{sq}^{r+} the q-axis flux linkage when positive d-axis current step, $+\Delta I_{sd}^r$, is applied, while λ_{sq}^{r-} is the q-axis flux linkage when negative d-axis current step, $-\Delta I_{sd}^r$, is applied.

$$L_{qdHF} = L_{dqHF} = \frac{\partial \lambda_{sq}}{\partial i_{sd}^r} \approx \frac{\Delta \lambda_{sq}}{\Delta i_{sd}^r} = \frac{\lambda_{sq}^{r+} - \lambda_{sq}^{r-}}{2\Delta I_{sd}^r} \quad (4.32)$$

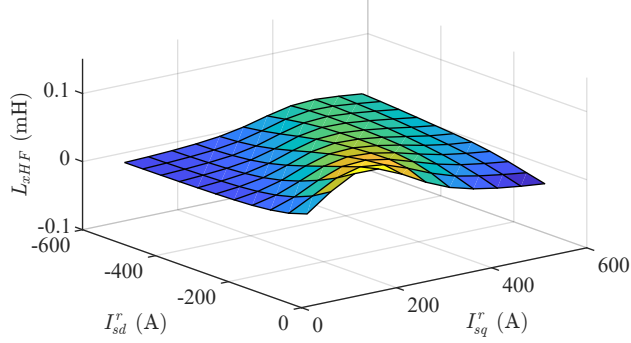


Figure 4.11: FEA results. Cross-coupling inductances vs. stator current at $T_r=20^\circ\text{C}$.

4.3.1.2 DC inductance estimation from HF inductance

As stated previously, HF and DC inductances differ depending on the machine operating point; while the DC inductance is defined as the linearized or apparent inductance from the origin of the flux-current curve to the operating point, see Fig. 4.12, the HF (or dynamic) inductance is defined as the variation of the flux respect the current (4.33)-(4.34) at the operating point, i.e. the slope of the flux-current curve at the operating point [42, 67]. This is schematically shown in Fig. 4.12.

$$L_{dDyn} = \frac{\partial \lambda_{sd}^r}{\partial i_{sd}^r} \quad (4.33)$$

$$L_{qDyn} = \frac{\partial \lambda_{sq}^r}{\partial i_{sq}^r} \quad (4.34)$$

Nevertheless, DC inductances can be obtained from the HF inductances by integration along the current trajectory of the machine, see (4.35) and (4.36), which provides instantaneous DC inductance estimation in both d and q-axis using the estimated HF inductance.

$$L_{dDC} = \frac{\int L_{dDyn} \partial i_{sd}^r - \lambda_{pm}}{I_{sd}^r} \quad (4.35)$$

$$L_{qDC} = \frac{\int L_{qDyn} \partial i_{sq}^r}{I_{sq}^r} \quad (4.36)$$

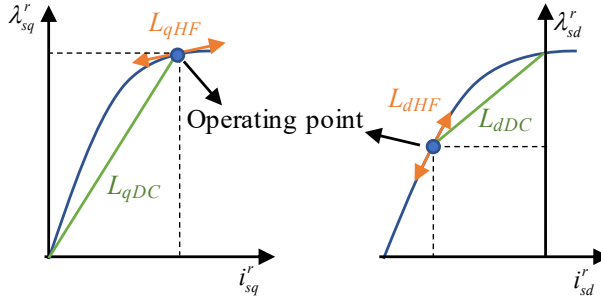


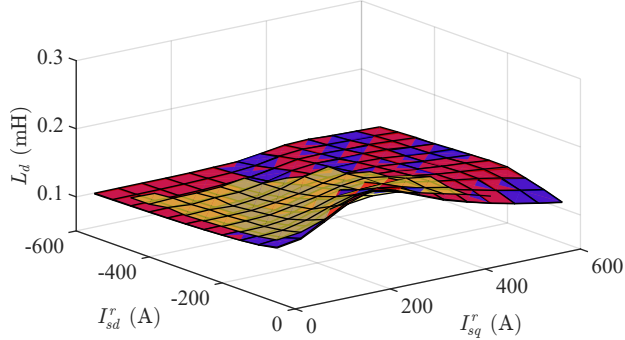
Figure 4.12: Schematic representation of DC or linearized inductance and HF or incremental inductance.

Fig. 4.13a and 4.13b show the estimated d and q-axis HF inductances vs. stator current considering the cross-coupling inductance, respectively. For the sake of comparison, Fig. 4.13a and 4.13b, also show the d and q-axis dynamic inductances obtained from FEA data using (4.33) and (4.34). It is observed that HF and dynamic inductances are matching as it was expected. Fig. 4.13c shows the estimated stator HF resistance. For the case of FEA results, the estimated resistance varies around the expected value of 8 m Ω (actual coil resistance in FEA simulation), while in experimental results, the expected resistance is increased due to end coils and the resistance of connection cables.

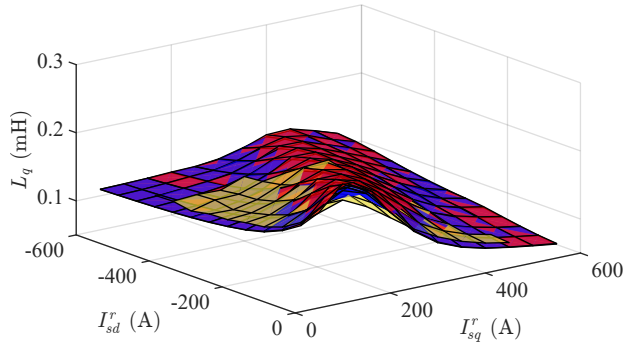
It can be also seen from Fig. 4.13c that the experimentally estimated resistance slightly varies with stator current, which could be due to small rotor angle alignment error and/or digital signal processing delays which have not been perfectly compensated in the experimental setup; note that also inductance estimation errors can lead to this effect as shown from (4.22) and (4.23).

In order to further enhance the stator flux observer estimation, instead of introducing the HF inductances into the flux observer, the DC inductance will be used, which are obtained from (4.35) and (4.36). Fig. 4.14a and 4.14b show the estimated d and q-axis DC inductances (FEA and experimental) and actual d and q-axis DC inductances (which are shown for comparison). It is observed that estimated, both FEA and experimental, and actual DC inductances are matching as it was expected.

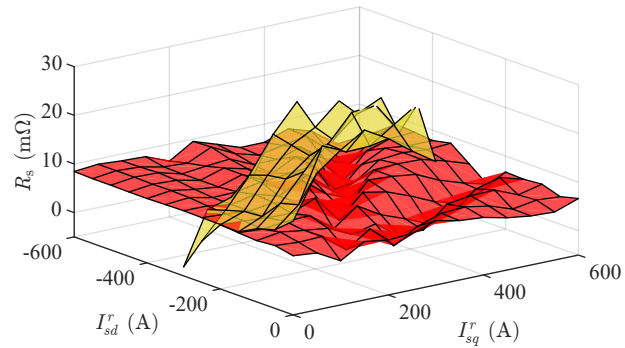
■ Dynamic inductance ■ FEA estimated HF inductance ■ Experimentally estimated HF inductance



(a) d-axis HF and Dynamic inductances vs. stator current



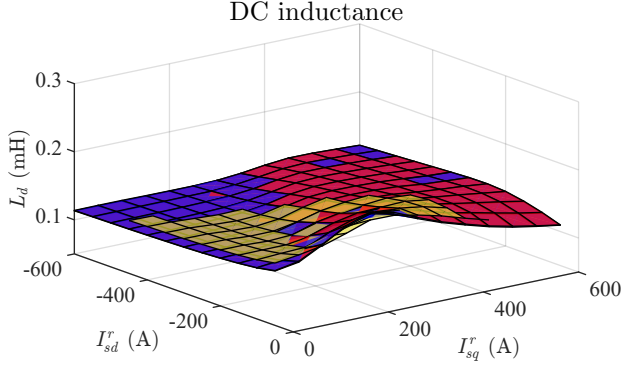
(b) q-axis HF and Dynamic inductances vs. stator current



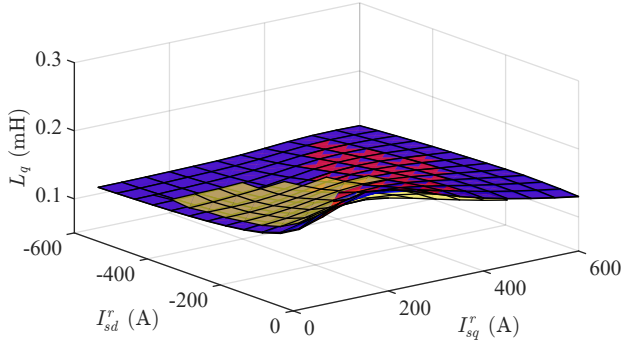
(c) HF stator resistance vs. stator current

Figure 4.13: FEA and experimental results. $I_{HF} = 0.05$ pu, $\omega_{HF} = 2\pi 500$ rad/s, $\omega_r = 500$ r/min and $T_r = 20$ °C

■ DC inductance ■ FEA estimated DC inductance ■ Experimentally estimated



(a) d-axis estimated and actual DC inductances vs. stator current



(b) q-axis estimated and actual DC inductances vs. stator current

Figure 4.14: FEA and experimental results. $I_{HF} = 0.05$ pu, $\omega_{HF} = 2\pi 500$ rad/s, $\omega_r = 500$ r/min and $T_r = 20$ °C

4.3.2 PM flux linkage estimation

The PM flux linkage, which is estimated using the square-wave current signal, as described in Section 4.2.2, is shown in Fig. 4.15 both FEA and experimentally. It can be observed that the experimental results exhibit lower PM flux linkage than FEA results; this is due to a lower PM magnetization level in the actual machine.

■ FEA estimated PM flux linkage ■ Experimentally estimated PM flux linkage

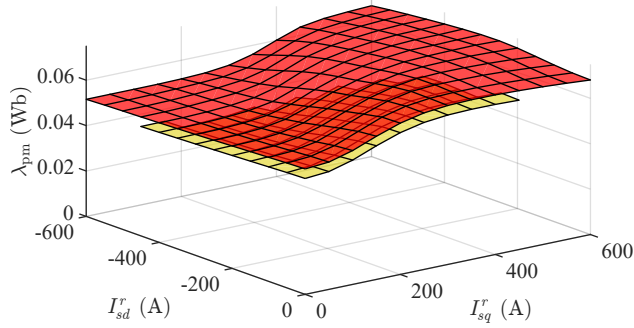


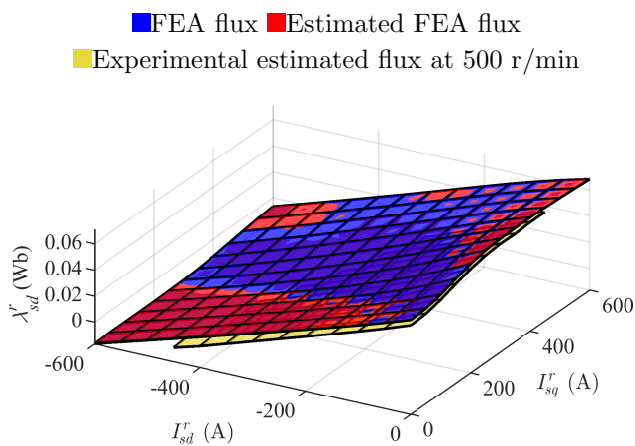
Figure 4.15: Estimated PM flux linkage vs. stator current. $\Delta I_{sd}^r=0.02$ pu, $\omega_r=500$ r/min and $T_r=20^\circ\text{C}$.

4.4 Torque estimation

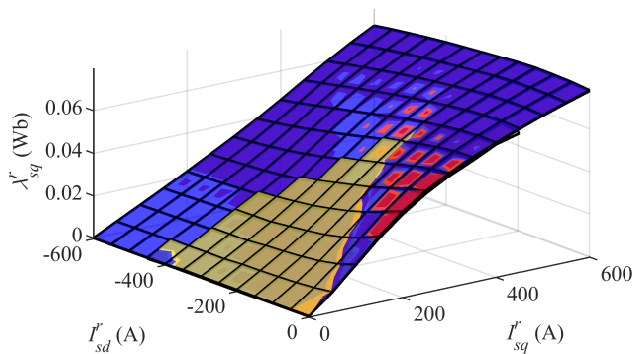
Results of the proposed method by means of FEA and experiments are provided in this section.

The estimated parameters, which has been already shown in Section 4.3 (L_d , L_q , R_s and λ_{pm}), are used in the Gopinath type flux observer, see Fig. 4.6. Estimated d and q-axis stator fluxes vs. stator current are shown in Fig. 4.16a and 4.16b, respectively, and actual machine flux (obtained from FEA data) is also represented for comparison. Consistently with Fig. 4.15 a lower PM flux linkage is observed in the experimental results, see Fig. 4.16a. The results for 0 r/min and 3000 r/min are not represented in Fig. 4.16 in order to maintain a clear figure representation.

Finally, the torque is estimated using (2.3) which is represented vs. stator current in Fig. 4.17a for FEA and in Fig. 4.17b experimentally. The estimation error 4.37 is shown in Fig. 4.17c, being \hat{T} the torque estimated by the proposed method and $T_{measured}$ the actual machine torque obtained from FEA or measured by the torque sensor, see Appendix A, for the experimental results. The estimation error for the experimental results is larger than for FEA simulations, which was expected due to e.g. non-linear behaviour of the inverter, finite sampling frequency or sensors resolution. Furthermore, the maximum torque estimation error magnitude is ≈ 7 Nm, which is 2.8% of rated machine torque and 4% of maximum torque at 450 A (maximum current during experimental results due



(a) Estimated and actual d-axis flux vs. stator current



(b) estimated and actual q-axis flux vs. stator current

Figure 4.16: FEA and experimental results. $I_{HF} = 0.05$ pu, $\omega_{HF} = 2\pi 500$ rad/s, $\omega_r = 500$ r/min and $T_r = 20$ °C

to inverter current limit).

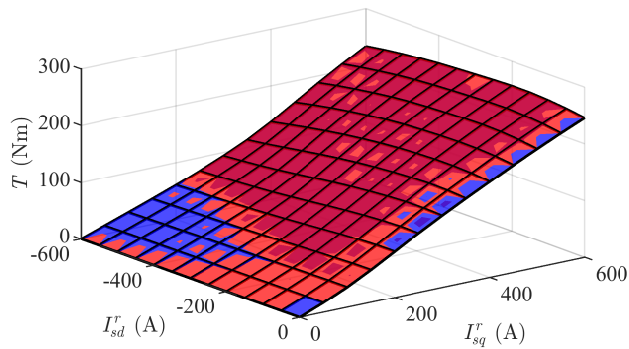
$$error = \hat{T} - T_{measured} \quad (4.37)$$

4.5 Conclusions

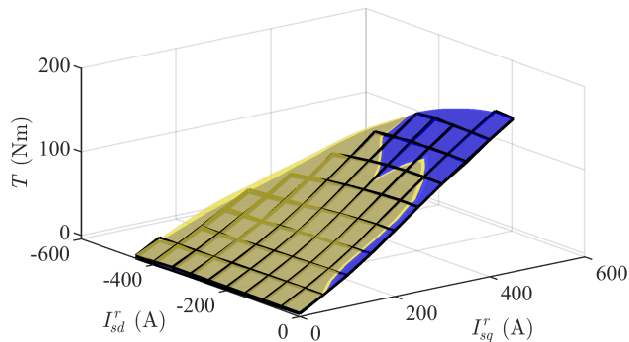
This dissertation proposes a torque estimation method for VLF-PMSMs based on the stator flux linkage estimation. Stator flux linkage is estimated online using

a Gopinath-type flux observer. The d and q-axis inductances and stator resistance are estimated online from the response of the machine to a pulsating HF current signal which is injected on top of the fundamental excitation and controlled in closed loop using resonant controllers. PM flux linkage is estimated from the response to a low-frequency, low-magnitude square-wave current which is also injected on top of the fundamental excitation. Cross-coupling inductance effect has been considered and DC inductance is obtained from HF inductances and used in the stator flux observer. Accurate stator flux estimation is obtained from flux observer using estimated parameters, leading to accurate torque estimation: maximum torque estimation error is in the range of $\approx 2.8\%$. Simulation and experimental results in the entire I_{sdq} map have been provided at three different rotor speeds to demonstrate the validity of the proposed technique.

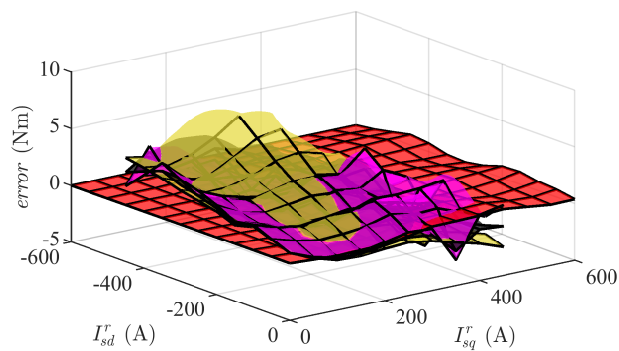
- Actual/Measured torque ■ FEA estimated torque
- Experimentally estimated torque at 0 r/min
- Experimentally estimated torque at 500 r/min
- Experimentally estimated torque at 3000 r/min



(a) Estimated and actual FEA torque



(b) estimated and measured output torque



(c) torque estimation error

Figure 4.17: FEA and experimental results. $I_{HF} = 0.05$ pu, $\omega_{HF} = 2\pi 500$ rad/s, $\omega_r = 500$ r/min and $T_r = 20$ °C

Chapter 5

PM Temperature estimation under six-step operation

5.1 Introduction

As it was discussed in previous sections, high speed operation of conventional PMSMs inherently reduces the efficiency of the machine as higher power losses are induced. This is mainly due to the use of negative d-axis current in the flux weakening region, higher harmonic content induced in the airgap magnetic field and higher mechanical losses due to dynamic frictions of the rotating parts involving fluids, i.e. bearings, fan or pumps and movement of the air mass within the airgap.

Mechanical losses can barely be reduced but losses derived from the use of field weakening can be drastically reduced when VF-PMSMs or VLF-PMSMs are used. However, in order to compensate the power loss increment in flux weakening operation for the whole drive, six-step operation at high speeds (e.g. above rated speed) is typically used in HEVs and EVs. This reduces the switching losses of the inverter as only six switching actions per electric cycle are needed. Nevertheless, the controllability of the drive is drastically reduced making the implementation of parameter estimation techniques specially challenging under six-step operation.

In six-step operation, the magnitude of the voltage vector, given by 5.1, is only determined by the dc bus voltage. Therefore, the phase of the voltage vector in the rotor reference frame becomes the only variable that can be used to control the torque when operating with a constant DC bus voltage [68]. Closed-loop voltage angle based torque control can be implemented by acting on the voltage angle [69].

$$|V_{sdq}^r| = \frac{2V_{DC}}{\pi} \quad (5.1)$$

Fig. 5.1 shows the experimental results of the torque developed by the VLF-PMSM machine (shown in Appendix A) for different voltage angles, 90°, 100° and 110°, the voltage angle being defined as represented in Fig. 5.2. These results have been obtained when the machine is controlled in open loop, as shown in Fig. 5.3.

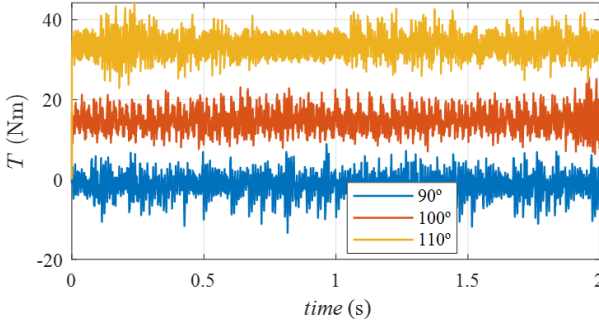


Figure 5.1: VLF-PMSM developed torque vs voltage angle under six-step operation.

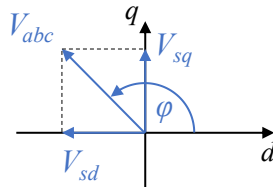


Figure 5.2: Definition of the injected voltage angle under six-step operation.

Six-step operation mainly reduces the switching losses in the inverter but other power losses are induced in the machine at high speeds such as Eddy current and

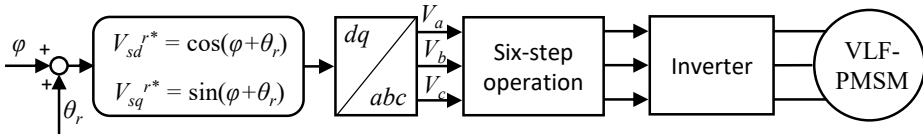


Figure 5.3: Six-step open loop control scheme.

hysteresis losses, what makes necessary the monitoring of the temperature of the most sensitive part of the machine: the PM.

Operating under six-step inherently injects harmonics in the machine terminal voltages (multiples of $6\omega_r$). These voltage harmonics and the resulting current harmonics could be used to estimate the machine inductance which depends on the machine saturation level and, therefore, on the PM temperature.

In this dissertation, the variation of d-axis current, sixth harmonic inductance and PM flux linkage for PM Temperature estimation under six-step operation are compared. It will be shown that the variation of d-axis current is the most interesting option due to its simplicity and sensitivity to PM thermal changes.

5.2 PM Temperature estimation under six-step operation

PM temperature variations have a direct impact on other machine parameters that can be used for PM temperature estimation purposes. In this dissertation the following parameters variations due to PM temperature are studied:

- **PM flux linkage:** the intrinsic PM flux variation of PM materials due to temperature can be used for PM temperature estimation purposes similarly to the method proposed in Chapter 3. Under six-step operation, the PM flux linkage, λ_{pm} , can be calculated from the q-axis voltage equation of the VLF-PMSM shown in (2.1). Assuming steady-state operation, the PM flux linkage can be obtained as in (5.2). However, the uncertainty of the

estimation rely on the stator resistance (R_s) and d-axis inductance (L_d) parameters.

$$\lambda_{pm} = \frac{V_{sq}^r - R_s I_{sq}^r - \omega_r L_d I_{sd}^r}{\omega_r} \quad (5.2)$$

- **Inductance:** PM flux variations affect the machine saturation level, therefore modifying the machine inductances. HF signal injection can be used during linear operation of electrical machines to estimate the machine inductances, as presented in Chapter 4. However, under six-step operation the injection of HF sinusoidal signals is not feasible. On the other hand, some current and voltage harmonics components are naturally produced under six-step operation such as sixth and twelfth harmonics. These components can be used to estimate machine inductance and its variation as the PM flux linkage is reduced with temperature.
- **Fundamental magnitude of the d-axis current:** under six-step operation the PM flux linkage variation leads to fundamental d-axis current variations. Assuming steady-state conditions, the d-axis current variation due to PM flux linkage is shown in (5.3). Using the d-axis fundamental current for PM flux linkage estimation is relatively simple since the current is a measured variable.

$$I_{sd}^r = \frac{V_{sq}^r - R_s I_{sq}^r - \omega_r \lambda_{pm}}{\omega_r L_d} \quad (5.3)$$

5.2.1 PM flux linkage

The use of PM flux linkage as an indicator of PM temperature has been shown to be a reliable method under linear operation of PMSMs in the literature [14–18] and for VLF-PMSMs in Chapter 3 of this dissertation.

However, under six-step operation, the estimation of PM flux linkage is challenging. The PM flux linkage can be estimated from (5.2) if the d-axis inductance is known. Due to the wide variations the inductances show in the Idq map, the use of LUTs to store the d-axis inductance for the entire current region of the machine can be a solution. In Fig. 5.4 the d-axis inductance vs. the machine stator current for different PM temperatures is represented. The variation of the d-axis inductance due to the PM temperature is significantly large, therefore, it should be also stored in a LUT, assuming the inherent increase in memory usage and computational burden of the microcontroller.

■ $T_r = 20\text{ }^\circ\text{C}$, ■ $T_r = 50\text{ }^\circ\text{C}$, ■ $T_r = 80\text{ }^\circ\text{C}$, ■ $T_r = 110\text{ }^\circ\text{C}$, ■ $T_r = 140\text{ }^\circ\text{C}$

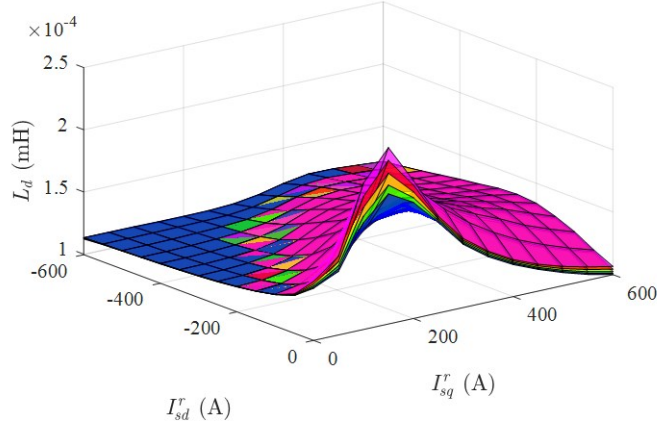


Figure 5.4: FEA results. d-axis inductance vs stator current and PM temperature

In any case, by using the d-axis inductance LUT, the PM flux linkage can be calculated from (5.2). Fig. 5.5 shows FEA results of the estimated PM flux linkage for different voltage angles, rotor speeds and PM temperatures.

■ $T_r = 20\text{ }^\circ\text{C}$, ■ $T_r = 50\text{ }^\circ\text{C}$, ■ $T_r = 80\text{ }^\circ\text{C}$, ■ $T_r = 110\text{ }^\circ\text{C}$, ■ $T_r = 140\text{ }^\circ\text{C}$

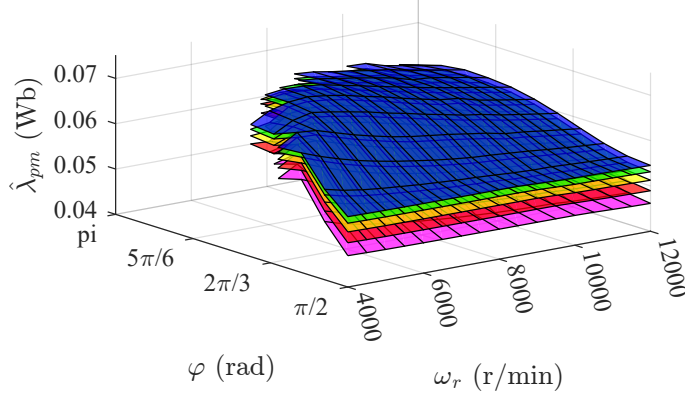


Figure 5.5: FEA results. PM flux linkage vs. injected voltage angle and speed for different PM temperatures.

Using the $20\text{ }^\circ\text{C}$ case as reference, the PM flux linkage variation, $\Delta\lambda_{pm}$, with PM temperature is shown in Fig. 5.6. It can be observed in Fig. 5.6, as expected, that the estimated PM flux linkage is reduced as the PM temperature

increases. Therefore the estimated PM flux linkage can be used to create a LUT or a regression model to estimate the PM temperature.

■ $T_r = 20$ °C, ■ $T_r = 50$ °C, ■ $T_r = 80$ °C, ■ $T_r = 110$ °C, ■ $T_r = 140$ °C

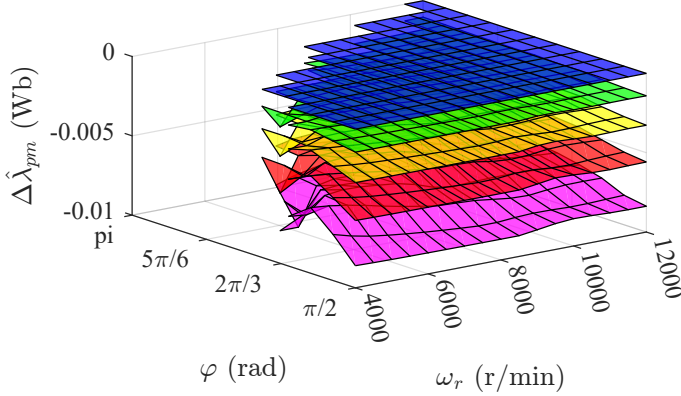


Figure 5.6: FEA results. PM flux linkage variation with temperature using the 20 °C case as reference for different PM temperatures

However, the use of the estimated PM temperature as one of the d-axis inductance LUT dimensions creates a feedback loop. The estimated PM temperature would be used to estimate the d-axis inductance and PM flux linkage, producing a new estimated PM temperature. This places concerns on stability/convergence of the estimation method.

5.2.2 Sixth harmonic inductance

The sixth harmonic of the injected voltage under six-step operation can be used to obtain an inductance estimation. The variation of the saturation level due to the PM flux linkage variation with PM temperature will be reflected in the inductance. Changes in the inductance can be used therefore to estimate the PM flux linkage. The sixth harmonic of the injected voltage can be modeled as in (5.4), where the rotating complex vectors positive $V_{6^{th}pc}$ and negative $V_{6^{th}nc}$ sequence components are considered.

$$v_{sdq6th}^r = |V_{6^{th}pc}|e^{j(6\omega_r + \phi)} + |V_{6^{th}nc}|e^{j(-6\omega_r + \phi)} \quad (5.4)$$

Rotating voltage complex vectors generate a current that is composed of symmetric and asymmetric components in electric machines. The symmetric component is produced by the mean inductance ΣL and the asymmetric component

by the differential inductance ΔL of the machine. Mean and differential inductances of the machine are defined in (5.5). If a machine is fairly symmetric ($L_d = L_q$) the differential inductance and asymmetric components are zero. The total current response considering the positive and negative sequences components of rotating voltage sixth harmonic, neglecting the resistance of the machine, is shown in (5.6).

$$\begin{aligned}\Sigma L &= \frac{L_d + L_q}{2} \\ \Delta L &= \frac{L_q - L_d}{2}\end{aligned}\quad (5.5)$$

$$i_{sdq6^{th}}^r = \left(\frac{|V_{6^{th}pc}|}{\omega_r \Sigma L} + \frac{|V_{6^{th}nc}|}{\omega_r \Delta L} \right) e^{j(6\omega_r + \phi_2)} + \left(\frac{|V_{6^{th}pc}|}{\omega_r \Delta L} + \frac{|V_{6^{th}nc}|}{\omega_r \Sigma L} \right) e^{j(-6\omega_r + \phi_2)} \quad (5.6)$$

Since both positive and negative sequence current components depend on mean and differential inductances, they cannot be directly decoupled. Therefore, a metric of the inductance based on the positive components of voltage and current is calculated in (5.7) and represented in Fig. 5.7 for different PM temperatures.

$$\hat{L} = \frac{|i_{sdq6^{th}pc}^r|}{|V_{6^{th}pc}| \omega_r} \quad (5.7)$$

■ $T_r = 20$ °C, ■ $T_r = 50$ °C, ■ $T_r = 80$ °C, ■ $T_r = 110$ °C, ■ $T_r = 140$ °C

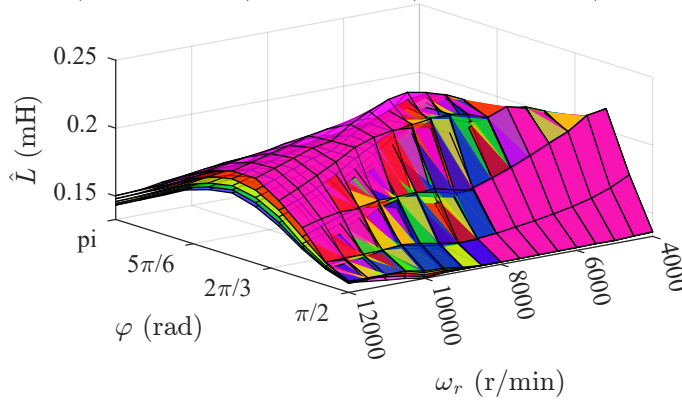


Figure 5.7: FEA Results. Inductance signature for different PM temperatures.

Using the 20 °C case as reference, the inductance variation, $\Delta\hat{L}$, with PM temperature is shown in Fig. 5.8. It can be observed that these results are highly non-linear and the sensitivity of the inductances to PM temperature variation highly depends in the operating point.

■ $T_r = 20$ °C, ■ $T_r = 50$ °C, ■ $T_r = 80$ °C, ■ $T_r = 110$ °C, ■ $T_r = 140$ °C

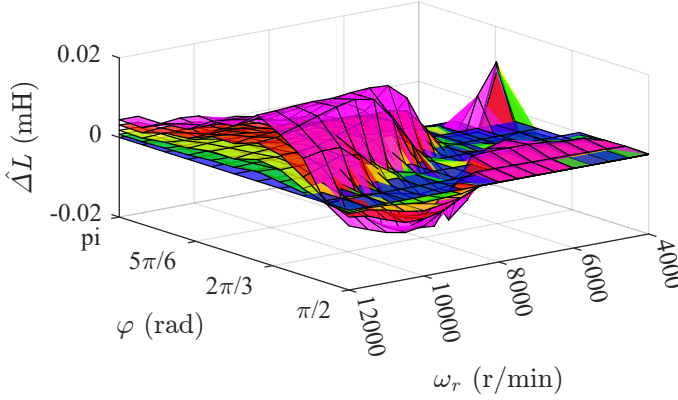


Figure 5.8: FEA Results. Inductance signature variations from 20 °C case for different PM temperatures.

5.2.3 D-axis current

The applied fundamental voltage during six-step operation depends on the DC-link voltage and injection angle. From (5.3), it can be seen that there is a cross-coupling between d and q-axes. For a given operating point with constant speed and injection angle, PM flux linkage variations lead to variations on the magnitude of the d-axis fundamental current. This correlation of d-axis fundamental current with PM flux linkage (and PM temperature) can be used to estimate the PM temperature from the measured stator currents. The fundamental d-axis current magnitude for different PM temperatures is shown in Fig. 5.9.

Fundamental d-axis current variations, ΔI_{sd}^r , due to PM temperature, using the 20 °C case as reference, are shown in Fig. 5.10 in the injected voltage angle and speed region obtained by FEA. These results are in good agreement with (5.3) since an increase of PM temperature leads to a reduction on the PM flux linkage and, therefore, the magnitude of d-axis fundamental current is increased.

■ $T_r = 20\text{ }^{\circ}\text{C}$, ■ $T_r = 50\text{ }^{\circ}\text{C}$, ■ $T_r = 80\text{ }^{\circ}\text{C}$, ■ $T_r = 110\text{ }^{\circ}\text{C}$, ■ $T_r = 140\text{ }^{\circ}\text{C}$

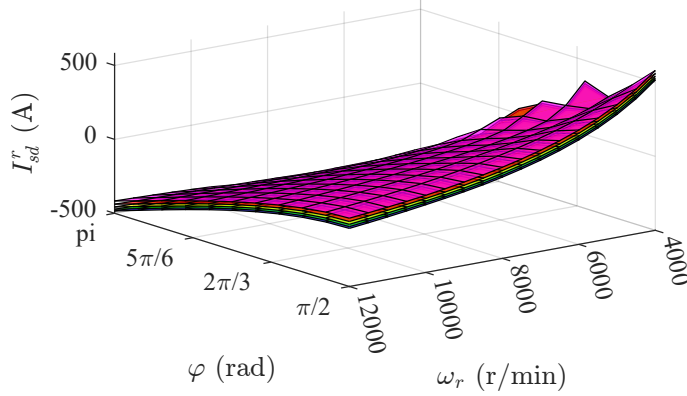


Figure 5.9: FEA results. d-axis fundamental current for different PM temperatures.

■ $T_r = 20\text{ }^{\circ}\text{C}$, ■ $T_r = 50\text{ }^{\circ}\text{C}$, ■ $T_r = 80\text{ }^{\circ}\text{C}$, ■ $T_r = 110\text{ }^{\circ}\text{C}$, ■ $T_r = 140\text{ }^{\circ}\text{C}$

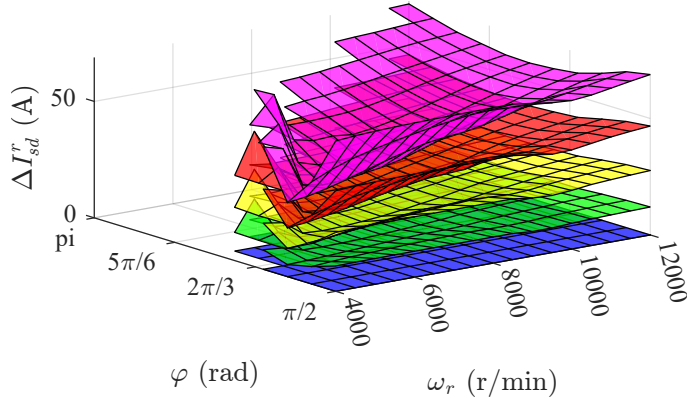


Figure 5.10: FEA results. d-axis current variations using the 20 °C case as reference for different PM temperatures.

It can be seen from Fig. 5.10 that d-axis current variation due to PM temperature is relatively large ($>0.3\text{ A}/^{\circ}\text{C}$) and therefore it provides high sensitivity.

From this discussion it can be concluded that the most promising PM temperature estimation method is the one based on d-axis current variation because its simplicity, direct measurement and lower parameter dependency. Therefore, d-axis current variation with PM temperature will be used in the experimental verification for PM temperature estimation under steady-state conditions and under injected voltage angle and speed transients.

5.3 Experimental verification

In this section, the use of the fundamental d-axis current magnitude to estimate the PM flux linkage is experimentally verified. The test bench used for the experimental verification of the proposed method and the wireless PM temperature measurement system used to verify the accuracy of PM estimated temperature is the same as the one mentioned in previous sections and it is described in detail in Appendix A. The test bench is composed of a conventional IPMSM controlled in speed and used as a load. The VLF-PMSM under test (parameters being shown in Table 2.1) is controlled in six-step open loop voltage angle-based torque control. Each machine is driven by a three-phase inverter which share the DC-link and are controlled using a TMS320F28335 microcontroller.

Six-step operation of the electric machine is limited to high speed operation in order to meet the maximum current limit of the inverter. Therefore, the experimental results are performed from 6000 r/min to 9000 r/min. The injected voltage angle was also limited to 120° .

Due to the harmonics naturally produced under six-step operation, the measured d-axis current has relatively large and fast variations on top of the fundamental d-axis current in the rotor synchronous reference frame. Therefore, the d-axis current will be filtered by a 4th order low pass filter with a cutoff frequency of 100 Hz in order to obtain the magnitude of the fundamental d-axis current that will be used to estimate the PM temperature. The bandwidth of the estimated PM temperature will be limited, considering the inherent large PM temperature time constant, by a 1st order 5 Hz low pass filter, as shown in Fig. 5.11.

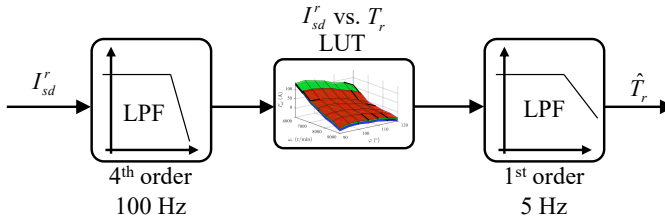


Figure 5.11: PM temperature estimation signal processing from measured d-axis current.

5.3.1 Steady state

Experiments are conducted in steady-state conditions and the d-axis current is measured and stored in the microcontroller for each operating point. The fundamental d-axis current value is obtained by filtering the measured current by a 4th order 100 Hz low pass filter in the rotor synchronous reference frame. Note that the fundamental frequency in the rotor synchronous reference frame is DC.

In Fig. 5.12 the magnitude of the fundamental d-axis current measured by the microcontroller for each operating point is shown for different PM temperatures. The results shown in Fig. 5.12 are in good agreement with FEA results, exhibiting a larger d-axis current for higher PM temperatures. The results for 6000 r/min and 110 °C could not be obtained because the fundamental current value in addition to current harmonics were surpassing the peak current of the inverter.

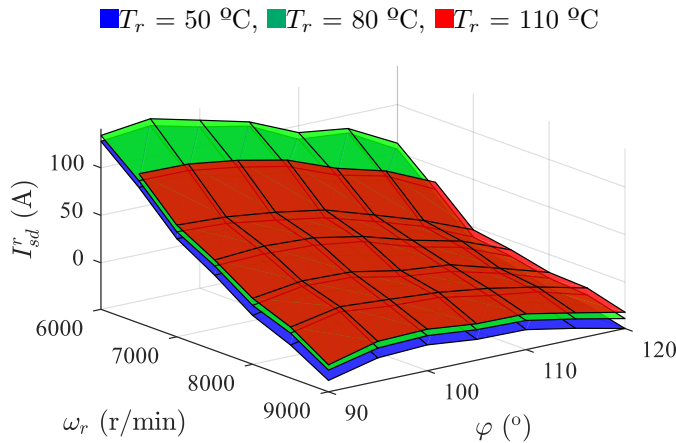


Figure 5.12: Experimental results. d-axis fundamental current for different PM temperatures.

The results shown in Fig. 5.12 are stored and used as LUT, linear interpolation being used between stored operating points. Using the same conditions of previously performed experiments (shown in Fig. 5.12), the LUT is used to estimate the PM temperature from the measured d-axis fundamental current magnitude using the signal processing shown in Fig. 5.11. The estimated PM temperature is shown in Fig. 5.13 and the estimation error is shown in Fig. 5.14. The error is seen to be lower than 6 °C.

In order to test the influence of transient conditions in the estimation method

based on the d-axis fundamental current, two experiments are performed: under injection angle transient and under speed transient. The signal processing shown in Fig. 5.11 will be used for these experiments, as well.

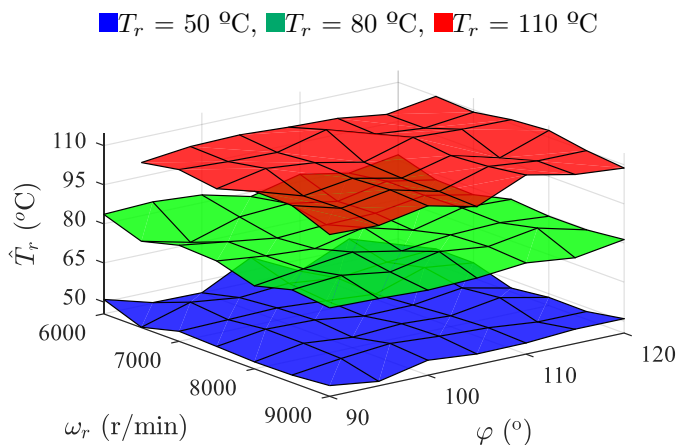


Figure 5.13: Experimental results. Estimated PM temperature using the fundamental d-axis current for different PM temperatures.

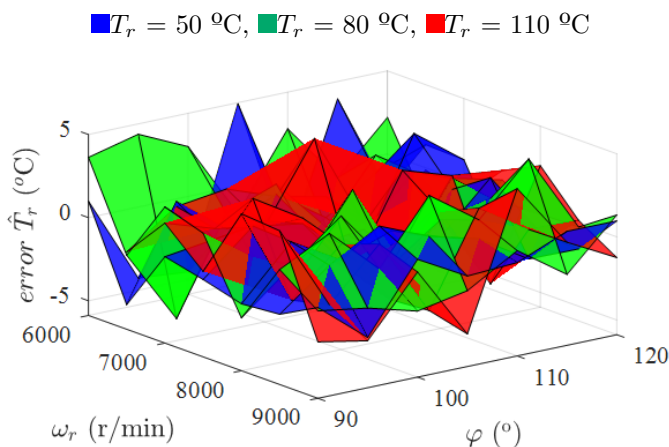


Figure 5.14: Experimental results. PM temperature estimation error using the fundamental d-axis current for different PM temperatures.

5.3.2 Injection angle transient

The voltage injection angle is smoothly varied from 95° to 105° in 0.4 s as seen in Fig. 5.15. The d-axis current sampled by the microcontroller during the injected voltage angle transient is shown in Fig. 5.16 in the rotor synchronous reference frame. The fundamental d-axis current is obtained by filtering the measured current by a 4th order 100 Hz low pass filter.

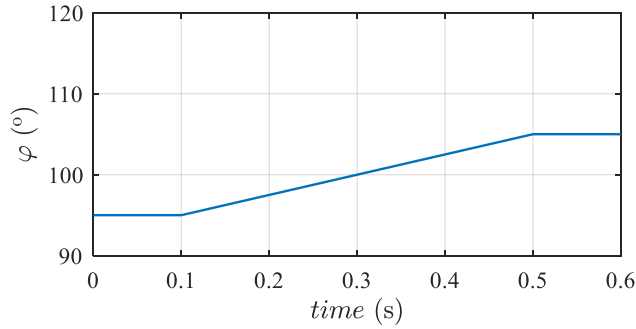


Figure 5.15: Experimental results. Voltage angle transient from 95° to 105° .

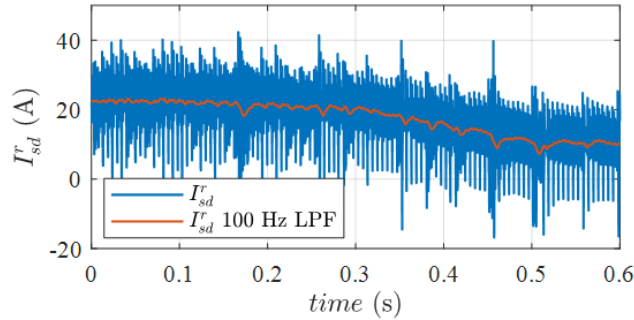


Figure 5.16: Experimental results. Measured and fundamental d-axis current during voltage angle transient. Measured at 10 kHz by the microcontroller.

The fundamental d-axis current is used to estimate the PM temperature from the stored LUT. The estimated PM temperature is shown in Fig. 5.17. The estimated PM temperature shows relatively high frequency ripple, these frequencies are assumed to not be present in the actual PM temperature because of its large time constant. Therefore, the PM temperature time constant can be considered in the estimated PM temperature by applying a 5 Hz low pass filter (also

shown in Fig. 5.17). The filtered estimated PM temperature is used with the measured PM temperature from the wireless PM temperature measured system (see Appendix A) to calculate the estimation error. The estimation error during voltage angle transient is shown in Fig. 5.18. It can be seen from Fig. 5.18 that the estimation error is slightly increased during transients, especially from 0.3 to 0.5s, but it is still lower than 4 °C error.

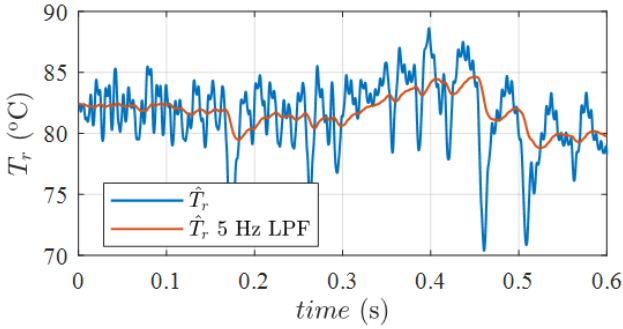


Figure 5.17: Experimental results. Estimated PM temperature during voltage angle transient.

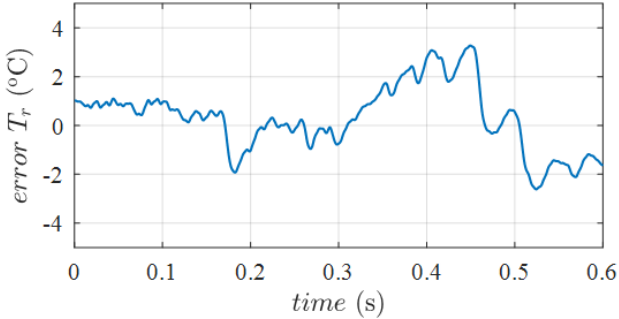


Figure 5.18: Experimental results. PM temperature estimation error during voltage angle transient.

5.3.3 Speed transient

The machine speed is smoothly varied from 8000 to 7500 r/min in 0.4 s as shown in Fig. 5.19 while maintaining a constant voltage angle. The d-axis current measured by the microcontroller during the machine speed transient is shown in

Fig. 5.20. The signal processing is the same as the one used for previous transient experiments, the measured d-axis current being filtered by a 4th order 100 Hz low pass filter to obtain the fundamental d-axis current.

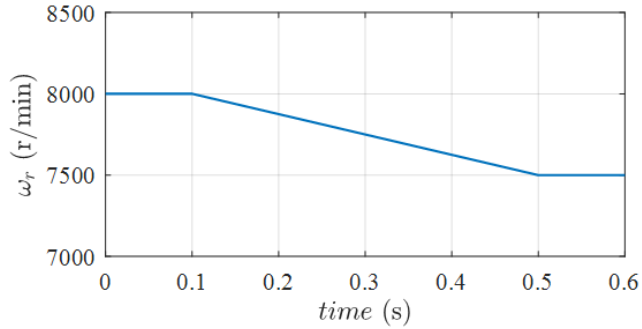


Figure 5.19: Experimental results. Speed transient during six-step operation.

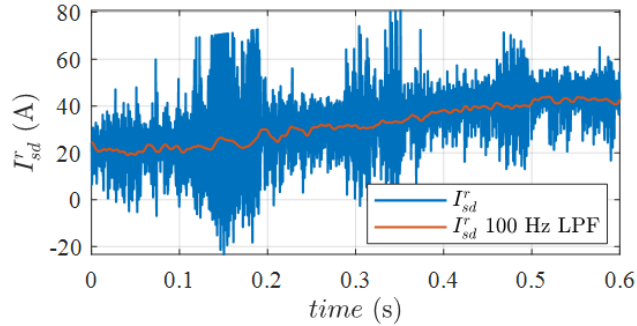


Figure 5.20: Experimental results. Measured and fundamental d-axis current during speed transient. Measured at 10 kHz by the microcontroller.

The fundamental d-axis current is used to estimate the PM temperature from the stored LUT. The estimated PM temperature is shown in Fig. 5.21. The estimated PM temperature is filtered by a 5 Hz low pass filter (also shown in Fig. 5.21) in order to consider the large PM temperature time constant. The measured PM temperature from the wireless PM temperature measured system (see Appendix A) is used to calculate the estimation error. The estimation error during voltage angle transient is shown in Fig. 5.22. It can be seen from Fig. 5.22 that the estimation error is increased during speed transients, showing larger estimation error than during voltage angle transients. The estimation error during the speed transient is under 8 °C.

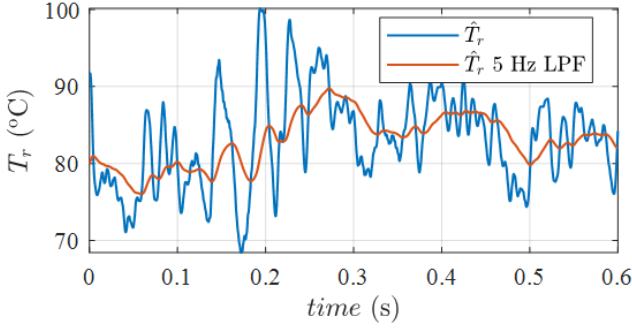


Figure 5.21: Experimental results. Estimated PM temperature during speed transient.

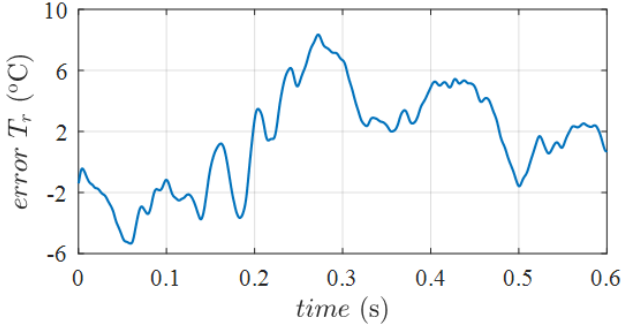


Figure 5.22: Experimental results. PM temperature estimation error during speed transient.

5.4 Conclusions

In this dissertation, the use of PM flux linkage, sixth harmonic inductance and d-axis current for PM temperature estimation under six-step operation has been studied. The most interesting option is the d-axis current variation because its simplicity, its direct measurement and lower parameter dependency. Experimental results at steady-state and during transients have been provided to demonstrate the validity of the proposed technique. Experimental results have been conducted for a VLF-PMSM machine but the proposed method could also be applied to conventional PMSMs.

Chapter 6

Conclusions and future work

6.1 Conclusions

VLF-PMSMs can increase the efficiency of EVs and HEVs and, therefore, increase their driving range by reducing the magnitude of the flux weakening current needed to match the Back-EMF with the available DC link voltage. Monitoring of the PM temperature is unavoidable in high performance PMSM drives to prevent irreversible demagnetization and to compensate the effect of PM temperature in the torque production process. Direct measurement of PM temperature requires the use of rotor mounted sensors and slip rings or wireless transmission which penalizes the robustness and cost of the system, PM temperature estimation being therefore preferred in industry applications.

The PM temperature estimation methods present in the literature use a linear relationship of the PM flux linkage with PM temperature. The variable PM flux linkage of VLF-PMSMs makes the extrapolation of the available techniques inaccurate. The present dissertation has explored the use of LUTs to consider the PM flux linkage variation with stator current. A voltage-model flux observer has been implemented to estimate the total stator flux of the machine. The PM flux linkage has been estimated from the total stator flux by the injection of a low frequency quasi-square-wave current signal in the d-axis. Finally, the PM temperature has been estimated from the PM flux linkage using LUTs. This method has been implemented online, working during normal operation of the machine.

PM temperature estimation under six-step operation in VLF-PMSMs has

been studied. The use of d-axis fundamental current has been shown to be a simple and reliable method to estimate the PM temperature in six-step operation. Experimental results at steady-state and during transients have been provided using a VLF-PMSM to demonstrate the validity of the proposed technique, but the method could be applied to any PMSM.

EVs and HEVs require precise torque control, torque measurement or estimation being therefore needed. Precise torque measurement is expensive, requires room, extra cables, and introduces reliability concerns, torque estimation being therefore preferred. The present dissertation has explored the use of combined LF and HF signal injection to enhance the precision of a Gopinath type flux observer. The HF signal is injected at 45° (between d- and q-axis) in order to simultaneously estimate both d- and q-axis inductances, reducing the adverse effects of HF signal injection. The estimated stator flux is used with measured currents to estimate the produced torque.

The performance of these methods have been tested by FEA simulations and experimentally using the experimental setup presented in Appendix A.

6.2 Contributions

The contributions made during the development of this thesis are summarized as follows:

- A method to estimate the PM temperature considering the variation of PM flux linkage with stator current for VLF-PMSMs by using LUTs has been proposed.
- A method to estimate the PM temperature under six-step operation based on the fundamental magnitude of the d-axis current has been addressed.
- A method to estimate stator inductances and resistance using a single HF current signal injection at 45° from the d-axis has been proposed. This method reduces the adverse effects of HF signal injection compared to the conventional HF current signal injection methods using two different frequencies or sequential injection of two signals.
- The effect of cross-coupling inductances in the proposed HF injection method has been analyzed, and a method to consider this effect by the injection of a LF quasi-square-wave signal has been proposed. It has been shown that

this effect is specially relevant in VLF-PMSMs since their rotor flux paths are coupled due to the rotor flux bridges (flux barriers partially removed) that create the PM leakage flux.

- The estimation of linearized (or DC) inductances from the HF (or dynamic) inductances has been addressed. This is accomplished by integrating the HF inductances along the current trajectory of the machine during normal operation.
- A method to estimate the developed torque of VLF-PMSMs, based on a Gopinath type flux observer enhanced with PM flux linkage and linearized (or DC) inductances estimation, has been proposed.

Several technical papers have been published in international journals and conferences derived from the work of this dissertation (see Section 6.2.1 and Section 6.2.2). Moreover, other contributions have been made during the development of this dissertation (see Section 6.2.3 and Section 6.2.4).

6.2.1 Contributions of the dissertation published in international journals

1. T. Kato, K. Sasaki, **D. F. Laborda**, D. Fernandez and D. Reigosa, “Magnet Temperature Estimation Methodology by Using Magnet Flux Linkage Observer for Variable Leakage Flux IPMSM”, in *IEEEJ Transactions on Industry Applications*, vol. 140, no. 4, pp. 265-271, April 2020, doi: 10.1541/ieejias.140.265

6.2.2 Contributions of the dissertation published in international conferences

2. **D. F. Laborda**, D. Reigosa, D. Fernandez, K. Sasaki, T. Kato and F. Briz, “Magnet Temperature Estimation in Variable Leakage Flux Permanent Magnet Synchronous Machines Using the Magnet Flux Linkage”, in *2020 IEEE Energy Conversion Congress and Exposition (ECCE)*, Detroit, MI, USA, 2020, pp. 6111-6117, doi:10.1109/ECCE44975.2020.9236059.
3. **D. F. Laborda**, D. Reigosa, D. Fernandez, K. Sasaki, T. Kato and F. Briz, “Enhanced Torque Estimation in Variable Leakage Flux PMSM Combining

High and Low Frequency Signal Injection”, in 2020 IEEE Energy Conversion Congress and Exposition (ECCE), Detroit, MI, USA, 2020, pp. 1764-1771, doi: 10.1109/ECCE44975.2020.9235869.

6.2.3 Other contributions published in international journals

4. M. Martinez, **D. F. Laborda**, D. Reigosa, D. Fernandez, J. M. Guerrero and F. Briz, ”SynRM Sensorless Torque Estimation Using High Frequency Signal Injection,” in IEEE Transactions on Industry Applications, doi: 10.1109/TIA.2021.3111840
5. D. F. Alonso, Y. Kang, **D. F. Laborda**, M. M. Gómez, D. D. Reigosa and F. Briz, ”Permanent Magnet Synchronous Machine Torque Estimation Using Low Cost Hall-Effect Sensors,” in IEEE Transactions on Industry Applications, vol. 57, no. 4, pp. 3735-3743, July-Aug. 2021, doi: 10.1109/TIA.2021.3075924.
6. D. Fernandez, **D. F. Laborda**, M. Martinez, D. Reigosa, A. B. Diez and F. Briz, “Resolver Emulation for PMSMs Using Low Cost Hall Effect Sensors”, in IEEE Transactions on Industry Applications, vol. 56, no. 5, pp. 4977-4985, Sept.-Oct. 2020, doi: 10.1109/TIA.2020.3008129.
7. C. González-Moral, **D. F. Laborda**, L. S. Alonso, D. Fernández, C. Rivas, D. Reigosa, “Battery Internal Resistance Estimation Using a Battery Balancing System Based on Switched Capacitors”, in IEEE Transactions on Industry Applications, vol. 56, no. 5, pp. 5363-5374, Sept.-Oct. 2020, doi: 10.1109/TIA.2020.3005382.

6.2.4 Other contributions published in international conferences

8. **D. F. Laborda**, J. M. Guerrero, M. O. Zapico, D. Fernández, D. D. Reigosa and F. Briz, ”Online PI Current Controller Tuning Based on Machine High-Frequency Parameters,” 2021 IEEE Energy Conversion Congress and Exposition (ECCE), 2021, pp. 5029-5035, doi: 10.1109/ECCE47101.2021.9595336.
9. M. Martinez, **D. F. Laborda**, D. Reigosa and F. Briz, ”Comparative Analysis of Torque Pulsations Measurement Methods for PMSM Drives,”

- 2021 IEEE Energy Conversion Congress and Exposition (ECCE), 2021, pp. 5129-5135, doi: 10.1109/ECCE47101.2021.9595735.
10. C. G. Moral, **D. F. Laborda**, J. M. G. Muñoz, C. Rivas and D. D. Reigosa, "Comparison Of Anti-Windup Alternatives For Parallel Controllers," 2021 IEEE Energy Conversion Congress and Exposition (ECCE), 2021, pp. 3524-3529, doi: 10.1109/ECCE47101.2021.9595940.
 11. M. O. Zapico, D. D. Reigosa, **D. F. Laborda**, M. M. Gómez, J. M. G. Muñoz and F. B. d. Blanco, "Use HF Signal Injection for Simultaneous Rotor Angle, Torque and Temperature Estimation in PMSMs," 2021 IEEE Energy Conversion Congress and Exposition (ECCE), 2021, pp. 5084-5091, doi: 10.1109/ECCE47101.2021.9595710
 12. Y. G. Kang, **D. F. Laborda**, D. Fernandez, D. Reigosa, and F. Briz, "Magnetic Resolver Using Hall-Effect Sensors" in 2020 IEEE Energy Conversion Congress and Exposition (ECCE), Detroit, MI, USA, 2020, pp. 2344-2350, doi:10.1109/ECCE44975.2020.9236184.
 13. D. F. Alonso, Y. Kang, **D. F. Laborda**, M. M. Gómez, D. D. Reigosa, and F. Briz, "Permanent Magnet Synchronous Machine Torque Estimation Using Low Cost Hall-Effect Sensors", in 2019 IEEE 10th International Symposium on Sensorless Control for Electrical Drives (SLED), Turin, Italy, 2019, pp. 1-6, doi: 10.1109/SLED.2019.8896292.
 14. M. Martinez, **D. F. Laborda**, D. Reigosa, D. Fernández, J. M. Guerrero, and F. Briz, "SynRM Sensorless Torque Estimation Using High Frequency Signal Injection", in 2019 IEEE 10th International Symposium on Sensorless Control for Electrical Drives (SLED), Turin, Italy, 2019, pp. 1-5, doi: 10.1109/SLED.2019.8896220.
 15. D. Fernandez, **D. F. Laborda**, M. Martinez, D. Reigosa, A. B. Diez and F. Briz, "Resolver Emulation for PMSMs Using Low Cost Hall Effect Sensors", in 2019 IEEE Energy Conversion Congress and Exposition (ECCE), Baltimore, MD, USA, 2019, pp. 5689-5693, doi: 10.1109/ECCE.2019.8913229
 16. C. González-Moral, **D. F. Laborda**, L. S. Alonso, D. Fernández, C. Rivas, D. Reigosa, "Battery Internal Resistance Estimation Using a Battery Balancing System Based on Switched Capacitors", in 2019 IEEE Energy Conversion Congress and Exposition (ECCE), Baltimore, MD, USA, 2019, pp. 2516-2522, doi: 10.1109/ECCE.2019.8912675

6.3 Future work

Several points could be addressed in the future to continue the research line of this dissertation:

- Combination of thermal models with the proposed PM temperature estimation method for VLF-PMSMs, extending the estimation to very low speeds and standstill where the Back-EMF is too small to be used.
- Simultaneous use of high-frequency signal injection for rotor position estimation and torque estimation.
- Evaluation of the proposed methods during standardized driving cycles such as the New European Driving Cycle (NEDC) or the World harmonized Light-duty vehicles Test Procedure (WLTP).
- Extension of the proposed torque estimation method for torque ripple estimation and minimization.

6.4 Dissertation funding

This work was funded in part by Nissan Motor co. under the research projects FUO-21-183, FUO-259-20, FUO-261-19, FUO-EM-274-18, in part by the Government of the Principality of Asturias under grant Severo Ochoa BP20-153, and in part by the University of Oviedo under PAPI 2019 grants (B modality).

Chapter 6

Conclusiones y trabajo futuro

6.1 Conclusiones

Las VLF-PMSMs pueden incrementar la eficiencia de EVs y HEVs, y por lo tanto aumentar su rango de funcionamiento al reducir la magnitud de la corriente de debilitamiento de flujo que necesitan para igualar la Back-EMF de la máquina con la tensión de continua disponible en el bus. Se requiere la monitorización de la temperatura de los imanes permanentes para prevenir la desmagnetización irreversible de los imanes y compensar el efecto de la temperatura en la producción de par. La medida directa de la temperatura de los imanes requiere el uso de sensores montados en el rotor de la máquina y anillos rozantes o sistemas de transmisión inalámbrica, lo cual reduce la robustez y aumenta el coste del sistema. Por lo tanto, la estimación de la temperatura de los imanes es preferible a su medida.

Los métodos de estimación de temperatura de imanes existentes en la literatura usan una relación lineal del enlace de flujo de los imanes con su temperatura. La variación del enlace de flujo de las VLF-PMSMs hace la extrapolación de las técnicas disponibles imprecisa. Este trabajo ha explorado el uso de LUTs para considerar el efecto de la variación del enlace de flujo de los imanes con la corriente de estator. Un observador de flujo basado en el modelo de tensión ha sido implementado para estimar el flujo total de estator de la máquina. El flujo de en-

lace de los imanes ha sido estimado desde el flujo total usando la inyección de una señal de corriente cuasi-cuadrada en el eje-d. Finalmente, la temperatura de los imanes ha sido estimada desde el enlace de flujo de los imanes usando las LUTs. Este método ha sido implementado online, actuando durante el funcionamiento normal de la máquina.

En el presente trabajo se ha estudiado la estimación de temperatura de los imanes permanentes de la VLF-PMSM funcionando en six-step. Se ha mostrado que el uso del valor fundamental de la corriente de eje-d es un método simple y de confianza para la estimación de la temperatura de los imanes en six-step. Se ha comprobado la validez del método mediante experimentos en régimen permanente y transitorios de velocidad y par.

Los EVs y HEVs requieren de un preciso control del par generado siendo, por lo tanto, la medida o la estimación de par necesarias. La medida precisa del par es cara, requiere espacio, cables extra e introduce problemas de fiabilidad, por lo tanto su estimación es preferible a su medida. El presente trabajo ha explorado el uso combinado de inyección de señales de alta y baja frecuencia para mejorar la precisión de un observador de flujo tipo Gopinath. La señal de alta frecuencia se inyecta a 45° (entre los ejes d y q) con el objetivo de estimar de forma simultánea las inductancias del eje-d y q, reduciendo los efectos adversos de la inyección de alta frecuencia. El flujo de estator estimado es usado junto a las medidas de corriente para estimar el par producido.

El rendimiento de estas técnicas ha sido comprobado mediante simulaciones de elementos finitos y experimentalmente, utilizando el equipo presentado en el Apéndice A.

6.2 Contribuciones

Las contribuciones realizadas durante el desarrollo de esta tesis se resumen a continuación:

- Se ha propuesto un método para estimar la temperatura de los imanes permanentes considerando la variación del enlace de flujo de los imanes con la corriente de estator para VLF-PMSMs usando LUTs.
- Se ha propuesto un método para estimar la temperatura de los imanes permanentes durante el funcionamiento en six-step basado en la magnitud de la corriente fundamental de eje-d.

- Se ha propuesto un método para estimar las inductancias y resistencia de estator usando una única señal de alta frecuencia a 45°. Este método reduce los efectos adversos de la inyección de alta frecuencia comparado con los métodos convencionales que usan dos frecuencias diferentes o la inyección secuencial de dos señales.
- El efecto de acoplamiento cruzado de las inductancias en el método propuesto de inyección de alta frecuencia ha sido analizado y se ha propuesto un método para considerar este efecto basado en la inyección de una señal de corriente cuasi-cuadrada de baja frecuencia. Se ha mostrado que este efecto es especialmente relevante en VLF-PMSMs debido a los puentes de flujo (barreras de flujo parcialmente eliminadas) presentes en el rotor para crear el efecto de flujo de dispersión variable característico de este tipo de máquinas.
- Se ha incluido la estimación de las inductancias linealizadas (o DC) desde las inductancias de alta frecuencia (o dinámicas). Esto se ha realizado mediante la integración de las inductancias de alta frecuencia a lo largo de la trayectoria de corriente de la máquina durante su funcionamiento.
- Se ha propuesto un método para estimar el par ejercido por VLF-PMSMs, basado en un observador de flujo tipo Gopinath mejorado con la estimación del enlace de flujo de los PMs y inductancias linealizadas (o DC).

Se han publicado varios artículos en revistas internacionales y conferencias internacionales derivadas del trabajo realizado en esta tesis doctoral (ver sección 6.2.1 y sección 6.2.2). Además, se han realizado otras contribuciones al campo de los accionamientos eléctricos durante el desarrollo de esta tesis doctoral (ver sección 6.2.3 y sección 6.2.4).

6.2.1 Contribuciones de la tesis doctoral publicadas revistas internacionales

1. T. Kato, K. Sasaki, **D. F. Laborda**, D. Fernandez and D. Reigosa, “Magnet Temperature Estimation Methodology by Using Magnet Flux Linkage Observer for Variable Leakage Flux IPMSM”, in *IEEEJ Transactions on Industry Applications*, vol. 140, no. 4, pp. 265-271, April 2020, doi: 10.1541/ieejias.140.265

6.2.2 Contribuciones de la tesis doctoral publicadas en congresos internacionales

2. **D. F. Laborda**, D. Reigosa, D. Fernandez, K. Sasaki, T. Kato and F. Briz, "Magnet Temperature Estimation in Variable Leakage Flux Permanent Magnet Synchronous Machines Using the Magnet Flux Linkage", in 2020 IEEE Energy Conversion Congress and Exposition (ECCE), Detroit, MI, USA, 2020, pp. 6111-6117, doi:10.1109/ECCE44975.2020.9236059.
3. **D. F. Laborda**, D. Reigosa, D. Fernandez, K. Sasaki, T. Kato and F. Briz, "Enhanced Torque Estimation in Variable Leakage Flux PMSM Combining High and Low Frequency Signal Injection", in 2020 IEEE Energy Conversion Congress and Exposition (ECCE), Detroit, MI, USA, 2020, pp. 1764-1771, doi: 10.1109/ECCE44975.2020.9235869.

6.2.3 Otras contribuciones publicadas en revistas internacionales

4. M. Martinez, **D. F. Laborda**, D. Reigosa, D. Fernandez, J. M. Guerrero and F. Briz, "SynRM Sensorless Torque Estimation Using High Frequency Signal Injection," in IEEE Transactions on Industry Applications, doi: 10.1109/TIA.2021.3111840
5. D. F. Alonso, Y. Kang, **D. F. Laborda**, M. M. Gómez, D. D. Reigosa and F. Briz, "Permanent Magnet Synchronous Machine Torque Estimation Using Low Cost Hall-Effect Sensors," in IEEE Transactions on Industry Applications, vol. 57, no. 4, pp. 3735-3743, July-Aug. 2021, doi: 10.1109/TIA.2021.3075924.
6. D. Fernandez, **D. F. Laborda**, M. Martinez, D. Reigosa, A. B. Diez and F. Briz, "Resolver Emulation for PMSMs Using Low Cost Hall Effect Sensors", in IEEE Transactions on Industry Applications, vol. 56, no. 5, pp. 4977-4985, Sept.-Oct. 2020, doi: 10.1109/TIA.2020.3008129.
7. C. González-Moral, **D. F. Laborda**, L. S. Alonso, D. Fernández, C. Rivas, D. Reigosa, "Battery Internal Resistance Estimation Using a Battery Balancing System Based on Switched Capacitors", in IEEE Transactions on Industry Applications, vol. 56, no. 5, pp. 5363-5374, Sept.-Oct. 2020, doi: 10.1109/TIA.2020.3005382.

6.2.4 Otras contribuciones en conferencias internacionales

8. **D. F. Laborda**, J. M. Guerrero, M. O. Zapico, D. Fernández, D. D. Reigosa and F. Briz, "Online PI Current Controller Tuning Based on Machine High-Frequency Parameters," 2021 IEEE Energy Conversion Congress and Exposition (ECCE), 2021, pp. 5029-5035, doi: 10.1109/ECCE47101.2021.9595336.
9. M. Martinez, **D. F. Laborda**, D. Reigosa and F. Briz, "Comparative Analysis of Torque Pulsations Measurement Methods for PMSM Drives," 2021 IEEE Energy Conversion Congress and Exposition (ECCE), 2021, pp. 5129-5135, doi: 10.1109/ECCE47101.2021.9595735.
10. C. G. Moral, **D. F. Laborda**, J. M. G. Muñoz, C. Rivas and D. D. Reigosa, "Comparison Of Anti-Windup Alternatives For Parallel Controllers," 2021 IEEE Energy Conversion Congress and Exposition (ECCE), 2021, pp. 3524-3529, doi: 10.1109/ECCE47101.2021.9595940.
11. M. O. Zapico, D. D. Reigosa, **D. F. Laborda**, M. M. Gómez, J. M. G. Muñoz and F. B. d. Blanco, "Use HF Signal Injection for Simultaneous Rotor Angle, Torque and Temperature Estimation in PMSMs," 2021 IEEE Energy Conversion Congress and Exposition (ECCE), 2021, pp. 5084-5091, doi: 10.1109/ECCE47101.2021.9595710
12. Y. G. Kang, **D. F. Laborda**, D. Fernandez, D. Reigosa, and F. Briz, "Magnetic Resolver Using Hall-Effect Sensors" in 2020 IEEE Energy Conversion Congress and Exposition (ECCE), Detroit, MI, USA, 2020, pp. 2344-2350, doi:10.1109/ECCE44975.2020.9236184.
13. D. F. Alonso, Y. Kang, **D. F. Laborda**, M. M. Gómez, D. D. Reigosa, and F. Briz, "Permanent Magnet Synchronous Machine Torque Estimation Using Low Cost Hall-Effect Sensors", in 2019 IEEE 10th International Symposium on Sensorless Control for Electrical Drives (SLED), Turin, Italy, 2019, pp. 1-6, doi: 10.1109/SLED.2019.8896292.
14. M. Martinez, **D. F. Laborda**, D. Reigosa, D. Fernández, J. M. Guerrero, and F. Briz, "SynRM Sensorless Torque Estimation Using High Frequency Signal Injection", in 2019 IEEE 10th International Symposium on Sensorless Control for Electrical Drives (SLED), Turin, Italy, 2019, pp. 1-5, doi: 10.1109/SLED.2019.8896220.
15. D. Fernandez, **D. F. Laborda**, M. Martinez, D. Reigosa, A. B. Diez and F. Briz, "Resolver Emulation for PMSMs Using Low Cost Hall Effect Sensors",

in 2019 IEEE Energy Conversion Congress and Exposition (ECCE), Baltimore, MD, USA, 2019, pp. 5689-5693, doi: 10.1109/ECCE.2019.8913229

16. C. González-Moral, **D. F. Laborda**, L. S. Alonso, D. Fernández, C. Rivas, D. Reigosa, “Battery Internal Resistance Estimation Using a Battery Balancing System Based on Switched Capacitors”, in 2019 IEEE Energy Conversion Congress and Exposition (ECCE), Baltimore, MD, USA, 2019, pp. 2516-2522, doi: 10.1109/ECCE.2019.8912675

6.3 Trabajo Futuro

A raíz del trabajo realizado en la presente tesis doctoral, existen varias líneas de investigación abiertas para su estudio futuro:

- La combinación de modelos térmicos con el método propuesto para estimar la temperatura de los imanes permanentes en VLF-PMSMs para extender el rango de estimación a velocidades muy bajas y velocidad nula, donde la Back-EMF es demasiado baja para ser usada.
- El uso simultáneo de inyección de señales de alta frecuencia para la estimación de par y posición.
- La evaluación de los métodos de estimación propuestos bajo ciclos de funcionamiento estándar como el “New European Driving Cycle” (NEDC) o el “World harmonized Light-duty vehicles Test Procedure” (WLTP).
- La extensión del método de estimación de par propuesto en la tesis para la estimación y minimización del rizado de par.

6.4 Financiación

Este trabajo ha sido financiado en parte por Nissan Motor co. bajo los proyectos de investigación FUO-21-183, FUO-259-20, FUO-261-19, FUO-EM-274-18, en parte por el Principado de Asturias bajo la beca Severo Ochoa BP20-153 y en parte por la Universidad de Oviedo bajo la beca PAPI 2019 (modalidad B).

Bibliography

- [1] I. P. on Climate Change, ed., *Climate Change 2021: The Physical Science Basis. Contribution of Working Group I to the Sixth Assessment Report of the Intergovernmental Panel on Climate Change*. New York, NY: Cambridge University Press. In Press., 2021.
- [2] I. P. on Climate Change and O. Edenhofer, eds., *Climate change 2014: mitigation of climate change: Working Group III contribution to the Fifth Assessment Report of the Intergovernmental Panel on Climate Change*. New York, NY: Cambridge University Press, 2014.
- [3] C. D. Anderson and J. Anderson, *Electric and Hybrid Cars: A History, 2d ed.* McFarland, Incorporated, Publishers, Apr. 2010.
- [4] K. T. Chau, *Electric Vehicle Machines and Drives: Design, Analysis and Application*. John Wiley & Sons, May 2015.
- [5] Jang-Mok Kim and Seung-Ki Sul, "Speed control of interior permanent magnet synchronous motor drive for the flux weakening operation," *IEEE Transactions on Industry Applications*, vol. 33, pp. 43–48, Jan. 1997.
- [6] V. Ostovic, "Memory motors," *IEEE Industry Applications Magazine*, vol. 9, pp. 52–61, Jan. 2003.
- [7] A. Athavale, T. Fukushige, T. Kato, C. Yu, and R. D. Lorenz, "Variable Leakage Flux IPMSMs for Reduced Losses Over a Driving Cycle While Maintaining Suitable Attributes for High-Frequency Injection-Based Rotor Position Self-Sensing," *IEEE Transactions on Industry Applications*, vol. 52, pp. 234–241, Jan. 2016.

-
- [8] B. S. Gagas, K. Sasaki, A. Athavale, T. Kato, and R. D. Lorenz, "Magnet Temperature Effects on the Useful Properties of Variable Flux PM Synchronous Machines and a Mitigating Method for Magnetization Changes," *IEEE Transactions on Industry Applications*, vol. 53, pp. 2189–2199, May 2017.
- [9] T. Kato, T. Matsuura, K. Sasaki, and T. Tanimoto, "Principle of variable leakage flux IPMSM using arc-shaped magnet considering variable motor parameter characteristics depending on load current," in *Proc. IEEE Energy Convers. Congr. Expo.*, pp. 5803–5810, Oct. 2017.
- [10] A. EL-Refaie, N. Harris, T. Jahns, and K. Rahman, "Thermal analysis of multibarrier interior PM synchronous Machine using lumped parameter model," *IEEE Transactions on Energy Conversion*, vol. 19, pp. 303–309, June 2004.
- [11] A. Boglietti, A. Cavagnino, D. Staton, M. Shanel, M. Mueller, and C. Mejuto, "Evolution and modern approaches for thermal analysis of electrical machines," *IEEE Transactions on Industrial Electronics*, vol. 56, no. 3, pp. 871–882, 2009.
- [12] C. Kral, A. Haumer, and S. B. Lee, "A Practical Thermal Model for the Estimation of Permanent Magnet and Stator Winding Temperatures," *IEEE Transactions on Power Electronics*, vol. 29, pp. 455–464, Jan. 2014.
- [13] D. Liang, Z. Zhu, J. Feng, S. Guo, Y. Li, A. Zhao, and J. Hou, "Estimation of 3-D Magnet Temperature Distribution Based on Lumped-parameter and Analytical Hybrid Thermal Model for SPMSM," *IEEE Transactions on Energy Conversion*, pp. 1–1, 2021.
- [14] D. E. G. Erazo, O. Wallscheid, and J. Böcker, "Improved Fusion of Permanent Magnet Temperature Estimation Techniques for Synchronous Motors Using a Kalman Filter," *IEEE Transactions on Industrial Electronics*, vol. 67, pp. 1708–1717, Mar. 2020.
- [15] A. Specht, O. Wallscheid, and J. Böcker, "Determination of rotor temperature for an interior permanent magnet synchronous machine using a precise flux observer," in *2014 International Power Electronics Conference (IPEC-Hiroshima 2014 - ECCE ASIA)*, pp. 1501–1507, May 2014. ISSN: 2150-6086.
- [16] O. Wallscheid, A. Specht, and J. Böcker, "Observing the Permanent-Magnet Temperature of Synchronous Motors Based on Electrical Fundamental Wave

- Model Quantities,” *IEEE Transactions on Industrial Electronics*, vol. 64, pp. 3921–3929, May 2017.
- [17] G. Feng, C. Lai, J. Tjong, and N. C. Kar, “Noninvasive Kalman Filter Based Permanent Magnet Temperature Estimation for Permanent Magnet Synchronous Machines,” *IEEE Transactions on Power Electronics*, vol. 33, pp. 10673–10682, Dec. 2018.
- [18] G. Feng, C. Lai, W. Li, M. Kelly, and N. C. Kar, “Simultaneous Stator Winding and Permanent Magnet Temperature Estimation for Permanent Magnet Synchronous Machines,” in *2018 XIII International Conference on Electrical Machines (ICEM)*, pp. 1945–1951, Sept. 2018. ISSN: 2381-4802.
- [19] D. D. Reigosa, D. Fernandez, H. Yoshida, T. Kato, and F. Briz, “Permanent-Magnet Temperature Estimation in PMSMs Using Pulsating High-Frequency Current Injection,” *IEEE Transactions on Industry Applications*, vol. 51, pp. 3159–3168, July 2015.
- [20] D. D. Reigosa, F. Briz, P. García, J. M. Guerrero, and M. W. Degner, “Magnet Temperature Estimation in Surface PM Machines Using High-Frequency Signal Injection,” *IEEE Transactions on Industry Applications*, vol. 46, pp. 1468–1475, July 2010.
- [21] M. Ganchev, C. Kral, and T. Wolbank, “Sensorless rotor temperature estimation of permanent magnet synchronous motor under load conditions,” in *IECON 2012 - 38th Annual Conference on IEEE Industrial Electronics Society*, pp. 1999–2004, Oct. 2012. ISSN: 1553-572X.
- [22] G. Feng, C. Lai, and N. C. Kar, “Particle-Filter-Based Magnet Flux Linkage Estimation for PMSM Magnet Condition Monitoring Using Harmonics in Machine Speed,” *IEEE Transactions on Industrial Informatics*, vol. 13, pp. 1280–1290, June 2017.
- [23] G. Feng, C. Lai, J. Tjong, and N. C. Kar, “Exploring the Phase Angle of Measured Speed Harmonic for Efficient Permanent Magnet Temperature Estimation of PMSMs,” *IEEE Transactions on Energy Conversion*, vol. 34, pp. 1475–1484, Sept. 2019.
- [24] D. Fernandez, D. Reigosa, J. M. Guerrero, Z. Q. Zhu, C. Suarez, and F. Briz, “Influence of PM Coating on PM Magnetization State Estimation Methods Based on Magneto-resistive Effect,” *IEEE Transactions on Industry Applications*, vol. 54, pp. 2141–2150, May 2018.

- [25] C. Lin, S. Liang, J. Chen, and X. Gao, "A Multi-Objective Optimal Torque Distribution Strategy for Four In-Wheel-Motor Drive Electric Vehicles," *IEEE Access*, vol. 7, pp. 64627–64640, 2019.
- [26] D. Neacsu and K. Rajashekara, "Comparative analysis of torque-controlled IM drives with applications in electric and hybrid vehicles," *IEEE Transactions on Power Electronics*, vol. 16, pp. 240–247, Mar. 2001.
- [27] Z. Zhang, R. Ma, L. Wang, and J. Zhang, "Novel PMSM Control for Anti-Lock Braking Considering Transmission Properties of the Electric Vehicle," *IEEE Transactions on Vehicular Technology*, vol. 67, pp. 10378–10386, Nov. 2018.
- [28] K. C. Yeo, G. Heins, and F. De Boer, "Comparison of torque estimators for PMSM," in *Australasian Universities Power Engineering Conference*, pp. 1–6, Dec. 2008.
- [29] B. Cheng and T. R. Tesch, "Torque Feedforward Control Technique for Permanent-Magnet Synchronous Motors," *IEEE Transactions on Industrial Electronics*, vol. 57, pp. 969–974, Mar. 2010.
- [30] M. Martinez, D. Reigosa, D. Fernández, J. M. Guerrero, and F. Briz, "PMSMs Torque Estimation Using Pulsating HF Current Injection," in *2018 IEEE 9th International Symposium on Sensorless Control for Electrical Drives (SLED)*, pp. 96–101, Sept. 2018. ISSN: 2166-6733, 2166-6725.
- [31] F. Jukic, D. Sumina, and I. Erceg, "Comparison of torque estimation methods for interior permanent magnet wind power generator," in *International Conference on Electrical Drives and Power Electronics (EDPE)*, pp. 291–296, Oct. 2017. ISSN: 1339-3944.
- [32] J. Xu, S. Panda, Y. Pan, T. Lee, and B. Lam, "Improved PMSM pulsating torque minimization with iterative learning and sliding mode observer," in *IEEE International Conference on Industrial Electronics, Control and Instrumentation*, vol. 3, (Nagoya, Japan), pp. 1931–1936, IEEE, 2000.
- [33] W. Qian, S. Panda, and J.-X. Xu, "Torque ripple minimization in PM synchronous motors using iterative learning control," *IEEE Transactions on Power Electronics*, vol. 19, pp. 272–279, Mar. 2004.
- [34] S.-K. Chung, H.-S. Kim, C.-G. Kim, and M.-J. Youn, "A new instantaneous torque control of PM synchronous motor for high-performance direct-drive

- applications,” *IEEE Transactions on Power Electronics*, vol. 13, pp. 388–400, May 1998.
- [35] X. Dong, W. Tianmiao, and W. Hongxing, “Comparison between model reference observer and reduced order observer of PMSM torque,” in *IEEE Conference on Industrial Electronics and Applications*, pp. 663–667, June 2011. ISSN: 2158-2297, 2156-2318.
- [36] Q. Liu and K. Hameyer, “High-Performance Adaptive Torque Control for an IPMSM With Real-Time MTPA Operation,” *IEEE Transactions on Energy Conversion*, vol. 32, pp. 571–581, June 2017.
- [37] Y.-R. Mohamed and T. Lee, “Adaptive self-tuning MTPA vector controller for IPMSM drive system,” *IEEE Transactions on Energy Conversion*, vol. 21, pp. 636–644, Sept. 2006.
- [38] W. F. Traoré and R. McCann, “Torque measurements in synchronous generators using giant magnetoresistive sensor arrays via the Maxwell stress tensor,” in *2013 IEEE Power Energy Society General Meeting*, pp. 1–5, July 2013. ISSN: 1932-5517.
- [39] Z. Lin, D. S. Reay, B. W. Williams, and X. He, “Online Modeling for Switched Reluctance Motors Using B-Spline Neural Networks,” *IEEE Transactions on Industrial Electronics*, vol. 54, pp. 3317–3322, Dec. 2007.
- [40] M. N. Uddin, “An Adaptive-Filter-Based Torque-Ripple Minimization of a Fuzzy-Logic Controller for Speed Control of IPM Motor Drives,” *IEEE Transactions on Industry Applications*, vol. 47, pp. 350–358, Jan. 2011.
- [41] J. F. Gieras, *Permanent magnet motor technology: design and applications*. CRC press, 2009.
- [42] W. Xu and R. D. Lorenz, “High-Frequency Injection-Based Stator Flux Linkage and Torque Estimation for DB-DTFC Implementation on IPMSMs Considering Cross-Saturation Effects,” *IEEE Transactions on Industry Applications*, vol. 50, pp. 3805–3815, Nov. 2014.
- [43] “Bomatec BMN-42SH.”
- [44] M. Haavisto, S. Tuominen, H. Kankaanpää, and M. Paju, “Time dependence of demagnetization and flux losses occurring in sintered nd-fe-b permanent magnets,” *IEEE Transactions on Magnetics*, vol. 46, no. 9, pp. 3582–3584, 2010.

- [45] D. Fernández, M. Martínez, D. Reigosa, J. M. Guerrero, C. M. Suárez Alvarez, and F. Briz, “Impact of machine magnetization state on permanent magnet losses in permanent magnet synchronous machines,” *IEEE Transactions on Industry Applications*, vol. 55, no. 1, pp. 344–353, 2019.
- [46] W. T. Martiny, R. M. McCoy, and H. B. Margolis, “Thermal relationships in an induction motor under normal and abnormal operation,” *Transactions of the American Institute of Electrical Engineers. Part III: Power Apparatus and Systems*, vol. 80, no. 3, pp. 66–76, 1961.
- [47] C. Mejuto, M. Mueller, M. Shanel, A. Mebarki, M. Reekie, and D. Staton, “Improved synchronous machine thermal modelling,” in *2008 18th International Conference on Electrical Machines*, pp. 1–6, 2008.
- [48] M. Kovačić, M. Vražić, and I. Gašparac, “Bluetooth wireless communication and 1-wire digital temperature sensors in synchronous machine rotor temperature measurement,” in *Proceedings of 14th International Power Electronics and Motion Control Conference EPE-PEMC 2010*, pp. T7–25–T7–28, 2010.
- [49] D. Fernandez, D. Reigosa, T. Tanimoto, T. Kato, and F. Briz, “Wireless permanent magnet temperature amp; field distribution measurement system for ipmsms,” in *2015 IEEE Energy Conversion Congress and Exposition (ECCE)*, pp. 3996–4003, 2015.
- [50] M. Ganchev, B. Kubicek, and H. Kappeler, “Rotor temperature monitoring system,” in *The XIX International Conference on Electrical Machines - ICEM 2010*, pp. 1–5, 2010.
- [51] S. Xiao and A. Griffo, “PWM-Based Flux Linkage and Rotor Temperature Estimations for Permanent Magnet Synchronous Machines,” *IEEE Transactions on Power Electronics*, vol. 35, pp. 6061–6069, June 2020.
- [52] D. Reigosa, D. Fernandez, T. Tanimoto, T. Kato, and F. Briz, “Comparative Analysis of BEMF and Pulsating High-Frequency Current Injection Methods for PM Temperature Estimation in PMSMs,” *IEEE Transactions on Power Electronics*, vol. 32, pp. 3691–3699, May 2017.
- [53] P. Jansen and R. Lorenz, “A physically insightful approach to the design and accuracy assessment of flux observers for field oriented induction machine drives,” *IEEE Transactions on Industry Applications*, vol. 30, pp. 101–110, Jan. 1994.

- [54] J. S. Lee, C.-H. Choi, J.-K. Seok, and R. D. Lorenz, “Deadbeat-Direct Torque and Flux Control of Interior Permanent Magnet Synchronous Machines With Discrete Time Stator Current and Stator Flux Linkage Observer,” *IEEE Transactions on Industry Applications*, vol. 47, pp. 1749–1758, July 2011.
- [55] H. Rehman, A. Derdiyok, M. Guven, and L. Xu, “A new current model flux observer for wide speed range sensorless control of an induction machine,” *IEEE Transactions on Power Electronics*, vol. 17, pp. 1041–1048, Nov. 2002.
- [56] K. Hurst, T. Habetler, G. Griva, and F. Profumo, “Zero-speed tachless IM torque control: simply a matter of stator voltage integration,” *IEEE Transactions on Industry Applications*, vol. 34, pp. 790–795, July 1998.
- [57] D. G. Holmes and T. A. Lipo, *Pulse Width Modulation for Power Converters: Principles and Practice*. New York: Wiley, 2003.
- [58] M. Hinkkanen and J. Luomi, “Modified integrator for voltage model flux estimation of induction motors,” *IEEE Transactions on Industrial Electronics*, vol. 50, pp. 818–820, Aug. 2003.
- [59] F. Tinazzi and M. Zigliotto, “Torque estimation in high-efficiency ipm synchronous motor drives,” *IEEE Transactions on Energy Conversion*, vol. 30, no. 3, pp. 983–990, 2015.
- [60] S. H. Kia, H. Heno, and G.-A. Capolino, “Torsional vibration assessment using induction machine electromagnetic torque estimation,” *IEEE Transactions on Industrial Electronics*, vol. 57, no. 1, pp. 209–219, 2010.
- [61] N. Amano, “Method of calculation of the motor torque,” Sep 2005.
- [62] P. Sue, D. Wilson, L. Farr, and A. Kretschmar, “High precision torque measurement on a rotating load coupling for power generation operations,” in *IEEE International Instrumentation and Measurement Technology Conference Proceedings*, pp. 518–523, May 2012. ISSN: 1091-5281, 1091-5281.
- [63] M. Martinez, D. Fernandez, D. Reigosa, J. M. Guerrero, and F. Briz, “Wireless torque pulsations measurement system for pmsms,” *IEEE Transactions on Industry Applications*, vol. 56, no. 6, pp. 6467–6476, 2020.
- [64] H.-S. Jung, D. Park, H. Kim, S.-K. Sul, and D. J. Berry, “Non-Invasive Magnet Temperature Estimation of IPMSM Based on High-Frequency Inductance With a Pulsating High-Frequency Voltage Signal Injection,” *IEEE Transactions on Industry Applications*, vol. 55, pp. 3076–3086, May 2019.

- [65] D. Reigosa, D. Fernández, M. Martínez, J. M. Guerrero, A. B. Diez, and F. Briz, “Magnet Temperature Estimation in Permanent Magnet Synchronous Machines Using the High Frequency Inductance,” *IEEE Transactions on Industry Applications*, vol. 55, pp. 2750–2757, May 2019.
- [66] K. Liu and Z. Q. Zhu, “Online estimation of the rotor flux linkage and voltage-source inverter nonlinearity in permanent magnet synchronous machine drives,” *IEEE Transactions on Power Electronics*, vol. 29, no. 1, pp. 418–427, 2014.
- [67] B. Shuang and Z.-Q. Zhu, “A novel method for estimating the high frequency incremental dq-axis and cross-coupling inductances in interior permanent magnet synchronous machines,” *IEEE Transactions on Industry Applications*, vol. 57, no. 5, pp. 4913–4923, 2021.
- [68] R. Monajemy and R. Krishnan, “Performance comparison for six-step voltage and constant back emf control strategies for pmsm,” in *Conference Record of the 1999 IEEE Industry Applications Conference. Thirty-Forth IAS Annual Meeting (Cat. No.99CH36370)*, vol. 1, pp. 165–172 vol.1, 1999.
- [69] H. Nakai, H. Ohtani, E. Satoh, and Y. Inaguma, “Development and testing of the torque control for the permanent-magnet synchronous motor,” *IEEE Transactions on Industrial Electronics*, vol. 52, no. 3, pp. 800–806, 2005.
- [70] R. Sepe and J. Lang, “Inverter nonlinearities and discrete-time vector current control,” *IEEE Transactions on Industry Applications*, vol. 30, no. 1, pp. 62–70, 1994.
- [71] J.-W. Choi and S.-K. Sul, “Inverter output voltage synthesis using novel dead time compensation,” *IEEE Transactions on Power Electronics*, vol. 11, no. 2, pp. 221–227, 1996.
- [72] A. Munoz and T. Lipo, “On-line dead-time compensation technique for open-loop pwm-vsi drives,” *IEEE Transactions on Power Electronics*, vol. 14, no. 4, pp. 683–689, 1999.
- [73] Z. Zhang and L. Xu, “Dead-time compensation of inverters considering snubber and parasitic capacitance,” *IEEE Transactions on Power Electronics*, vol. 29, no. 6, pp. 3179–3187, 2014.

Appendix A

Experimental setup

A.1 Power system

The test bench used for the experimental verification of the estimation methods proposed in this thesis can be seen in Fig. A.1. The test bench is composed of a conventional IPMSM used as a load, the VLF-PMSM under test (parameters being shown in Table 2.1), each machine being driven by a three-phase inverter. The inverters share the DC-link and are controlled using a TMS320F28335 microcontroller.

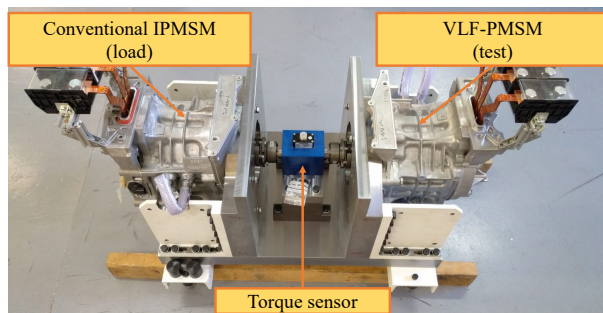


Figure A.1: Test bench.

In the Fig. A.2, the power system connection scheme is shown and the actual

power system setup can be seen in Fig. A.3. This connection scheme allows to recirculate the energy bidirectionally between the two machines, i.e. during steady state operation of the tech bench, the power used by one of the machines will be provided by the other machine since they share the speed and have opposite torque production. The losses of the power system must be provided externally by the transformer and rectifier shown in Fig. A.2. Additionally, in Fig. A.3 the water cooling system for the electric machines and inverters, composed of two water pumps, two radiators and two reservoirs, are shown.

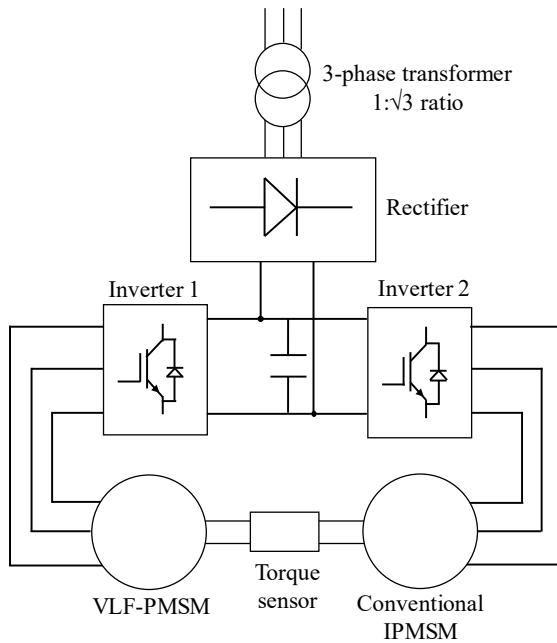


Figure A.2: Power system connection scheme.

The designed motor test bench has four rubber shock absorbers in its attachment to the floor in order to absorb any torque pulsation or vibrations, in Fig. A.4 one shock absorber is shown. This reduces the undesired shocks that the tech bench could suffer with rapid torque spikes if abnormal operation or emergency stops of the drive are produced during any experiment.

Inverters and motors are connected by shielded power cables with a section of 120 mm², tinned copper shield and TPU insulation material. All phases have 3 m cable length for both machines. A detailed figure of the power cable is shown

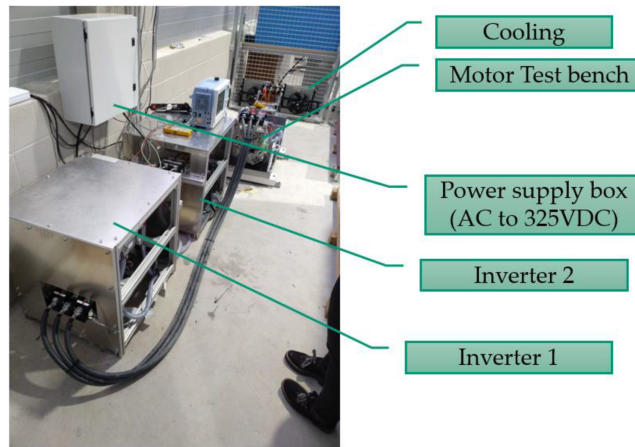


Figure A.3: Power system of the experimental setup.



Figure A.4: Test bench attachment to the floor and a rubber shock absorber.

in Fig. A.5.

The system power losses are supplied by a three phase grid and a diode rectifier VUO62-12NO7, shown in Fig. A.6. This rectifier has a maximum blocking voltage of 1200 V and 60 A output current, being enough to supply the desired power to the DC link.

Fig. A.7 shows the control box with the control PCBs and the auxiliary systems including the resolver to encoder converter, the reset buttons for the inverters and the power supply. The PCBs used to control the inverters and test motors are shown in Fig. A.8. These PCBs are designed as modular multi-



Figure A.5: 120 mm² shielded power cable used to connect machines and inverters.



Figure A.6: Three phase diode rectifier VUO62-12NO7.

purpose control PCBs being prepared to handle different number of analog and digital signals depending on the desired application. They have two inputs for incremental encoders and up to 16 analog input channels, up to 12 different input error signals by optic fiber, up to 20 multipurpose digital I/O ports and up to 12 PWM output signals. The PWM output signals are sent by optic fibre to the inverters to prevent from electromagnetic noise interference. The microcontroller used in these control cards is a TMS320F28335 from Texas Instruments.

In order to measure the stator temperature, some thermocouples are available in the stator of the machine. These thermocouples are sensed by the thermocouple data logger TC-08 from Pico Technology, shown in Fig. A.9. It has up to 8 thermocouple inputs, and also provides the cool junction temperature signal. This system is specially relevant to decouple the stator resistance variation due to stator coils temperature change.

A.2 PM temperature measurement system

In order to verify the accuracy of the proposed PM temperature estimation methods, the PMs temperatures are measured by means of thermocouples. A

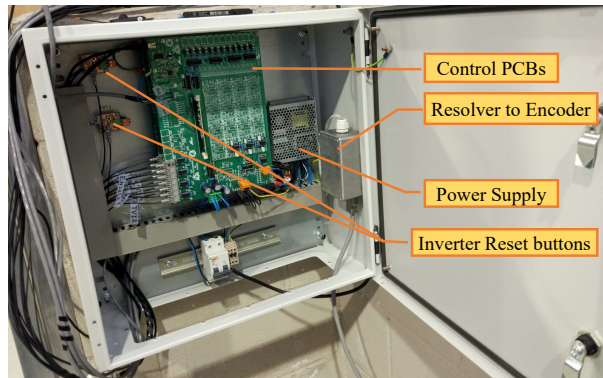


Figure A.7: Control box with the control card and auxiliary systems.

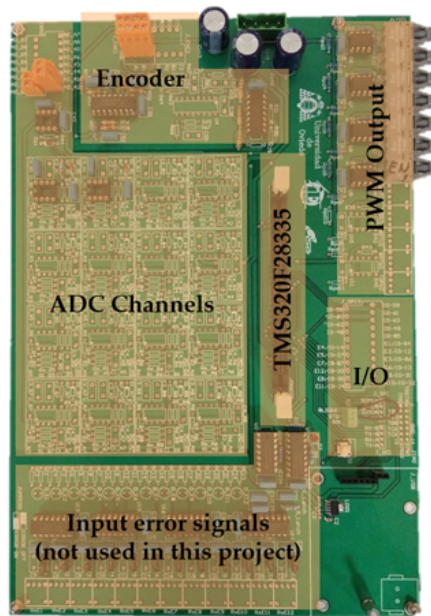


Figure A.8: Control PCB.

wireless PM temperature measurement system similar to the one used in [65] has been developed and implemented for performance evaluation of the estimation method. Fig. A.10 shows a picture of the wireless PM temperature measurement system along with the aluminum case attached to the rear part of the rotor. This system has been designed and balanced in order to withstand the rotor high

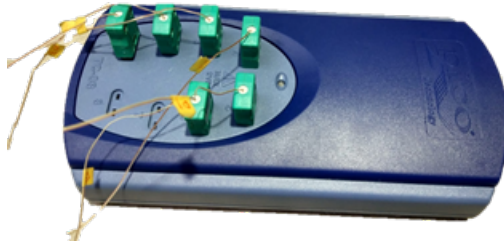


Figure A.9: TC-08 from Pico Technology.

speed up to 12000 r/min.

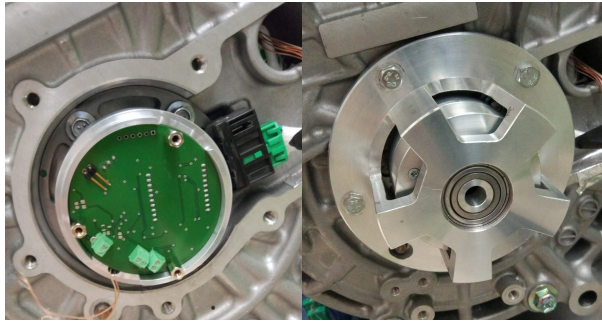


Figure A.10: Wireless PM temperature measurement system along with the aluminum case attached to the rear part of the rotor.

The wireless PM temperature measurement system is composed of connectors for temperature sensors (thermocouples), a filtering and conditioning stage, a digital temperature sensor with I²C interface for the cold junction temperature measurement, a general-purpose microcontroller, a battery and a WiFi module.

Thermocouples are two electrical conductors made of different metals. At one end, the two conductors form an electrical junction and are used as the hot junction measuring point. At the other end (cold junction), a small voltage can be measured between conductors proportional to the temperature difference between the hot and cold junctions.

The small voltage provided by the thermocouples need to be adapted to values that can be read by the microcontroller analog ports, as K-type thermocouples used in this application typically provide $41\mu\text{V}/^\circ\text{C}$. High precision instrumentation operational amplifiers are used to amplify and filter the differential signal provided by thermocouples. The bandwidth of the analog filters used for this ap-

plication is not very demanding since the time constant of the PM temperature is quite low (less than $0.1 \text{ }^{\circ}\text{C/s}$).

The digital temperature sensor is placed close to the connectors in order to minimize temperature tracking errors. The measured cold junction temperature is transmitted to the microcontroller through the I²C interface. This interface has a data transmission speed of 400 kbit/s what provides enough headroom to transmit the sensor temperature data in real time.

The microcontroller is used to convert the analog signals to digital values, acquire the cold junction temperature from the I²C temperature sensor, calculate the total measured temperature and send the data to the wireless transmission device. Therefore, the requirements for this device are low, being possible to use a general-purpose microcontroller with analog-to-digital converters, I²C communication interface and a compatible communication interface with the wireless device (in this case UART).

A small 2 cell 200 mAh Li-Ion battery is used and supplies this system for hours. The use of larger capacity batteries could extend the the autonomy of the PM temperature measurement system, however, since this system is meant to work at high rotational speeds, the design criteria was to minimize the weight.

The wireless device is used to send the PM temperature to a computer where the data is represented and logged. Fig. A.11 shows a schematic representation of the PM temperature measurement system along with a screenshot of the desktop application during a experiment. The main characteristics of this measurement system are summarized in Table A.1.

Table A.1: Main characteristics of the PM temperature measurement system

Sensor temperature limit	250 $^{\circ}\text{C}$
Resolution	0.0625 $^{\circ}\text{C}$
Measurement range	0 $^{\circ}\text{C}$ to 125 $^{\circ}\text{C}$
Bandwidth	1.25 kHz
Number of sensors	3

The temperature measurement range is enough as the PMs used in the VLF-PMSM under test are neodymium type with a maximum working temperature of 140 $^{\circ}\text{C}$. The evolution of the PM temperature with time is usually slow (a few Celsius degrees per minute) being, therefore, the measurement system bandwidth large enough for this application.

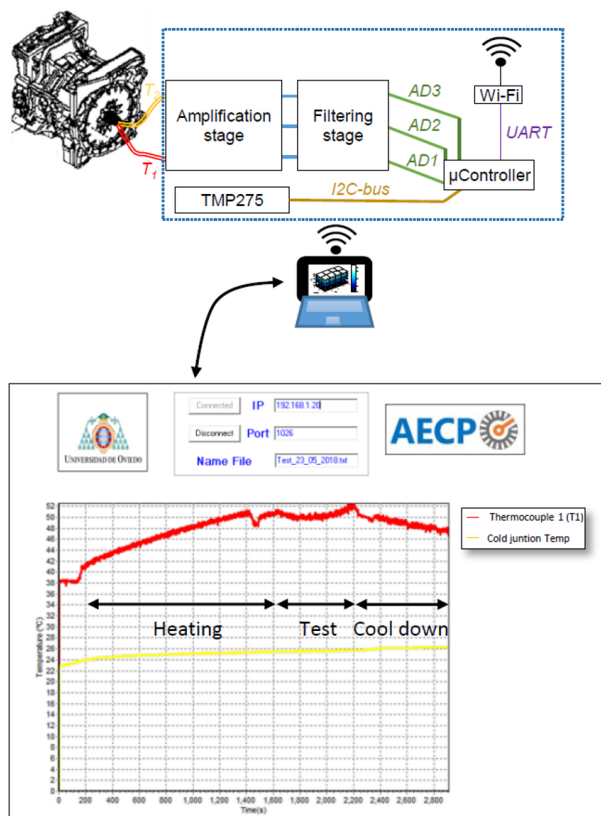


Figure A.11: Schematic representation of the temperature measurement system and desktop application.

A.3 Torque sensor

In order to verify the accuracy of the proposed torque estimation method, the output torque of the VLF-PMSM is measured by the torque sensor shown in Fig. A.12. This sensor is composed of the measuring system located in the rotational part of the sensor, the power supply adaptation and cabling in the stationary part of the sensor and a capacitive interface system to couple rotational and stationary parts. The installed torque sensor has a measurement range of ± 500 Nm being larger than the maximum torque provided by the VLF-PMSM under test. In this measurement range, the torque sensor has a measurement error of 0.1%, being accurate enough for precise validation of torque estimation methods. The maximum speed of the torque sensor is 15000 r/min what allows to

withstand the maximum speed of the VLF-PMSM during the experiments (10000 r/min). It also provides a relatively low resolution (360 pulses per mechanical revolution) additional output encoder signal. The characteristics of the torque sensor transducer used in this dissertation are shown in Table A.2.



Figure A.12: Torque transducer of Interface Inc.

Table A.2: Main characteristics of the torque sensor

Measurement range	± 500 Nm
Accuracy	0.1% error
Maximum speed	15000 r/min

A.4 Inverter nonlinearities evaluation

A.4.1 Introduction

Control signals from microcontrollers or control devices, in general, cannot provide enough power to drive an electric machine. Electronic power inverters are used to transform the DC link voltage from an external power source to the commanded AC voltage signals. The power electronic switching devices (IGBTs or MOSFETs) present in the inverters can work in the active or saturation region. Using these devices in their active region provides a linear output with quite small waveform distortion, however the voltage and current that these devices withstand in the active region produce large conduction losses, reduces the

efficiency of the system and requires a powerful cooling system. Due to this, linear operation of power electronic devices is only used in applications where the energy efficiency is not important, such as audio amplifiers.

On the other hand, the power electronic devices can operate in the saturation region behaving similarly to a solid state switch. In this operating region, the voltage drop that they have to withstand is quite small what reduces the conduction losses, increasing the efficiency. However, this limits the number of different output voltage values that can be obtained depending on the inverter topology. Conventional inverters can only produce two different voltages per inverter leg by connecting their output to the higher or lower sides of the DC bus. Multilevel converters use more switching devices and other auxiliary components to increase the number of possible different output voltage levels.

In any case, the discretization of the output voltage of inverters makes impossible to directly reproduce the commanded voltage signals, the use of modulation techniques being required. Modulation techniques, such as Pulse Width Modulation (PWM), allows the reproduction of the commanded voltage signals at the cost of increased switching losses, the addition of switching harmonics and loss of linearity.

These issues contribute to the output voltage waveform distortion, leading to additional distortion in the controlled currents in electric machines.

A.4.2 Current Waveform Distortion

Current waveform distortion produced by inverter nonlinearities can be classified as follows:

- **Deadzone:** the inverter deadzone is its most significant nonlinearity. It is produced by the unintentional connection of the output phase of the inverter to the higher or lower side of the DC link. This unintended connection is created by the freewheeling anti-parallel diodes of the power switching devices when the output phase current is not zero. This is an unavoidable effect since both high side and low side switching devices must be commanded to be open during a small time period (deadtime). This is performed during the turn-off and turn-on of switching devices in the same inverter leg, in order to prevent inverter leg short-circuits.

The waveform distortion produced by the inverter deadzone in a machine phase current can be seen in Fig. [A.13](#). During the deadtime, the phase

current will flow through the freewheeling diodes of the inverter. Therefore the output phase of the inverter will be connected to the lower side of the DC link while the current is flowing from the inverter to the machine (positive current); and connected to the higher side of the DC link while the current is flowing from the machine to the inverter (negative current). This effect produces a modification of the output applied voltage that depends on the direction of the current, the deadtime duration and the DC link voltage value [70–72]. The switching devices parasitic and/or snubber capacitance can be also taken into account in order to produce a more accurate modelling of the output voltage deadzone [73]. The parasitic capacitance and snubber capacitance of switching devices should be charged before the freewheeling diodes start conducting, adding an output voltage distortion depending on the magnitude of capacitance and output current.

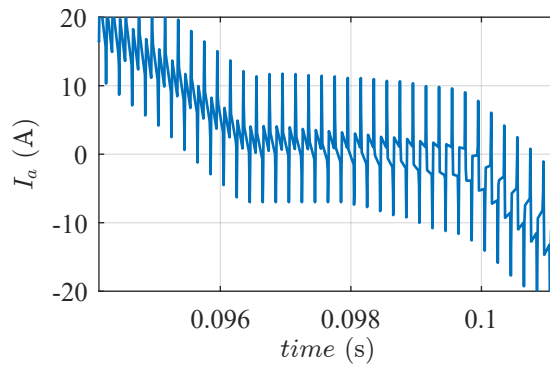


Figure A.13: Machine phase current distortion due to inverter deadzone.

- **Current ripple:** the use of PWM lead to HF current components related to the PWM carrier frequency. This is usually not a major concern since anti-aliasing filters or synchronous sampling are used in the current acquisition. Generally, the output voltage is filtered by inductors and capacitors (LC filters) reducing the magnitude of PWM HF components in the current waveform. In electric machines, the stator coils act as a LPF, filtering the PWM HF components in the current waveform. Fig. A.14 shows the current ripple

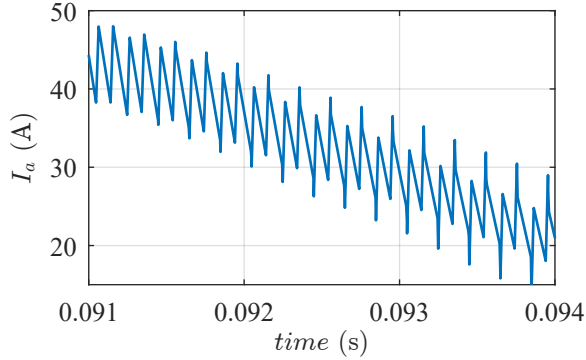


Figure A.14: Current ripple in machine phase current due to PWM switching.

A.4.3 Compensation

Several compensation techniques have been proposed in the literature [70–73], in this dissertation compensation of the deadzone to improve the current waveforms has not been used. However, the current regulators react to inverter deadzone producing DC and 6th harmonic components in the synchronous reference frame regulator output voltage command.

Since voltage sensors are not usually present in industrial machine drives, the output of current regulators are used for the proposed PM temperature and torque estimation methods. In order to accurately estimate the output applied voltage, the 6th harmonic is filtered by a LPF. On the other hand, the DC component cannot be filtered since it is overlapped with the fundamental frequency voltage component.

A commissioning process is performed in order to calculate the effect on the DC component of current regulator voltage command. In Fig. A.15 the magnitude and angle of the distorted voltage are shown. It can be seen from Fig. A.15a that, for currents larger than 50 A, the magnitude of the distorted voltage ΔV_{sdq}^r is fairly constant. In Fig. A.15b, the distorted voltage ΔV_{sdq}^r angle is shown along with the machine fundamental current angle I_{sdq}^r for the sake of comparison. The angle of the distorted voltage ΔV_{sdq}^r is in phase with machine fundamental current as shown in Fig. A.15b. These result are in good agreement with the models proposed in [70–73]. It can be also seen from Fig. A.15a that the parasitic and snubber capacitance of the inverter is small enough to be safely neglected [73]. Therefore, a constant voltage compensation of ≈ 12 V in phase with stator current could be used to correctly estimate the actually applied volt-

age fundamental component magnitude. There were no significant differences for the different machine speeds used during this commissioning process.

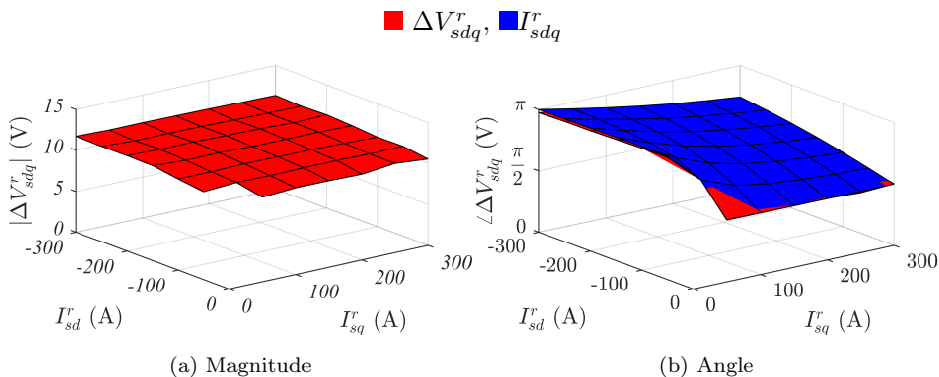


Figure A.15: Magnitude and angle of the voltage distortion due to inverter deadzone.

The commanded voltage is shown in Fig. A.16 before and after compensation for $I_{sd}^r = 0$ A and $I_{sq}^r = 100$ A and $\omega_r = 500$ r/min. It can be seen in Fig. A.16a that the predicted/commanded voltage has an error of ≈ 12 V in phase with fundamental current (aligned with q-axis). In Fig. A.16b, the predicted/commanded voltage after the compensation overlaps with the measured voltage waveform.

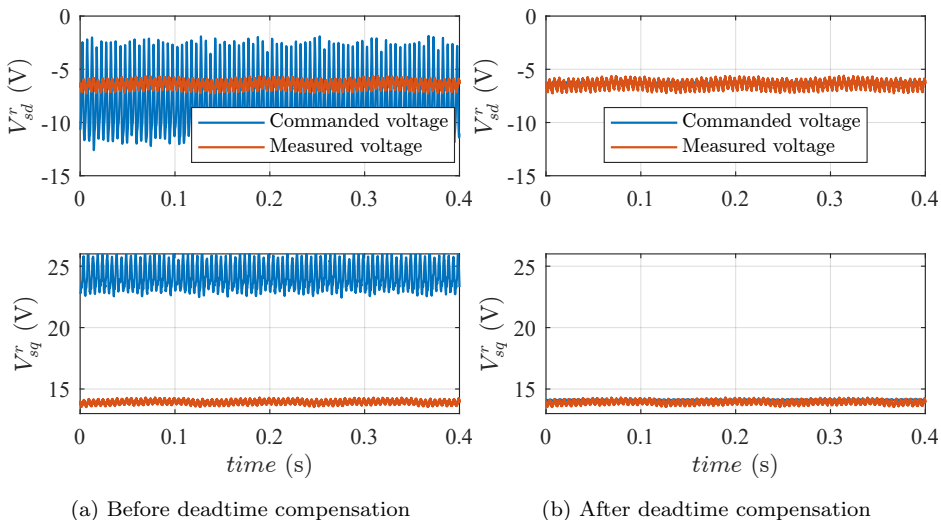


Figure A.16: Comparison between commanded and measured inverter output voltage, before and after compensation for $I_{sd}^r = 0$ A and $I_{sq}^r = 100$ A.







Appendix B

Publications

B.1 Peer-reviewed journal publications

B.1.1 SynRM Sensorless Torque Estimation Using High Frequency Signal Injection

SynRM Sensorless Torque Estimation Using High-Frequency Signal Injection

Maria Martinez , Member, IEEE, Diego F. Laborda , David Reigosa , Daniel Fernandez , Member, IEEE, Juan M. Guerrero , Senior Member, IEEE, and Fernando Briz , Senior Member, IEEE

Abstract—Precise output torque control is often required in applications using synchronous reluctance machines. Direct measurement of torque has drawbacks due to both cost and reliability issues. To overcome these limitations, the development of torque estimation methods has received significant research attention. Most of the existing torque estimation methods require knowledge of machine parameters, suffering, therefore, from parameter sensitivity. Load and saturation are recognized as the primary source of parameter variation. This article proposes the use of a high-frequency signal injection for the online estimation of the machine parameters required for torque estimation. The improvement in the torque estimation will be especially relevant in deep-saturation regions. The method operates without interfering with the normal operation of the machine.

Index Terms—High-frequency signal injection, synchronous reluctance machines (SynRMs), online parameter estimation, torque estimation.

I. INTRODUCTION

SYNCHRONOUS reluctance machines (SynRMs) are characterized by their high tolerance to overcurrents and/or overheating, and overall increased robustness compared with other types of ac machines such as permanent-magnet synchronous machines (PMSMs) or induction motors (IMs), resulting from the absence of brushes, permanent magnets, or coils in the rotor. Compared with PMSMs, SynRMs have a robust structure that facilitates their use in harsh ambient, and are also more cost effective [1]–[3]. Compared with IMs, the absence of cage winding results into a reduction of the rotor losses

Manuscript received November 1, 2020; revised April 23, 2021 and August 3, 2021; accepted August 23, 2021. Date of publication September 10, 2021; date of current version November 19, 2021. This work was supported in part by the Research, Technological Development and Innovation Programs of the Spanish Ministry Economy and Competitiveness of the Spanish Government under the project MINECO-17-ENE2016-80047-R; in part by the Government of the Principality of Asturias under Grant Severo Ochoa PA-20-PF-BP19-010 and the Project IDI/2018/000188; in part by the University of Oviedo under Grant PAPI 2018-PF-12; and in part by grants of the European Regional Development Fund (ERDF). Paper 2020-IDC-1467.R2, presented at the 2019 IEEE 10th International Symposium on Sensorless Control for Electrical Drives (SLED), Turin, Italy, Sep. 9–10, and approved for publication in the IEEE TRANSACTIONS ON INDUSTRY APPLICATIONS by the Industrial Drives Committee of the IEEE Industry Applications Society. (Corresponding author: Maria Martinez.)

The authors are with the Department of Electrical Engineering, University of Oviedo, 33204 Gijón, Spain (e-mail: martinezgmaria@uniovi.es; dflaborda@uniovi.es; reigosa@isa.uniovi.es; fernandezalodaniel@uniovi.es; guerrero@uniovi.es; fernando@isa.uniovi.es).

Color versions of one or more figures in this article are available at <https://doi.org/10.1109/TIA.2021.3111840>.

Digital Object Identifier 10.1109/TIA.2021.3111840

0093-9994 © 2021 IEEE. Personal use is permitted, but republication/redistribution requires IEEE permission. See <https://www.ieee.org/publications/rights/index.html> for more information.

and a lighter structure that improves their dynamic behavior. These characteristics make them a promising alternative for high-performance applications, like traction applications up to low-speed high-power machines or industrial tools [2]. However, their high nonlinear behavior resulting from saturation results in large variation of the inductances with the operating conditions [3]–[6]. Consequently, torque control based on the mathematical modeling of the machine will be drastically affected in terms of precision and dynamics [3], [6]–[13].

Many high-performance applications, such as robotics, machine tools, and electric vehicle/hybrid electric vehicles applications require precise control of the output torque produced by the machine [1], [3], [6]. Thus, torque measurement or estimation is, therefore, required [8]–[12]. Rotary torque transducers based on strain gauges are likely the preferred option for the first case [14]–[19]. However, this type of sensors could introduce resonances into the system and require precise mounting and calibration to ensure accurate measurements [20]. Alternatively, torque can be measured using systems based on the torsional displacement measurement [21], systems based on the magnetoelastic effect [22], or systems based on the giant magnetoresistive effect [23]. However, regardless of the method being used, precise torque measurement is expensive, and requires extra elements (sensor, cables, connectors,...), that could reduce the reliability and increase the overall cost of the drive. As an alternative, torque can be estimated.

Torque estimation methods can be roughly divided into two main groups: those based on the general torque equation (GTE) [8], [9], [24], [25] and indirect estimation methods [12], [13], [24], [26]–[37]. Indirect estimation methods include electric power and shaft speed measurement-based method [26]; flux observers-based methods [12], [13], [24], [26]–[37]; and optimal recursive estimation algorithms [12]. Most of the torque estimation methods reported in the literature [12], [13], [24]–[42] require precise knowledge of machine parameters (e.g., resistances or inductances). Consequently, parameter variation with the operating conditions (i.e., saturation level and temperature) can lead to large torque estimation errors, saturation being the main concern for the SynRM. Look-up-tables (LUTs) are frequently used for online machine parameter adaptation [25], [41]; unfortunately, LUTs fail in the event of any type of machine degradation, and often require large memory usage.

To overcome LUTs limitations, online parameter estimation methods have been proposed [43]–[45]. Injection of a high-frequency (HF) signal into the stator terminals of the machine

has been reported to be a viable option for the online machine parameter estimation. These methods can operate in the whole speed range, including zero speed, and without interfering with the normal operation of the machine.

However, HF injection-based parameters estimation methods proposed so far [41], [43]–[45] typically make the following two assumptions: 1) machine is assumed to have a purely inductive behavior and 2) the relationship between the high-frequency parameters and the fundamental parameters are assumed to be linear. While these assumptions can be acceptable for PMSMs, they can be problematic for the case of SynRMs [3], [46], [47].

This article proposes a new online machine parameter estimation method, aimed to enhance the torque estimation based on GTE for SynRMs. The parameters involved in the GTE are estimated from the machine reaction to an HF signal injected in the stator terminals. The proposed method shares some similarities with [43], where two pulsating HF currents were used to estimate the machine parameters; two HF current controllers being, therefore, required to inject the two pulsating HF currents. In this article, machine parameters will be estimated from the injection of a single rotating HF voltage signal. Reducing the injected signals from two HF currents to one HF voltage will reduce the adverse effects due to the HF signals and simplify the implementation of the method. Additionally, a detailed study of the relationship between the HF parameters and fundamental parameters (i.e., those involved in the torque equation) will be presented. An accurate modeling of this relationship will be key to improve the torque estimation accuracy in the whole operating range of the machine. The proposed method can be used in the whole speed operating range of the machine, including stand still, eliminating, therefore, the need of additional controllers that are traditionally used to enable smooth transition between current- to voltage-based models in flux observed-based torque estimation techniques [32], [41].

This article is organized as follows. The Fundamental model of a SynRM is presented in Section II; parameter estimation using the rotating voltage HF signal is presented in Section III; torque estimation based on the GTE using the estimated HF parameters is presented in Section IV; simulation results obtained by means of finite-element analysis (FEA) are shown in Section V; implementation of the method and experimental results are presented in Section VI, and finally, Section VII concludes this article.

II. FUNDAMENTAL MODEL OF A SYNRM

The fundamental model of a SynRM in a reference frame synchronous with the rotor is given by [3], [5], [6]

$$v_{sd}^r = R_d i_{sd}^r + \frac{d\lambda_{sd}^r}{dt} - \omega_r \lambda_{sq}^r \quad (1)$$

$$v_{sq}^r = R_q i_{sq}^r + \frac{d\lambda_{sq}^r}{dt} + \omega_r \lambda_{sd}^r \quad (2)$$

where R_d and R_q are the dq -axes resistances, i_{sd}^r and i_{sq}^r are the dq -axes stator currents, v_{sd}^r and v_{sq}^r are the dq stator voltages, λ_{sd}^r and λ_{sq}^r are dq -axes stator flux linkages, and ω_r is the mechanical rotational speed.

The output torque is defined as

$$T_e = \frac{3}{2}P (\lambda_{sd}^r i_{sq}^r - \lambda_{sq}^r i_{sd}^r) \quad (3)$$

The aforementioned equation can be also expressed as a function of the stator inductances (also known as apparent inductances) (5), the torque being (4). It is noted that T_e defined in (4) stands for the mean output torque of the machine.

It can be observed from (4) that the reluctance torque production by a SynRM depends on the saliency effect, i.e., it is proportional to the difference between d - and q -axes inductances.

$$T_e = \frac{3}{2}P ((L_d - L_q) i_{sd}^r i_{sq}^r) \quad (4)$$

$$L = \frac{\lambda}{i} = \frac{N^2 \mu_s(H)A}{l} \quad (5)$$

where i is the current, λ is the resulting flux linkage, N is the number of turns of the stator winding, μ_s is the static permeability of the material, A is the mean cross-sectional area of the magnetic circuit, and l is the mean length of the magnetic circuit. The static permeability defined in (5) is defined as the ratio of flux density (B) versus field intensity (H). As the relationship between B and H for ferromagnetic materials is usually nonlinear, the static permeability is not constant but a nonlinear function of H [48]–[50].

It is noted, therefore, that dq -axes inductances values can change with the machine operating point

$$L_{d(I_{sd}, I_{sq})} = L_{d0} (1 + \alpha_{I_{sd}d(I_{sd}, I_{sq})} I_{sd}^r + \alpha_{I_{sd}dq(I_{sd}, I_{sq})} I_{sq}^r) \quad (6)$$

$$L_{q(I_{sd}, I_{sq})} = L_{q0} (1 + \alpha_{I_{sq}q(I_{sd}, I_{sq})} I_{sd}^r + \alpha_{I_{sq}dq(I_{sd}, I_{sq})} I_{sq}^r) \quad (7)$$

where L_{d0} and L_{q0} are the dq -axes synchronous inductances when there is no dq fundamental current injection; I_{sd}^r and I_{sq}^r are the fundamental dq -axes stator current magnitude; $\alpha_{I_{sd}d(I_{sd}, I_{sq})}$ and $\alpha_{I_{sd}dq(I_{sd}, I_{sq})}$ are the coefficients linking the d -axis inductance with the d -axis fundamental current (I_{sd}^r) due to saturation and q -axis fundamental current (I_{sq}^r) due to cross coupling, respectively; similarly, $\alpha_{I_{sq}q(I_{sd}, I_{sq})}$ and $\alpha_{I_{sq}dq(I_{sd}, I_{sq})}$ are the coefficients linking the q -axis inductance with the q -axis fundamental current (I_{sq}^r) due to saturation and d -axis fundamental current (I_{sd}^r) due to cross coupling, respectively.

Substituting (6) and (7) into (4), the GTE can be written as

$$T_e(I_{sd}, I_{sq}) = \frac{3P}{2} ((L_{d(I_{sd}, I_{sq})} - L_{q(I_{sd}, I_{sq})}) i_{sd}^r i_{sq}^r) \quad (8)$$

It has to be noted that the variation of inductances with load, (6), (7), will depend on the machine design, different functions could be used to model this behavior, e.g., linear, quadratic, or higher order polynomials. A commissioning process would be, therefore, required to obtain the required coefficients [3].

III. PARAMETER ESTIMATION USING ROTATING HF VOLTAGE INJECTION

Machine parameters can be estimated in real time from the machine response to a small HF signal, which is added on

top of the fundamental voltage applied for torque production. This section describes the physical principles of the dq -axes HF inductances estimation using this method.

The HF model representing the behavior of a synchronous machine (9) can be deduced from the corresponding fundamental frequency model (1), (2) [51], [52].

$$\begin{bmatrix} v_{sdHF}^r \\ v_{sqHF}^r \end{bmatrix} = \begin{bmatrix} R_{dHF} + pL_{dHF} & -\omega_r L_{qHF} \\ \omega_r L_{dHF} & R_{qHF} + pL_{qHF} \end{bmatrix} \begin{bmatrix} i_{sdHF}^r \\ i_{sqHF}^r \end{bmatrix} \quad (9)$$

where

v_{sdHF}^r : d -axis HF voltage in the rotor reference;

v_{sqHF}^r : q -axis HF voltage in the rotor reference;

i_{sdHF}^r : d -axis HF current in the rotor reference;

i_{sqHF}^r : q -axis HF current in the rotor reference;

L_{dHF} : d -axis HF inductance;

L_{qHF} : q -axis HF inductance;

p : differential operator. Equivalent to the s variable in Laplace transform.

If a rotating HF voltage signal is injected into the stator terminal of the machine (10), the HF currents induced in the stator windings are given by (11) and (12).

$$v_{sdqHF}^{r*} = V_{HF}^{r*} e^{j(\omega_{HF}t)} = \begin{bmatrix} V_{sdHF}^{r*} \\ V_{sqHF}^{r*} \end{bmatrix} = \begin{bmatrix} V_{HF}^{r*} \cos(\omega_{HF}t) \\ V_{HF}^{r*} \sin(\omega_{HF}t) \end{bmatrix} \quad (10)$$

$$i_{sdHF}^r = \frac{R_{qHF} + j\omega_{HF}L_{qHF}}{(R_{dHF} + j\omega_{HF}L_{dHF})(R_{qHF} + j\omega_{HF}L_{qHF}) + \omega_r^2 L_{dHF}L_{qHF}} \cdot \left[v_{sdHF}^{r*} + \frac{\omega_r L_{qHF} v_{sqHF}^{r*}}{R_{qHF} + j\omega_{HF}L_{qHF}} \right] \quad (11)$$

$$i_{sqHF}^r = \frac{R_{dHF} + j\omega_{HF}L_{dHF}}{(R_{dHF} + j\omega_{HF}L_{dHF})(R_{qHF} + j\omega_{HF}L_{qHF}) + \omega_r^2 L_{dHF}L_{qHF}} \cdot \left[v_{sqHF}^{r*} - \frac{\omega_r L_{dHF} v_{sdHF}^{r*}}{R_{dHF} + j\omega_{HF}L_{dHF}} \right] \quad (12)$$

It can be seen from (11) and (12) that modeling of L_{dHF} and L_{qHF} is not straightforward due to cross coupling between d - and q -axes and fundamental-speed-dependent terms. However, if the frequency of the injected HF signal is sufficiently higher than the rotor frequency, the rotor-speed-dependent terms can be safely neglected, the HF currents induced in the stator can be, therefore, simplified to (13) and (14). An orientative value for this assumption can be $\omega_{HF} \geq \omega_r + 2\pi 500 \text{ rad/s}$ [43].

$$i_{sdHF}^r = \frac{v_{sdHF}^{r*}}{(R_{dHF} + j\omega_{HF}L_{dHF})} \quad (13)$$

$$i_{sqHF}^r = \frac{v_{sqHF}^{r*}}{(R_{qHF} + j\omega_{HF}L_{qHF})} \quad (14)$$

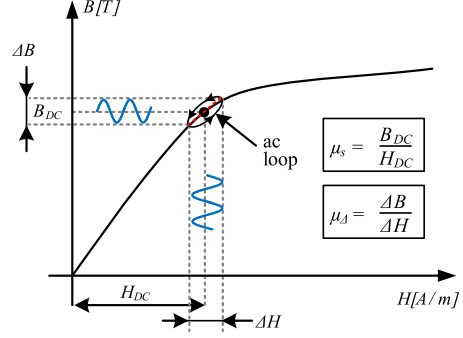


Fig. 1. Typical BH curve of a ferromagnetic material: Static, incremental, and differential permeability definition.

Estimation of L_{dHF} and L_{qHF} can be finally obtained from the imaginary part of the dq HF impedance

$$Z_{dHF} = R_{dHF} + j\omega_{HF}L_{dHF} = \frac{v_{sdHF}^{r*}}{i_{sdHF}^r} \quad (15)$$

$$Z_{qHF} = R_{qHF} + j\omega_{HF}L_{qHF} = \frac{v_{sqHF}^{r*}}{i_{sqHF}^r} \quad (16)$$

$$L_{dHF} = \frac{\Im(Z_{dHF})}{\omega_{HF}} \quad (17)$$

$$L_{qHF} = \frac{\Im(Z_{qHF})}{\omega_{HF}} \quad (18)$$

IV. TORQUE ESTIMATION USING dq HF INDUCTANCES

The previous section has shown that real-time HF inductances estimation is possible from the machine response to an HF signal. It is important to notice, however, that HF inductances are not the inductances in the GTE.

As seen in Section II, inductances in the GTE are the apparent inductances, which are given by the static permeability, μ_s (5) (see Fig. 1). Therefore, this definition only applies for the case of a static magnetic field (i.e., constant) excitation.

However, if a small HF alternating (ac) magnetic field is superposed on the static magnetic field, a minor hysteresis loop will be produced. The associated incremental permeability, μ_{Δ} , is defined as [48], [49]

$$\mu_{\Delta} = \frac{\Delta B}{\Delta H} \quad (19)$$

The area of the hysteresis loop will depend on the magnitude of the HF signal being injected. Assumed that the magnitude of the HF signal is small, the trajectory followed in the hysteresis loop can be approximated by a straight line (see Fig. 1). This line will be tangent to the HB curve at the H-B coordinates corresponding to the dc excitation. In this case, the incremental

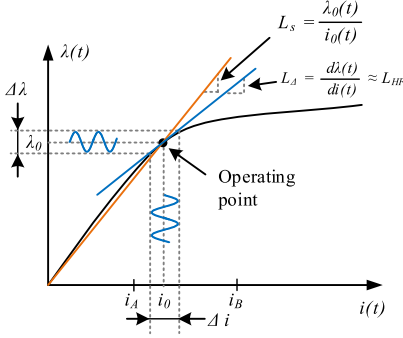


Fig. 2. Definition of the incremental and synchronous inductance.

permeability μ_{Δ} can be approximated to the differential permeability μ_d , defined as [48]–[50]

$$\mu_d = \frac{dB}{dH} \approx \mu_{\Delta} \quad (20)$$

Therefore, the term inductance may be defined in different ways with respect to the BH curve of the ferromagnetic materials and the injection and measured variables [48], [49]. This is discussed in the following subsection.

A. Apparent and Synchronous Inductance Definition

From the earlier discussion, the apparent inductances and the incremental can be defined as follows.

- 1) The apparent (or synchronous) inductance governs the steady-state behavior of the electrical machine. This inductance is given by the static permeability (5) and can be graphically represented as the slope of the linearized characteristic of flux linkage versus current through the origin and the operating point of the magnetizing curve (see Fig. 2).

$$L_s = \frac{\lambda(t)}{i(t)} \quad (21)$$

- 2) The incremental (or differential) inductance governs the transient behavior of electrical machines. The incremental inductances are given by the differential permeability (20) and can be graphically represented as the slope of the tangential line at the operating point of the magnetizing curve, as shown in Fig. 2. As a result, the dq -axes HF inductances, L_{dHF} , L_{qHF} , estimated using the proposed method (17), (18) can be assumed to be equal to the differential inductance.

$$L_{\Delta} = \frac{d\lambda(t)}{di(t)} \approx L_{HF} \quad (22)$$

Fig. 3 shows the corresponding synchronous and incremental inductances for the magnetizing curve shown in Fig. 2. It is seen from Fig. 3 that HF inductance could be assumed to be approximately equal to the synchronous inductances at low

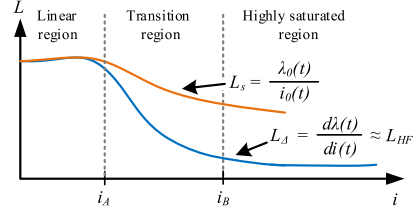


Fig. 3. Incremental and synchronous inductances of Fig. 2.

excitation levels [i.e., linear region ($0 \leq i < i_A$)]. However, once the machine starts to saturate (i.e., knee at $i \approx i_A$), a linear relationship between synchronous and HF inductances cannot be assumed anymore.

From the relationship between (21) and (22), it can be concluded that for current levels $> i_A$, the synchronous inductance can be directly estimated from the estimated HF inductances as follows:

$$\hat{L}_s(i) = \frac{\int_{0^+}^i L_{HF} di}{i} \quad (23)$$

It is noted that the aforementioned equation only applies when the fundamental current is > 0 . However, when fundamental current equals to 0 A, $L_{HF} = L_s$ holds (see Fig. 3), and additionally no torque would be produced. Therefore, using (23) will be necessary to guarantee accurate torque estimation at any torque level > 0 .

Particularizing (23) for d - and q -axes and substituting it into the GTE, torque can be finally estimated as

$$\hat{T}_c = \frac{3P}{2} \left[\left(\frac{\int_{0^+}^i L_{dHF}(L_{sd}, I_{sq}) di_{sd}^r}{i_{sd}^r} - \frac{\int_{0^+}^i L_{qHF}(I_{sd}, I_{sq}) di_{sq}^r}{i_{sq}^r} \right) i_{sd}^r i_{sq}^r \right] \quad (24)$$

Note that cross-coupling terms have not been taken into account. Also note that all the preceding discussions does not introduce any restriction to the signals feeding the machine, other than being high frequency. Therefore, it applies to any form of HF excitation.

V. SIMULATION RESULTS

This section shows simulation results of the proposed method obtained by means of FEA. Fig. 4 shows the schematic representation of the machine that will be used both for simulation and experimental verification, the parameters being shown in Table I. It corresponds to a commercial 4p SynRM [53]. L_{d0} and L_{q0} shown in Table I have been measured using the procedure described in [54]. Figs. 5 and 6 show simulations results changing both dq -axes fundamental currents from 0 to 3.9 A (1 p.u.), with the machine rotating at rated speed (1500 r/min).

Fig. 5(a) and 5(b) shows the measured d - and q -axes magnetic fluxes. Fig. 5(c) and 5(d) shows the estimated synchronous,

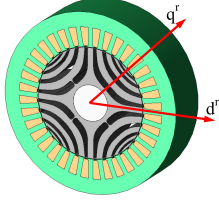


Fig. 4. Schematic representation of the four-pole SynRM test machine.

TABLE I
MACHINE PARAMETERS

Rated torque	T_{rated}	9.55 Nm
Rated speed	n_{rated}	1500 rpm
Rated current	I_{rated}	3.9 A _{rms}
Poles pairs	P	2
d -axis inductance	L_{d0}	450 mH
q -axis inductance	L_{q0}	250 mH

L_{dDC} and L_{qDC} , and HF, L_{dHF} and L_{qHF} , inductances using (21) and (22). It can be observed that once the machine starts to saturate, the HF inductance cannot be assumed to be equal to the synchronous inductance anymore (see Fig. 3). This is an expected result, as the estimated HF inductances (22) are defined by the differential permeability (20).

Fig. 5(e) and 5(f) shows the estimated dq -axes dc inductances, \hat{L}_{dDC} and \hat{L}_{qDC} , obtained by integration of the HF inductances shown in Fig. 5(c) and 5(d), using (23). Fig. 5(g) and 5(h) shows the estimation error. It is seen that synchronous inductances can be accurately estimated from the response to the injected HF signal even at high saturation level.

Fig. 6(a) and 6(b) shows the actual torque provided by FEA (T_{meas}), the estimated torque using the GTE assuming constant inductances ($\hat{T}_{L_{dq0}}$) and the estimated torque using the estimated dc inductances shown in Fig. 5(e) and 5(f) ($\hat{T}_{\hat{L}_{dqDC}}$). Fig. 6(c) and 6(d) shows the torque estimation errors defined as $T_{meas} - \hat{T}_{L_{dq0}}$ and $T_{meas} - \hat{T}_{\hat{L}_{dqDC}}$. It can be observed that torque estimations using the proposed method significantly improve the accuracy especially for large values of the dq -axes current, i.e., when the machine is highly saturated. It is observed that the maximum torque estimation error using the GTE with constant inductances is < 3.3 Nm ($\approx 34\%$ of rated torque), being reduced to < 0.16 Nm ($\approx 1.7\%$ of rated torque) when dc inductances are estimated using the HF inductances.

VI. EXPERIMENTAL RESULTS

Experimental results have been conducted in a test bench consisting of the test machine [53], a load machine (1.85-kW IM) [55], and a torque sensor [56], which is used to assess the accuracy of the proposed method. Fig. 7 shows the experimental setup. Details of the experimental setup parameters are summarized in Table II.

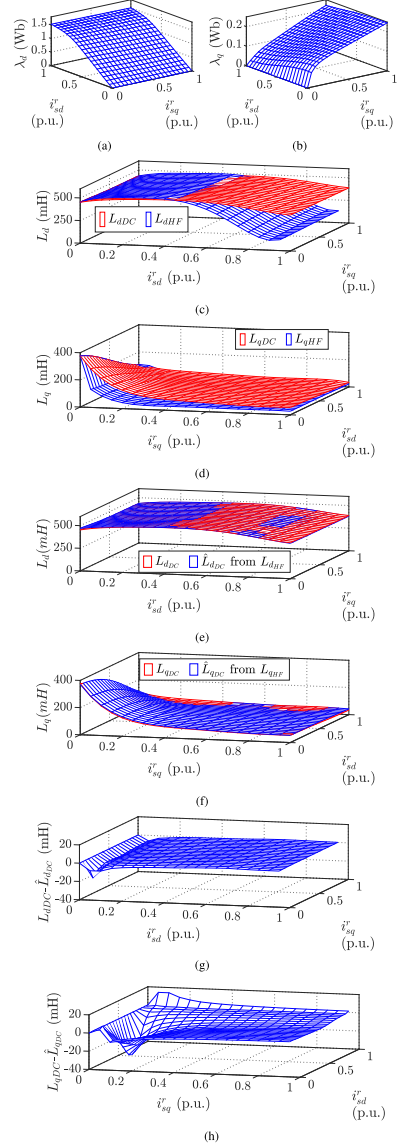


Fig. 5. FEA simulation results. (a) Measured d -axis flux. (b) Measured q -axis flux. (c) DC and HF d -axis inductances [see (21) and (22)]. (d) DC and HF q -axis inductances [see (21) and (22)]. (e) DC and estimated dc d -axis inductances [see (21) and (23)]. (f) DC and estimated dc q -axis inductances [see (21) and (23)]. (g) d -axis synchronous inductance estimation error. (h) q -axis synchronous inductance estimation error.

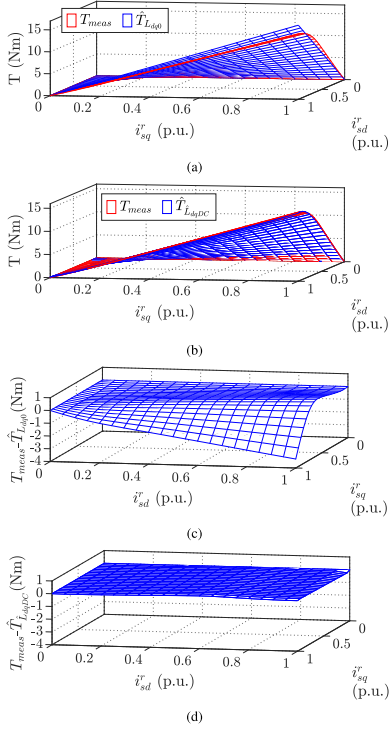


Fig. 6. FEA simulation results. (a) Measured and estimated torque assuming constant machine parameters. (b) Measured and estimated torque when dc inductances are estimated using the HF inductances. (c) Torque estimation error assuming constant machine parameters. (d) Torque estimated error from estimated dc parameters.

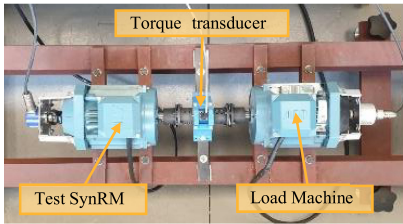


Fig. 7. Experimental set-up: Picture of the test bench.

Fig. 8(a) shows the inverter control block diagram, while Fig. 8(b) shows the signal processing for torque estimation using a rotating HF voltage signal injection.

Inputs of the signal processing block are the commanded HF voltage v_{sdqHF}^{r*} , the induced HF currents i_{sdqHF}^r , and the fundamental commanded current i_{sdq}^{r*} . Fig. 9(a) and 9(b) shows

TABLE II
EXPERIMENTAL TEST CONDITIONS

Power converter switching frequency, f_s	10kHz
Fundamental rotational speed, n_r	600 r.p.m.
High-frequency voltage magnitude, V_{HF}	40V
Frequency of the injected HF signal, ω_{HF}	$2 \cdot \pi \cdot 500$ rad/s
Low-Pass Filter bandwidth, bw_{LPP}	$2 \cdot \pi \cdot 100$ rad/s
High-Pass Filter bandwidth, bw_{HPF}	$2 \cdot \pi \cdot 5$ rad/s
Torque transducer measurement range [57]	± 50 Nm
Torque transducer combined error* [57]	$< 0.50\%$
Encoder resolution	4096
Accuracy Hall-effect based-current sensors	1%

*According to the calibrating curve provided by the manufacturer.

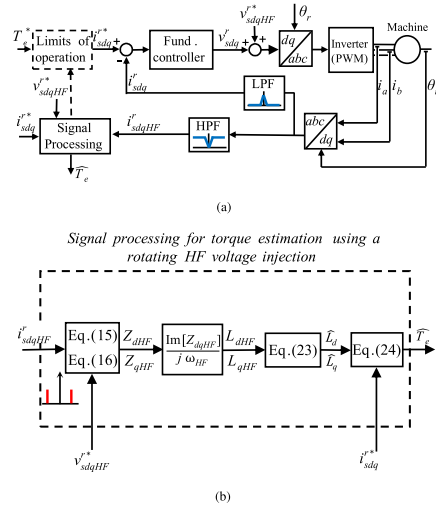


Fig. 8. Implementation of torque estimation using the rotating HF voltage injection. (a) Power converter and control overview. (b) Signal processing.

the commanded dq -axes HF voltage and the corresponding fast Fourier transform (FFT). An HF voltage of 40 V and 500 Hz has been used for all the experimental results. Fig. 9(c) and 9(d) shows the resulting stator dq -axes HF currents and the corresponding FFT. A discrete high-pass filter (HPF) of 5-Hz bandwidth has been used to remove the fundamental current component from the measured stator currents. Fig. 9(e) and 9(f) shows the dq -axes measured fundamental currents and the corresponding FFT after decoupling the induced HF currents and when the test machine is operated at its rated current. A discrete second-order low-pass filter (LPF) with a bandwidth of 100 Hz has been used to remove the HF current from the measured current.

Dq -axes HF inductances are estimated from the HF voltages and currents shown in Fig. 9(a) and 9(c) using (17) and (18) [see Fig. 9(g)]. The synchronous inductances L_{dDC} and L_{qDC} are obtained using (23) [see Fig. 9(h)], torque estimation \hat{T}_e

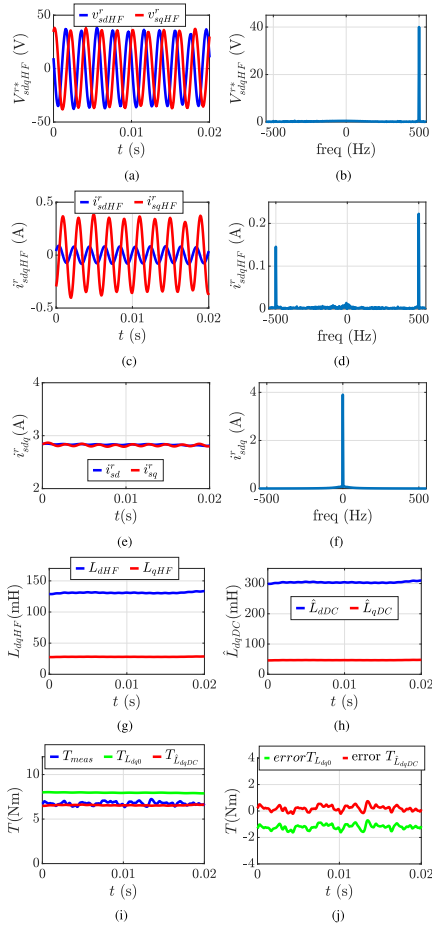


Fig. 9. Experimental results. (a) Injected HF voltage, v_{sdqHF}^* . (b) FFT of v_{sdqHF}^* . (c) Induced HF currents, i_{sdqHF}^* . (d) FFT of i_{sdqHF}^* . (e) Fundamental measured currents, i_{sdq}^* . (f) FFT of i_{sdq}^* . (g) Estimated dq -axes HF inductances [see (17) and (18)]. (h) Estimated dc synchronous inductances (23). (i) Estimated and measured torque. (j) Estimation errors, $T_{meas} - \hat{T}_{Ldq0}$ and $T_{meas} - \hat{T}_{LdqDC}$. $i_{sdq}^* = 1$ p.u. $\omega_r = 0.4$ p.u.

being finally obtained using (24). Fig. 9(i) shows the measured torque using the torque transducer (T_{meas}), the estimated torque using (4) (GTE) assuming constant inductances (\hat{T}_{Ldq0}), and the estimated torque using the estimated dc inductances in Fig. 9(i) (\hat{T}_{LdqDC}). Finally, Fig. 9(j) shows the estimation errors.

Fig. 10 shows the actual and estimated torque using the proposed method (24) when there is a step-like change in the

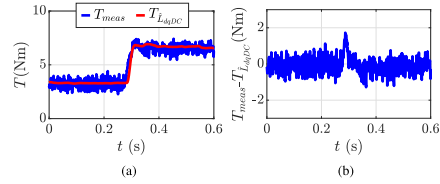


Fig. 10. Experimental results. (a) Estimated and measured torque. (b) Estimated torque error. Transient response to a step-like change in the dq -axes current command, i_{sdq}^* , from 0.6 to 1 p.u., with a current angle, β , of 45° . $\omega_r = 0.4$ p.u.

dq -axes current command, i_{sdq}^* , from 0.6 to 1 p.u. with a current angle $\beta = 45^\circ$ (i.e., dq -axes HF and synchronous inductances have been estimated from 0 to 0.6 p.u. current level in steps of 0.05 p.u. following the procedure described in Fig. 9 before applying the step-like change). It can be observed from the error shown in Fig. 10(b) that the torque estimator responds in the range of milliseconds.

Fig. 11 shows experimental results when the dq -axes fundamental currents, i_{sd}^* and i_{sq}^* , changes from 0 to 1 p.u. in steps of 0.05 p.u., and the machine rotates at 0.4 p.u. (600 r/min). It is noted that according to (23), the smaller the current steps, the better the resolution of the synchronous inductance estimation, being the step size critical when the machine enters in the transition region (see Fig. 1). The current step size has been chosen to accurately estimate both dq -axes inductances when the machine enters in the saturation region [see Fig. 5(a) and 5(b)].

Fig. 11(a) and 11(b) shows the estimated d - and q -axes HF inductances, L_{dHF} and L_{qHF} using (17) and (18) and the estimated synchronous inductances, \hat{L}_{dDC} and \hat{L}_{qDC} applying (23). Fig. 11(c) and 11(d) shows the measured torque using the torque transducer (T_{meas}), the estimated torque using (4) (GTE) assuming constant inductances (\hat{T}_{Ldq0}), and the estimated torque from the estimated dc inductances in Fig. 11(a) and 11(b) (\hat{T}_{LdqDC}).

Fig. 11(e) and 11(f) shows the torque estimation errors. Errors are seen to significantly decrease using the proposed method (24), especially in the high-saturation region. It is observed that the maximum torque estimation error when using the GTE assuming constant inductances is < 3.15 Nm (i.e., $< 33\%$ of the rated torque of the machine), while it is reduced to < 0.38 Nm (i.e., $< 3.9\%$ of the rated torque of the machine) when using the proposed method. These results are in good agreement with the simulation results shown in Fig. 6(c) and 6(d). Discrepancies between FEA simulations and experimental results should be expected due assembling tolerances and/or mismatches between real materials and modeled materials. It is observed that the maximum error using the proposed method (24) occurs when the machine operates outside the maximum torque per ampere (MTPA) region (i.e., when the fundamental current, i_{sdq}^* , has a current angle β different from 45° [see Fig. 11(f)]). This effect is a matter of ongoing research.

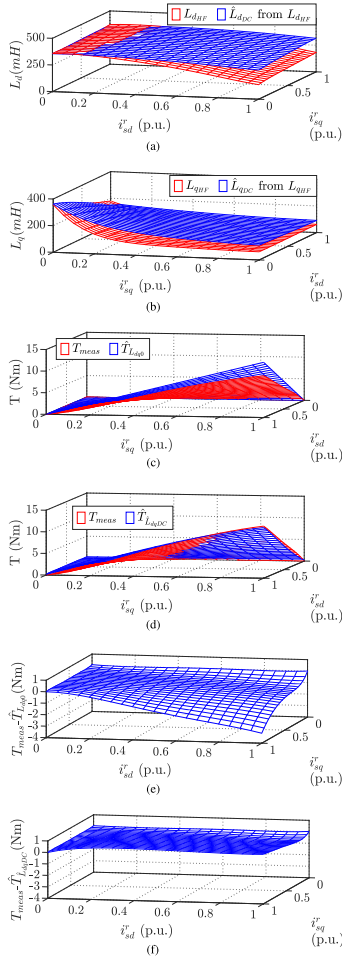


Fig. 11. Experimental results. (a) d -axis HF (17) and estimated dc inductances (23). (b) q -axis HF (18) and dc inductances (23). (c) Measured and estimated torque assuming constant machine parameters. (d) Measured and estimated torque when dc inductances are estimated using the HF inductances. (e) Torque estimation error assuming constant machine parameters. (f) Torque estimation error from estimated dc parameters.

VII. CONCLUSION

This article proposes a method to enhance the SynRM torque estimation using GTE by means of online parameter estimation. It has been demonstrated that synchronous inductances in the GTE can be accurately obtained by integrating the estimated HF inductances along the fundamental current. The proposed method has been shown to reduce significantly the torque

estimation error, especially under deep saturation. Appealing properties of the proposed method are its capability to operate in real time, under any speed and load condition, and without requiring a commissioning process. However, implementation of the proposed method in applications in which the machine operates in the saturation region for long periods of time can be especially challenging, as this reduces the opportunities of refreshing the estimates. Additionally, continuous estimation of the synchronous inductance would be required for having a reduced torque estimation error, especially when the machine enters in the transition magnetic operating region.

REFERENCES

- [1] A. Vagati, "The synchronous reluctance solution: A new alternative in ac drives," in *Proc. 20th Annu. Conf. IEEE Ind. Electron.*, 1994, vol. 1, pp. 1–13.
- [2] C. Babetto, G. Bacco, G. Berardi, and N. Bianchi, "High speed motors: A comparison between synchronous pm and reluctance machines," in *Proc. IEEE Energy Convers. Congr. Expo.*, 2017, pp. 3927–3934.
- [3] M. Zimmermann, A. Lange, and B. Piepenreier, "Experimental results and parameter identification of a permanent magnet assisted synchronous reluctance machine with a ribless rotor," in *Proc. IEEE Int. Magn. Conf.*, 2018, pp. 1–5.
- [4] J. Malan and M. J. Kamper, "Performance of a hybrid electric vehicle using reluctance synchronous machine technology," *IEEE Trans. Ind. Appl.*, vol. 37, no. 5, pp. 1319–1324, Sep/Oct. 2001.
- [5] H. Huang, Y. Hu, Y. Xiao, and H. Lyu, "Research of parameters and anti-demagnetization of rare-earth-less permanent magnet-assisted synchronous reluctance motor," *IEEE Trans. Magn.*, vol. 51, no. 11, pp. 1–4, Nov. 2015.
- [6] T. Lubin, H. Razik, and A. Rezzoug, "Magnetic saturation effects on the control of a synchronous reluctance machine," *IEEE Trans. Energy Convers.*, vol. 17, no. 3, pp. 356–362, Sep. 2002.
- [7] T. Matsuo and T. A. Lipo, "Field oriented control of synchronous reluctance machine," in *Proc. IEEE Power Electron. Specialist Conf.*, Jun. 1993, pp. 425–431.
- [8] S. S. Maroufian and P. Pillay, "Torque characterization of a synchronous reluctance machine using an analytical model," *IEEE Trans. Transport. Electric.*, vol. 4, no. 2, pp. 506–516, Jun. 2018.
- [9] R. Shi, H. A. Toliyat, and A. El-Atabli, "A DSP-based direct torque control of five-phase synchronous reluctance motor drive," in *Proc. IEEE Appl. Power Electron. Conf. Expo.*, 2001, vol. 2, pp. 1077–1082.
- [10] A. Shinke, M. Hasegawa, and K. Matsui, "Torque estimation for synchronous reluctance motors using robust flux observer to magnetic saturation," in *Proc. IEEE Int. Symp. Ind. Electron.*, Jul. 2009, pp. 1569–1574.
- [11] A. Yousefi-Talouki, P. Pescetto, G. Pellegrino, and I. Boldea, "Combined active flux and high-frequency injection methods for sensorless direct-flux vector control of synchronous reluctance machines," *IEEE Trans. Power Electron.*, vol. 33, no. 3, pp. 2447–2457, Mar. 2018.
- [12] Se-Kyo Chung, Hyun-Soo Kim, Chang-Gyun Kim, and Myung-Joong Yoon, "A new instantaneous torque control of PM synchronous motor for high-performance direct-drive applications," *IEEE Trans. Power Electron.*, vol. 13, no. 3, pp. 388–400, May 1998.
- [13] S. Kim *et al.*, "Robust torque control of dc link voltage fluctuation for SynRM considering inductances with magnetic saturation," *IEEE Trans. Magn.*, vol. 46, no. 6, pp. 2005–2008, Jun. 2010.
- [14] G. Heins, M. Thiele, and T. Brown, "Accurate torque ripple measurement for PMSM," *IEEE Trans. Instrum. Meas.*, vol. 60, no. 12, pp. 3868–3874, Dec. 2011.
- [15] Interface, *Torque Sensors: T5*. 2019. [Online]. Available: <https://interfaceforce.co.uk/>. Accessed: Sep. 1, 2019.
- [16] HBM, *HBM Torque Sensors*. [Online]. Available: <https://www.hbm.com/en/0264/torque-transducers-torque-sensors-torque-meters/>. Accessed: Oct. 16, 2019.
- [17] Futek, *Futek Torque Sensors*. [Online]. Available: <https://www.futek.com/store/Torque%20Sensors>, Accessed: Oct. 16, 2019.
- [18] Magtrol *Motors Testing and Sensors. Magtrol Torque Transducers*. [Online]. Available: <https://www.magtrol.com/product-category/torque-transducers/>. Accessed: Oct. 16, 2019.
- [19] TE Connectivity, *Measure Reaction and Rotating Torque*. [Online]. Available: <https://www.te.com/global-en/products/sensors/torque-sensors.html>. Accessed: Oct. 16, 2019.

- [20] M. Martínez, D. Fernández, D. Reigosa, J. M. Guerrero, and F. Briz, "Wireless torque pulsations measurement system for PMSMs," *IEEE Trans. Ind. Appl.*, vol. 56, no. 6, pp. 6467–6476, Nov./Dec. 2020.
- [21] P. Sue, D. Wilson, L. Farr, and A. Kretschmar, "High precision torque measurement on a rotating load coupling for power generation operations," in *Proc. IEEE Int. Instrum. Meas. Technol. Conf.*, May 2012, pp. 518–523.
- [22] J. Zakrzewski, "Combined magnetoelastic transducer for torque and force measurement," *IEEE Trans. Instrum. Meas.*, vol. 46, no. 4, pp. 807–810, Aug. 1997.
- [23] W. F. Traoré and R. McCann, "Torque measurements in synchronous generators using giant magnetostrictive sensor arrays via the maxwell stress tensor," in *Proc. IEEE Power Energy Soc. Gen. Meeting*, Jul. 2013, pp. 1–5.
- [24] K. C. Yeo, G. Heins, and F. D. Boer, "Comparison of torque estimators for PMSM," in *Proc. Australas. Universities Power Eng. Conf.*, Dec. 2008, pp. 1–6.
- [25] B. Cheng and T. R. Tesch, "Torque feedforward control technique for permanent-magnet synchronous motors," *IEEE Trans. Ind. Electron.*, vol. 57, no. 3, pp. 969–974, Mar. 2010.
- [26] F. Jukic, D. Sumina, and I. Erceg, "Comparison of torque estimation methods for interior permanent magnet wind power generator," in *Proc. IEEE Int. Conf. Elect. Drives Power Electron.*, Oct. 2017, pp. 291–296.
- [27] J. X. Xu, S. K. Panda, Y. J. Pan, T. H. Lee, and B. H. Lam, "Improved PMSM pulsating torque minimization with iterative learning and sliding mode observer," in *Proc. IEEE Int. Conf. Ind. Electron., Control Instrum.*, 2000, vol. 3, pp. 1931–1936.
- [28] B. H. Lam, S. K. Panda, and J. X. Xu, "Torque ripple minimization in PM synchronous motors an iterative learning control approach," in *Proc. IEEE Int. Conf. Power Electron. Drive Syst.*, 1999, vol. 1, pp. 144–149.
- [29] X. Dong, W. Tianmiao, and W. Hongxing, "Comparison between model reference observer and reduced order observer of PMSM torque," in *Proc. IEEE Conf. Ind. Electron. Appl.*, Jun. 2011, pp. 663–667.
- [30] Q. Liu and K. Hameyer, "High-performance adaptive torque control for an IPMSM with real-time MTPA operation," *IEEE Trans. Energy Convers.*, vol. 32, no. 2, pp. 571–581, Jun. 2017.
- [31] Y. A.-I. Mohamed and T. K. Lee, "Adaptive self-tuning MTPA vector controller for IPMSM drive system," *IEEE Trans. Energy Convers.*, vol. 21, no. 3, pp. 636–644, Sep. 2006.
- [32] P. L. Jansen and R. D. Lorenz, "A physically insightful approach to the design and accuracy assessment of flux observers for field oriented induction machine drives," *IEEE Trans. Ind. Appl.*, vol. 30, no. 1, pp. 101–110, Jan. 1994.
- [33] O. Buechholz and J. Böcker, "Gopinath-observer for flux estimation of an induction machine drive system," in *Proc. IEEE Southern Power Electron. Conf.*, Dec. 2017, pp. 1–7.
- [34] K.-H. Zhao *et al.*, "Accurate torque-sensorless control approach for interior permanent-magnet synchronous machine based on cascaded sliding mode observer," *J. Eng.*, vol. 2017, no. 7, pp. 376–384, 2017.
- [35] G.-D. Andreescu, C. I. Pitic, F. Blaabjerg, and I. Boldea, "Combined flux observer with signal injection enhancement for wide speed range sensorless direct torque control of IPMSM drives," *IEEE Trans. Energy Convers.*, vol. 23, no. 2, pp. 393–402, Jun. 2008.
- [36] X. Xiao, C. Chen, and M. Zhang, "Dynamic permanent magnet flux estimation of permanent magnet synchronous machines," *IEEE Trans. Appl. Supercond.*, vol. 20, no. 3, pp. 1085–1088, Jun. 2010.
- [37] K. Liu and Z. Q. Zhu, "Online estimation of the rotor flux linkage and voltage-source inverter nonlinearity in permanent magnet synchronous machine drives," *IEEE Trans. Power Electron.*, vol. 29, no. 1, pp. 418–427, Jan. 2014.
- [38] M. N. Uddin, "An adaptive-filter-based torque-ripple minimization of a fuzzy-logic controller for speed control of IPM motor drives," *IEEE Trans. Ind. Appl.*, vol. 47, no. 1, pp. 350–358, Jan. 2011.
- [39] T. Liu, I. Husain, and M. Elbuluk, "Torque ripple minimization with on-line parameter estimation using neural networks in permanent magnet synchronous motors," in *Proc. 33rd Annu. Meeting IEEE Ind. Appl. Soc.*, Oct. 1998, vol. 1, pp. 35–40.
- [40] Z. Lin, D. S. Reay, B. W. Williams, and X. He, "Online modeling for switched reluctance motors using B-spline neural networks," *IEEE Trans. Ind. Electron.*, vol. 54, no. 6, pp. 3317–3322, Dec. 2007.
- [41] W. Xu and R. D. Lorenz, "High-frequency injection-based stator flux linkage and torque estimation for DB-DTFC implementation on IPMSMs considering cross-saturation effects," *IEEE Trans. Ind. Appl.*, vol. 50, no. 6, pp. 3805–3815, Nov. 2014.
- [42] B. Hafez, A. Abdel-Khalik, A. M. Massoud, S. Ahmed, and R. D. Lorenz, "Single sensor three-phase permanent magnet synchronous motor drive based on luenberger style-observers," in *Proc. 15th IEEE Int. Conf. Elect. Mach. Syst.*, Oct. 2012, pp. 1–6.
- [43] M. Martínez, D. Reigosa, D. Fernández, J. M. Guerrero, and F. Briz, "Enhancement of permanent-magnet synchronous machines torque estimation using pulsating high-frequency current injection," *IEEE Trans. Ind. Appl.*, vol. 56, no. 1, pp. 358–366, Jan. 2020.
- [44] D. Reigosa, D. Fernandez, T. Tanimoto, T. Kato, and F. Briz, "Comparative analysis of BEMF and pulsating high-frequency current injection methods for PM temperature estimation in PMSMs," *IEEE Trans. Power Electron.*, vol. 32, no. 5, pp. 3691–3699, May 2017.
- [45] Y. G. Kang, D. Reigosa, B. Sarioglu, and R. D. Lorenz, "D- and q-axis inductance estimation and self-sensing condition monitoring using 45° angle high-frequency injection," *IEEE Trans. Ind. Appl.*, vol. 57, no. 1, pp. 506–515, 2021.
- [46] M. Martínez, D. F. Laborda, D. Reigosa, D. Fernández, J. M. Guerrero, and F. Briz, "SynRM sensorless torque estimation using high frequency signal injection," in *Proc. IEEE 10th Int. Symp. Sensorless Control Elect. Drives*, Sep. 2019, pp. 1–5.
- [47] M. Martínez *et al.*, "Comparative analysis of high frequency signal injection based torque estimation methods for SPMSM, IPMSM and SynRM," *Energies*, vol. 13, no. 3, Jan. 2020, Art. no. 592. [Online]. Available: <https://www.mdpi.com/1996-1073/13/3/592>
- [48] W. J. Croisant, C. A. Feickert, and M. K. McInerney, "A differential magnetic permeability model for pulsed magnetic field calculations," *IEEE Trans. Magn.*, vol. 32, no. 5, pp. 4326–4328, Sep. 1996.
- [49] M. S. Perdigo, M. F. Menke, R. R. A. SeidelPinto, and J. M. Alonso, "A review on variable inductors and variable transformers: Applications to lighting drivers," *IEEE Trans. Ind. Appl.*, vol. 52, no. 1, pp. 531–547, Jan./Feb. 2016.
- [50] A. Ganji, P. Guillaume, R. Pintelon, and P. Lataire, "Induction motor dynamic and static inductance identification using a broadband excitation technique," *IEEE Trans. Energy Convers.*, vol. 13, no. 1, pp. 15–20, Mar. 1998.
- [51] D. D. Reigosa, D. Fernandez, H. Yoshida, T. Kato, and F. Briz, "Permanent-magnet temperature estimation in PMSMs using pulsating high-frequency current injection," *IEEE Trans. Ind. Appl.*, vol. 51, no. 4, pp. 3159–3168, Jul. 2015.
- [52] H. Jung, D. Park, H. Kim, S. Sul, and D. J. Berry, "Non-invasive magnet temperature estimation of IPMSM based on high-frequency inductance with a pulsating high-frequency voltage signal injection," *IEEE Trans. Ind. Appl.*, vol. 55, no. 3, pp. 3076–3086, May 2019.
- [53] ABB. ABB products: 3GAL092007-ASB. [Online]. Available: <https://new.abb.com/products/es/3GAL092007-ASB>. Accessed: Dec. 15, 2019.
- [54] V. Bobek, "PMSM electrical parameters measurement," *Freescall Semiconductor*, vol. 7, no. 8, p. 16, 2013.
- [55] ABB. ABB products: 3GAA092003-ASE, pp. 1–16. [Online]. Available: <https://new.abb.com/products/3GAA092003-ASE>. Accessed: Dec. 15, 2019.
- [56] DELTA REGIS. *Serie DRTX: DRTX-3138-50* C. [Online]. Available: <https://deltaregis.com/>. Accessed: Dec. 15, 2019.



Maria Martínez (Member, IEEE) received the M.S. and Ph.D. degrees in electrical engineering from the University of Oviedo, Gijón, Spain, in 2017 and 2020, respectively.

She is currently an Assistant Professor with the Electrical Engineering Department, University of Oviedo. She was an Intern with the Nissan Advanced Technology Center, Japan, in 2019, and a Visiting Student with Aalborg University, Denmark, in 2015. Her research interests include machine diagnostics, wireless measurement systems, sensorless control, and digital signal processing.

Dr. Martínez was the recipient of the IEEE Power Electronics Society Ph.D. Thesis Talk Award in 2020.



Diego F. Laborda received the B.S. degree in industrial electronic engineering in 2016 and the M.S. degree in electric energy conversion and power electronics engineering in 2018, from the University of Oviedo, Gijón, Spain, where he is currently working toward the Ph.D. degree in electrical engineering.

He has been a Researcher with the Department of Electrical, Electronic, Computers and Systems Engineering, University of Oviedo, since 2018. His research interests include electric machines and power electronics for electric vehicles, wireless measurement systems, and digital signal processing.



Juan M. Guerrero (Senior Member, IEEE) received the M.E. degree in industrial engineering and the Ph.D. degree in electrical and electronic engineering from the University of Oviedo, Gijón, Spain, in 1998 and 2003, respectively.

Since 1999, he has been in different teaching and research positions with the Department of Electrical, Computer and Systems Engineering, University of Oviedo, where he is currently an Associate Professor. From February to October 2002, he was a Visiting Scholar with the University of Wisconsin, Madison, WI, USA. From June to December 2007, he was a Visiting Professor with the Tennessee Technological University, Cookeville. His research interests include control of electric drives and power converters, electric traction, and renewable energy generation.



David Reigosa was born in Spain, in 1979. He received the M.E. and Ph.D. degrees in electrical engineering from the University of Oviedo, Gijón, Spain, in 2003 and 2007, respectively.

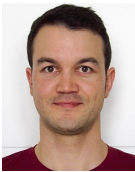
He is currently a Full Professor with the Electrical Engineering Department, University of Oviedo. From 2004 to 2008, he was awarded with fellowship of the Personnel Research Training Program funded by the Regional Ministry of Education and Science of the Principality of Asturias. He was a Visitor Scholar with the Wisconsin Electric Machines and Power Electronics Consortium, University of Wisconsin, Madison, WI, USA, in 2007. He was a Visitor Professor with the Electrical Machines and Drives Group, University of Sheffield, Sheffield, U.K., in 2016. His research interests include sensorless control of induction motors, permanent-magnet synchronous motors, and digital signal processing.

Dr. Reigosa was the recipient of nine IEEE Industry Applications Society Conference and IEEE Energy Conversion Congress and Exposition Prize Paper Awards.



Fernando Briz (Senior Member, IEEE) received the M.S. and Ph.D. degrees in electrical engineering from the University of Oviedo, Gijón, Spain, in 1990 and 1996, respectively.

He is currently a Full Professor with the Department of Electrical, Computer and Systems Engineering, University of Oviedo. Dr. Briz received an IEEE TRANSACTIONS ON INDUSTRY APPLICATIONS Award and nine IEEE Industry Applications Society Conference and IEEE Energy Conversion Congress and Exposition (ECCE) prize paper awards. He is Past Chair of the Industrial Drives Committee of the Industrial Power Conversion System Department (IPCSD) of the IAS. Currently he is Vice Chair of IPCSD. He has served in scientific committees and as Vice Chair or Technical Program Chair of several conferences, including ECCE, IEEE International Electric Machines & Drives (IEMDC), International Conference on Electrical Machines (ICEM), International Conference on Electrical Machines and Systems (ICEMS) and Symposium on Sensorless Control for Electrical Drives (SLED), and is a Member of the Steering Committee of IEEE Journal of Emerging and Selected Topics in Power Electronics (JESTPE) and Associate Editor of IAS and JESTPE Transactions. His topics of interest include electronic power converters and ac drives, power systems, machine monitoring and diagnostics and digital signal processing.



Daniel Fernandez (Member, IEEE) received the M.S. and Ph.D. degrees in electrical engineering from the University of Oviedo, Spain, in 2013 and 2017 respectively.

He is currently an Assistant Professor with the Department of Electrical, Computer and Systems Engineering, University of Oviedo. From July to December 2013, he was an Intern with the Nissan Advanced Technology Center, Japan. From August to November 2015, he was a Visiting Student with the University of Sheffield, and from May to July 2019, he was a Visiting Professor with the University of Padova. His research interests include design, control, and diagnostics of electric machines and drives.

Dr. Fernandez was the recipient of four IEEE Industry Applications Society Conference Prize Paper Awards and the University of Oviedo Outstanding Ph.D. Thesis Award in 2018.

B.1.2 Permanent Magnet Synchronous Machine Torque Estimation Using Low Cost Hall-Effect Sensors

Permanent Magnet Synchronous Machine Torque Estimation Using Low Cost Hall-Effect Sensors

Daniel Fernández Alonso , YeGu Kang , Diego Fernández Laborda , María Martínez Gómez ,
David Díaz Reigosa , and Fernando Briz 

Abstract—Torque measurement/estimation in permanent magnet synchronous machines (PMSMs) is required in a large variety of applications. Direct torque measurement by means of torque transducers is typically limited to laboratory applications due to cost, reliability, and room concerns. Alternatively, torque can be estimated. Torque estimation methods require accurate knowledge of machine parameters. Injection of a high frequency (HF) signal in the stator via inverter has been shown to be a viable option for online machine parameters identification in PMSMs. However, this introduces concerns on the performance of the machine due to the noise, vibration, and additional losses produced by the HF signal. This article proposes a torque estimation method for PMSMs using low cost Hall-effect sensors. The method is based on the dependency of the leakage flux complex vector due to interaction between permanent magnet flux and stator coil flux and does not interfere with the drive operation of the machine.

Index Terms—Hall-effect sensors, leakage flux complex vector, permanent magnet synchronous machines (PMSM) leakage flux, torque estimation.

I. INTRODUCTION

PERMANENT magnet synchronous machines (PMSMs) are commonly used in industrial automation for traction, robotics, wind energy, or aerospace applications. The use of PMSMs has been gradually increasing and replacing other machine types due to their power density, torque capabilities, dynamics, and efficiency [1], [2]. Accurate control, diagnostics and monitoring of PMSM drives, are required in industrial applications. Machine torque is a variable required to e.g., enhance

controllability [3], find the maximum torque per ampere (MTPA) trajectory [4], early fault detection [5], or as a redundant parameter for improving safety [6]. In electric vehicles or hybrid-electric vehicles, accurate torque measurement/estimation is required for the implementation of torque vectoring [7], antilock braking system (ABS), vehicle stability control or antislip regulator controller [8].

PMSMs torque can be measured or estimated. Torque measurement systems can be roughly classified according to the measured variable: torsional strain between shafts or torsional displacement of a shaft. Torque transducers measure torsional strain between two rotating shafts, typically using strain gauges [9],[10], while torsional displacement is measured using optical sensors [11], [12]. Measured signals can be transmitted to the stationary part using slip rings, optical grating, or wirelessly. However, all torque measurement systems are typically expensive and bulky. Also, they lower the robustness of the drive and their performance can be compromised by environmental conditions e.g., due to electromagnetic interference. Torque transducers also require well-balanced mechanical coupling systems, which extend the shaft length, increasing the system inertia and modifying mechanical resonances. For these reasons, torque transducers are typically limited to laboratory and test equipment. Torque estimation techniques are therefore the preferred option for industrial applications.

A variety of PMSMs torque estimation methods have been proposed, including those based on the general torque equation; use of neural networks; use of flux observers; and use of high-frequency signal injection. General torque equation-based methods require accurate knowledge of machine parameters, e.g., permanent magnet (PM) flux linkage or the inductances [14], [15], which will vary with machine operating conditions. Torque estimation algorithms based on neural networks require large computational capability and are also parameter dependent [16]. Flux observers have been used for torque estimation purposes [17], [18], their main disadvantage being the machine parameters dependency. PMSMs parameters can also be estimated by means of high-frequency signal injection-based methods [19], [20], which are independent of machine working conditions. The main drawbacks of these techniques are the additional losses, noise, and vibration induced due to the injected HF signal. Table I summarizes advantages and disadvantages of the torque estimation methods discussed abovementioned.

This article proposes a method for torque estimation using the flux measurements provided by linear Hall-effect sensors

Manuscript received October 28, 2020; revised March 3, 2021; accepted April 3, 2021. Date of publication April 27, 2021; date of current version July 16, 2021. This work was supported by the knowledge generation and scientific and technological strengthening Program of the Spanish Ministry of Science and Innovation under Grant MCI-20-PID2019-106057RB-I00 Paper 2020-IDC-1421.R1 presented at the 2019 IEEE 10th International Symposium on Sensorless Control for Electrical Drives, Torino, Italy, Sep. 9 to Sep. 10, and approved for publication in the IEEE TRANSACTIONS ON INDUSTRY by the Electric Machines Committee of the IEEE Industry Applications Society. (Corresponding author: Daniel Fernandez Alonso.)

Daniel Fernández Alonso, Diego Fernández Laborda, María Martínez Gómez, David Díaz Reigosa, and Fernando Briz are with the University of Oviedo, 33003 Gijón, Spain (e-mail: fernandezalodaniel@uniovi.es; dflaborda@uniovi.es; martinezgmaria@uniovi.es; reigosa@isa.uniovi.es; fernando@isa.uniovi.es).

YeGu Kang is with the Wisconsin Electric Machines and Power Electronics Consortium, University of Wisconsin-Madison, Madison, WI 53715 USA (e-mail: kangyegoo@gmail.com).

Color versions of one or more figures in this article are available at <https://doi.org/10.1109/TIA.2021.3075924>.

Digital Object Identifier 10.1109/TIA.2021.3075924

0093-9994 © 2021 IEEE. Personal use is permitted, but republication/redistribution requires IEEE permission. See <https://www.ieee.org/publications/rights/index.html> for more information.

TABLE I
TORQUE MEASUREMENT/ESTIMATION METHODS

	Cost	Parameter dependency	Computational time	Robustness	Accuracy
Torque transducers	Very High	Null	Null	Very Low	Very High
Torque Equation [14],[15]	Null	Very High	Very Low	Very High	Low
Neural networks [16]	Null	Low	Very High	Very High	Medium-High
Observer [17],[18]	Null	High	High	Very High	Medium
HF injection [19],[20]	Null	High	High	Very High	Medium
Hall-sensor based	Null*	High	Very Low	High	Medium

*Cost of the proposed system will be null in case the PMSM is equipped with linear Hall sensors.

[21]–[25]. Hall-effect sensors are typically used in PMSM for initial position estimation including polarity [21]–[25], but can also be used for diagnostic and monitoring purposes e.g., PM temperature estimation [26], rotor load defects detection [27], or improve fault tolerant capability [28]. The proposed method is based on the dependency of the flux measured by the Hall-effect sensors on the PM flux and the stator coils currents. Hall-effect sensors located in the stator provide stationary measurement of PM leakage flux, which is affected by d - and q - axes currents in a different manner; flux weakening current changes its amplitude, whereas torque current shifts PM flux lines to induce torque [26]. The proposed method is insensitive to magnet temperature or flux-weakening current and can be applied to both surface permanent magnet synchronous machines (SPMSMs) and interior permanent magnet synchronous machines (IPMSMs) [29].

This article is organized as follows: Hall-effect sensor-based flux leakage measurement in PMSMs is presented in Section II, torque estimation using leakage flux is presented in Section III, experimental results are provided in Section IV, and conclusion is finally presented in Section V.

II. HALL-EFFECT SENSOR-BASED LEAKAGE FLUX MEASUREMENT IN PMSMS

This section describes the leakage flux measurement system in PMSMs. Fig. 1 shows the IPMSM and the SPMSM designs that will be used for the analysis of the proposed method. The IPMSM is a prototype and the SPMSM is commercial machine from ABB. Their main characteristics are shown in Table II.

Fig. 1 (a) and (c) show the location of the three Hall-effect sensors (H_a , H_b , and H_c) in each machine. Fig. 1(b) and (d) show the coordinate system, with x -axis being aligned with the rotor tangential direction and y -axis being aligned with the radial direction. Axial flux (z -axis) does not contain useful information for torque estimation purposes at the current location and will not be further referenced. The phase shift among sensors is 120 electrical degrees. This corresponds to 40 mechanical degrees in the 6-pole IPMSM in Fig. 1(a), and 30 mechanical degrees in the 8-pole SPMSM in Fig. 1(c).

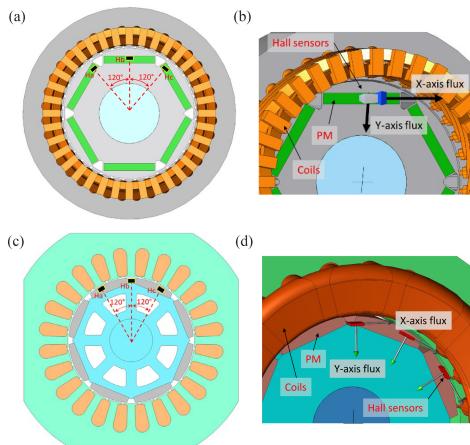


Fig. 1. Schematic representation and sensors location. (a) Two-dimensional (2-D). (b) 3-D for the IPMSM. (c) 2-D. (d) 3-D for the SPMSM; x and y correspond to the tangential and radial directions, respectively.

TABLE II
ELECTRIC AND GEOMETRIC MACHINE PARAMETERS

	SPMSM	IPMSM
P_{rated} (kW)	6.6	7.5
I_{rated} (A)	15	14
n_{rated} (rpm)	1000	1000
Stator slots	24	36
Number of poles	8	6
Rotor radius (mm)	57	54.2
Magnets	-	N42 SH
Magnet dimensions: width, height and length (mm)	36x9x28	42x6x50
Magnet position from shaft center (mm)	52.5	44.6
Hall sensor position, xyz (mm)	0, 0, 5	0, 0, 5
Airgap length (mm)	1.2	0.4
Inner stator radius (mm)	59.4	55
Outer stator radius (mm)	93	88
Stack length (mm)	84	100

Fig. 2 shows flux lines distribution on y - z plane of the IPMSM obtained by means of finite element analysis (FEA). It can be observed that the maximum concentration of leakage flux lines occurs at the edge of the PM. Therefore, this is considered the most suitable location for the Hall-effect sensors.

An example of the FEA calculated magnetic leakage flux density along the x -axis direction (tangential) and y -axis direction (radial) seen by the sensors during a rotor revolution is shown in Fig. 3. It can be observed that the flux at the sensors' location consist of quasi-sinusoidal fundamental wave plus harmonics, the phase shift of the fundamental wave among sensors being 120°. It is observed that the magnitude in the radial direction is around twice of that in the tangential direction. Therefore, radial

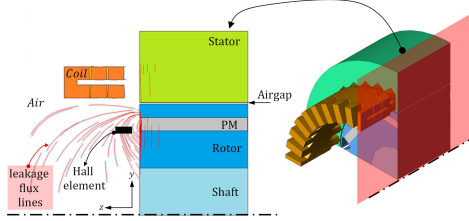


Fig. 2. FEA results. Leakage flux on y - z plane under no load conditions and Hall sensor location.

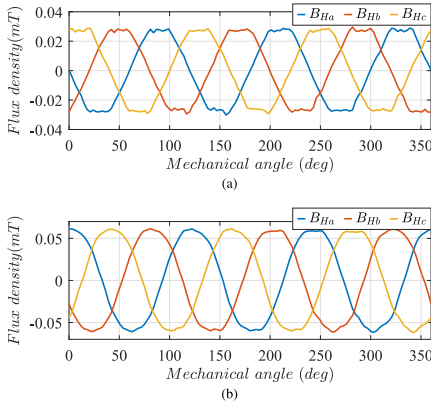


Fig. 3. FEA results. Flux density at sensors location for the IPMSM case. (a) Tangential (x -axis). (b) Radial direction (y -axis).

flux measurements (i.e., y -axis) will be used in this article for torque estimation purposes.

III. TORQUE ESTIMATION USING THE MEASURED LEAKAGE FLUX BY HALL-EFFECT SENSORS

A. Torque Estimation

The total torque induced in a PMSM is defined by (1), where p is the number of pole pairs of the machine, λ_{ds}^r and λ_{qs}^r are the d - and q - axes stator flux linkages, and i_{ds}^r and i_{qs}^r are the d - and q - axes currents in a reference frame synchronous with the rotor, respectively. Assuming a similar behavior of λ_{ds}^r and λ_{qs}^r in the stator and rotor cores, as it will be shown later, radial and tangential leakage flux components, λ_{lds}^r and λ_{lqs}^r are given by the interaction of the coil flux and PM flux and can be measured using Hall-effect sensors. The leakage flux measured by the Hall-effect sensors will be labeled as B_{Ham} , B_{Hbm} , and B_{Hcm} where subindex m stands for x or y component. From the three measurements a leakage flux complex vector \vec{B}_{ldqs}^s (2) in the stator reference frame is defined considering (3). The leakage flux complex vector in the stator reference frame \vec{B}_{ldqs}^s can be transformed to a rotor synchronous reference frame \vec{B}_{ldqs}^r (4).

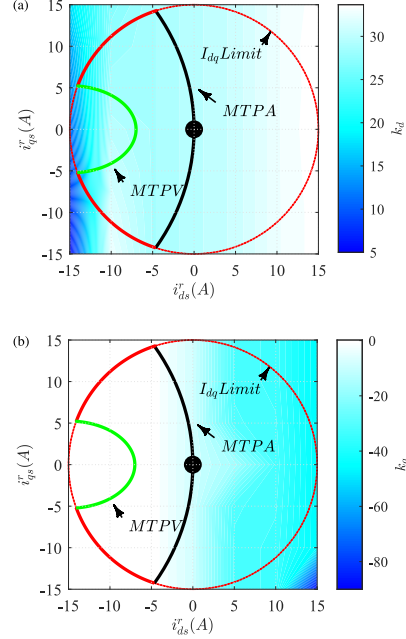


Fig. 4. FEA results of the relationship between stator flux linkage and leakage flux measured by the Hall-effect sensors for the IPMSM. (a) d -axis (k_d). (b) q -axis (k_q).

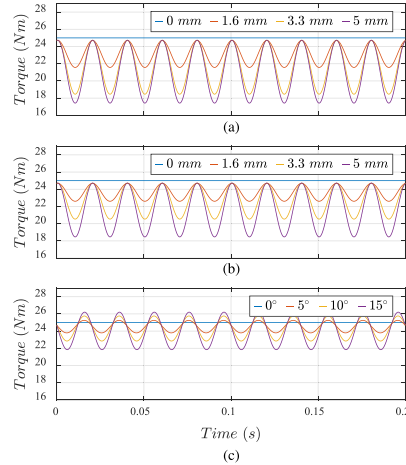


Fig. 5. Torque estimation for mounting errors in one sensor. (a) Radial displacement. (b) Axial displacement. (c) Axial displacement (i.e., phase shift). $n = 500$ rpm.

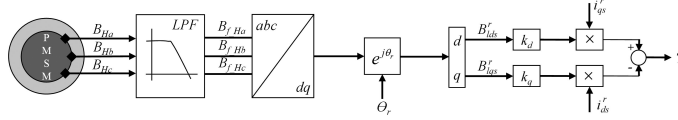


Fig. 6. Block diagram for torque estimation using leakage flux components.

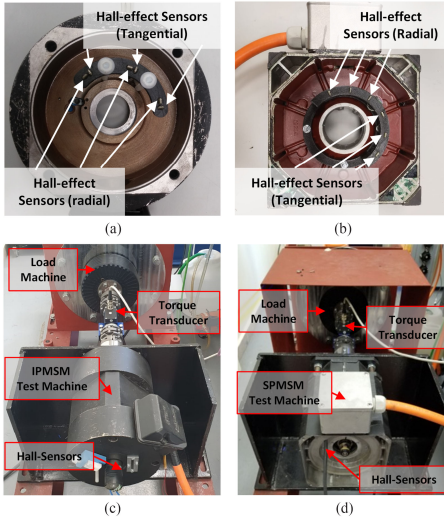
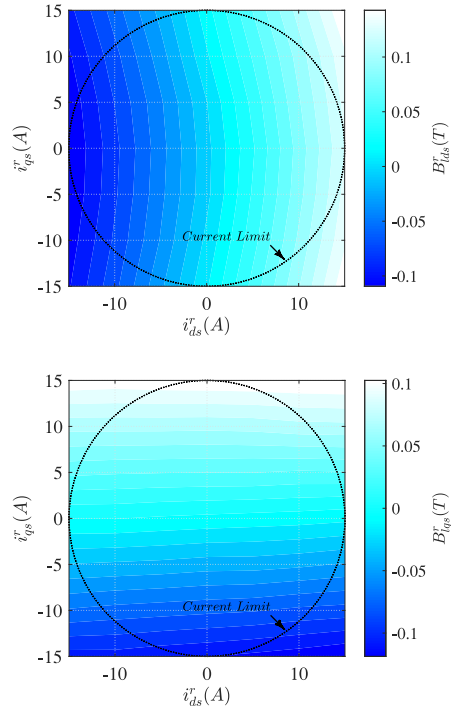


Fig. 7. Test machines. (a) IPMSM end-shield with the Hall-effect sensors. (b) SPMSM end-shield with the Hall-effect sensors. (c) Test bench for the IPMSM. (d) Test bench for the SPMSM.

The relationship between the stator flux linkage, $\vec{\lambda}_{ids}^r$, and the leakage flux density, \vec{B}_{ids}^r , measured by the Hall-effect sensors is given by the coefficients k_d and k_q as shown by (5) and (6), respectively; k_d and k_q as a function of i_{ds}^r and i_{qs}^r are shown in Fig. 4. It can be observed that k_d is highly dependent on d -axis current but is barely affected by q -axis current [see Fig. 4(a)]. k_q in Fig. 4(b) presents similar trends but is nearly constant in the second and third quadrants of the dq plane. It is concluded from (5) to (6) and Fig. 4 that machine torque could be modeled as (7). k_d and k_q depend on the machine geometry, materials and sensor active area. In this work, they will be estimated experimentally from the measured leakage flux maps and torque.

For operating conditions with low or no flux weakening operation, (i.e., negative d -axis current), the term $k_d B_{ids}^r i_{qs}^r$ is dominant; k_d can be considered as a constant under these working conditions, see Fig. 4(a). For high flux weakening operation, the term $k_q B_{ids}^r i_{ds}^r$ becomes dominant, k_q can be assumed constant under these working conditions, see Fig. 4(b).

$$T = \frac{3p}{2} (\lambda_{ds}^r i_{qs}^r - \lambda_{qs}^r i_{ds}^r) \quad (1)$$

Fig. 8. -IPMSM experimental results. (a) d -axis leakage flux measured in the I_{dq} plane. (b) q -axis leakage flux measured in the I_{dq} plane. $n = 500$ rpm and I_{dq} step = 5A.

$$\vec{B}_{ids}^s = \frac{2}{3} (B_{Ham} + a B_{Hbm} + a^2 B_{Hcm}) \quad (2)$$

$$a = e^{j2\pi/3} \quad (3)$$

$$\vec{B}_{ids}^r = \vec{B}_{ids}^s e^{j\theta_r} \quad (4)$$

$$k_d = \frac{\lambda_{ds}^r}{B_{ids}^r} \quad (5)$$

$$k_q = \frac{\lambda_{qs}^r}{B_{ids}^r} \quad (6)$$

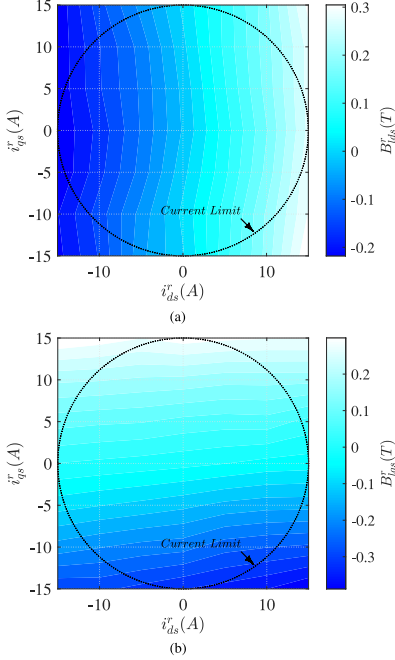


Fig. 9. – SPMSM experimental results. (a) d -axis leakage flux measured in the I_{dq} plane. (b) q -axis leakage flux measured in the I_{dq} plane. $n = 500$ rpm and I_{dq} step = 5A.

$$\hat{T} = \frac{3p}{2} (k_d B_{ldq}^r i_{qs}^r - k_q B_{lqs}^r i_{ds}^r) \quad (7)$$

$$\varepsilon = \frac{T - \hat{T}}{T} \times 100 \quad (8)$$

The block diagram of the proposed torque estimation method is shown in Fig. 6. The inputs of the control block diagram are the measured leakage flux signals (B_{Ham} , B_{Hbm} , and B_{Hcm}), which are low-pass filtered to remove high-frequency induced noise. This filter is analog to prevent aliasing, with a cutoff frequency of 5 kHz. The flux leakage complex vector (2) is obtained afterwards and transformed to a rotor synchronous reference frame. The resulting d - and q -axes leakage flux components are multiplied by the corresponding scaling factors and stator currents to provide the estimated torque (7).

B. Implementation Issues

Mounting errors can be due to axial displacement, radial displacement, or angular displacement [21].

Axial and radial displacement induces a variation of the magnetic flux density measured by the sensor both in x - and y -axes directions, where the measured magnetic flux densities decrease as the sensor is moved further away from the magnet.

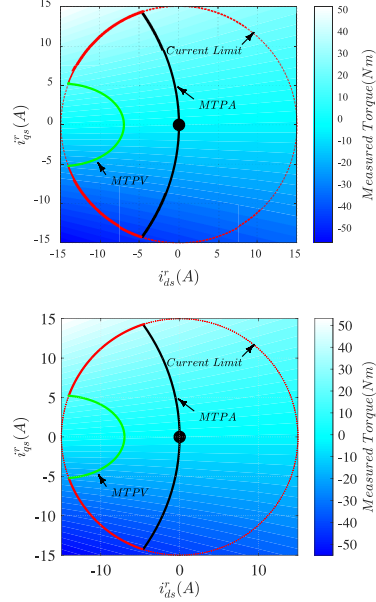


Fig. 10. IPMSM torque. (a) Measurement using a torque transducer. (b) Estimated using the proposed method. Dotted lines delimit constant torque regions. $n = 500$ rpm and I_{dq} step = 5A.

This variation can be modeled as a variation of the gain of the sensor, which adds a positive and a negative sequence at $\pm\omega$ to the fundamental component of the leakage flux complex vector, \vec{B}_{ldqs}^s . Angular displacement among sensors also adds a positive and a negative sequence at $\pm\omega$ to the fundamental component of the leakage flux complex vector, \vec{B}_{ldqs}^s , but shifted $\pi/2$ [21]. The positive and negative sequence will produce oscillations in both the d , B_{ldq}^s and q , B_{lqs}^s leakage flux components that will be reflected on the torque estimation. Fig. 5 shows the oscillations produced in the estimated torque when one sensor is shifted in the radial an axial direction up to 5 mm and when the sensor is shifted up to 15 electrical degrees.

Different magnetization state of the magnets due to assembling tolerances or partial (local) demagnetization may also affect the developed torque of the machine. When uniform demagnetization occurs, the output torque of the machine will be reduced (for a given current). The proposed method will detect this variation, i.e., a uniform demagnetization does not affect to the method applicability. When nonuniform demagnetization occurs, the mean output torque of the machine will be slightly reduced (for a given current). The proposed method will detect this variation since the leakage flux will be reduced accordingly, i.e., a nonuniform demagnetization does not affect to the method applicability.

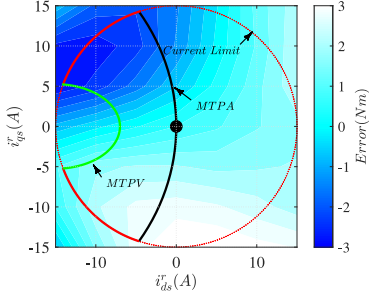


Fig. 11. IPMSM torque error. $n = 500$ rpm and I_{dq} step = 5A.

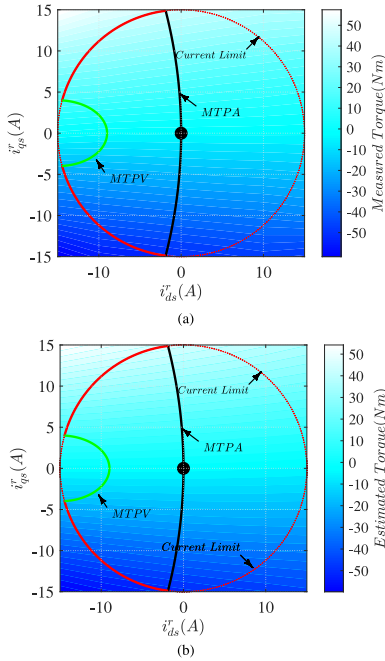


Fig. 12. SPMSM torque. (a) Measurement using a torque transducer. (b) Estimated using the proposed method. Dotted lines delimit constant torque regions. $n = 500$ rpm and I_{dq} step = 5A.

IV. EXPERIMENTAL RESULTS

As discussed in Fig. 1, Hall-effect sensors [30] are attached to the end shield of the IPMSM and SPMSM as shown in Fig. 7(a) and Fig. (b), respectively. The test machines are fed by an inverter, the switching frequency is set to 10 kHz. A torque transducer (T25 from Interface) of ± 100 Nm with a combined

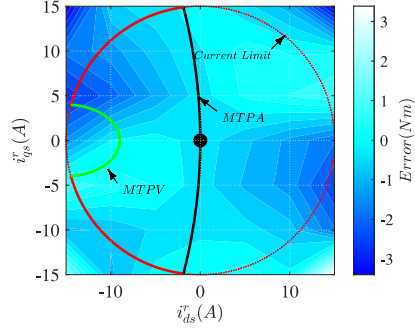


Fig. 13. SPMSM torque error. $n = 500$ rpm and i_{dq}^r step = 5A.

error (i.e., due to nonrepeatability and temperature) of $\pm 0.1\%$ is used for torque measurement in both cases. The machines are mechanically coupled to a motion-controlled PMSM that will operate as a load. These machines will be experimentally evaluated using the test benches shown in Fig. 7(c) and (d), their main design parameters being shown in Table II.

Conventional linear Hall-effect sensors typically used in commercial PMSMs will be used in this work [30]. Although practical implementation of the method proposed can be achieved using only radial and tangential flux, an arrangement of two sets of three flux sensors capable of measuring both tangential and radial leakage flux has been installed in the motor end-shields as shown in Fig. 7(a) and (b). Experimental results will be conducted at a constant rotational speed, n , of 500 rpm; experimental results at different speeds are not included because the flux measurement is speed independent [26]. Magnet temperature variation has not been included in the study because it has been extensively studied in [26]. As shown in [26], as the PM temperature raise, both PM flux linkage and PM leakage flux decrease. The proposed method will estimate a lower torque as the PM temperature increases according to (7) and [26], so estimated torque will not be affected.

A. Magnetic Flux Density Measurement

Figs. 8 and 9 show the variation of B_{ids}^r and B_{iqs}^r within the I_{dq} plane for the IPMSM and the SPMSM shown in Fig. 1, respectively. As expected, B_{ids}^r decreases when flux weakening current is applied (i.e., negative i_{ds}^r), whereas increases when flux intensifying current (i.e., positive i_{ds}^r) is applied. Figs. 8(a) and 9(a) also show a slight dependency of B_{ids}^r and i_{qs}^r , due to the cross coupling between the d - and q - axes. Figs. 8(b) and 9(b) show that B_{iqs}^r is highly dependent on i_{qs}^r in both machines, which was expected since B_{iqs}^r is mainly due to i_{qs}^r . B_{iqs}^r is slightly affected by d -axis flux due to cross coupling between axis as shown in Figs. 8(b) and 9(b).

B. Experimental Results for the IPMSM

The proposed torque estimation method is experimentally validated in the IPMSM shown in Figs. 1 and 7. For the experimental results shown in this section, the rotor speed is kept constant at 500 rpm and d - and q -axes currents are varied from -1 to 1 pu in steps of 0.33 pu. Under these conditions, torque is measured using the torque transducer and estimated using the Hall-effect signals (B_{Ha} , B_{Hb} , and B_{Hc}). Color map in Fig. 10(a) shows the measured torque on the I_{dq} plane; a discontinuous line shows the limit for the current complex vector, the figure also shows machine's MTPA and Maximum Torque Per Voltage (MTPV) trajectories.

Fig. 10(b) shows the estimated torque using (7) on the I_{dq} plane. Fig. 11 shows the absolute torque error, i.e., difference between Fig. 9(a) and (b). A maximum error of ± 3 Nm is observed, which is limited to -2.5 to 3.3 Nm in the second and third quadrants of the I_{dq} plane (i.e., machine can either operate as a motor or as a generator). In any case, estimation error is affected by both i_{ds}^r and i_{qs}^r . It can be observed that the absolute error increases as the operating point moves along the MTPA curve and reaches its maximum at high flux weakening levels. If second or fourth quadrant are considered, the absolute estimation error ± 3 Nm. Fig. 11 also shows that the estimation error is affected by both i_{ds}^r and i_{qs}^r currents.

C. Experimental Results for the SPMSM

The proposed torque estimation method is experimentally validated in an SPMSM equipped with the same Hall-effect sensors as the IPMSM and under the same working conditions. Fig. 12(a) shows the resulting measured torque on the I_{dq} plane using the torque transducer; a discontinuous line shows the limit for the current complex vector, the figure also shows machine's MTPA and MTPV trajectories. Fig. 12(b) shows the resulting estimated torque on the I_{dq} plane using (7). Fig. 13 shows the absolute torque error, the error varying from ± 3.2 Nm. Fig. 12 also shows that the maximum error was obtain when the machine is operating along the MTPA line (i.e., typical operating region of SPMSMs) is ± 0.5 Nm. The estimation error is barely affected by both i_{ds}^r and i_{qs}^r currents for the SPMSM.

D. Online Torque Estimation

The control block diagram shown in Fig. 6 is used for online torque estimation, which has been performed on the IPMSM shown in Fig. 1. Fig. 14 shows online torque estimation experimental results when Id current is set to zero and Iq varies with time. Fig. 14(a) shows the d and q -axis currents, the measured leakage flux densities, B_{Ha} , B_{Hb} , and B_{Hc} , are shown in Fig. 14(b), whereas the leakage flux complex vector components are shown in Fig. 14(c). The resulting measured and estimated torque based on (7) are shown in Fig. 14(d), with $k_q = 1.993$ and $k_d = 31.323$. These values have been set to minimize the peak error when the machine is being operated in the second quadrant of the I_{dq} plane, according to Fig. 4. The absolute estimation error is shown in Fig. 14(e), which is seen to be within ± 2 Nm. Fig. 14 (f) shows the relative error (8). As expected, the relative

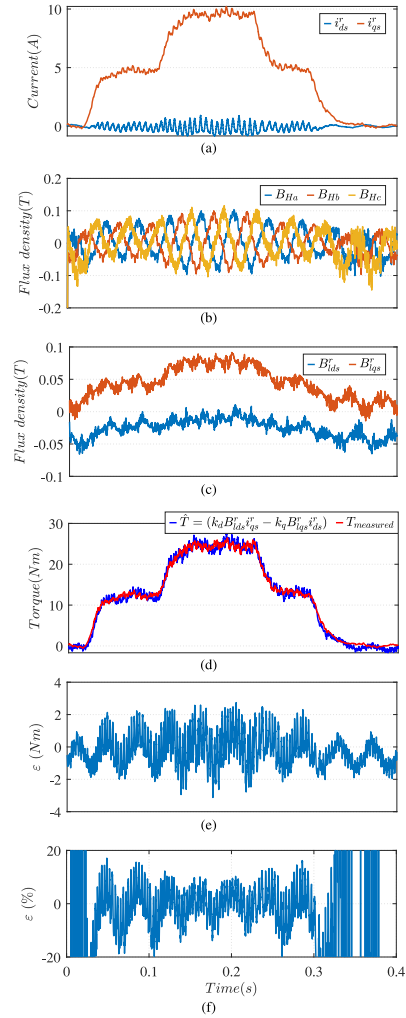


Fig. 14. Online torque estimation in an IPMSM for Iq current variation. (a) Current commands. (b) Measured flux signals. (c) Leakage flux complex vector components. (d) Measured and estimated torque. (e) Estimation error (absolute). (f) Estimation error (relative). $n = 500$ rpm.

error tends to infinity when the actual torque is zero. It can also be observed that when the actual torque is different from zero, the estimated error remains within $\pm 10\%$; according to Fig. 5, oscillations in Fig. 14 are due to assembling tolerances of the sensors in test bench.

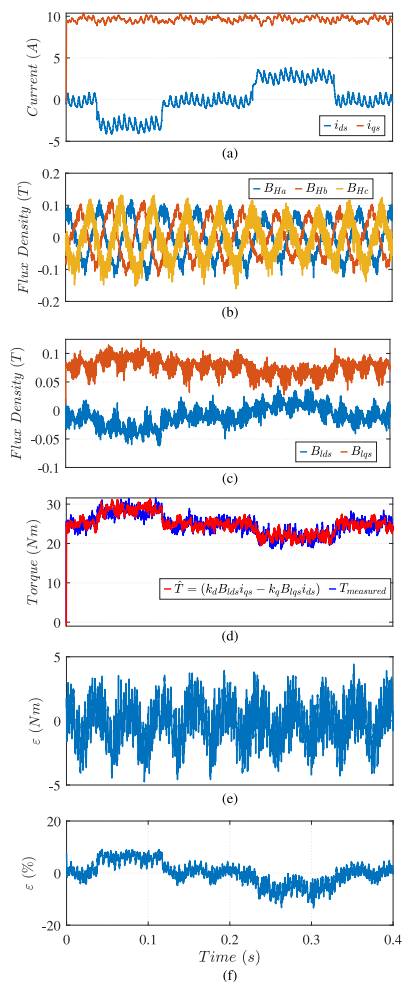


Fig. 15. Online torque estimation in an IPMSM for I_d current variation. (a) Current commands. (b) Measured flux signals. (c) Leakage flux complex vector components. (d) Measured and estimated torque based on (7) are shown in Fig. 15(d), with $k_q = 1.993$ and $k_d = 31.323$ as in Fig. 14. The absolute estimation error is shown in Fig. 15(e), and the relative estimation error is shown in Fig. 15(f).

Fig. 15 shows online torque estimation experimental results when I_q current is set to 10 A and I_d varies with time. Fig. 15(a) shows the d and q -axis currents, the measured leakage flux densities, B_{Ha} , B_{Hb} , and B_{Hc} , are shown in Fig. 15(b), whereas the leakage flux complex vector components are shown in Fig. 15(c). The resulting measured and estimated torque based on (7) are shown in Fig. 15(d), with $k_q = 1.993$ and $k_d = 31.323$ as in Fig. 14. The absolute estimation error is shown in Fig. 15(e),

which is seen to be within ± 3 Nm. Fig. 15(f) shows the relative error (8). It can be observed that the estimated error remains in the $\pm 10\%$ range. However, the average value is near zero, and according to Fig. 5, oscillations in Fig. 15 are due to assembling tolerances of the sensors in the machine.

V. CONCLUSION

Torque estimation in PMSMs using Hall-effect sensors has been analyzed in this work. The proposed method relies on the measurements provided by linear Hall-effect sensors typically used in commercial PMSM drives for motion control. The flux measured by the Hall-effect sensors is used to define a leakage flux complex vector, which is used for torque estimation purposes. Experimental results have been presented for a SPMSM and an IPMSM to demonstrate the viability of the proposed method.

ACKNOWLEDGMENT

The authors would like to thank BOMATEC for the support providing magnet samples.

REFERENCES

- [1] L. Tang, L. Zhong, M. F. Rahman, and Y. Hu, "A novel direct torque control for interior permanent-magnet synchronous machine drive with low ripple in torque and flux—a speed-sensorless approach," *IEEE Trans. Ind. Appl.*, vol. 39, no. 6, pp. 1748–1756, Nov./Dec. 2003, doi: [10.1109/TIA.2003.818981](https://doi.org/10.1109/TIA.2003.818981).
- [2] D. C. Hanselman, *Brushless Permanent Magnet Motor Design*. New York, NY, USA: McGraw-Hill, 1994.
- [3] C. Yu, T. Fukushige, N. Limsuwan, T. Kato, D. D. Reigosa, and R. D. Lorenz, "Variable-flux machine torque estimation and pulsating torque mitigation during magnetization state manipulation," *IEEE Trans. Ind. Appl.*, vol. 50, no. 5, pp. 3414–3422, Sep./Oct. 2014, doi: [10.1109/TIA.2014.2305768](https://doi.org/10.1109/TIA.2014.2305768).
- [4] F. Tinazzi and M. Zigliotto, "Torque estimation in high-efficiency IPM synchronous motor drives," *IEEE Trans. Energy Convers.*, vol. 30, no. 3, pp. 983–990, Sep. 2015, doi: [10.1109/TEC.2015.2408214](https://doi.org/10.1109/TEC.2015.2408214).
- [5] S. H. Kia, H. Henao, and G. Capolino, "Torsional vibration assessment using induction machine electromagnetic torque estimation," *IEEE Trans. Ind. Electron.*, vol. 57, no. 1, pp. 209–219, Jan. 2010, doi: [10.1109/TIE.2009.2034181](https://doi.org/10.1109/TIE.2009.2034181).
- [6] N. Amano, "Method of calculating engine torque," U.S. Patent 20030204302 A1, 2004.
- [7] B. Knauder *et al.*, "Electric torque vectoring for electric vehicles," *ATZ Elektron Worldwide*, vol. 9, pp. 50–55, 2014, doi: <https://doi.org/10.1365/s38314-014-0268-0>.
- [8] M. Boisvert and P. Micheau, "Estimators of wheel slip for electric vehicles using torque and encoder measurements," *Mech. Syst. Signal Process.*, vol. 76–77, pp. 665–676, 2016, doi: <https://doi.org/10.1016/j.ymssp.2016.02.017>.
- [9] H. Zhao, "Present situation and development review of torque measurement," *Appl. Mechanics Mater.*, vol. 422, pp. 141–145, 2013.
- [10] F. Umbach, H. Acker, J. Kluge, and W. Langheinrich, "Contactless measurement of torque," *Mechatronics*, vol. 12, pp. 1023–1033, 2002.
- [11] P. Sue, D. Wilson, L. Farr, and A. Kretschmar, "High precision torque measurement on a rotating load coupling for power generation operations," in *Proc. IEEE Int. Instrum. Meas. Technol. Conf.*, 2012, pp. 518–523, doi: [10.1109/I2MTC.2012.6229149](https://doi.org/10.1109/I2MTC.2012.6229149).
- [12] J. Delvaux and P. Sue, "High resolution torque measurement on a rotating shaft," U.S. Patent 6 795 779, 2004.
- [13] A. Niedworok, "Dynamic torque measurement of drive transmission in vehicles being in motion using strain gauges measurement technique and wireless data transmission," in *Proc. 16th Eur. Conf. Power Electron. Appl.*, 2014, pp. 1–8, doi: [10.1109/EPE.2014.6910707](https://doi.org/10.1109/EPE.2014.6910707).
- [14] K. C. Yeo, G. Heins, and F. De Boer, "Comparison of torque estimators for PMSM," in *Proc. Australas. Universities Power Eng. Conf.*, 2008, pp. 1–6.

- [15] B. Cheng and T. R. Tesch, "Torque feedforward control technique for permanent-magnet synchronous motors," *IEEE Trans. Ind. Electron.*, vol. 57, no. 3, pp. 969–974, Mar. 2010, doi: [10.1109/TIE.2009.2038951](https://doi.org/10.1109/TIE.2009.2038951).
- [16] T. Liu, I. Husain, and M. Elbuluk, "Torque ripple minimization with on-line parameter estimation using neural networks in permanent magnet synchronous motors," in *Proc. Conf. Rec. IEEE Ind. Appl. Conf. 33rd IAS Annu. Meeting*, 1998, pp. 35–40, doi: [10.1109/IAS.1998.732256](https://doi.org/10.1109/IAS.1998.732256).
- [17] X. Zhang and Z. Li, "Sliding-mode observer-based mechanical parameter estimation for permanent magnet synchronous motor," *IEEE Trans. Power Electron.*, vol. 31, no. 8, pp. 5732–5745, Aug. 2016.
- [18] Y. Feng, X. Yu, and F. Han, "High-order terminal sliding-mode observer for parameter estimation of a permanent-magnet synchronous motor," *IEEE Trans. Ind. Electron.*, vol. 60, no. 10, pp. 4272–4280, Oct. 2013.
- [19] W. Xu and R. D. Lorenz, "High-frequency injection-based stator flux linkage and torque estimation for db-dtc implementation on IPMSMs considering cross-saturation effects," *IEEE Trans. Ind. Appl.*, vol. 50, pp. 3805–3815, Nov. 2014.
- [20] M. Martinez, D. Reigosa, D. Fernandez, J. M. Guerrero, and F. Briz, "PMSMs torque estimation using pulsating HF current injection," in *IEEE 9th Int. Symp. Sensorless Control Elect. Drives*, Sep. 2018, pp. 96–101.
- [21] D. Reigosa, D. Fernandez, C. González, S. B. Lee, and F. Briz, "Permanent magnet synchronous machine drive control using analog hall-effect sensors," *IEEE Trans. Ind. Appl.*, vol. 54, no. 3, pp. 2358–2369, May/Jun. 2018, doi: [10.1109/TIA.2018.2802950](https://doi.org/10.1109/TIA.2018.2802950).
- [22] X. Song, J. Fang, and B. Han, "High-precision rotor position detection for high-speed surface PMSM drive based on linear hall-effect sensors," *IEEE Trans. Power Electron.*, vol. 31, no. 7, pp. 4720–4731, Jul. 2016, doi: [10.1109/TPEL.2015.2479642](https://doi.org/10.1109/TPEL.2015.2479642).
- [23] Q. Ni *et al.*, "A new position and speed estimation scheme for position control of PMSM drives using low-resolution position sensors," *IEEE Trans. Ind. Appl.*, vol. 55, no. 4, pp. 3747–3758, Jul./Aug. 2019, doi: [10.1109/TIA.2019.2904934](https://doi.org/10.1109/TIA.2019.2904934).
- [24] G. Liu, B. Chen, and X. Song, "High-precision speed and position estimation based on hall vector frequency tracking for PMSM with bipolar hall-effect sensors," *IEEE Sensors J.*, vol. 19, no. 6, pp. 2347–2355, Mar. 2019, doi: [10.1109/JSEN.2018.2885020](https://doi.org/10.1109/JSEN.2018.2885020).
- [25] Z. Yu, M. Qin, X. Chen, L. Meng, Q. Huang, and C. Fu, "Computationally efficient coordinate transformation for field-oriented control using phase shift of linear hall-effect sensor signals," *IEEE Trans. Ind. Electron.*, vol. 67, no. 5, pp. 3442–3451, May 2020, doi: [10.1109/TIE.2019.2922920](https://doi.org/10.1109/TIE.2019.2922920).
- [26] D. Fernandez *et al.*, "Permanent magnet temperature estimation in PM synchronous motors using low-cost hall effect sensors," *IEEE Trans. Ind. Appl.*, vol. 53, no. 5, pp. 4515–4525, Sep./Oct. 2017, doi: [10.1109/TIA.2017.2705580](https://doi.org/10.1109/TIA.2017.2705580).
- [27] Y. Park *et al.*, "Online detection and classification of rotor and load defects in PMSMs based on hall sensor measurements," *IEEE Trans. Ind. Appl.*, vol. 55, no. 4, pp. 3803–3812, Jul./Aug. 2019, doi: [10.1109/TIA.2019.2911252](https://doi.org/10.1109/TIA.2019.2911252).
- [28] L. Dong, Y. Huang, J. Jatskevich, and J. Liu, "Improved fault-tolerant control for brushless permanent magnet motor drives with defective hall sensors," *IEEE Trans. Energy Convers.*, vol. 31, no. 2, pp. 789–799, Jun. 2016, doi: [10.1109/TEC.2016.2526621](https://doi.org/10.1109/TEC.2016.2526621).
- [29] D. F. Alonso, Y. Kang, D. F. Laborda, M. M. Gómez, D. D. Reigosa, and F. Briz, "Permanent magnet synchronous machine torque estimation using low cost hall-effect sensors," in *Proc. IEEE 10th Int. Symp. Sensorless Control Elect. Drives*, 2019, pp. 1–6, doi: [10.1109/SLED.2019.8896292](https://doi.org/10.1109/SLED.2019.8896292).
- [30] A. Microsystems, "Linear hall-effect sensor ICs with analog output available in a miniature, low-profile surface-mount package," *A1308-0-DS*, Rev.11 datasheet, Feb. 2020.

B.1.3 Battery Internal Resistance Estimation Using a Battery Balancing System Based on Switched Capacitors

Battery Internal Resistance Estimation Using a Battery Balancing System Based on Switched Capacitors

Cristina Gonzalez Moral [✉], *Student Member, IEEE*, Diego Fernández Laborda [✉], *Student Member, IEEE*,
Lidia Sánchez Alonso, Juan Manuel Guerrero [✉], *Member, IEEE*, Daniel Fernandez [✉], *Member, IEEE*,
Carlos Rivas Pereda [✉], *Senior Member, IEEE*, and David Díaz Reigosa [✉], *Senior Member, IEEE*

Abstract—Battery management systems (BMSs) are key components in battery storage systems in order to guarantee their safe operation and improve their performance, reliability, and efficiency. BMSs monitor critical parameters in the battery as state of charge (SOC), state of health (SOH), or temperature. Direct measure of SOC or SOH is not possible, while temperature, on the other hand, can be measured with different types of sensors. These sensors, although cost-effective, raise concerns regarding cabling, signal conditioning and acquisition systems, increasing cost, complexity, and decreasing reliability. The internal resistor of the battery has already been successfully used to estimate these parameters. BMS can also include the function of balancing (equalizing) cells of a battery pack. Among all available equalizing systems, those based on switched capacitors are interesting due to their simplicity and easy scalability. This article proposes an internal resistance (IR) estimation method for LiFePO₄ batteries using signals naturally produced by a switched-capacitor equalizer (SCE). The IR will be used to estimate the battery temperature. It will be shown that the method can operate online and without interfering with the regular operation of the SCE.

Index Terms—Internal resistance (IR) estimation, LFP/LiFePO₄ batteries, switched-capacitor equalizer (SCE), temperature estimation.

I. INTRODUCTION

THE use of battery-based energy storage systems (ESS) has highly increased in the last decades [1]. They can be found

Manuscript received January 24, 2020; revised April 16, 2020 and June 1, 2020; accepted June 22, 2020. Date of publication June 29, 2020; date of current version September 18, 2020. Paper 2020-SECS-0079.R2, presented at 2019 IEEE ENERGY CONVERSION CONGRESS AND EXPOSITION (ECCE), Baltimore, MD USA, Sep. 29–Oct. 3, and approved for publication in the IEEE TRANSACTIONS ON INDUSTRY APPLICATIONS by the Renewable and Sustainable Energy Conversion Systems Committee of the IEEE Industry Application Society. This work was supported in part by the Research, Technological Development, and Innovation Programs of the Spanish Ministry Economy and Competitiveness, under Grant MINECO-17-ENE2016-80047-R, in part by the “Oviedo Siembra Talento” program of the Oviedo City Council, and in part by the Government of Asturias under project IDI/2018/000188 and FEDER funds. (*Corresponding author: Cristina Gonzalez Moral.*)

Cristina Gonzalez Moral and Carlos Rivas Pereda are with the Electrotécnica Industrial y Naval, S.L. (ELINSA), 15008 A Coruña, Spain (e-mail: cgonzalez@elinsa.org; crivas@elinsa.org).

Diego Fernández Laborda, Lidia Sánchez Alonso, Juan Manuel Guerrero, Daniel Fernandez, and David Díaz Reigosa are with the Department of Electrical Computer, and System Engineering, University of Oviedo, 33204 Gijón, Spain (e-mail: dflaborda@uniovi.es; uo250173@uniovi.es; guerrero@uniovi.es; fernandezalodaniel@uniovi.es; diazdavid@uniovi.es).

Color versions of one or more of the figures in this article are available online at <https://ieeexplore.ieee.org>.

Digital Object Identifier 10.1109/TIA.2020.3005382

in a broad range of applications, such as electric vehicles [2], smart grids [3], aerospace applications [4], and all kinds of small appliances applications as mobile devices [5].

There is a wide variety of rechargeable battery (secondary batteries) technologies that could be used for ESS, as nickel-cadmium (NiCd), Pb-acid, or lithium-ion (Li-ion). Among these, Li-ion batteries (LIBs) are one of the most appealing batteries for high-capacity ESS due to their high energy density, good temperature operation range, low self-discharge, high efficiency, and high cell voltage compared with NiCd or Pb-acid [5], [6].

Since the cell voltage and/or current in any of these cases is low compared with typical industrial requirements, battery packs are built stacking cells in series and/or parallel configurations [2], [6]. Manufacturing tolerances, temperature differences, cell distribution inside the pack (which affects the battery temperature), among other reasons, result in voltage imbalances among cells during normal pack operation. These imbalances accelerate the aging of cells and result in an increase of the internal battery resistance and a decrease in its capacity. Mismatches in voltage among cells also increase the internal battery temperature, decreasing, therefore, operation safety [7], [8]. Thermal behavior is also heavily affected by how the battery is employed in terms of current demand and sudden load changes [9]. Active materials in the LIBs can be potentially damaged in the case of overvoltage or undervoltage [10], [11]. For all these reasons, battery management systems (BMS) are needed to increase the overall safety of the system: monitor critical parameters as temperature, state of charge (SOC) or state of health (SOH) [3]–[13], control operational conditions and cell balancing, extend the life of the battery and ensure a safe range of operation for all the cells forming the pack [6], [12].

One of the main features of BMSs is the equalizing of cells, which allows us to maximize the energy extracted from the battery pack without compromising safety [11]. Among proposed equalizers in the literature, the SCEs [11], [14]–[18] are one of the most appealing techniques to equalize single cells due to its low cost and simplicity. They can be used to balance all kinds of battery chemistries, as Pb-acid or nickel-based [14] or LIBs [11], [17], [18]. Unlike other equalizers, SCEs can work effectively both during battery charging or discharging [7]. SCEs equalize cells in terms of voltage, which means that there will be energy

transfer between the cells while there is a voltage difference among them.

Another important feature of a BMS is battery temperature knowledge. Batteries' temperature can be directly measured using temperature sensors [19]. These sensors, although cheap, raise concerns regarding cabling, signal conditioning and acquisition systems, increasing cost, system complexity, and the number of elements susceptible to failure [20], [21]. As an alternative, the batteries' temperature can be estimated. Temperature estimation methods based on the dependency of a battery parameter with its temperature are the most popular [19]–[23]. On the other hand, since SOC and SOH cannot be directly measured, estimation methods must be implemented [12].

Several methods to estimate battery parameters can be found in the literature: the real part [19], [21], the imaginary part [20], the magnitude [21], and the phase shift [23] of the battery impedance being the most relevant. This kind of methods estimate the battery impedance from the battery terminal voltages and currents when the battery is being connected to a power converter that has the capability of injecting some high-frequency signal superimposed on top of the fundamental dc component, i.e., these methods work in an analogous way to the electrochemical impedance spectroscopy (EIS) analysis [20] but only for a single frequency.

This article, which is the extended version of the conference paper [1], proposes an online battery internal resistance (IR) [24] estimation method, i.e., during cell balancing, for SCEs. The IR of the battery is estimated using signals produced by the SCE regular operation; the IR will be used for cell temperature estimation, therefore this method cannot be directly compared to [19]–[23]. Nevertheless, and since battery packs can be connected to the rest of the system using a power converter, both estimation methods could be employed simultaneously, thus increasing the reliability of the temperature estimation. Besides, and as it will further explained in Section IV, once the cells are equalized, there is no voltage difference among them, nor equalization current, meaning that the IR can no longer be estimated with the proposed method. Due to this, combining the proposed method in this article with the ones proposed in [19]–[23], in those cases where a power converter is employed to connect the battery pack to the rest of the system, could be a way of expanding the cell temperature estimation. The current level and SOC could also affect the proposed method, this will be analyzed in Section IV.

The article is organized as follows: the basis of SCEs is presented in Section II; electrical modeling of batteries is discussed in Section III; the proposed method for battery IR estimation is presented in Section IV; simulations and experimental results are shown in Sections V and VI, respectively; conclusions are finally presented in Section VII.

II. SWITCHED-CAPACITOR EQUALIZER

This section presents a brief review of different equalizing methodologies, focusing on switched-capacitor equalizers (SCEs). Battery/cell equalizers extract energy from the most charged cell of a battery pack and either dissipate or transfer it to a less-charged cell. The first method is known as passive

balancing and the second as active balancing. Passive balancing is relatively inexpensive and easy to implement, although dissipating excessive energy makes it inefficient. Due to this, recent research efforts are focused on active balancing methods. Methods for active balancing can be classified according to different criteria, as the connections between the cells (cell-to-cell, pack-to-cell, cell-to-pack...) or according to the circuit topology (shunting, shuttling, or energy conversion methods) [7], [12]. Shunting methods transfer the energy from one cell to another without any external energy storage device, unlike shuttling methods that use external energy storage devices, e.g., capacitors, inductors, or other batteries. The so-called energy conversion methods [7] use isolated converters for equalizing the cells. This solution is the most expensive among them and often used to balance packs of cells, while the other two are more suitable to equalize single cells.

Among shuttling active balancing methods, one of the most appealing methods to equalize single cells is the switched capacitor equalizer [14], due to its low cost and simplicity. This cell-to-cell equalizer balances the voltage of N cells with $N-1$ capacitors and $2N$ switches, see Fig. 1(a). The switches continuously work during regular operation of the battery with a fixed duty cycle of 50% but the corresponding dead time to avoid shortcircuit, alternating ON/OFF states between switches "a" and "b." This results in a very easy system that can work without any control strategy: there will be energy transfer between the cells if there is a voltage difference among them. This can be seen in Fig. 1(b), where T_s is the switching period and dt is the dead time. This way, each capacitor is connected half of the switching period in parallel with one cell and the second half with an adjacent cell, transferring energy from the one with the highest voltage to the one with the lowest voltage. This is schematically shown in Fig. 1(c) assuming $VB_1 > VB_2 > VB_3$. In the state 1 (in red), B1 charges C_{12} and B2 charges C_{23} , i.e., they are connected in parallel, and in state 2 (blue), C_{12} discharges over B2 and C_{23} discharges over B3.

The main advantages of this equalizer are that it does not require control, it is fully scalable, cost-effective, and easy to implement. In addition, and unlike other methods, it can work effectively both in charge and discharge [7]. As a drawback, cells only transfer energy effectively to their adjacent ones, so the energy might need to flow through a large number of cells, which increases the losses and the equalization time [11]. Another drawback is that the equalization speed depends on the voltage difference, so the process becomes slower as the voltage difference decreases. Note that this equalizer may induce losses if the switching is maintained once the cells are voltage balanced. To avoid this, a voltage threshold to start and stop the equalization may be selected. Since SCEs can be used with different types of battery chemistry [14], the selection of this threshold will depend both on the application and the cells that are being balanced. For example, when equalizing lead-acid cells, the threshold can be higher than when equalizing LiFePO_4 , since the latter has a much flatter SOC-OCV curve [12]. This threshold will also be related to the resolution of the acquisition system, as will be explained in Section VI. It can be concluded that it is not straightforward to give a threshold figure valid for any battery chemistry/application.

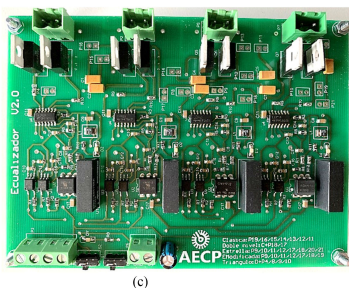
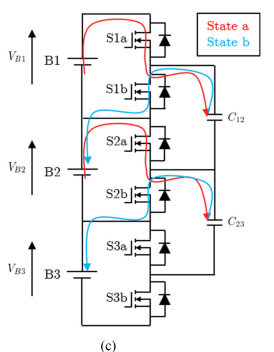
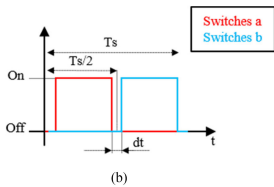
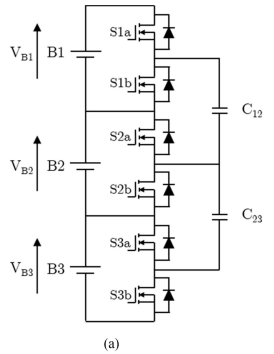


Fig. 1. Switched capacitor equalizer with three cells. (a) Schematic with three cells. (b) Switching function. (c) Paths for the energy at both switching states. (d) Prototype for balancing up to four cells.

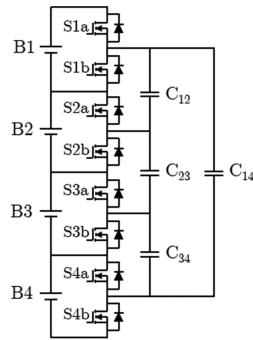


Fig. 2. Double-tiered SCE.

A prototype for an SCE to balance four cells is shown in Fig. 1(d). This prototype will be used for the experimental verification of the proposed battery IR estimation method.

The SCE from Fig. 1(a) can have large equalization time, especially if the capacity of the cells is high or they are extremely unbalanced. However, it is expected that this time is reduced if the SCE is permanently connected since it will not allow large unbalances among cells. To reduce this time, different SCE topologies have been proposed. These equalizers improve the equalization time at the price of increasing the number of components used or the loss of modularity. These alternative SCE topologies are briefly analyzed in the following paragraphs [11], [14]–[18].

A. SCE Topologies

- 1) Basic SCE [14]; Fig. 1. Explained earlier in this section.
- 2) Double-tiered SCE [11], [15], [16]; Fig. 2. An extra capacitor bridges the capacitors in the first row, so batteries have two paths to exchange charge, reducing the equalization time. As a drawback, there is a need for adding an extra capacitor to the system, which must withstand the combined voltage of all the capacitors, compromising the scalability of the topology.
- 3) Chain structure using additional switches or capacitors [11]; Fig. 3. Requires four additional switches compared to the double-tiered SCE, top and bottom cells become, therefore, adjacent, forcing them to exchange energy between them and their adjacent cells only, and not with all the cells in the pack as in the previous case. The scalability of this topology is compromised as in the previous case since the voltage that the new switches must withstand is the same as the whole battery pack.
- 4) Star-structured SCE [15]; Fig. 4 left. It requires one additional capacitor respect to the classic proposal and connects the capacitors in a star-structure that allows the interconnection of all the cells at the same time, which decreases the equalization time (making it independent of the initial imbalance status of the string) and efficiency. As a drawback, the scalability is

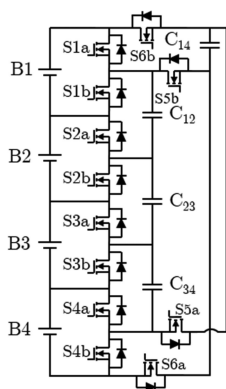


Fig. 3. Chain structure using additional switches or capacitors.

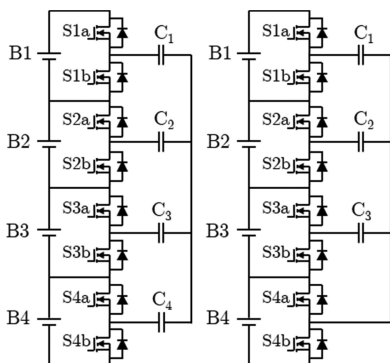


Fig. 4. Star-structured SCE (left) and star-structured SCE with one less capacitor (right).

again compromised because the voltage that each capacitor must withstand is different. A variation of this equalizer with one less capacitor can be seen in Fig. 4 right, [15], [17].

5) Delta-structured SCE [18]: Fig. 5. This equalizer adds capacitors in such a way that there is always one capacitor connecting any two cells, allowing the interconnection of all the cells at the same time. As the double-tiered SCE, it maintains the number of switches but increases the number of capacitors (in a higher number) while reducing the equalization time. The voltage that each capacitor must hold is different and dependent on the cells they are bridging.

A summary of the SCEs presented in this section is given in Table I, which shows a comparison among SCEs based on the number of switches and capacitors depending on the number of series-connected cells (N), if the equalization time varies with

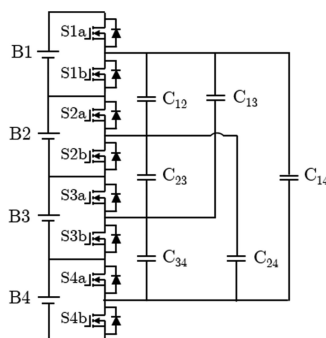


Fig. 5. Delta-structured SCE.

TABLE I
COMPARATIVE OF DIFFERENT SWITCHED-CAPACITOR METHODS

	Switches	Capacitors	Variable equalization time	Equal capacitors
SCE classic [14]	$2N$	$(N - 1)$	YES	YES
Double-tiered [11][15][16]	$2N$	$(N - 1) + 1$	YES	NO
Chain structure [11]	$2N+4$	$(N - 1) + 1$	YES	YES
Star-structure [15][17]	$2N$	N or $(N - 1)$	NO	NO
Delta-structure [18]	$2N$	$\sum_{i=1}^{i=N-1} (N - i)$	NO	NO

a change in the position of the cells and if the capacitors can be all equal or not depending on the voltage that they should withstand.

The previous discussion considered only balancing systems based on switched capacitors. They all have, in common, the same working principle, being cost-effective solutions easy to implement, thanks to the absence of control. The main difference among them is the number of components and their connection, which changes the equalization time. There are more complex systems based on the same principle that combine inductors and capacitors to improve the performance in terms of speed and losses, such as achieving zero-current switching [25]. However, the increased difficulty in the design and number of components makes them impractical for low-cost applications.

III. ELECTRICAL EQUIVALENT BATTERY MODEL

There are several ways of modeling the battery behavior: electrochemically (complex and difficult to obtain), mathematically (abstract and application-focused), and electrically (electrical equivalent models based on a combination of electrical passive

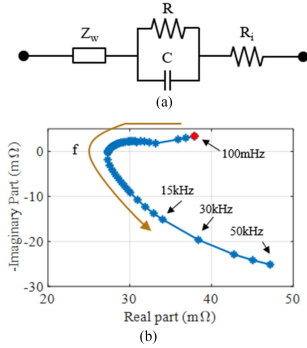


Fig. 6. Randles equivalent model derived from the EIS analysis. (a) Circuit. (b) Nyquist plot.

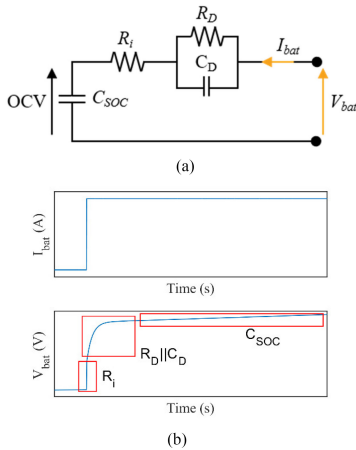


Fig. 7. (a) Thèvenin equivalent model of a battery. (b) Response of a battery to a current step.

elements). The latter are the most appealing due to their intuitiveness and computational burden [9], [26]. Among electrical models, the Randles [20], [26]–[28], see Fig. 6, and the Thèvenin [9], [26], [29], [30], see Fig. 7, models are the most commonly used.

The Randles model [Fig. 6(a)] is obtained from the EIS, a standard methodology for battery characterization. It consists of applying ac voltage to the battery and measures the resulting current to estimate the impedance at different frequencies [Fig. 6(b)] [27], [28]. Each range of frequencies is dominated by different phenomena in the battery [diffusion effect, solid-electrolyte interface (SEI) resistance, metal collectors, etc.] [20].

TABLE II
BATTERY MODEL PARAMETERS

Parameter	Value	Parameter	Value
R_i	50 mΩ	C_{SOC}	19 kF
R_D	6.7 mΩ	C_{EQ}	22 μF
C_D	48F		

In Fig. 6(a), Z_w represents the Warburg impedance, which accounts for the diffusion phenomena (low frequencies). The RC circuit corresponds to the electrolyte and SEI resistance on the anode. Finally, R_i is the IR, point in Fig. 6(b) when the battery impedance changes from capacitive to inductive [20], [27]. Fig. 6(b) shows the EIS analysis (Nyquist plot) of the LiFePO₄ cell used in this article; the x-axis represents the resistance and the y-axis represents the reactance (sign reversed), while each point in the graph corresponds to a different frequency. The frequency increases following the arrow direction where the red point indicates the smallest analyzed frequency.

On the other hand, the Thèvenin model, see Fig. 7(a), can be obtained from the battery response to a current step; parameter identification is obtained from the voltage transient response, see Fig. 7(b) [29]. In Fig. 7(b), R_i is the cell IR, accounting for the resistance of the contacts, terminals, collectors, electrodes, and electrolyte, while R_D and C_D model the dynamic response, resulting from the effect of diffusion and charge transportation. Finally, C_{SOC} models the battery capacity, C_{SOC} voltage representing the battery open-circuit voltage (OCV) [26], [30].

The transfer function of this model is shown in (1). The first term on the right-hand side of (1) corresponds to the IR, R_i , and is obtained from the initial response to the current step, see Fig. 7(b). The second term on the right-hand side of (1) is the dynamic RC circuit, a first-order system corresponding to the exponential part of the voltage variation, see Fig. 7(b). The last term on the right-hand side of (1) is C_{SOC} , a pole at the origin, which accounts for the continuously increasing slope in the voltage in Fig. 7(b) due to a constant current.

$$G(s) = \frac{V_{bat}(s)}{I_{bat}(s)} = R_i + \frac{R_D}{1 + R_D C_D s} + \frac{1}{s} C_{SOC} \quad (1)$$

Among these models, the Thèvenin one is the most appropriate for battery parameter identification using an SC equalizer, since the process for extracting the parameters involved in (1) (i.e., step response) is similar to the steps produced in the battery as a result of the SC switching.

IV. BATTERY PARAMETER IDENTIFICATION BASED ON SC EQUALIZERS

This section presents the proposed method for battery IR estimation using signals produced by the SCE operation. A simplified scheme of an SCE is presented in Fig. 8(a), where the battery and SCE parameters are shown in Table II. The circuit is connected at the instant t_i , and the waveforms resulting from this connection are shown in Fig. 8(b), which resemble SCE waveforms. Note that applying an impulse in the voltage is

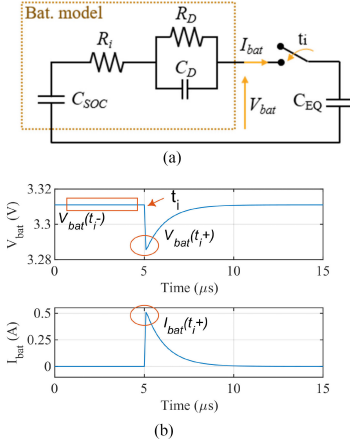


Fig. 8. (a) Simplification of the SCE, modeling the battery as a first-order Thévenin model. (b) Resulting voltage and current waveforms.

analogous to applying an impulse in the current from the point of view of battery parameter estimation [29].

Before the switch connection, there is no current circulation, so the voltage measured [V_{bat} in Fig. 8(a)] is the OCV (the voltage in the capacitor C_{SOC}). After the switch connection, there is a current flowing from/to the battery and consequently a voltage drop in the battery IR, R_i , exists. Therefore, R_i can be obtained from (2). $V_{bat}(t_i+)$ and $I_{bat}(t_i+)$ are the voltage and current right after the connection instant (t_i), see Fig. 8(b), while $V_{bat}(t_i-)$ is the OCV [see Fig. 8(b)].

$$R_i = \frac{|V_{bat}(t_i-) - V_{bat}(t_i+)|}{|I_{bat}(t_i+)|} \quad (2)$$

When using this SCE, two different currents may be superimposed, the current through the series-connected cells due to the charge/discharge of the battery and the transient current due to the switching of the SCE. The first current, which will be dc, can be controlled provided that the battery is connected to a power converter. The second current cannot be controlled since it depends on the voltage difference between the cells been equalized. As seen in [21], the current level may affect slightly the IR estimation. This effect can be compensated using an analogous procedure as shown in [21], using a look-up table to decouple the current level effect on the estimation.

The IR measured in batteries can change depending on the frequency of the signal used for measurement. The IR measured using the proposed procedure is a high-frequency resistance since the transient response of the battery is used for the estimation. At high frequencies, the IR is dominated by the leads and metal collectors of the battery [30]. Due to this, SOC is not expected to affect the estimation, since it does not affect the high-frequency impedance on LIBs [21], [23].

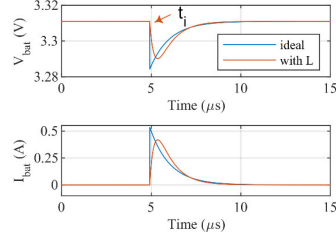


Fig. 9. Resulting waveform from the simplified circuit in Fig. 8(a) comparing the ideal case (blue waveforms) with the case with a series inductor (orange waveforms).

SCEs can effectively work both during the charge and discharge of the cell [7]. In case the battery is being charged or discharged, the method is similarly applied with the exception of the current in Fig. 8(b) will include this charging/discharging current. In this case, a more general equation, (3) should be used. $I_{bat}(t_i)$ is the current before the commutation, in this case, the current been charging/discharging the battery. The absolute value allows, as in (2), the equation to be used for both charging and discharging. The results remain unchanged.

$$R_i = \frac{|V_{bat}(t_i-) - V_{bat}(t_i+)|}{|I_{bat}(t_i+) - I_{bat}(t_i-)|} \quad (3)$$

The limitations of the method can be extracted directly from (3): once the batteries are equalized, there is no voltage difference among them, nor equalization current, meaning that R_i cannot be estimated this way. The SCE used in this article (see Fig. 1) equalizes based on voltage differences among cells, however, LiFePO₄ cells can have a rather flat OCV-SOC curve [12], so it may not achieve a perfect balance in terms of SOC. This is a limitation of the SCE employed in this article. Nevertheless, this SCE can be used with any LIB technology with less flatness OCV-SOC [12]. Besides, and as stated in the introduction, this method can be combined with signal-injection based battery resistance estimation methods to estimate temperature. This would increase the reliability of the estimation, allowing to estimate the desired parameters even when the method proposed in this article cannot be employed.

A. Effect of Inductive Parasitic Components

As will be seen in Section V, the circuitry has some unavoidable parasitic inductances due to, e.g., cabling that affect the waveforms shown in Fig. 8(b). This effect can be simulated by adding a small inductor (an inductor of 0.1 nH has been used to emulate this effect) in series with C_{EQ} in Fig. 8(a). The resulting waveforms are shown in Fig. 9. The orange waveform represents the response of the battery's voltage and current when the inductor is added to the circuit, in comparison with the blue waveforms that show the ideal case.

Since V_{bat} is measured at the battery terminals, the existence of this parasitic inductor does not affect the estimation of the IR.

Any combination of voltage and current from the graph would result in the IR estimation. However, peak values are preferred since they provide a high signal-to-noise ratio. Equation (3) can be rewritten as (4), where V_{batpeak} and I_{batpeak} correspond to the peak values for current and voltage, respectively, right after t_i .

V_{batpeak} and I_{batpeak} can be obtained from the derivatives of V_{bat} and I_{bat} , respectively, which can be approximated by (5) using the Euler approximation, where X_{bat} represents either the current or the voltage, X'_{bat} represents either the discrete-time derivative of the current or the voltage, k represents the current time instant, and T_s is the sampling time. V_{batpeak} and I_{batpeak} are theoretically acquired when X_{bat} is zero; in practice, when there is a change in the sign of X'_{bat} .

$$R_i = \frac{|V_{\text{bat}}(t_i) - V_{\text{batpeak}}|}{|I_{\text{batpeak}} - I_{\text{bat}}(t_i)|} \quad (4)$$

$$X'_{\text{bat}} = \frac{X_{\text{bat}}(k) - X_{\text{bat}}(k-1)}{T_s} \quad (5)$$

B. Battery Temperature Estimation

It is generally expected [13], [20], [23] that the battery resistance decreases as temperature increases at low frequencies. In this region, the electrolyte and SEI dominate the behavior of the battery and follows the Arrhenius law [20]. However, it must be noted that the proposed method estimates the IR, R_i in Fig. 8, which is dominated by the metal collectors and leads [30], which resistances increase as the temperature does [13], [23]. Hence, IR can be modeled as a linear function of the battery temperature (6), provided that the metallic part of the battery dominates the response. $R_{\text{bat}0}$ is the battery resistance (R_i) at the room temperature (T_o), T_{bat} is the battery temperature and α_{bat} is the temperature coefficient; $R_{\text{bat}0}$ and α_{bat} can be measured during a commissioning process. The battery temperature is finally estimated from (7).

It is finally noted that although the method proposed in this article is evaluated for the classical topology, see Fig. 1(a), it can be extended to any other switched-capacitor topology, see Section II-A.

$$R_{\text{bat}} = R_{\text{bat}0}(1 + \alpha_{\text{bat}}(T_{\text{bat}} - T_o)) \quad (6)$$

$$T_{\text{bat}} = \frac{R_{\text{bat}} - R_{\text{bat}0}}{R_{\text{bat}0}\alpha_{\text{bat}}} + T_o \quad (7)$$

V. SIMULATIONS

An SCE with two cells was implemented in MATLAB/Simulink, see Fig. 10.

The equalizer main parameters are shown in Table III. Cells are implemented using the battery model from Simscape Electrical toolbox, with LiFePO₄ battery equivalent parameters. A 30% difference in SOC between cells is set as the initial condition: the most charged battery has an OCV of 3.312 V and the less charged one has an OCV of 3.284 V.

Fig. 11(a) shows the voltage and current of the most charged cell (B1 in Fig. 10) when it is connected in parallel to the balancing capacitor at $t = 5 \mu\text{s}$. Voltage and current waveforms

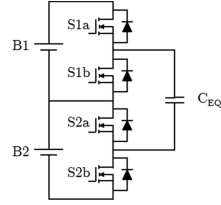


Fig. 10. SCE with two batteries and one capacitor.

TABLE III
EQUALIZER AND BATTERY CHARACTERISTIC PARAMETERS

Parameter	Value
Nominal battery voltage	3.2 V
Nominal current	3.2 A
Maximum charge current	1C
Maximum discharge current	3C
Battery capacity	3200 mAh
Equalizer capacitor	22 μF
IR (R_i)	50 m Ω

are seen to be in good agreement with the ones obtained with the Thèvenin model, see Fig. 8(b). The estimated IR (2) is $\approx 50 \text{ m}\Omega$, which matches R_i defined in Table III and included in the cell model for the simulation. The same results are obtained if the parasitic inductor is added in series with C_{eq} [Fig. 11(b)], as it was explained in Section IV-A.

Simulation results with more than two cells have also been carried out. A simulation scenario with three cells (ideal case), see Fig. 1(a), has been used, voltage and current are measured for B2, since this cell will share energy with both the upper (B1) and lower (B3) cells. SOCs of B1, B2, and B3 are 80%, 50% and 20% respectively. The resulting waveforms for a switching cycle (voltage and current) can be seen in Fig. 12.

As expected, in the first half of the switching cycle B2 charges the bottom capacitor (C_{23}) since its voltage is higher than the one from B3. In the second half of the switching cycle, B2 receives energy from the upper capacitor (C_{12}), since B1 has a higher voltage than B2. The cell IR can be calculated from any of these two transient responses with identical results. Different SOCs and arrangement of the cells would not interfere with the method either.

VI. EXPERIMENTAL RESULTS

The SCE shown in Fig. 1(c) was used to carry out the experimental results. A two-cell arrangement has been used to be consistent with the simulation results shown in Section V. Current and voltage waveforms were measured with a Yokogawa 701932 current probe and with a Yokogawa 701938 voltage probe, respectively. Signals were captured with a Yokogawa 720250 12-bit 2-channel module plugged into a Yokogawa DL850 ScopeCoder. Parameters of the cell and SCE are shown in Table II.

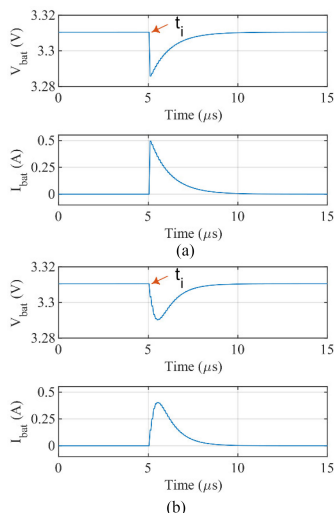


Fig. 11. Resulting waveform from the equalizer. (a) Simulink, ideal case. (b) Simulink, case with the parasitic inductor ($f_s = 20$ kHz, SOC differences = 30%).

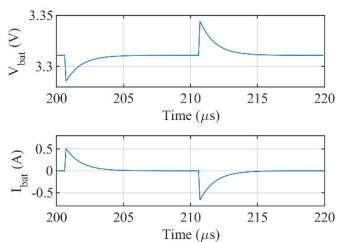


Fig. 12. Voltage and current in one cycle for B2 cell in an SCE with three series-connected cells [see Fig. 1(a)].

In addition to the parameters shown in Table III, the equivalent series resistance of the equalization capacitor is 0.7Ω [31]. This resistance will affect several aspects of the system: 1) it affects the equalization time and the efficiency of the equalization [11]; 2) it will affect the sensitivity of the method, i.e., the bigger this resistance, the smaller will be the current peak and the highest the accuracy needed in the measurement system. It is also noted that the ON resistance of the MOSFETs will affect in a similar way; the ON resistance of the selected MOSFET is $2.4 \text{ m}\Omega$ [32]. In general, when designing an SCE, and since they are intended for low-cost applications, a good compromise among parasitic resistances, the overall performance of the components and cost must be achieved.

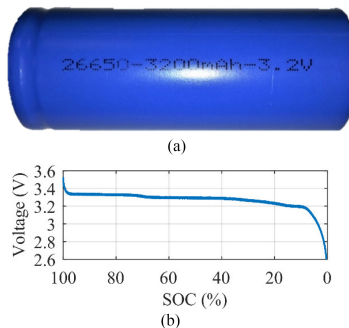


Fig. 13. (a) LiFePO₄ cell and (b) OCV-SOC curve of the cell.

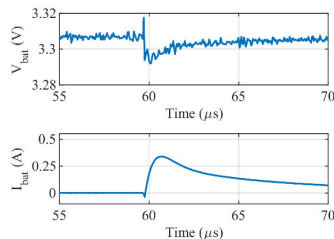


Fig. 14. Experimental results ($f_s = 20$ kHz, $T = 20$ °C, SOC differences = 30%).

The LiFePO₄ cell used in this article is shown in Fig. 13(a). Voltage measurement is performed at cell terminals. Cell voltage and current in one switching cycle are shown in Fig. 14. It can be seen that the current has a smoother response than in the ideal simulation [Fig. 11(a)], and similar to Fig. 11(b), due to inductive parasitic components present in the actual system, as it was previously explained in Section IV-A, hence (4) is used to estimate the IR.

The OCV-SOC curve of LiFePO₄ batteries is rather flat [see Fig. 13(b)] [12], meaning that the accuracy of the measurement system should be carefully analyzed. As stated in [12], a good target for SOC and IR estimation in these batteries would be in the range of 1–2 mV. The least significant bit (LSB) indicates the resolution of an acquisition system and is the result of dividing the full-scale range of the acquisition system by the number of discrete values obtained with n bits (8) [33]. With a 12-bits resolution acquisition system, which is a common resolution in digital processors nowadays (e.g., DSPs), the LSB would be < 1 mV, which is in the recommended range in [12].

$$\text{LSB} = \frac{\text{FSR}}{2^n} \quad (8)$$

Besides, the method does not work when the cells are equalized within the LSB limit, see Section IV. The LSB would be,

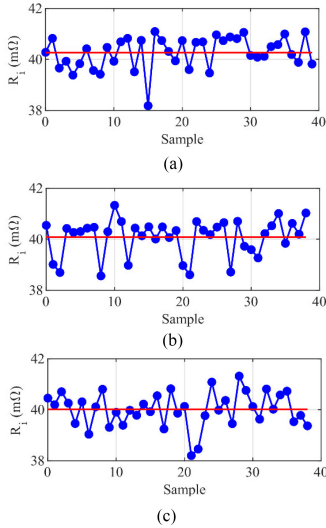


Fig. 15. Cell 1 IR estimation using the experimental data collected from the equalizer (blue) and mean value of the estimated resistance (red). (a) 10 kHz. (b) 20 kHz. (c) 30 kHz.

then, the minimum threshold below where the proposed method would not work. In practice, this value will increase due to unavoidable noise in the real signals, as can be appreciated in Fig. 14. This methodology could be used with any LIB chemistries (not only in LiFePO_4 batteries which have the flattest profile among LIBs) [14]. It is finally noted that the voltage variation is expected to be always smaller than the current variation, so the current variation will not be a problem before the voltage variation is.

A. Resistance Variation With Switching Frequency

Switching frequency in an SCE can be optimized for a given capacity of the equalizing capacitors [34], in such a way that the capacitor can be fully charged/discharged during its switching cycle without staying charged/discharged for long before the next commutation. The maximum equalization frequency is related to the driver (driving the MOSFETs). In addition, increasing the switching frequency allows for a capacitor size reduction, but it also increases the switching losses in the MOSFETs, thus reducing the efficiency. In the case of the setup used in this article [see Fig. 1(d)], the maximum switching frequency is ≈ 50 kHz.

Fig. 15 shows the estimated cell resistance for a set of experimental data captured with the SCE working at 10, 20, and 30 kHz; the mean value of the estimated cell resistance is shown in red.

The mean value at all the frequencies of the estimated resistances shown in Fig. 15 is similar at all the frequencies since

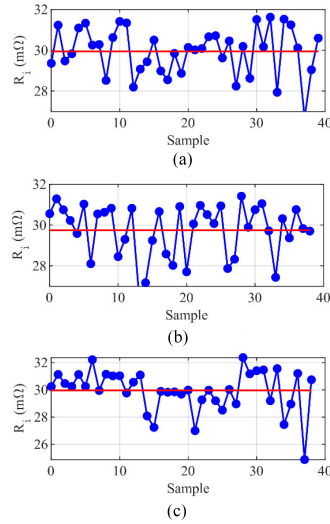


Fig. 16. Cell 2 IR estimation using the experimental data collected from the equalizer (blue) and mean value of the estimated resistance (red). (a) 10 kHz. (b) 20 kHz. (c) 30 kHz.

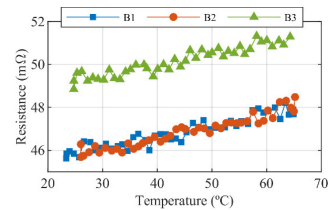


Fig. 17. Cell resistance versus cell temperature for different cells.

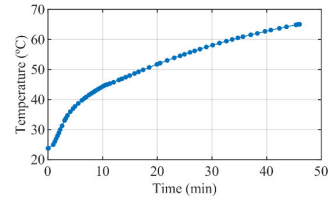


Fig. 18. Temperature evolution of the cell with time.

the resistance being estimated is R_i , which depends on the voltage/current at the switching instant, which is independent of the SCE switching frequency. It is also noted that SOC, SOH, or temperature-time constants are significantly larger than battery resistance estimation time [35], meaning that averaging

TABLE IV
THERMAL COEFFICIENTS FOR THE DIFFERENT CELLS EVALUATED

Cell	Thermal coefficient α_{bat} (1/°C)
1 (blue in Fig. 19)	0.057
2 (orange in Fig. 19)	0.0626
3 (green in Fig. 19)	0.0601
Average	0.0598

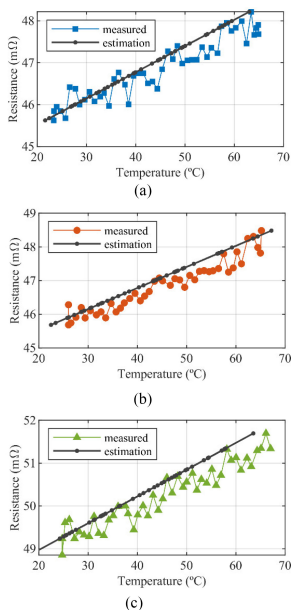


Fig. 19. Measured and estimated temperatures for three different cells. (a)–(c) B1–B3.

the measurements for a certain period could be an acceptable and easy solution to reject measurement noise. Experimental results are repeated with another cell (see Fig. 16) with the same characteristics, to show the replicability of the methodology. It is shown that the R_i mean value is independent of the switching frequency. However, the absolute value of R_i is different: for the first cell the mean value of R_i is ≈ 40 m Ω , while for the second one is ≈ 30 m Ω . This was expected due to differences among cells existing in practice [7], [8].

B. Resistance Variation With Temperature

Fig. 17 shows the estimated IR for three different cells as the temperature increases. The cells are slowly heated (for around 45 min, see Fig. 18) up to 65 °C while capturing current, voltage, and temperature. The temperature of the cells is monitored using LM35 temperature sensors [36], placed on the surface of the cell.

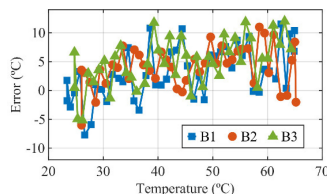


Fig. 20. Error between measured and estimated temperature.

It can be observed from Fig. 17 how the cell resistance increases almost linearly with temperature for all tested cells.

It can be observed from Fig. 17 that, although there is an offset among IRs, the rate of variation of IR with temperature is similar for all cells under test. Offsets present among cells will not affect the accuracy of the proposed method because the cell temperature will be estimated from variations of the resistance with temperature respect to the room temperature resistance (R_{bat0}) as seen in (7).

Fig. 19 shows the measured and estimated temperature using (7). First, the slope that best fits the temperature variation for each of the three cells was obtained (see Table IV), then, the average value of this slope ($\alpha_{bat} = 16.72$ 1/°C) is used to estimate the temperature for all cells under test. The temperature estimation error for the three cells analyzed is shown in Fig. 20; the temperature estimation error is seen to be less than ≈ 12 °C for any point, with a mean value of 4 °C and a standard deviation of 4.11 °C. Due to this difference, it is important to analyze more than one point every time, as seen in Figs. 15 and 16, so the conclusions in terms of temperature are valid.

VII. CONCLUSION

This article proposes the use of signals naturally produced by SCEs to estimate the battery IR. The method operates without interfering with the regular operation of both the equalizer and battery and is valid for a wide range of switching frequencies. The IR estimate can be used to obtain the battery's temperature. However, its main limitation is that once the cells are equalized the IR cannot be estimated. Experimental results have been provided to demonstrate the viability of the proposed method.

ACKNOWLEDGMENT

The authors wish to acknowledge the support and motivation provided by the University of Oviedo, Spain, and Electrotécnica Industrial y Naval, S.L. (ELINSA), Spain.

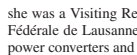
REFERENCES

- [1] C. G. Moral *et al.*, "Battery internal resistance estimation using a battery balancing system based on switched capacitors," in *Proc. IEEE Energy Convers. Congr. Expo.*, Sep. 2019, pp. 2516–2522.
- [2] D. Anseán, M. González, V. M. García, J. C. Viera, J. C. Antón, and C. Blanco, "Evaluation of LiFePO₄ batteries for electric vehicle applications," *IEEE Trans. Ind. Appl.*, vol. 51, no. 2, pp. 1855–1863, Mar./Apr. 2015.

- [3] Z. Miao, L. Xu, V. R. Disfani, and L. Fan, "An SOC-based battery management system for microgrids," *IEEE Trans. Smart Grid*, vol. 5, no. 2, pp. 966–973, Mar. 2014.
- [4] J. P. Fellner, G. J. Loeber, S. P. Vukson, and C. A. Riepenhoff, "Lithium-ion testing for spacecraft applications," *J. Power Sources*, vol. 119–121, pp. 911–913, Jun. 2003.
- [5] G. Pistoia, *In Battery Operated Devices and Systems*. Amsterdam, The Netherlands: Elsevier, 2009.
- [6] E. Chemali, M. Preindl, P. Malysz, and A. Emadi, "Electrochemical and electrostatic energy storage and management systems for electric drive vehicles: state-of-the-art review and future trends," *IEEE J. Emerg. Sel. Topics Power Electron.*, vol. 4, no. 3, pp. 1117–1134, Sep. 2016.
- [7] J. Cao, N. Schofield, and A. Emadi, "Battery balancing methods: A comprehensive review," in *Proc. IEEE Veh. Power Propulsion Conf.*, Sep. 2008, pp. 1–6.
- [8] W. F. Bentley, "Cell balancing considerations for lithium-ion battery systems," in *Proc. 12th Annu. Battery Conf. Appl. Adv.*, 1997, pp. 223–226.
- [9] Z. Yang, D. Patil, and B. Fahimi, "Electrothermal modeling of lithium-ion batteries for electric vehicles," *IEEE Trans. Veh. Technol.*, vol. 68, no. 1, pp. 170–179, Jan. 2019.
- [10] S. W. Moore and P. J. Schneider, "A review of cell equalization methods for lithium ion and lithium polymer battery systems," SAE Tech. Paper 2001-01-0959, Mar. 2001.
- [11] M. Kim, C. Kim, J. Kim, and G. Moon, "A Chain structure of switched capacitor for improved cell balancing speed of Lithium-Ion batteries," *IEEE Trans. Ind. Electron.*, vol. 61, no. 8, pp. 3989–3999, Aug. 2014.
- [12] H. Rahimi-Eichi, U. Ojha, F. Baronti, and M. Chow, "Battery management system: An overview of its application in the smart grid and electric vehicles," *IEEE Ind. Electron. Mag.*, vol. 7, no. 2, pp. 4–16, Jun. 2013.
- [13] A. E. Mejdoubi, H. Gualous, H. Chaoui, and G. Alcicek, "Experimental investigation of calendar aging of lithium-ion batteries for vehicular applications," in *Proc. 5th Int. Electromagn. Compatib. Conf.*, Sep. 2017, pp. 1–5.
- [14] C. Pascual and P. T. Krein, "Switched capacitor system for automatic series battery equalization," *Proc. IEEE Appl. Power Electron. Conf.*, Feb. 1997, pp. 848–854.
- [15] Y. Ye, K. W. E. Cheng, Y. C. Fong, X. Xue, and J. Lin, "Topology, modeling, and design of switched-capacitor-based cell balancing systems and their balancing exploration," *IEEE Trans. Power Electron.*, vol. 32, no. 6, pp. 4444–4454, Jun. 2017.
- [16] A. C. Baughman and M. Ferdowsi, "Double-tiered switched-capacitor battery charge equalization technique," *IEEE Trans. Ind. Electron.*, vol. 55, no. 6, pp. 2277–2285, Jun. 2008.
- [17] Y. Shang, N. Cui, B. Duan, and C. Zhang, "Analysis and optimization of star-structured switched-capacitor equalizers for series-connected battery strings," *IEEE Trans. Power Electron.*, vol. 33, no. 11, pp. 9631–9646, Nov. 2018.
- [18] Y. Shang, C. Zhang, N. Cui, and C. C. Mi, "A delta-structured switched-capacitor equalizer for series-connected battery strings," *IEEE Trans. Power Electron.*, vol. 34, no. 1, pp. 452–461, Jan. 2019.
- [19] R. R. Richardson, P. T. Ireland, and D. A. Howey, "Battery internal temperature estimation by combined impedance and surface temperature measurement," *J. Power Sources*, vol. 265, pp. 254–261, Nov. 2014.
- [20] N. S. Spinner, C. T. Love, S. L. Rose-Pehrsson, and S. G. Tuttle, "Expanding the operational limits of the single-point impedance diagnostic for internal temperature monitoring of lithium-ion batteries," *Electrochimica Acta*, vol. 174, pp. 488–493, Aug. 2015.
- [21] C. Gonzalez Moral, D. Fernandez, J. M. Guerrero, D. Reigosa, C. Rivas, and F. Briz, "Thermal monitoring of LiFePO₄ batteries using switching harmonics," *IEEE Trans. Ind. Appl.*, to be published, doi: 10.1109/TIA.2020.2988425.
- [22] J. G. Zhu, Z. C. Sun, X. Z. Wei, and H. F. Dai, "A new lithium-ion battery internal temperature on-line estimate method based on electrochemical impedance spectroscopy measurement," *J. Power Sources*, vol. 274, pp. 990–1004, Jan. 2015.
- [23] J. P. Schmidt, S. Arnold, A. Loges, D. Werner, T. Wetzel, and E. Ivers-Tiffée, "Measurement of the internal cell temperature via impedance: Evaluation and application of a new method," *J. Power Sources*, vol. 243, pp. 110–117, Dec. 2013.
- [24] D. Ansean, M. Gonzalez, J. C. Viera, V. M. Garcia, J. C. Alvarez, and C. Blanco, "Electric vehicle Li-Ion battery evaluation based on internal resistance analysis," in *Proc. IEEE Veh. Power Propulsion Conf.*, Oct. 2014, pp. 1–6.
- [25] Y. Yuanmao, K. W. E. Cheng, and Y. P. B. Yeung, "Zero-current switching switched-capacitor zero-voltage-gap automatic equalization system for series battery string," *IEEE Trans. Power Electron.*, vol. 27, no. 7, pp. 3234–3242, Jul. 2012.
- [26] Min Chen and G. A. Rincon-Mora, "An accurate electrical battery model capable of predicting runtime and I-V performance," *IEEE Trans. Energy Convers.*, vol. 21, no. 2, pp. 504–511, Jun. 2006.
- [27] B. Pattipati, C. Sankavaram, and K. Pattipati, "System identification and estimation framework for pivotal automotive battery management system characteristics," *IEEE Trans. Syst., Man, Cybern., Part C Appl. Rev.*, vol. 41, no. 6, pp. 869–884, Nov. 2011.
- [28] S. Buller, M. Thele, E. Karden, and R. W. D. Doncker, "Impedance-based non-linear dynamic battery modeling for automotive applications," *J. Power Sources*, vol. 113, no. 2, pp. 422–430, Jan. 2003.
- [29] B. Schweighofer, K. M. Raab, and G. Brasseur, "Modeling of high power automotive batteries by the use of an automated test system," *IEEE Trans. Instrum. Meas.*, vol. 52, no. 4, pp. 1087–1091, Aug. 2003.
- [30] M. A. Roscher and D. U. Sauer, "Dynamic electric behavior and open-circuit-voltage modeling of LiFePO₄-based lithium ion secondary batteries," *J. Power Sources*, vol. 196, pp. 331–336, Jan. 2011.
- [31] KEMET, "Tantalum surface mount capacitors – standard tantalum: T491 industrial grade MnO₂," Feb. 2020. [Online]. Available: https://content.kemet.com/datasheets/KEM_T2005_T491.pdf. Accessed on: April 4, 2020.
- [32] INFINEON, "IRLB8314PbF datasheet," Aug. 2018. [Online]. Available: <https://www.infineon.com/dgdl/irlb8314pbf.pdf?fileId=5546d462533600a4015356604d6f258f>. Accessed on: April 4, 2020.
- [33] B. Widrow, I. Kollar, and M. C. Liu, "Statistical theory of quantization," *IEEE Trans. Instrum. Meas.*, vol. 45, no. 2, pp. 353–361, Apr. 1996.
- [34] Y. Ye and K. W. E. Cheng, "Modeling and analysis of series-parallel switched-capacitor voltage equalizer for battery/supercapacitor strings," *IEEE J. Emerg. Sel. Topics Power Electron.*, vol. 3, no. 4, pp. 977–983, Dec. 2015.
- [35] Y. Zou, X. Hu, H. Ma, and S. E. Li, "Combined state of charge and state of health estimation over lithium-ion battery cell cycle lifespan for electric vehicles," *J. Power Sources*, vol. 273, pp. 793–803, Jan. 2015.
- [36] Texas Instruments, LM35 precision centigrade temperature sensors datasheet, Aug. 1999. Revised Dec. 2017.



Cristina González Moral (Student Member, IEEE) received the B.S. degree in industrial electronic engineering and the M.S. degree in power electronic engineering from the University of Oviedo, Gijón, Spain, in 2014 and 2016. She is currently working toward the Ph.D. degree in electrical engineering in collaboration with the company Electrotécnica Industrial y Naval, La Coruña, Spain.



Since 2016, she has been a Researcher with the Department of Electrical, Electronic, Computers and Systems Engineering, University of Oviedo. In 2018, she was a Visiting Researcher with the PEL group in the École Polytechnique Fédérale de Lausanne in Switzerland. Her research interests include batteries, power converters and drives.

Miss. Moral is a Board Member in the IEEE student branch chapter IAS / PELS / PES from the University of Oviedo.



Diego Fernández Laborda (Student Member, IEEE) received the B.S. degree in industrial electronic engineering and the M.S. degree in electric energy conversion and power electronics engineering from the University of Oviedo, Gijón, Spain in 2016 and 2018, respectively, where he is currently working toward the Ph.D. degree in electrical engineering.

Since 2018, he has been a Researcher with the Department of Electrical, Electronic, Computers and Systems Engineering, University of Oviedo. His research interests include electric machines and power electronics for electric vehicles, wireless measurement systems, and digital signal processing.



Lidia Sánchez Alonso received the B.S. degree in industrial chemical engineering from the University of Oviedo, Gijón, Spain, in 2019, where she is currently working toward the master's degree in power electronics engineering.

Her research interests include batteries and power converters.



Juan Manuel Guerrero (Member, IEEE) received the M.E. degree in industrial engineering and the Ph.D. degree in electrical and electronic engineering from the University of Oviedo, Gijón, Spain, in 1998 and 2003, respectively.

Since 1999, he has occupied different teaching and research positions with the Department of Electrical, Computer and Systems Engineering, University of Oviedo, where he is currently an Associate Professor. From February to October 2002, he was a Visiting Scholar with the University of Wisconsin—Madison.

From June to December 2007, he was a Visiting Professor with the Tennessee Technological University, Cookeville, TN, USA. His research interests include control of electric drives and power converters, smart grids, and renewable energy generation.



Daniel Fernandez (Member, IEEE) received the M.S. degree in power electronic engineering and the Ph.D. degree in electrical engineering from the University of Oviedo, Gijón, Spain, in 2013 and 2017, respectively.

He was an Intern with the Nissan Advanced Technology Center in 2013 and a Visiting Student with the University of Sheffield in 2015. His research interests include design, monitoring and diagnostics of electric machines, and control of electric drives and magnetics.

Dr. Fernandez was the recipient of a fellowship of the Personnel Research Training Program funded by the Regional Ministry of Education and Science of the Principality of Asturias in 2013 and the recipient of four IEEE Industry Applications Society Conference Prize Paper Awards.



Carlos Rivas Pereda (Senior Member, IEEE) was born in Bilbao, Spain, in 1973. He received the B.Sc. and M.Sc. degrees from Mondragon University, Mondragon, Spain, and the Ph.D. degree in industrial electronics engineering from the Swiss Federal Institute of Lausanne, Lausanne, Switzerland, in 2003.

He joined different technical companies. In 2005, he joined Electrotécnica Industrial y Naval as R&D Manager. He has been participating in several R&D projects for industry, navy, and energy such as smart-grids, power converters, and energy management. He has also supervised several M.Sc. and Ph.D. thesis. He has published more than 15 scientific papers. His current research interests include new converters topologies and uses and power converters manufacturing.

Dr. Pereda is currently a Member of Editorial Board for *Dinamo Técnica* magazine.



David Díaz Reigosa (Senior Member, IEEE) was born in Spain in 1979. He received the M.E. and Ph.D. degrees in electrical engineering from the University of Oviedo, Oviedo, Spain, in 2003 and 2007, respectively.

He is currently an Associate Professor with the Electrical Engineering Department, University of Oviedo. From 2004 to 2008, he was awarded a fellowship of the Personnel Research Training Program funded by Regional Ministry of Education and Science of the Principality of Asturias. He was a Visitor Scholar with the Wisconsin Electric Machines and Power Electronics Consortium, University of Wisconsin—Madison, in 2007. He was a Visitor Professor with the University of Sheffield, Sheffield, U.K., Electrical Machines and Drives Group, in 2016.

He was the recipient of nine IEEE Industry Applications Society Conference and IEEE Energy Conversion Congress and Exposition prize paper awards. His research interests include sensorless control of induction motors, permanent magnet synchronous motors, and digital signal processing.

B.1.4 Resolver Emulation for PMSMs Using Low Cost Hall-Effect Sensors

Resolver Emulation for PMSMs Using Low Cost Hall-Effect Sensors

Daniel Fernandez , Member, IEEE, Diego Fernandez , Maria Martinez , Student Member, IEEE, David Reigosa , Member, IEEE, Alberto B. Diez, Member, IEEE, and Fernando Briz , Senior Member, IEEE

Abstract—Control of permanent magnet synchronous machines (PMSMs) requires absolute rotor position measurement/estimation, as well as the magnet polarity detection for the machine start-up, encoders/resolvers being normally used for this purpose. However, these sensors can account for a large portion of the overall drive cost, and require additional room and cabling, therefore penalizing the size and reliability of the drive. This article proposes a method to emulate a resolver in machines using low cost Hall-effect sensors. The proposed Hall-effect resolver system is a new type of angular position sensor for PMSMs. This allows to control machines which do not include a resolver from inverters which require a resolver signal to operate.

Index Terms—Hall-effect sensors, permanent magnet synchronous machines (PMSMs), resolver emulation, rotor speed and position measurement.

I. INTRODUCTION

PERMANENT magnet synchronous machines (PMSMs) have become very popular during the last decades due to their high efficiency, high power density, and superior dynamic response compared with other types of machines, e.g., induction, wound field, or synchronous reluctance machines. Control of PMSMs requires the absolute position of the rotor, i.e., including magnet polarity prior to startup of the machine [1], [2]. Both absolute encoders [3]–[6] and resolvers [16]–[22] comply with this requirement. On the contrary, incremental encoders will require some additional mechanism to obtain the rotor initial position. Combined use of incremental encoder and Hall-effect sensors [3]–[10] provides the absolute position.

Table I shows a comparative analysis of position sensors normally used in industry applications. Optical encoders are likely

TABLE I
POSITION SENSORS

	Cost	Accuracy	Robustness	Position
Incremental optical encoder [3]–[6]	↑	↑↑↑	↓	Incremental
Incremental magnetic encoder [8]–[10]	↑	↑	↑	Incremental
Absolute optical encoder [3]–[6]	↑↑	↑↑↑	↓	Absolute
Wound field resolver [16]–[19]	↑↑↑	↑↑	↑↑	Absolute
Variable reluctance resolver [20]–[21]	↑	↑↑	↑↑↑	Absolute
Planar Coil/Capacitor [23]–[25]	ND	↑	↓↓	Absolute
Contactless Hall-based [26]–[27]	↓↓↓	↓	↑	Absolute
Proposed HER	↓↓↓	↑	↑↑	Absolute

the preferred option in general purpose applications; however, they are less robust than magnetic encoders and resolvers, the last being the preferred option for, e.g., hybrid-electric vehicles and electric vehicles motors [13]–[15], aircrafts, satellite antennas, or robots [11]–[13]. Although resolvers provide absolute position, its use always implies additional hardware (a resolver to digital converter is needed [12], [17], [18]), room and cabling, therefore penalizing cost, size, and reliability of the drive.

In addition of conventional position sensors, a number of alternative solutions have been reported in the literature. A planar angular position sensor is proposed in [23], with a similar working principle as a variable reluctance (VR) resolver. However, this sensor is highly sensitive to electromagnetic interference due to its construction and requires and additional electronic circuit to operate. The sensor proposed in [24] provides angular position output that is not compatible with standard encoder or resolver signals. In [25], a contactless capacitive angular position sensor is proposed, but it is characterized for presenting a nonlinear behavior. Other noncontact angular positions sensors based on Hall-effect devices for automotive applications (e.g., throttle position detection, shaft position, etc.) are also commercially available [26], [27]. The main drawbacks of these methods are the robustness decrease, inertia increase, and extra room.

This article proposes a method to emulate resolvers using the signals provided by low-cost Hall-effect sensors, Hall-effect

Manuscript received November 26, 2019; revised February 13, 2020 and April 24, 2020; accepted June 7, 2020. Date of publication July 9, 2020; date of current version September 18, 2020. Paper 2019-IDC-1346.R2, presented at the 2019 IEEE Energy Conversion Congress and Exposition, Baltimore, MD USA, 29 Sep.–3 Oct., and approved for publication in the IEEE TRANSACTIONS ON INDUSTRY APPLICATIONS by the Industrial Drives Committee of the IEEE Industry Applications Society. This work was supported in part by the Research, Technological Development and Innovation Programs of the Spanish Ministry Economy and Competitiveness, under Grant MINECO-17-ENE2016-80047-R and in part by the Government of Asturias under project IDI/2018/000188 and FEDER funds. (Corresponding author: Daniel Fernandez.)

The authors are with the Department of Electrical, Computer and System Engineering, University of Oviedo, Gijón 33204, Spain (e-mail: fernandezalodaniel@uniovi.es; dflaborda@uniovi.es; martinezgmaria@uniovi.es; reigosa@isa.uniovi.es; alberto@isa.uniovi.es; fernando@isa.uniovi.es).

Color versions of one or more of the figures in this article are available online at <https://ieeexplore.ieee.org>.

Digital Object Identifier 10.1109/TIA.2020.3008129

0093-9994 © 2020 IEEE. Personal use is permitted, but republication/redistribution requires IEEE permission. See <https://www.ieee.org/publications/rights/index.html> for more information.

resolver (HER), which is an extension of [28]. Stability of the HER system is evaluated and compared with standard sensors. Uses of the HER system could be twofold: first, it would enable the use of machines that do not include a resolver, with electric drives that require a resolver signal to operate and second, a new type of position sensor for PMSM. Appealing properties of the HER system are reduced cost as well as simple, light, and robust construction, as there are no moving parts or couplings.

This article is organized as follows: design and operation principles of resolvers are presented in Section II, emulation of a resolver using Hall-effect sensors is presented in Section III, machine and Hall-effect sensors placement is presented in Section IV, experimental results are presented in Section V, and conclusions are presented in Section VI.

II. RESOLVER DESIGN AND PRINCIPLES OF OPERATION

This section briefly reviews the design and operating principles of resolvers. Commercial resolvers can be classified into wound field (WF) [16]–[19] and VR [20], [21]. WF resolvers include an excitation winding in the rotor, which is magnetically coupled with two identical stator windings having 90° mutual electrical phase shift [16]–[19]. A sinusoidal voltage, typically called carrier, is applied to the rotor windings, via brushes and rings or alternatively by means of a magnetic coupling (i.e., rotating transformer) [16]–[19]. The resulting voltages in the two-stator windings are a *sine* and *cosine* signal whose angle is modulated by the rotor angle. WF resolvers have a wide temperature range of operation, are small and light, and with a simple and robust construction; in addition they are highly insensitive to noise and tolerate long transmission cables length [16]–[19]. On the other hand, VR resolvers have both the output and the excitation windings in the stator; no brushes or rotating transformer being therefore required. In general, VR resolvers are even less expensive and more robust than WF resolvers [13], [14], [20], [21].

Resolvers can be seen as a special type of rotary transformer that couples a primary winding [Input, see Fig. 1(a)] with two secondary windings [Output 1 and 2, see Fig. 1(a)] that are 90 electrical degrees phase shifted; note that Fig. 1(a) shows a schematic representation of a VR resolver. Excitation signal, i.e., V_{source} in Fig. 1(a), is typically a sinusoidal signal (1), see Fig. 1(b), where V_0 and ω_{source} are the magnitude and frequency of the excitation signal, respectively. The excitation frequency depends on the resolver type. Brushless resolvers typically operate in the range of 1 to 10 kHz, while VR resolvers operate around 10 kHz. For the sake of compatibility with conventional resolvers, frequencies of 2 and 10 kHz will be used in this article.

The output signals of the resolver are (2) and (3), $V_{out,1}$ and $V_{out,2}$, respectively, see Fig. 1(c) and (d), where k is the transformation ratio of the resolver, θ_r is the position of the resolver, ω_r is the rotating frequency of the resolver, and X is a multiplication factor for the angle [13]

$$V_{source} = V_0 \sin(\omega_{source}t) \quad (1)$$

$$V_{out,1} = V_0 \sin(\omega_{source}t) * k * \sin(X\theta_r) \quad (2)$$

$$V_{out,2} = V_0 \sin(\omega_{source}t) * k * \cos(X\theta_r). \quad (3)$$

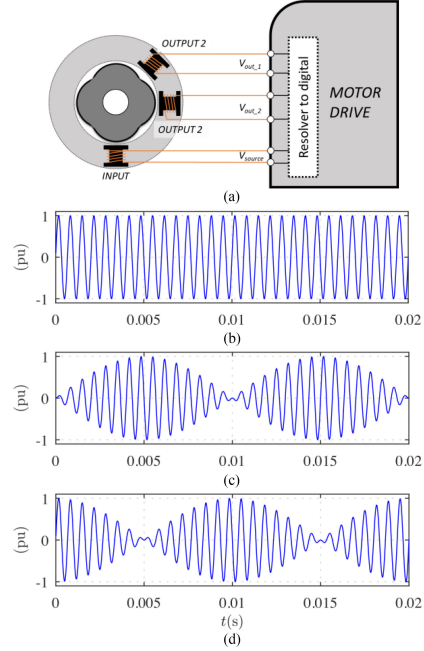


Fig. 1. Basic operation of a VR resolver. (a) Schematic representation of VR resolver and motor drive. (b) Excitation of the resolver, V_{source} . (c) Output 1 of the resolver, $V_{out,1}$ (i.e., sine). (d) Output 2 of the resolver, $V_{out,2}$ (i.e., cosine). $\omega_{source} = 2 \cdot \pi \cdot 500$ rad/s, $\omega_r = 2 \cdot \pi \cdot 50$ rad/s.

$V_{out,1}$ and $V_{out,2}$ fed a resolver-to-digital (R/D) converter [11]–[22], which typically includes a demodulation stage [12], [17]–[19], [32], [33]; $V_{out,1}$ and $V_{out,2}$ after the demodulation being expressed by (4) and (5). A large variety of methods have been proposed to obtain the rotor position, θ_r , from (4) and (5) [12], [17]–[19], [32], [33]

$$V'_{out,1} = k * \sin(X\theta_r) \quad (4)$$

$$V'_{out,2} = k * \cos(X\theta_r). \quad (5)$$

III. EMULATION OF A RESOLVER USING HALL-EFFECT SENSORS

This section presents the proposed system to emulate a resolver using Hall-effect sensors.

Hall-effect sensors are typically used to convert a magnetic flux density signal into a voltage signal (i.e., Hall voltage). It consists on a semiconductor element (i.e., Hall element), see Fig. 2, which fed with a current I_z . In the presence of a magnetic field (\vec{B}_y in Fig. 2), the induced Hall voltage (V_H) is proportional to both the current applied, I_z , and the magnetic flux density, \vec{B}_y , (6), where hw is the cross-sectional area of the element, e is the

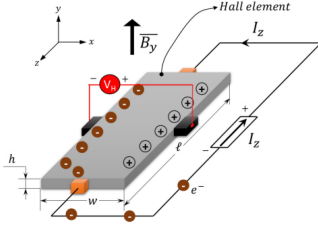


Fig. 2. Schematic representation of the Hall-effect phenomenon.

charge of the electron, and n stands for the charge carrier density. Since e , hw , and n are constants, V_H will be proportional to \bar{B}_y and I_z .

$$V_H = \frac{I_z \bar{B}_y}{nhwe} \quad (6)$$

$$V_H = k(I_z \bar{B}_y). \quad (7)$$

Fig. 3 shows a schematic representation of the test machine that will be used for the experimental verification of the proposed HER system. The HER system consists of two Hall-effect sensors, 90 electrical degrees phase shifted, HALL-1 and HALL-2 in Fig. 3(a). The sensors will be mounted on the end frame of the machine, measuring field in the radial direction; i.e., the sensors will measure the leakage flux in y -axis direction (B_y), see Fig. 3(b) and (c), which will vary as the rotor rotates [29]. The output of HALL-1 and HALL-2 will consist of a *sine* and *cosine* waveforms containing the position information [28]–[30].

Hall sensors are normally fed using a dc current. The resulting output signals of the two Hall-effect sensors are shifted by 90° as shown in Fig. 4(a).

However, it is possible to feed the sensors using a sinusoidal signal (either voltage or current), i.e., same as WF and VR resolvers [16]–[21]. The output signals from the two Hall-effect sensors are shown in Fig. 4(b). The peak value of the resulting signals will be proportional to the magnet leakage flux density seen by the sensor and to the current feeding the sensor (7). Similarities between the signals in Fig. 4(b) are those produced by traditional resolvers in Fig. 1(c) and (d) evident, what strongly support the idea that the same signal processing used with the resolver signals could be applied to the signals produced by the Hall sensors. It is noted that in this case, there is no element attached to the rotor, the solution being therefore simple, compact, and robust.

It must be noted that the proposed method assumes a linear response of the sensor with the excitation signal. To validate this assumption, a sensor was placed on top of a PM [see Fig. 5(a)], being subjected therefore to a constant field. The sensor was fed with a sinusoidal voltage V_{in} shown in Fig. 5(b) [see Fig. 5(a)]. Fig. 5(c) and (d) shows the output of the sensor, V_{out} , and excitation signal V_{in} versus output of the sensor [$V_{in} - V_{out}$, see Fig. 5(d)]. The results in Fig. 5 confirm the linear response of the sensor with respect its sinusoidal excitation.

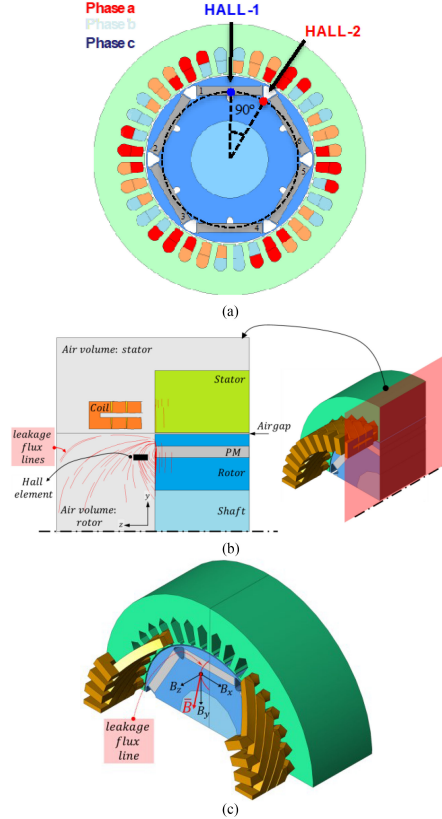


Fig. 3. (a) Two-dimensional (2-D) schematic representation of the machine and sensors location on the cross section (x - y). (b) FEA result of a leakage flux and sensor location, y - z plane. (c) Sensor location and leakage flux vector components.

IV. EXPERIMENTAL TEST BENCH

The HER system has been implemented in an IPMSM, its design being shown in Fig. 3. Table II shows the ratings and dimensions of the machine. Hall-effect sensors [31] have been attached to the end shield to the machine, see Fig. 3(c); i.e., the sensors are placed between the rotor and end shield.

Assembly of the sensors does not differ from standard Hall-effect sensors already available in some machines [34], [35], while cabling between sensors and drive is the same as for standard resolvers [16]–[21]. The phase shift among sensors is 90 electrical degrees, which corresponds to 30 mechanical degrees in a 6-pole machine, see Fig. 6(a); the output of the two Hall-effect sensors will be therefore two sinusoidal signals, 90° phase shifted (i.e., *sine* and *cosine* waveforms). Hall-effect

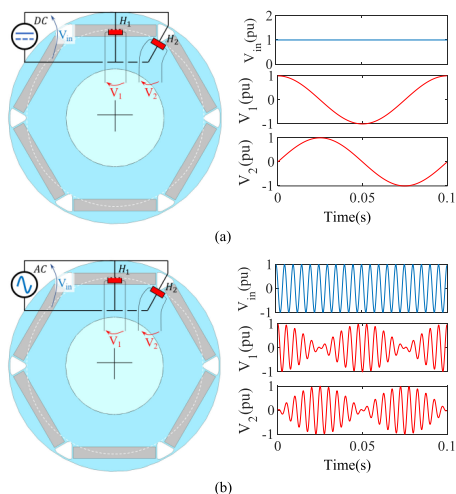


Fig. 4. Schematic representations of the Hall-effect sensors supply system and resulting signals as the machine rotates at $\omega = 10$ Hz for: (a) dc excitation and (b) ac excitation.

TABLE II
MACHINE PARAMETERS

P_{RATED} (kW)	7.5	I_{RATED} (A)	14
ω_{RATED} (rpm)	1000	Stator slots	36
Poles	6	Rotor radius (mm)	54.2
Magnet dimensions: width, height and length (mm)	42x6x10	Magnet position from shaft (mm)	44.6
Airgap length (mm)	0.8	Inner stator radius (mm)	55
Outer stator radius (mm)	88	Sensor position:	
		• Radius (mm)	44.6
		• Distance from the rotor in axial direction (mm)	5

sensors that have been used, [31], are standard sensors typically used for motion control in PMSMs [28]–[30]. Standard Hall-effect sensors used in PMSM drives measure the magnetic flux density along one direction, i.e., they are 1-D sensors; Hall-effect sensors used in this work are oriented in the radial direction, i.e., y-axis direction [see Fig. 6(a)], which is expected to provide high sensitivity to PM leakage flux and low sensitivity to stator current [28]–[30].

Stator of the machine is shown in Fig. 6(b). Fig. 6(c) shows the test bench consisting of the test machine and a load machine [36]. Fig. 6(d) shows a schematic representation of the test bench, including load machine, test machine, and connection between the test machine and drive. It can be observed from Fig. 6(d) that the Hall-effect sensors are mounted on the end shield of the non-drive end of the machine; Hall-effect sensors being connected to the “Resolver to digital” control board of the drive [37].

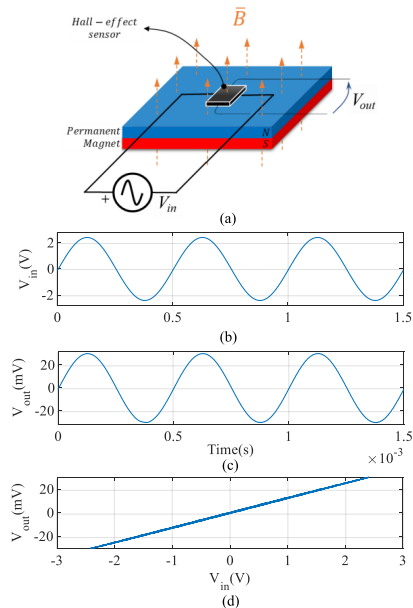


Fig. 5. (a) Schematic representation of the setup for testing Hall-effect sensor linearity. (b) Excitation of the Hall-effect sensor, V_{in} . (c) Output of the Hall-effect sensor, V_{out} . (d) V_{source} versus V_{out} . $\omega_{source} = 2 \cdot \pi \cdot 2000$ rad/s, $V_{source} = 2.3$ V.

V. EXPERIMENTAL RESULTS

Experimental results of the HER system are presented in this section for different working conditions of the machine.

A 2 kHz, 5 V_{peak} signal was used to feed the sensor in Figs. 7 and 8, 10 kHz 10 V was used in Figs. 10 to 13. These signals are similar to those used by conventional resolvers, meaning that they can feed directly any existing circuitry designed for the signal processing of conventional resolvers.

It is finally noted that the input impedance of the Hall sensor is $\sim 725 \Omega$ [31], the total power consumption of the HER sensor (RMS) being ~ 34.5 mW (~ 17.2 mW per sensor). Input impedance of conventional resolvers (VR and Brushless) varies from $\sim 50 \Omega$ to $\sim 150 \Omega$, leading to power consumptions in the range of 250 to 500 mW.

Fig. 7(b) and (c) shows the output signals of the two Hall-effect sensors, V_{out_1} (sine) and V_{out_2} (cosine) when the machine is rotating at 40 Hz and with no fundamental current. Fig. 8(a) and (b) shows the speed and position measured using the HER sensor, an encoder with 4096 pulses per revolution is also shown for comparison purposes. Fig. 8(c) shows position error. It is observed that under no load condition the peak error in the estimated position is < 0.07 rad.

Fig. 9 shows the signal processing used for speed and position estimation. Measured flux densities H_1 and H_2 are multiplied by

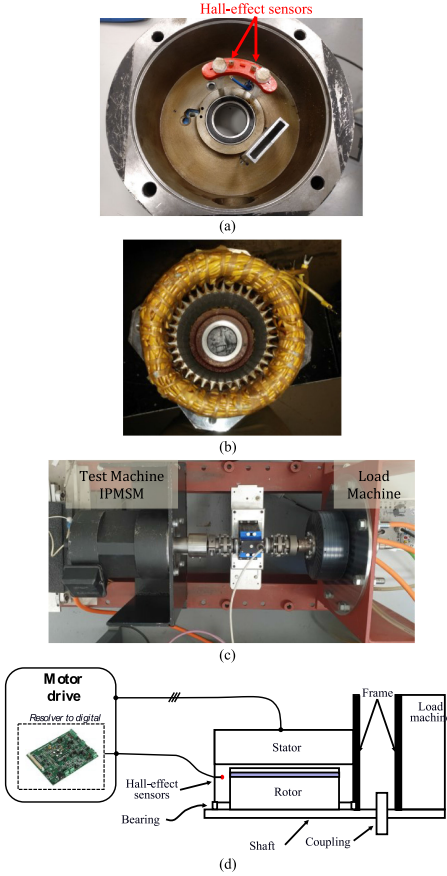


Fig. 6. Machine design and experimental setup. (a) Machine end shield with the Hall-effect sensors. (b) Machine stator. (c) Test bench. (d) Schematic representation of the test bench and drive.

the carrier signal at the demodulation. A second-order low pass filter with a cutoff frequency of 1 kHz is used to remove high frequency noise. The angle of the resulting V_α and V_β signals (8) is obtained using a synchronous reference frame phase-locked loop, which provides the estimated rotor speed and position [38]

$$\vec{V}_{\alpha\beta}^s = V_\alpha + jV_\beta \quad (8)$$

$$\vec{V}_{dq}^r = \vec{V}_{\alpha\beta}^s e^{-j\theta_r}. \quad (9)$$

The bandwidth of the proposed HER will depend primarily on the bandwidth of the PLL, which has been set to 230 Hz.

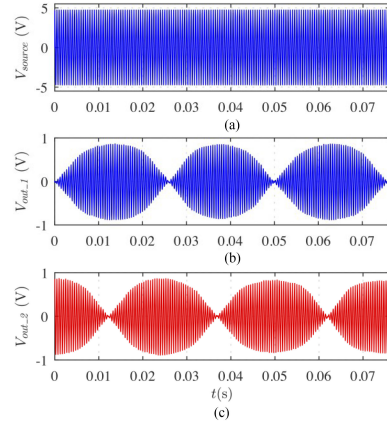


Fig. 7. (a) Excitation of the Hall-effect sensors, V_{source} . (b) Output of Hall-effect sensor 1, V_{out_1} . (c) Output of Hall-effect sensor 2, V_{out_2} . $\omega_{source} = 2 \cdot \pi \cdot 2000$ rad/s, $V_{source} = 5$ V, $\omega_r = 2 \cdot \pi \cdot 40$ rad/s, $I_d = I_q = 0$ pu.

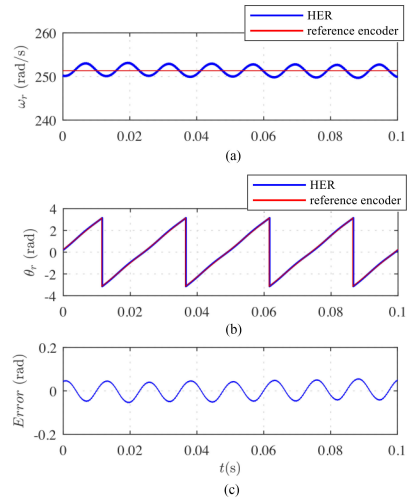


Fig. 8. Experimental results using the HER system (blue) and a conventional encoder (red). (a) Measured speed. (b) Measured position. (c) Position error. $\omega_{source} = 2 \cdot \pi \cdot 2000$ rad/s, $V_{source} = 5$ V, $\omega_r = 2 \cdot \pi \cdot 40$ rad/s, $I_d = I_q = 0$ pu.

The bandwidth of the Hall sensor 250 kHz, and can be therefore safely neglected [31].

A. Influence of dq Axes Currents

Both d - and q -axis stator currents [29] are expected to interfere with the leakage flux due to the magnets measured by the

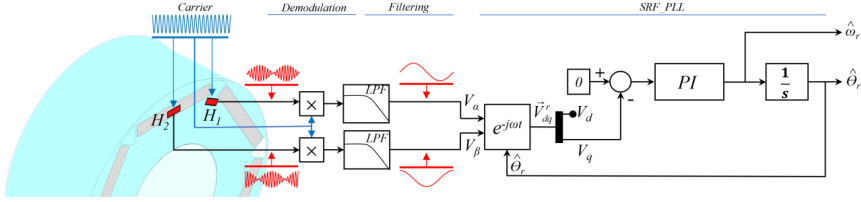


Fig. 9. Schematic representation of the signal processing used for speed and position estimation.

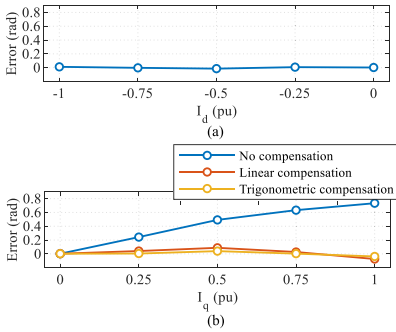


Fig. 10. Angular position error (a) when I_d is varied (flux weakening), (b) when I_q is varied (torque current), with and without compensation. $\omega_{source} = 2 \cdot \pi \cdot 10000$ rad/s, $V_{source} = 10$ V, $\omega_r = 200$ rpm.

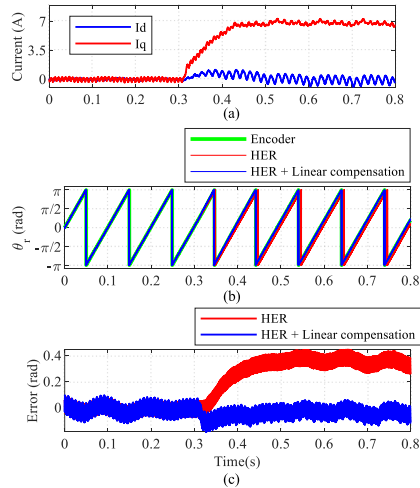


Fig. 12. Response to a q -axis current step (a) d - and q -axis current, (b) estimated position using the HER without and with q -axis current compensation. Position provided by the encoder is also shown, and (c) estimation error. $\omega_{source} = 2 \cdot \pi \cdot 10000$ rad/s, $V_{source} = 10$ V, $\omega_r = 200$ rpm.

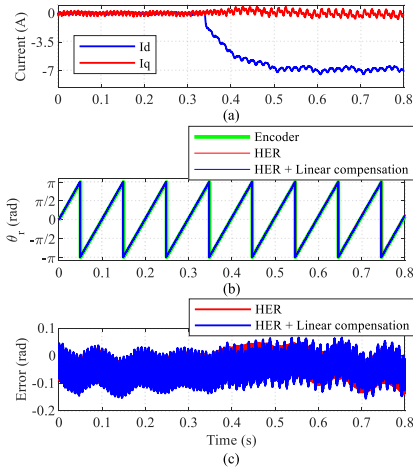


Fig. 11. Response to a d -axis current step (a) d - and q -axis current, (b) measured position using the HER without and with q -axis current compensation, as from the encoder, and (c) estimated position error. $\omega_{source} = 2 \cdot \pi \cdot 10000$ rad/s, $V_{source} = 10$ V, $\omega_r = 200$ rpm.

Hall-effect sensors. d -axis current will affect only to the amplitude of the measured signals, but with no effect on the angles, as it is aligned with the magnet. q -axis current affects the phase of the leakage flux waveform, resulting therefore in a position error.

Fig. 10(a) shows the estimated position error when d -axis current is varied from 0 to -1 pu (i.e., flux weakening) in steps of 0.25 pu. As expected, d -axis currents do not affect to the accuracy. Similarly Fig. 9(b) shows the results when q -axis current is varied from 0 to 1 pu in steps of 0.25 pu. As expected, the error increases almost linearly with the q -axis current. However, this error can be compensated, two different options have been evaluated.

- 1) Linear compensation using (10): the compensation angle, $\Delta\theta$ being proportional to the q -axis current

$$\Delta\theta = aI_q. \quad (10)$$

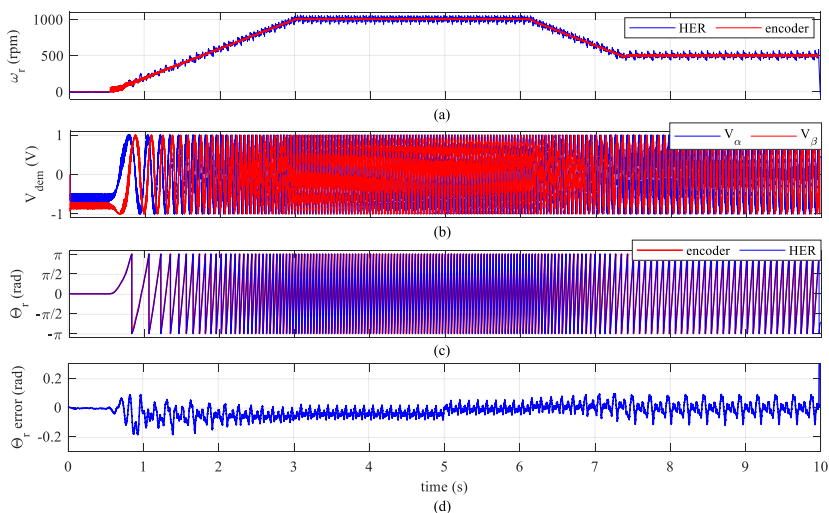


Fig. 13. Response to a speed ramp (a) estimated and measured speed, (b) measured leakage flux after demodulation, (c) estimated position, and (d) estimated position error. $\omega_{source} = 2 \cdot \pi \cdot 10000$ rad/s, $V_{source} = 10$ V.

- 2) Trigonometric compensation using (11); the compensation angle that relies on two constants, a and b

$$\Delta\theta = \tan^{-1} \left(\frac{aI_d}{b} \right). \quad (11)$$

Compensation constants are experimentally approximated. Fig. 10(b) shows the position error using these two compensation methods, both leading to similar results (i.e., error < 0.1 rad).

Performance of the proposed HER during transient operation has been also analyzed. Fig. 11 shows the experimental results when a d -axis current step of -0.5 pu is applied at $t = 0.35$ s with the machine operating at constant speed. Fig. 11(a) shows the measured d - and q -axis currents. Fig. 11(b) shows the rotor position measured with the proposed system without and with compensation of q -axis current effects as well as the rotor position measured with the encoder. It is noted that the error does not increase due to transients in the d -axis current.

Similarly, Fig. 12 shows the case when a q -axis current step of -0.5 pu is applied (at $t = 0.35$ s for the case of without and with linear compensation, in the second case the error remaining < 0.1 rad).

B. Operation at Variable Speed

Performance of the HER is expected to be independent of speed. Fig. 13 shows the sensor signals and the estimated speed and position when the speed varies as shown in Fig. 13(a). Results in Fig. 13(d) show a maximum position error of ± 0.05 rad in steady state, which slightly increases during transients. Maximum error of commercially available VR resolvers ranges from

± 0.01 rad for four-pole variable resolvers to ± 0.018 rad for two-pole variable resolvers. Maximum error of commercially available brushless resolvers is in the range of ± 0.006 rad.

VI. CONCLUSION

This article proposes a method to emulate a resolver using low cost Hall-effect sensors. The proposed HER device consists of two Hall-effect sensors, mounted on the end shield of the machine, 90 electrical degrees phase shifted, which measure the magnetic flux leakage of the PMSM.

Compared to commercial resolvers, the proposed HER sensor has higher error, but in turn it provides several advantages.

- 1) Very low cost.
- 2) Reduced size, which eases its integration in the drive, its impact on system inertia being negligible.
- 3) Increased robustness, as there are no moving parts or coupling.
- 4) Lower power consumption than conventional resolvers and full compatibility with resolver circuitry.
- 5) Experimental results have been provided to demonstrate the viability of the proposed HER system.

REFERENCES

- [1] R. Nalepa and T. Orłowska-Kowalska, "Optimum trajectory control of the current vector of a non-salient pole PMSM in the field-weakening region," *IEEE Trans. Ind. Electron.*, vol. 59, no. 7, pp. 2867–2876, Jul. 2012.
- [2] D. C. Hanselman, *Brushless Permanent Magnet Motor Design*. New York, NY, USA: Mc-Graw Hill, 1994.
- [3] Maxonmotorusa.com, "Maxon sensor—Key information," Mar. 23, 2017. [Online]. Available: <http://www.maxonmotorusa.com/>

- [4] Siemens.com, "Three-phase synchronous motors based on permanent magnet technology," Catalog D 86.2 • 2007, Mar. 23, 2017. [Online]. Available: <http://w3.siemens.com/mc/mc-solutions/en/motors/>
- [5] Technosoft.com, "Drive solutions for motion control applications," Product Overview, Mar. 23, 2017. [Online]. Available: <http://www.technosoftmotion.com/en/products>
- [6] Abbmotion.com, "Intelligent Servo Drives and Intelligent Motors," MotiFelex e180 motion control, Mar. 23, 2017. [Online]. Available: <http://www.abbmotion.com/products/servodrives/overview.asp>
- [7] Y. Netzer, "Linear electric encoder with facing transmitter and receiver," U.S. Patent US2004/02525032A1, Dec. 16, 2004.
- [8] P. Kejik, S. Reymond, and R. S. Popovic, "Purely CMOS angular position sensor based on a new Hall microchip," in *Proc. 34th Annu. Conf. IEEE Ind. Electron.*, Nov. 10–13, 2008, pp. 1777–1781.
- [9] P. Kejik, S. Reymond, and R. S. Popovic, "Circular Hall transducer for angular position sensing," in *Proc. Transducers Eurosensors XXI Conf.*, Jun. 10–14, 2007, pp. 2593–2596.
- [10] C. S. Anoop, B. George and J. Kumar, "Tunneling magneto-resistor based angle transducer," in *Proc. 5th Int. Conf. Sensing Technol.*, Nov. 28/Dec. 1, 2011, pp. 431–435.
- [11] A. Murray, B. Hare, and A. Hirao, "Resolver position sensing system with integrated fault detection for automotive applications," in *Proc. SENSORS, IEEE*, Jun. 2002, vol. 2, pp. 864–869
- [12] X. Yongxiang, Z. Dianchen, W. Yanyu, Z. Jibin and S. Jing, "DSP based all-digital resolver-to-digital conversion using DSRF-PLL," *IEEE 7th Int. Power Electron. Motion Control Conf.*, Jun. 2012, pp. 1210–1215.
- [13] C.-S. Jin, I.-S. Jang, J.-N. Bae, J. Lee, and W.-H. Kim, "Proposal of improved winding method for VR resolver," *IEEE Trans. Magn.*, vol. 51, no. 3, Mar. 2015, Art. no. 8102404
- [14] L. Sun, "Analysis and improvement on the structure of variable reluctance resolvers," *IEEE Trans. Magn.*, vol. 44, no. 8, pp. 2002–2008, Aug. 2008.
- [15] K.-C. Kim, C. S. Jin, and J. Lee, "Magnetic shield design between interior permanent magnet synchronous motor and sensor for hybrid electric vehicle," *IEEE Trans. Magn.*, vol. 45, no. 6, pp. 2835–2838, Jun. 2009.
- [16] J. Figueiredo, "Resolver models for manufacturing," *IEEE Trans. Ind. Electron.*, vol. 58, no. 8, pp. 3693–3700, Aug. 2011.
- [17] L. Pecly, R. Schindeler, D. Cleveland, and K. Hashtrudi-Zaad, "High-precision resolver-to-velocity converter," *IEEE Trans. Instrum. Meas.*, vol. 66, no. 11, pp. 2917–2928, Nov. 2017.
- [18] M. Benammar and A. S. P. Gonzales, "A novel resolver converter based on a modified tracking method," in *Proc. 10th IEEE Int. Conf. Netw., Sens. Control*, Apr. 2013, pp. 586–590.
- [19] R. Hoseinnezhad, A. Bab-Hadiashar, and P. Harding, "Calibration of resolver sensors in electromechanical braking systems: A modified recursive weighted least-squares approach," *IEEE Trans. Ind. Electron.*, vol. 54, no. 2, pp. 1052–1060, Apr. 2007.
- [20] L. Z. Sun, J. B. Zou, and Y. P. Lu, "New variable-reluctance resolver for rotor-position sensing," in *Proc. IEEE Region 10th Conf. TENCN*, Nov. 2004, vol. 4, pp. 5–8.
- [21] "Design-oriented modelling of axial-flux variable-reluctance resolver based on magnetic equivalent circuits and Schwarz-Christoffel mapping," *IEEE Trans. Ind. Appl.*, vol. 65, no. 5, pp. 4322–4330, May 2018.
- [22] C. Attaianesi and G. Tomasso, "Position measurement in industrial drives by means of low-cost resolver-to-digital converter," *IEEE Trans. Instrum. Meas.*, vol. 56, no. 6, pp. 2155–2159, Dec. 2007.
- [23] B. P. Reddy, A. Murali, and G. Shaga, "Low cost planar coil structure for inductive sensors to measure absolute angular position," in *Proc. 2nd Int. Conf. Frontiers Sens. Technol.*, 2017, pp. 14–18.
- [24] H. Pu, H. Wang, X. Liu, Z. Yu, and K. Peng, "A high-precision absolute angular position sensor with Vernier capacitive arrays based on time grating," *IEEE Sens. J.*, vol. 19, no. 19, pp. 8626–8634, Oct. 1, 2019.
- [25] M. Gasulla, Xiujun Li, G. C. M. Meijer, L. van der Ham, and J. W. Spronck, "A contactless capacitive angular-position sensor," in *Proc. SENSORS, IEEE*, vol. 2, pp. 880–884.
- [26] P. Kejik, S. Reymond, and R. S. Popovic, "Circular Hall transducer for angular position sensing," in *Proc. Transducers Int. Solid-State Sensors, Actuators Microsyst. Conf.*, 2007, pp. 2593–2596.
- [27] K. Bienczyk, "Angle measurement using a miniature Hall effect position sensor," in *Proc. 2nd Int. Students Conf. Electrodynamic Mechatron.*, 2009, pp. 21–22.
- [28] D. Fernandez, D. F. Laborada, M. Martinez, D. Reigosa, A. B. Diez, and F. Briz, "Resolver emulation for PMSMs using low cost Hall-effect sensors" in *Proc. IEEE Energy Convers. Congr. Expo.*, 29 Sep.–3 Oct., 2019, pp. 5689–5693.
- [29] D. Fernandez *et al.*, "Permanent magnet temperature estimation in PM synchronous motors using low cost hall effect sensors," *IEEE Trans. Ind. Appl.*, vol. 53, no. 5, pp. 4515–4525, Sep./Oct. 2017.
- [30] Y. Park *et al.*, "Online detection of rotor eccentricity and demagnetization faults in PMSMs based on Hall-Effect field sensor measurements," *IEEE Trans. Ind. Appl.*, vol. 55, no. 3, pp. 2499–2509, 2019.
- [31] ChenYang-Sensors and Measurements, "Selection guide of Hall effect sensor elements/ICs," CYSJ106C, Jan. 2, 2019. [Online]. Available: <http://www.hallsensors.de>
- [32] F. Janabi-Sharifi, V. Hayward, and C.-S. J. Chen, "Discrete-time adaptive windowing for velocity estimation," *IEEE Trans. Control Syst. Technol.*, vol. 8, no. 6, pp. 1003–1009, Nov. 2000.
- [33] F. Yiyong, B. Zhuo, and C. Pengfei, "Simulation on the angular velocity and displacement measuring system based on DSRF-PLL," in *Proc. IEEE Int. Conf. Syst. Sci. Eng.*, Jul. 2014, pp. 221–226.
- [34] Faulhaber.com, "Brushless DC servomotors," Series 22...BX432 3268...BX4, Jan. 9, 2019. [Online]. Available: <https://fmcc.faulhaber.com>
- [35] 2020. [Online]. Available: <http://www.allegromicro.com/en/Products/Magnetic-Linear-And-Angular-Position-Sensor-ICs/Linear-Position-Sensor-ICs/A1301-2.aspx>
- [36] ABB motors, "Low-voltage three-phase induction motor, M2QA225M2A," Jan. 9, 2019. [Online]. Available: <https://www.abb.com/product>
- [37] Analog Devices, "AD2S1210, 10-bit to 16-bit resolver-to-digital converter," Jan. 9, 2019. [Online]. Available: www.analog.com
- [38] J. Bergas-Jané, C. Ferrater-Simón, G. Gross, R. Ramírez-Pisco, S. Galceran-Arellano, and J. Rull-Duran, "High-accuracy all-digital resolver-to-digital conversion," *IEEE Trans. Ind. Electron.*, vol. 59, no. 1, pp. 326–333, Jan. 2012.



Daniel Fernandez (Member, IEEE) received the M.S. degree in power electronic engineering and the Ph.D. degree in electrical and electronic engineering from the University of Oviedo, Gijón, Spain, in 2013 and 2017 respectively.

From July to December 2013, he was an Intern with the Nissan Advanced Technology Center, Japan. From August to November 2015, he was a Visiting Student with The University of Sheffield, and from May to July 2019, he was a Visiting Professor with the University of Padova. He is currently an Assistant Professor with the University of Oviedo. His research interests include design, control, and diagnostics of electric machines and drives.

Mr. Fernandez was the recipient of a Fellowship of the Personnel Research Training Program funded by the Regional Ministry of Education and Science of the Principality of Asturias in 2013. He was also the recipient of the University of Oviedo Outstanding Ph.D. Thesis Award in 2018.



Diego Fernandez received the B.S. degree in industrial electronic engineering in 2016 and the M.S. degree in electrical energy conversion and power electronics engineering in 2018, from the University of Oviedo, Gijón, Spain. He is currently working toward the Ph.D. degree in electrical engineering from the University of Oviedo, Gijón, Spain.

He has been a Researcher with the Department of Electrical, Electronic, Computers and Systems Engineering, University of Oviedo, since 2018. His research interests include electric machines and power electronics for electric vehicles, wireless measurement systems, and digital signal processing.



Maria Martinez (Student Member, IEEE) received the M.S. and Ph.D. degrees in electrical engineering from the University of Oviedo, Gijón, Spain, in 2017 and 2020, respectively.

She is currently a Postdoctoral Researcher with the Department of Electrical, Electronic, Computers and Systems Engineering, University of Oviedo. She was an Intern with the Nissan Advanced Technology Center, Atsugi, Japan, in 2019, and a Visiting Student with Aalborg University, Aalborg, Denmark, in 2015.

Her topics of interest include machine diagnostics, wireless measurement systems, sensorless control and digital signal processing.

Ms. Martinez is currently a Board Member of the IAS/PELS/PES Student Branch Chapter of the University of Oviedo.



Alberto B. Diez (Member, IEEE) received the M.S. and Ph.D. degrees from the University of Oviedo, Gijón, Spain, in 1983 and 1988, respectively.

He is currently a Full Professor and the Director with the Department of Electrical Engineering, University of Oviedo. He was a member of the Executive Committee D2 "Rolling-Flat Products" of European Commission from 1998 to 2004. His research interests include control systems, high-performance ac drive control, and industrial supervision, and control processes.



David Reigosa (Member, IEEE) was born in Spain, in 1979. He received the M.E. and Ph.D. degrees in electrical engineering from the University of Oviedo, Gijón, Spain, in 2003 and 2007, respectively.

He is currently an Associate Professor with the Department of Electrical Engineering, University of Oviedo. He was a Visitor Scholar with the Wisconsin Electric Machines and Power Electronics Consortium, University of Wisconsin, Madison, in 2007. He was a Visitor Professor with the University of Sheffield, Sheffield, U.K., Electrical Machines and

Drives Group, in 2016. His research interests include sensorless control of induction motors, permanent magnet synchronous motors, and digital signal processing.

Dr. Reigosa was the recipient of the Fellowship of the Personnel Research Training Program funded by Regional Ministry of Education and Science of the Principality of Asturias, from 2004 to 2008. He was also the recipient of eight IEEE Industry Applications Society Conference and IEEE Energy Conversion Congress and Exposition prize paper awards.



Fernando Briz (Senior Member, IEEE) received the M.S. and Ph.D. degrees from the University of Oviedo, Gijón, Spain, in 1990 and 1996, respectively.

He is currently a Full Professor with the Department of Electrical, Computer and Systems Engineering, University of Oviedo. His topics of interest include electronic power converters and ac drives, power systems, machine monitoring and diagnostics, and digital signal processing.

Dr. Briz was the recipient of the IEEE TRANSACTIONS ON INDUSTRY APPLICATIONS Award and nine IEEE Industry Applications Society Conference and IEEE Energy Conversion Congress and Exposition prize paper awards. He is currently the Vice-Chair of the Industrial Power Conversion System Department of the IAS.

B.2 Conference papers

B.2.1 Magnet Temperature Estimation in Variable Leakage Flux Permanent Magnet Synchronous Machines Using the Magnet Flux Linkage

Magnet Temperature Estimation in Variable Leakage Flux Permanent Magnet Synchronous Machines Using the Magnet Flux Linkage

Diego F. Laborda
University of Oviedo
Dept. of Elect., Computer &
System Engineering
Gijón, Spain
dflaborda@uniovi.es

David Díaz Reigosa
University of Oviedo
Dept. of Elect., Computer &
System Engineering
Gijón, Spain
diazdavid@uniovi.es

Daniel Fernández
University of Oviedo
Dept. of Elect., Computer &
System Engineering
Gijón, Spain
fernandezalodaniel@uniovi.es

Kensuke Sasaki
Nissan Motor Co. Ltd
EV System Laboratory
Atsugi, Kanagawa, Japan
kensuke-sasaki@mail.nissan.co.jp

Takashi Kato
Nissan Motor Co. Ltd
EV System Laboratory
Atsugi, Kanagawa, Japan
katou-t@mail.nissan.co.jp

Fernando Briz
University of Oviedo
Dept. of Elect., Computer &
System Engineering
Gijón, Spain
fernando@isa.uniovi.es

Abstract—Permanent magnet synchronous machines (PMSMs) performance is highly dependent on the Permanent Magnets (PMs) temperature. Knowledge of the PMs temperature is therefore of great importance both for control and monitoring purposes. An increase in the PM temperature during motor operation, decreases PMs magnetic flux strength and consequently the PMSM torque production capability, eventually causing irreversible demagnetization of the PMs; for the case of variable leakage flux PMSMs (VLF- PMSMs), it will affect the variable leakage property of the machine, which will place additional concerns on the machine control. This paper proposes a PM temperature estimation method for VLF-PMSMs from the PM flux linkage. PM flux linkage is obtained from the response of the machine to a small-amplitude, low frequency, square-wave signal (either voltage or current). The signal is injected on top of the fundamental excitation, allowing on-line temperature estimation without interfering with the operation of the machine

Keywords— Permanent magnet, temperature estimation, Variable leakage flux machine, VLF- PMSMs, magnet flux linkage.

I. INTRODUCTION

Permanent Magnet Synchronous Motors (PMSMs) are the preferred option for electric and hybrid-electric vehicles (EV & HEV) due to their high torque density, wide speed capability, and higher efficiency. A concern for this type of machine is the need to inject negative d-axis current to counteract permanent magnet (PM) flux linkage when the drive operates at high speeds, to match the back electromotive force (Back-EMF) with the available DC voltage [1]. This operating mode is known as flux-weakening and is characterized by an inherent copper and core loss increase due to the continuous application of negative d-axis current and the extra harmonics produced in the airgap field [1]. Extra losses will reduce the efficiency, the associated temperature increase eventually affecting the life expectancy of the machine. Variable flux PMSMs (VF-PMSMs) [2] and variable leakage flux PMSMs (VLF-PMSMs) machine designs

[3] are aimed to reduce or even avoid the injection of flux weakening current and its subsequent adverse effects.

Independent of the PMSM design, magnet thermal monitoring is a major concern since an increase in the PM temperature results in a decrease of the PM strength which negatively impacts the torque production capability. Furthermore, excessive temperature can lead to irreversible demagnetization. The variation of the PM strength with temperature places additional concerns both in VF-PMSMs and VLF-PMSMs. In VF-PMSMs a variation of the PM strength will affect the magnetization/demagnetization process and torque control. In VLF-PMSMs a variation of the PM strength will affect the variable leakage property of the machine, eventually reducing the accuracy controlling torque. Knowledge of PM temperature can be useful for monitoring or torque control purposes, the accuracy requirements for the second being typically higher [4].

Direct measurement of PM temperature requires the use of rotor mounted sensors and slip rings or wireless transmission which penalizes the robustness and cost of the system. Alternatively, PM temperature can be estimated. PM temperature estimation methods can be roughly classified into thermal models [5][6], back-EMF based methods [6], and signal injection methods [7]–[9]. Thermal models require knowledge of stator and rotor geometry, materials and cooling system, which makes them highly dependent on the machine design. On the contrary, BEMF and signal injection methods do not require previous knowledge of the geometry and cooling system of the machine [6]–[9]. Both methods require the stator temperature to compensate for the stator resistance variation with temperature [6]–[9]. However, this is not a major drawback in principle, as the stator winding temperature is normally measured in standard machines by means of contact type sensors [6]–[9]. While signal injection methods can work in the whole speed range, back-

EMF based methods are not suitable for low speeds or standstill as the back-EMF is proportional to speed.

Already published signal injection methods [7]–[9] estimate the PM temperature from the variation of the machine high frequency resistance/inductance with PM temperature; these methods are sensitive to saturation and magnetostrictive effect [10]. On the contrary, the method proposed in this paper uses PM flux linkage variation with temperature. PM flux linkage can be obtained from the stator flux linkage, a small-amplitude, low frequency, square-wave voltage or current signal is injected in the stator windings for this purpose. The main advantage of the proposed method compared to [7]–[9] is that it does not rely on stator resistance or inductance changes with temperature, not being therefore affected by saturation nor magnetostrictive effect.

This paper is organized as follows: the proposed temperature estimation method based on PM flux linkage variation is presented in Section II; simulation results are shown in Section III; the test bench that will be used for experimental verification of the method is shown in IV; conclusions are finally provided in Section V.

II. TEMPERATURE ESTIMATION BASED ON PM FLUX LINKAGE VARIATION

This section describes the principles and implementation of the proposed temperature estimation method. PM flux linkage decreases as PM temperature increases [7]–[9],[11], meaning that PM flux linkage is a reliable metric for PM temperature. While this is an undesirable behavior since a decrease of the PM flux linkage reduces the machine torque production capability, it can be potentially used for PM temperature estimation purposes. PM flux linkage is the only responsible for back-EMF at no load, but it is hardly decoupled from stator flux linkage created by stator currents at loaded condition. In order to estimate the PM flux linkage, the method proposed in [12] is used. Fig. 1 shows both the torque/current control block diagram of a VLF-PMSMs and the proposed temperature estimation control block diagram, the main blocks being:

- Flux observer: estimates the stator flux linkage ($\hat{\lambda}_{sdq}^r$) from the measured stator current (i_{sdq}^r) and the commanded stator voltage (i.e. the output of the current regulator, v_{sdq}^{r*}).
- PM flux linkage estimator: it is estimated from the stator flux linkage provided by the flux observer, $\hat{\lambda}_{sdq}^r$, in combination with the response of the machine to a small-amplitude, low frequency, squarewave current that will be injected on top of the fundamental current (Δi_{sdq}^{r*}) [12].
- A look-up table (LUT) that links the estimated PM flux linkage and the PM temperature [13].

All these blocks are described in detail following:

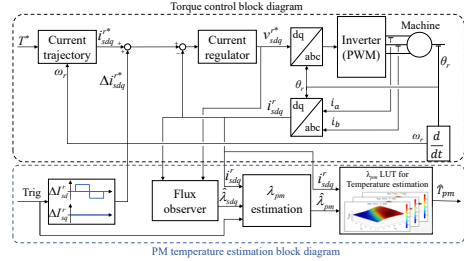


Fig. 1 – Temperature estimation system scheme.

A. Flux observer

Different stator flux observers have been proposed in the literature, the main types being voltage model [14][15], current model based [16] and Gopinath type [14]. Eq. (1) and (2) show the d and q-axis stator flux linkages as a function of stator d and q-axis voltages, currents and stator resistance, i.e. voltage model of a PMSM, where λ_{sd}^s and λ_{sq}^s are d and q-axis flux linkages in the stator reference frame, V_{sd}^s and V_{sq}^s are the d and q-axis stator voltages in the stator reference frame, I_{sd}^s and I_{sq}^s are the d and q-axis stator currents in the stator reference frame, and R_s is the stator resistance. Equations (3) and (4) show the d and q-axis stator flux linkages as a function of stator currents, inductances and magnet flux linkage, typically known as current model, where λ_{sd}^r and λ_{sq}^r are d and q-axis flux linkages in the rotor reference frame, I_{sd}^r and I_{sq}^r are the d and q-axis stator currents in the rotor reference frame, L_d and L_q are the d and q-axis inductances, and λ_{pm} is the magnet flux linkage. Finally, the voltage and current model can be combined in a Gopinath type flux observer [14]. The advantages and drawbacks of these three models can be seen in Table I.

$$\lambda_{sd}^s(t) = \int (V_{sd}^s(t) - R_s \cdot I_{sd}^s(t)) dt \quad (1)$$

$$\lambda_{sq}^s(t) = \int (V_{sq}^s(t) - R_s \cdot I_{sq}^s(t)) dt \quad (2)$$

$$\lambda_{sd}^r = I_{sd}^r L_d + \lambda_{pm} \quad (3)$$

$$\lambda_{sq}^r = I_{sq}^r L_q \quad (4)$$

TABLE I. ADVANTAGES AND DRAWBACKS OF FLUX MODELS

	CURRENT MODEL	VOLTAGE MODEL	GOPINATH
Parameter independency	✘	✘	✘
No initial state error	✓	✘	✓
Estimation in the whole speed range, including standstill	✓	✘	✓

The current model can be used to estimate stator flux in the whole speed range of the machine, but parameters, such as magnet flux linkage and inductances, must be previously known. On the other hand, voltage model can be used to estimate machine flux at high speeds [15], at low speeds it becomes inaccurate due to the diminishing magnitude of the Back-EMF with the speed and it cannot be used at standstill. In addition, as a pure integrator is required to estimate the flux, there is an initial

estimation error (integration constant) which needs to be compensated.

Gopinath type flux observers combine voltage (at high speed) and the current models (at low speed including standstill), a PI controller being used to make a smooth transition between models. The controller bandwidth will set the transition frequency from current to voltage model. This type of flux observer provides reliable estimation in the whole speed range of the machine, including standstill, being more sensitive to machine parameters at low speeds.

From the previous discussion, it is concluded that, although the current model and Gopinath type flux observers can be used in the whole speed range of the machine, the only model that contains information about the PM flux linkage is the voltage model (1)-(2). Therefore, a voltage model flux observer in stator reference frame will be used for PM temperature estimation in this paper.

Fig. 2 shows the implementation of the flux observed based on the voltage model (1)-(2). The estimated stator flux linkage in the stator reference frame, λ_{sd}^s , is obtained from the (1)-(2) after applying a high pass filter (HPF) to avoid the infinite DC gain of the pure integrator. Adaptive phase and magnitude compensation of HPF effects have been implemented. The estimated stator flux linkage in the rotor reference frame, λ_{sd}^r , is obtained by applying Park's transformation to the estimated stator flux linkage; a low pass filter (LPF) is finally used to eliminate high frequency harmonics of the stator flux linkage; i.e. only the fundamental component of the stator flux linkage will be used for temperature estimation.

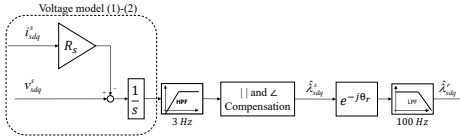


Fig. 2 – Voltage model flux observer in stationary reference frame.

B. PM flux linkage estimator

PM flux linkage is estimated from the stator flux linkage when a small-amplitude, low frequency, quasi-square wave current is added to the fundamental current [12][13]. The stator d-axis flux linkage response from the injected d-axis current will be used to estimate the PM flux linkage, as shown in Fig. 3.

The d-axis stator flux linkage, λ_{sd}^r , is represented by (5), λ_{sd}^{r+} is the d-axis flux linkage when positive d-axis current step, i.e. ΔI_{sd}^r , is applied (6), while λ_{sd}^{r-} is the d-axis flux linkage when negative d-axis current step, i.e. $-\Delta I_{sd}^r$, is applied (7). The stator flux linkages, λ_{sd}^r , λ_{sd}^{r+} and λ_{sd}^{r-} are estimated using the flux observer discussed in the previous subsection. $\hat{\lambda}_{pm}^+$ (estimated PM flux linkage when applying positive ΔI_{sd}^r) and $\hat{\lambda}_{pm}^-$ (estimated PM flux linkage when applying negative ΔI_{sd}^r)

are estimated from (8) and (9) respectively. Finally $\hat{\lambda}_{pm}$ is obtained as the average value of $\hat{\lambda}_{pm}^+$ and $\hat{\lambda}_{pm}^-$ in (10).

$$\lambda_{sd}^r = \lambda_{pm}^r + L_d \cdot I_{sd}^r \quad (5)$$

$$\lambda_{sd}^{r+} = \lambda_{pm}^+ + L_d \cdot (I_{sd}^r + \Delta I_{sd}^r) \quad (6)$$

$$\lambda_{sd}^{r-} = \lambda_{pm}^- + L_d \cdot (I_{sd}^r - \Delta I_{sd}^r) \quad (7)$$

$$\hat{\lambda}_{pm}^+ = \frac{1}{\Delta I_{sd}^r} \left[I_{sd}^r \hat{\lambda}_{sd}^{r+} - (I_{sd}^r + \Delta I_{sd}^r) \hat{\lambda}_{sd}^r \right] \quad (8)$$

$$\hat{\lambda}_{pm}^- = \frac{1}{\Delta I_{sd}^r} \left[(I_{sd}^r - \Delta I_{sd}^r) \hat{\lambda}_{sd}^{r-} - I_{sd}^r \hat{\lambda}_{sd}^r \right] \quad (9)$$

$$\hat{\lambda}_{pm} = \frac{\hat{\lambda}_{pm}^+ + \hat{\lambda}_{pm}^-}{2} \quad (10)$$

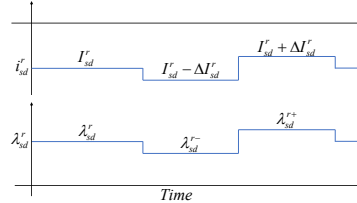


Fig. 3 – Schematic representation of the injected stator d-axis current, fundamental and small-amplitude, low frequency, squarewave currents, (i_{sd}^r) and resulting stator d-axis flux (λ_{sd}^r).

C. Temperature estimation

PM temperature estimation using PM flux linkage is especially challenging in VLF-PMSMs due to the variation of PM flux linkage with the stator current. Look-up tables (LUTs) will be used to compensate for this effect [13]. LUTs are built storing the estimated PM flux linkage ($\hat{\lambda}_{pm}$) values for different currents and PM temperatures. Linear interpolation is used to calculate PM temperature when the actual current or estimated PM value differs from stored values.

Fig. 4 shows an example of LUT which provides the PM flux linkage vs. stator current and PM temperature for the VLF-PMSMs test machine that will be used for the experimental verification of the method. It can be observed from Fig. 4 that the PM flux linkage decreases as the PM temperature (T_r) increases; this variation will be used for temperature estimation. It can be also observed that the PM flux linkage is heavily affected by stator current, which was an expected result due to the inherent variable leakage flux property of VLF-PMSMs.

Fig. 5 shows an example of the linear interpolation that has been performed to estimate the PM temperature when the d-axis is 0 A and the q-axis current is 400 A. The black dots in Fig. 5 are obtained from Fig. 4 at $I_{sd}^r = 0$ A and $I_{sq}^r = 400$ A, a linear interpolation (blue line) being performed in this case.

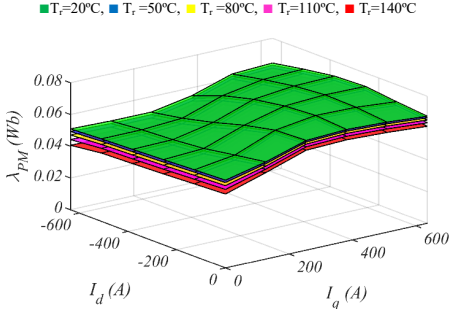


Fig. 4 – FEA results. PM flux linkage vs. stator current and PM temperature LUTs. $\omega_r=3750$ rpm, $T_r=20, 50, 80, 110$ and 140°C .

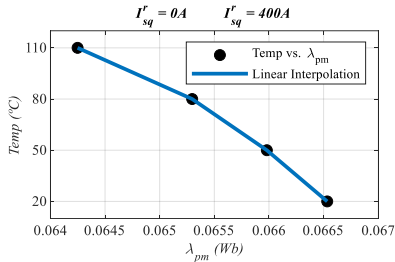


Fig. 5 – FEA results. Estimated PM flux linkage ($\hat{\lambda}_{pm}$) and linear interpolation for $I_{sq}^r = 0A$, $I_{sq}^r = 400A$ and $T_r=20, 50, 80$ and 110°C .

III. SIMULATION RESULTS

Fig. 6 shows the schematic representation of the VLF-PMSMs that will be used both for simulation and experimental verification of the proposed method, the parameters being shown in Table II. The machine is a 110kW, 8 poles VLF-PMSM. Fig. 7a and 7b show the commanded d and q-axis currents, respectively, a square-wave current of $|\Delta I_{sd}^r|=6.4$ A (0.01 pu) being superposed to the fundamental d-axis current. Fig. 7c and 7d show the estimated stator d and q-axis flux linkage for different PM temperatures with the response to the currents shown in Fig. 7a and 7b; the stator flux linkages have been obtained using the flux observer described in Section II. Fig. 8 shows the estimated PM flux linkage, which is obtained from (6)-(10) after injecting a square-wave current signal, see Fig. 7a, at each fundamental dq-axis current level.

TABLE II. MACHINE PARAMETERS				
P_{Rload} [kW]	I_{Rload} [A]	ω_r [rpm]	T_{Rload} [Nm]	Poles
110	640	10000	250	8

After the PM flux linkage is estimated, it is introduced in the stored LUTs to estimate temperature. During normal operation of the machine, the current operating point does not necessarily match with the stored values, in that case, interpolation of stored values must be performed. Linear and cubic spline interpolation methods are evaluated in this paper. Additionally, in order to

relate PM flux to temperature, the PM flux vs. temperature points must be interpolated in the stored LUTs. Linear and cubic spline interpolation methods are examined, and their performance is compared. It was found that quadratic regression of the PM flux vs. temperature provides accurate estimation, therefore it is also compared with interpolation methods.

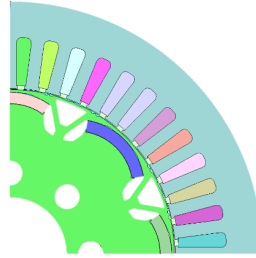


Fig. 6 – Schematic representation of the test machine.

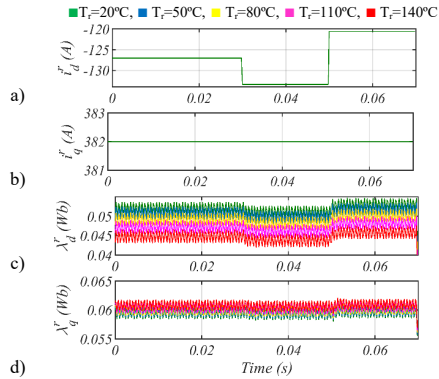


Fig. 7 – FEA results. a) d-axis and b) q-axis current c) estimated d-axis stator flux linkage and d) estimated q-axis stator flux linkage. $I_{sd}^r = -127A$, $I_{sq}^r = 382A$, $\omega_r=3750$ rpm, $T_r=20, 50, 80, 110$ and 140°C .

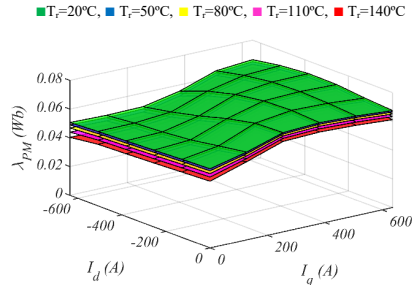


Fig. 8 – FEA results. Estimated PM flux linkage. $\omega_r=3750$ rpm, $T_r=20, 50, 80, 110$ and 140°C .

For operating point interpolation evaluation, new FEA simulations are performed at current levels different from the stored in the LUTs. Using the stored LUTs values, the PM flux at new simulated current levels is calculated through interpolations and compared with actual PM flux from FEA results at different temperatures ($T_i=20, 50, 80, 110$ and 140°C). Fig. 9a and 9b show linear interpolation and cubic spline interpolation error, respectively. It is observed that, for this VLF-PMSM, the interpolation error is similar in both cases, therefore linear interpolation is preferred because it is computationally faster.

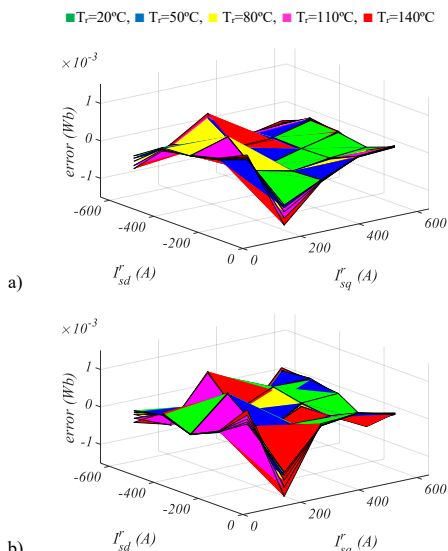


Fig. 9 – FEA results. a) introduced error by linear interpolation vs. stator current and b) introduced error by cubic spline interpolation vs. stator current. $\omega_r=3750$ rpm, $T_i=20, 50, 80, 110$ and 140°C

For PM flux vs. temperature interpolation, it is not possible to perform additional FEA simulations at other temperatures because the PM material behavior is only defined at 20, 50, 80, 110 and 140°C , therefore $T_i=80^\circ\text{C}$ is removed from interpolation and selected as test point. Fig. 10 shows linear, cubic spline interpolations and quadratic regression performed at zero stator current operating point. Their performance is compared using the actual PM flux linkage from FEA results at 80°C , and PM temperature is obtained using proposed interpolations and regression. Fig. 11 shows the temperature estimation error that these interpolations introduce in the temperature estimation method at 80°C . It is observed that cubic spline interpolation has very good accuracy, while the linear interpolation method exhibits larger error. Quadratic regression shows slightly worse accuracy than cubic spline interpolation but at a lower

computational cost. For final temperature estimation results, the linear interpolation accuracy is considered acceptable.

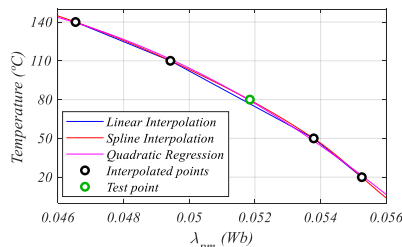


Fig. 10 – FEA results. Actual PM flux linkage (λ_{pm}) vs. PM temperature and interpolations for $I_{sd}^r=0\text{A}$, $I_{sq}^r=0\text{A}$ and $T_i=20, 50, 80, 110$ and 140°C .

■ Linear Interpolation, ■ Spline Interpolation, ■ Quadratic Regression

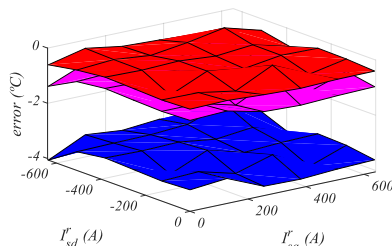


Fig. 11 – FEA results. Introduced temperature estimation error by PM flux interpolations vs. stator current at $T_i=80^\circ\text{C}$ and $\omega_r=3750$ rpm

Finally, using the estimated PM flux linkage and stored LUTs, the PM temperature is estimated. Fig. 12 shows the estimated temperature and the estimation error, which is seen to be within 10°C . This error can be considered adequate for demagnetization prevention purposes but might be excessive for precise torque control purposes.

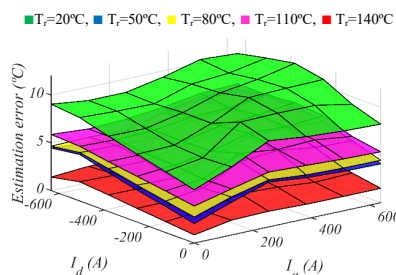


Fig. 12 – FEA results. Temperature estimation error. $\omega_r=3750$ rpm, $T_i=20, 50, 80, 110$ and 140°C .

IV. EXPERIMENTAL SETUP AND RESULTS

A. Experimental setup

The test bench used for the experimental verification of the method can be seen in Fig. 13. The test bench is composed of a conventional IPMSM used as a load, the VLF-PMSM under test (parameters shown in Table II). Fig. 14 shows a schematic representation of the power system setup, where each machine is driven by a three-phase inverter with shared DC-link. The inverters are controlled using a TMS320F28335 microcontroller. Fig. 15 shows the control box with the control PCB and auxiliary systems.

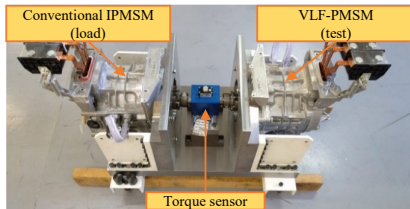


Fig. 13 – Test bench.

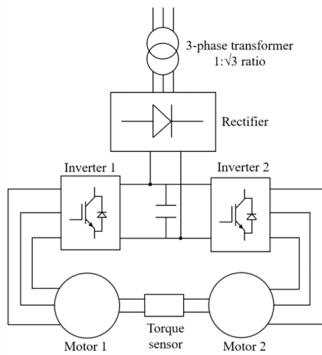


Fig. 14 – Experimental setup power system scheme.

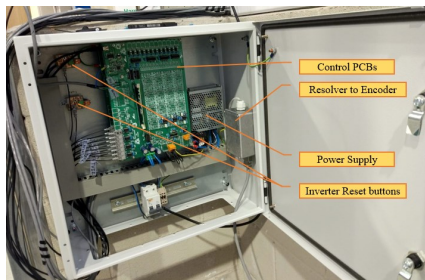


Fig. 15 – Control box with the control card and auxiliary systems.

In order to verify the accuracy of the proposed PM estimation method, the rotor PMs temperature is measured by means of thermocouples. A wireless PM temperature measurement system has been developed and implemented to transmit the measured PM temperature to a PC that will collect the PMs temperatures. Fig. 16 shows a picture of the wireless PM temperature measurement system along with the aluminum case attached to the rear part of the rotor. The temperature measurement system includes all analog signal conditioning, anti-aliasing filters, a microcontroller with a 10-bit analog to digital converters and a Wi-Fi transmission module. One single-cell LiPo battery is used to deliver power to the whole measurement system.

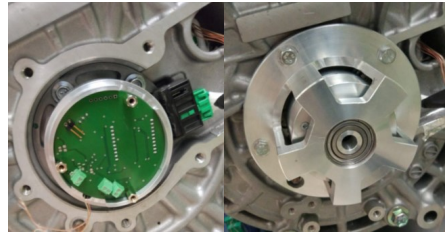


Fig. 16 – Wireless PM temperature measurement system along with the aluminum case attached to the rear part of the rotor.

B. Experimental results

First, the PM flux linkage of test machine is obtained with the stator flux observer and PM flux linkage estimation method presented in Section II at different temperatures ($T_r=20, 50, 80$ and 110°C). Fig. 17 shows the online estimated PM flux linkage along with the FEA results at 20°C for comparison. Experimental results exhibit lower PM flux linkage than FEA results, this is due to slightly lower magnetization of the PMs in the actual test machine. Despite this offset in the experimental results, the variable leakage flux capability can be observed, where the PM flux linkage increases at high load conditions (high q-axis current). It can be observed from Fig. 17 that experimental results have been performed up to 450 A, this was due to stator temperature limitations. The results shown in Fig. 17 will be stored in the microcontroller memory for PM temperature estimation during machine normal operation.

Fig. 18 shows the experimental results of the proposed PM temperature estimation method. Fig. 18a shows the d and q-axis currents that have been injected, Fig. 18b shows the estimated and measured temperatures and Fig. 18c shows the temperature estimation error. It can be observed that the temperature estimation error is $<5^\circ\text{C}$, what can be considered adequate for PM temperature monitoring applications.

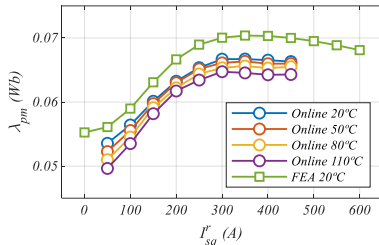


Fig. 17 – Experimental results. Estimated PM flux linkage and FEA results vs. q-axis stator current. $I_{sd}^* = -100A$, $\omega_r = 3000$ rpm, $T_r = 20, 50, 80$ and $110^\circ C$.

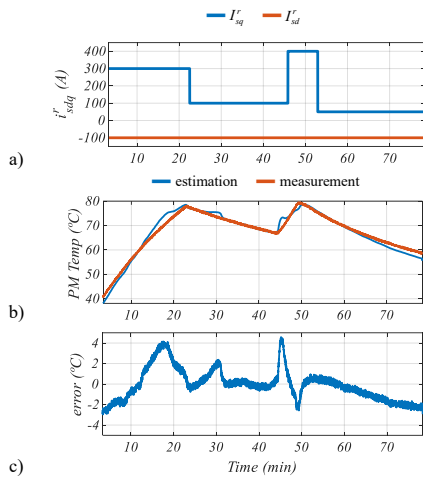


Fig. 18 – Experimental results. a) d and q-axis current used during the experiment, b) Estimated and measured rotor PM temperature, c) estimation error.

V. CONCLUSIONS

This paper proposes a method for PM temperature estimation in VLF-PMSMs based on the PM flux linkage variation with temperature. PM flux linkage is obtained from the stator flux linkage of the machine after applying a small-amplitude, low frequency, square wave current signal, which is superposed on top of the fundamental current excitation. The method requires LUTs linking the PM flux linkage vs. stator current and PM temperature. Simulation and experimental results have been provided to demonstrate the validity of the proposed technique. The accuracy of the proposed method has been verified by using a wireless PM temperature measurement system.

REFERENCES

- [1] Jang-Mok Kim and Seung-Ki Sul, "Speed control of interior permanent magnet synchronous motor drive for the flux weakening operation", *IEEE Trans. Ind. Appl.*, 33(1): 43–48, Jan. 1997.
- [2] V. Ostovic, "Memory motors", *IEEE Ind. Appl. Mag.*, 9(1): 52–61, Jan. 2003.
- [3] A. Athavale, T. Fukushige, T. Kato, C. Yu, and R. D. Lorenz, "Variable Leakage Flux IPMSMs for Reduced Losses Over a Driving Cycle While Maintaining Suitable Attributes for High-Frequency Injection-Based Rotor Position Self-Sensing", *IEEE Trans. Ind. Appl.*, 52(1): 234–241, Jan. 2016.
- [4] S. Li, B. Sarlioglu, S. Jurkovic, N. R. Patel, and P. Savagian, "Comparative Analysis of Torque Compensation Control Algorithms of Interior Permanent Magnet Machines for Automotive Applications Considering the Effects of Temperature Variation", *IEEE Trans. Transp. Electrification*, 3(3): 668–681, Sep. 2017.
- [5] A. M. EL-Refai, N. C. Harris, T. M. Jahns, and K. M. Rahman, "Thermal analysis of multibarrier interior PM synchronous Machine using lumped parameter model", *IEEE Trans. Energy Convers.*, 19(2): 303–309, Jun. 2004.
- [6] C. Kral, A. Haumer, and S. B. Lee, "A Practical Thermal Model for the Estimation of Permanent Magnet and Stator Winding Temperatures", *IEEE Trans. Power Electron.*, 29(1): 455–464, Jan. 2014.
- [7] D. D. Reigosa, D. Fernandez, H. Yoshida, T. Kato, and F. Briz, "Permanent-Magnet Temperature Estimation in PMSMs Using Pulsating High-Frequency Current Injection", *IEEE Trans. Ind. Appl.*, 51(4): 3159–3168, Jul. 2015.
- [8] D. D. Reigosa, F. Briz, P. Garcia, J. M. Guerrero, and M. W. Degner, "Magnet Temperature Estimation in Surface PM Machines Using High-Frequency Signal Injection", *IEEE Trans. Ind. Appl.*, 46(4): 1468–1475, Jul. 2010.
- [9] M. Ganchev, C. Kral, and T. Wolbank, "Sensorless rotor temperature estimation of permanent magnet synchronous motor under load conditions", in *Conf. IEEE Ind. Electron. Soc.*, 2012, pp: 1999–2004.
- [10] D. Fernandez, D. Reigosa, J. M. Guerrero, Z. Q. Zhu, C. Suarez, and F. Briz, "Influence of PM Coating on PM Magnetization State Estimation Methods Based on Magnetoresistive Effect", *IEEE Trans. Ind. Appl.*, 54(3): 2141–2150, May 2018.
- [11] D. Reigosa, D. Fernandez, T. Tanimoto, T. Kato, and F. Briz, "Comparative Analysis of BEMF and Pulsating High-Frequency Current Injection Methods for PM Temperature Estimation in PMSMs", *IEEE Trans. Power Electron.*, 32(5): 3691–3699, May 2017.
- [12] T. Kato, T. Matsuura, K. Sasaki, and T. Tanimoto, "Principle of variable leakage flux IPMSM using arc-shaped magnet considering variable motor parameter characteristics depending on load current", in *Proc IEEE Energy Convers Congr Expo*, 2017, pp: 5803–5810.
- [13] T. Kato, K. Sasaki, D. F. Laborda, D. Fernández, D. Reigosa, "Magnet temperature estimation methodology by using magnet flux linkage observer for variable leakage flux IPMSM", *IEEJ Journal of Industry Applications*, 140(4): 265–271, Apr. 2020.
- [14] P. L. Jansen and R. D. Lorenz, "A physically insightful approach to the design and accuracy assessment of flux observers for field oriented induction machine drives", *IEEE Trans. Ind. Appl.*, 30(1): 101–110, Jan. 1994.
- [15] J. S. Lee, C.-H. Choi, J.-K. Seok, and R. D. Lorenz, "Deadbeat-Direct Torque and Flux Control of Interior Permanent Magnet Synchronous Machines With Discrete Time Stator Current and Stator Flux Linkage Observer", *IEEE Trans. Ind. Appl.*, 47(4): 1749–1758, Jul. 2011.
- [16] H. Rehman, A. Derdiyok, M. K. Guven, and Longya Xu, "A new current model flux observer for wide speed range sensorless control of an induction machine", *IEEE Trans. Power Electron.*, 17(6): 1041–1048, Nov. 2002.

B.2.2 Enhanced Torque Estimation in Variable Leakage Flux PMSM Combining High and Low Frequency Signal Injection

Enhanced Torque Estimation in Variable Leakage Flux PMSM Combining High and Low Frequency Signal Injection

Diego F. Laborda
University of Oviedo
Dept. of Elect., Computer &
System Engineering
Gijón, Spain
dflaborda@uniovi.es

David Díaz Reigosa
University of Oviedo
Dept. of Elect., Computer &
System Engineering
Gijón, Spain
diazdavid@uniovi.es

Daniel Fernández
University of Oviedo
Dept. of Elect., Computer &
System Engineering
Gijón, Spain
fernandezalodaniel@uniovi.es

Kensuke Sasaki
Nissan Motor Co. Ltd
EV System Laboratory
Atsugi, Kanagawa, Japan
kensuke-sasaki@mail.nissan.co.jp

Takashi Kato
Nissan Motor Co. Ltd
EV System Laboratory
Atsugi, Kanagawa, Japan
katou-t@mail.nissan.co.jp

Fernando Briz
University of Oviedo
Dept. of Elect., Computer &
System Engineering
Gijón, Spain
fernando@isa.uniovi.es

Abstract— Torque measurement/estimation in Variable Leakage Flux Permanent Magnet Synchronous Motors (VLF-PMSMs) is required in many applications. Torque measurement systems are expensive, require extra room, add weight, can introduce resonances into the system and can be sensitive to electromagnetic interference. Alternatively, torque can be estimated, accurate knowledge of machine parameters being often required in this case, which for the case of VLF-PMSMs can be a serious drawback due to the large variation of machine parameters with the operating condition. This paper proposes a torque estimation method for VLF-PMSMs based on stator flux linkage estimation. Machine parameters involved in stator flux linkage estimation are obtained from the response of the machine to a pulsating high frequency current signal and a low frequency and small magnitude, square-wave current signal. Both signals are injected on top of the fundamental excitation and without interfering therefore with the normal operation of the machine.

Keywords— Torque estimation, VLF-PMSMs, variable leakage flux machine, high frequency signal injection, HF signal injection, low frequency signal injection, LF signal injection.

I. INTRODUCTION

Permanent Magnet Synchronous Motors (PMSMs) have been the preferred option for electric and hybrid-electric vehicles (EV & HEV) due to their high torque density, wide speed capability and higher efficiency. Variable flux PMSMs (VF-PMSMs) [1] and variable leakage flux PMSMs (VLF-PMSMs) [2]–[3] have recently been proposed as an alternative to traditional PMSMs in EV & HEV. Their main advantage over traditional PMSMs is that flux-weakening current required in traditional PMSMs to match the back electromotive force with the available voltage in the DC link [4], is highly reduced or even eliminated [1]–[3].

EV & HEV require precise control of the torque produced by the machine [5]–[7], torque measurement/estimation being therefore needed. If torque is to be measured, torque transducers

based on strain gauges are likely the preferred option. Less popular alternatives are systems based on torsional displacement methods [8]. Regardless of the method being used, precise torque measurement is expensive, requires room and extra cables, and introduces reliability concerns, torque estimation being therefore preferred [9]–[20]. Torque estimation methods can be roughly classified into torque equation-based methods [9]–[11] and indirect estimation methods [12]–[20]. All these methods [9]–[20] require precise knowledge of machine parameters (resistances, inductances or magnet flux) which can vary with the operating conditions of the machine (e.g. temperature or saturation).

This paper proposes a method to improve the accuracy of torque estimation in VLF-PMSMs. Torque equation requires knowledge of stator flux linkage. Machine parameters needed for stator flux linkage estimation are d and q -axis inductances, stator resistance and permanent magnets (PMs) flux. d and q -axes inductances and stator resistance will be estimated from the response of the machine to a pulsating high frequency (HF) current signal, while the PM flux linkage will be estimated from the response of the machine to a low frequency square-wave current signal. Both signals are low magnitude and are injected on top of the fundamental excitation.

The paper is organized as follows: Section II shows the fundamental model of a VLF-PMSM; Section III presents the proposed torque estimation method; Section IV provides FEA evaluation of the method. Finally, conclusions are provided in Section V.

II. FUNDAMENTAL MODEL OF A VLF-PMSM

The fundamental model of a VLF-PMSM in a reference frame synchronous with the rotor is given by (1) where p stands for the derivative respect to time, R_d , R_q , L_d and L_q are the d and q -axes resistances and inductances respectively, ω_r is the rotor

speed and λ_{pm} is the PM flux linkage; d -axis being aligned with PMs flux. The output torque can be expressed as (2) [21], where P is the number of poles, and λ_{sd}^r and λ_{sq}^r are the stator dq -axis flux linkages, (3) and (4) respectively.

$$\begin{bmatrix} v_{sd}^r \\ v_{sq}^r \end{bmatrix} = \begin{bmatrix} R_d & 0 \\ 0 & R_q \end{bmatrix} \begin{bmatrix} i_{sd}^r \\ i_{sq}^r \end{bmatrix} + P \begin{bmatrix} L_d & 0 \\ 0 & L_q \end{bmatrix} \begin{bmatrix} \dot{i}_{sd}^r \\ \dot{i}_{sq}^r \end{bmatrix} + \begin{bmatrix} 0 & -\omega_r L_q \\ \omega_r L_d & 0 \end{bmatrix} \begin{bmatrix} i_{sd}^r \\ i_{sq}^r \end{bmatrix} + \begin{bmatrix} 0 \\ \lambda_{pm} \omega_r \end{bmatrix} \quad (1)$$

$$T_{out} = \frac{3P}{2} \left[\lambda_{sd}^r i_{sq}^r - \lambda_{sq}^r i_{sd}^r \right] \quad (2)$$

$$\lambda_{sd}^r = i_{sd}^r L_d + \lambda_{pm} \quad (3) \quad \lambda_{sq}^r = i_{sq}^r L_q \quad (4)$$

III. TORQUE ESTIMATION BASED ON FLUX OBSERVER ENHANCED WITH ON-LINE PARAMETERS ESTIMATION

This section presents the proposed torque estimation method based on a flux observer enhanced with on-line parameters estimation. It is observed from (2)-(4) that the output torque of a VLF-PMSM is a function of dq -axes stator flux linkages, which depend on the dq -axes inductances, dq -axes resistances and PM flux [21]. These parameters vary during normal machine operation e.g. due to temperature or saturation. Fig. 2a-d shows the dq -axes inductances, stator resistance and PM flux linkage vs. dq -axes currents of the VLF-PMSMs that will be used for the experimental verification of the proposed method, obtained through FEA. It is observed from this figure that the variation of these parameters with the machine operating condition cannot be ignored, machine parameters estimation being therefore needed. Fig. 1 shows the proposed torque estimation method as well as its integration with machine control.

Torque estimation will require a) stator resistance and inductances estimation, b) stator flux linkage estimation and c) PM flux linkage estimation, this is described in the following sections.

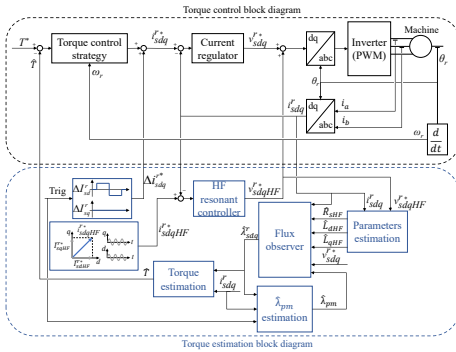


Fig. 1 – Integration of torque estimation and torque control.

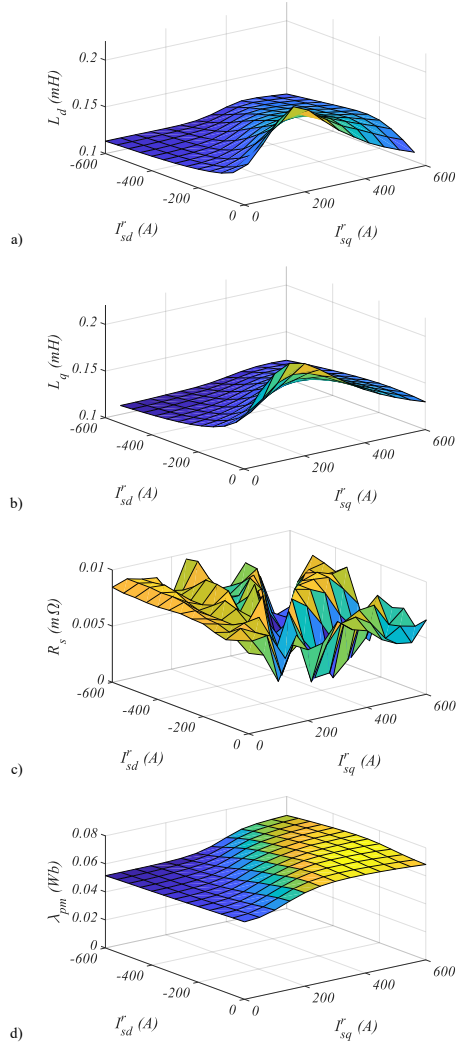


Fig. 2 – a) d -axis inductance vs. stator current, b) q -axis inductance vs. stator current, c) stator resistance vs. stator current and d) PM flux linkage vs. stator current. $I_{HF}=0.05$ pu, $\omega_{HF}=2*\pi*500$ rad/s, $\Delta L_d=0.02$ pu, $\omega_r=500$ rpm and $T_r=20^\circ\text{C}$.

A. Resistance and inductances estimation using high frequency signal injection

Injection of a high frequency signal has been shown to be a reliable method for resistance and inductance estimation [11],[22],[23]. In this paper, the injection of a pulsating high frequency current will be used to estimate stator resistance and inductances needed by the flux observer. The method has some similarities with the proposal in [11]. However, the method in [11] required two pulsating HF currents while only one HF signal is required in the method proposed in this paper. This reduces the adverse effects of the HF signal and simplifies the implementation.

If the PMSM is fed with a HF voltage/current, the magnet flux dependent term in (1) can be safely neglected, as it does not contain any HF component, the HF model shown in (5) is obtained, where R_{dHF} , R_{qHF} , L_{dHF} and L_{qHF} are the d and q -axes high frequency resistances and inductances, respectively; i_{sdHF}^r and i_{sqHF}^r are the d and q -axes high frequency currents; v_{sdHF}^r and v_{sqHF}^r are the d and q -axes high frequency voltages; d and q -axis HF inductances and resistances can be obtained by injecting a pulsating HF at 45° from the d axis, (6) of magnitude I_{HF}^r and frequency ω_{HF} (see Fig. 1). A resonant controller can be used for this purpose [11]. The HF voltages that will be commanded by the resonant controller will be of the form shown in (7).

$$\begin{bmatrix} v_{sdHF}^r \\ v_{sqHF}^r \end{bmatrix} = \begin{bmatrix} R_{dHF} & 0 \\ 0 & R_{qHF} \end{bmatrix} \begin{bmatrix} i_{sdHF}^r \\ i_{sqHF}^r \end{bmatrix} + p \begin{bmatrix} L_{dHF} & 0 \\ 0 & L_{qHF} \end{bmatrix} \begin{bmatrix} \dot{i}_{sdHF}^r \\ \dot{i}_{sqHF}^r \end{bmatrix} + \begin{bmatrix} 0 & -\omega_r L_{qHF} \\ \omega_r L_{dHF} & 0 \end{bmatrix} \begin{bmatrix} i_{sdHF}^r \\ i_{sqHF}^r \end{bmatrix} \quad (5)$$

$$i_{sdHF}^{r*} = \begin{bmatrix} \bar{I}_{sdHF}^{r*} \\ \bar{I}_{sqHF}^{r*} \end{bmatrix} = \begin{bmatrix} I_{HF}^r \cos(\omega_{HF} t) \\ I_{HF}^r \cos(\omega_{HF} t) \end{bmatrix} \quad (6)$$

$$v_{sdHF}^{r*} = \begin{bmatrix} \bar{V}_{sdHF}^{r*} \\ \bar{V}_{sqHF}^{r*} \end{bmatrix} = \begin{bmatrix} (R_{dHF} + j\omega_{HF} L_{dHF}) \bar{I}_{sdHF}^r - \omega_r L_{qHF} \bar{I}_{sqHF}^r \\ (R_{qHF} + j\omega_{HF} L_{qHF}) \bar{I}_{sqHF}^r + \omega_r L_{dHF} \bar{I}_{sdHF}^r \end{bmatrix} \quad (7)$$

L_{dHF} can be estimated from the measured d -axis HF current, i_{sdqHF}^r (8), and the commanded d -axis HF voltage, v_{sdqHF}^r (9). Both (8) and (9) can be separated into positive sequence ($i_{sdqHFpc}^r$ and $v_{sdqHFpc}^r$) and negative sequence ($i_{sdqHFnc}^r$ and $v_{sdqHFnc}^r$) components, (10) and (11). The d -axis HF impedance, (12) can be obtained either from the positive or negative sequence component, the d -axis HF inductance being its imaginary part (13).

$$i_{sdqHF}^r = \begin{bmatrix} \bar{I}_{sdHF}^{r*} \\ 0 \end{bmatrix} = \begin{bmatrix} I_{HF}^r \cos(\omega_{HF} t) \\ 0 \end{bmatrix} \quad (8)$$

$$v_{sdqHF}^r = \begin{bmatrix} \bar{V}_{sdHF}^{r*} \\ 0 \end{bmatrix} = \begin{bmatrix} (R_{dHF} + j\omega_{HF} L_{dHF}) \bar{I}_{sdHF}^r - \omega_r L_{qHF} \bar{I}_{sdHF}^r \\ 0 \end{bmatrix} \quad (9)$$

$$i_{sdqHF}^{r*} = \frac{i_{sdqHF}^r}{2} e^{j\omega_{HF} t} + \frac{i_{sdqHF}^r}{2} e^{-j\omega_{HF} t} = i_{sdqHFpc}^r + i_{sdqHFnc}^r \quad (10)$$

$$v_{sdqHF}^{r*} = \frac{v_{sdqHF}^r}{2} e^{j(\omega_{HF} t - \varphi_{2d})} + \frac{v_{sdqHF}^r}{2} e^{j(-\omega_{HF} t + \varphi_{2d})} = v_{sdqHFpc}^r + v_{sdqHFnc}^r \quad (11)$$

$$Z_{dHF} = R_{dHF} - \omega_r L_{qHF} + j\omega_{HF} L_{dHF} = \frac{v_{sdqHFpc}^r}{i_{sdqHFpc}^r} = \frac{v_{sdqHFnc}^r}{i_{sdqHFnc}^r} \quad (12)$$

$$L_{dHF} = \Im[Z_{dHF}] / \omega_{HF} \quad (13)$$

L_{qHF} can be estimated from the measured q -axis HF current, i_{sdqHF}^{r*} (14), and the commanded q -axis HF voltage, v_{sdqHF}^{r*} (15), using (16)-(19) similarly as for d -axis HF inductance estimation.

$$i_{sdqHF}^{r*} = \begin{bmatrix} 0 \\ \bar{I}_{sqHF}^{r*} \end{bmatrix} = \begin{bmatrix} 0 \\ I_{HF}^r \cos(\omega_{HF} t) \end{bmatrix} \quad (14)$$

$$v_{sdqHF}^{r*} = \begin{bmatrix} 0 \\ \bar{V}_{sqHF}^{r*} \end{bmatrix} = \begin{bmatrix} 0 \\ (R_{qHF} + j\omega_{HF} L_{qHF}) \bar{I}_{sqHF}^r + \omega_r L_{dHF} \bar{I}_{sdHF}^r \end{bmatrix} \quad (15)$$

$$i_{sdqHF}^{r*} = \frac{i_{sdqHF}^r}{2} e^{j\omega_{HF} t} + \frac{i_{sdqHF}^r}{2} e^{-j\omega_{HF} t} = i_{sdqHFpc}^r + i_{sdqHFnc}^r \quad (16)$$

$$v_{sdqHF}^{r*} = \frac{v_{sdqHF}^r}{2} e^{j(\omega_{HF} t - \varphi_{2q})} + \frac{v_{sdqHF}^r}{2} e^{j(-\omega_{HF} t + \varphi_{2q})} = v_{sdqHFpc}^r + v_{sdqHFnc}^r \quad (17)$$

$$Z_{qHF} = R_{qHF} + \omega_r L_{dHF} + j\omega_{HF} L_{qHF} = \frac{v_{sdqHFpc}^r}{i_{sdqHFpc}^r} = \frac{v_{sdqHFnc}^r}{i_{sdqHFnc}^r} \quad (18)$$

$$L_{qHF} = \Im[Z_{qHF}] / \omega_{HF} \quad (19)$$

dq -axes HF resistance can be obtained from (20) and (21), the stator HF resistance R_{sHF} (22) being the average of the d and q -axis resistances.

$$R_{dHF} = \Re[Z_{dHF}] + \omega_r L_{qHF} \quad (20)$$

$$R_{qHF} = \Re[Z_{qHF}] - \omega_r L_{dHF} \quad (21)$$

$$R_{sHF} = \frac{R_{dHF} + R_{qHF}}{2} \quad (22)$$

B. Stator flux linkage estimation

Different stator flux observers have been proposed in the literature, the voltage model (23)-(24) and the current model (3)-(4) based being the preferred options [24]-[25]. Gopinath type flux observer was proposed in [25], combining the voltage and current models. The advantages and drawbacks of both models can be seen in Table I.

$$\lambda_{sd}^s(t) = \int (V_{sd}^s(t) - R_s \cdot I_{sd}^s(t)) dt \quad (23)$$

$$\lambda_{sq}^s(t) = \int (V_{sq}^s(t) - R_s \cdot I_{sq}^s(t)) dt \quad (24)$$

The current model can be used to estimate stator flux in the whole speed range of the machine but parameters, such as magnet flux linkage and inductances, must be previously known. On the other hand, voltage model can be used to estimate machine flux at high speeds [24], at low speeds it becomes inaccurate due to the diminishing magnitude of the Back-EMF

with speed and it cannot be used at standstill. In addition, as a pure integrator is required to estimate the flux, there is an initial estimation error (integration constant) which needs to be compensated.

Gopinath type flux observers combine voltage at high speed and the current model at low speed including standstill, a PI controller being used to make a smooth transition between models. The controller bandwidth will set the transition frequency from current to voltage model. This type of flux observer provides reliable estimation in the whole speed range of the machine, including standstill, being more sensitive to machine parameters at low speeds.

TABLE I. ADVANTAGES AND DRAWBACKS OF FLUX MODELS

	CURRENT MODEL	VOLTAGE MODEL	GOPINATH
Parameter independency	✘	✘	✘
No initial state error	✔	✘	✔
Estimation in the whole speed range, including standstill	✔	✘	✔

The Gopinath type flux observer shown in Fig. 3 will be used in this paper to estimate the stator flux linkage [25]. Observer parameters are estimated using HF signal injection. PM flux linkage estimation discussed in the next section will be used to further enhance the stator flux linkage estimation.

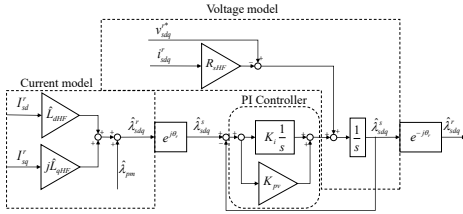


Fig. 3 – Gopinath type flux observer scheme.

C. PM flux linkage estimation

PM flux linkage is relatively easy to estimate from the back-EMF at no load but is difficult to estimate when the machine is loaded. The method proposed in [26] is used, in which λ_{pm} is estimated from the stator flux linkage in combination with the response of the machine to the injection of a quasi-square-wave, small-amplitude and low frequency, current signal (ΔI_{sd}^r). Both signals are injected on top of the fundamental current [26].

The PM flux linkage is estimated from the response of the machine to a low frequency, small magnitude, quasi-square-wave current signal of magnitude ΔI_{sd}^r injected on top of the fundamental current [26], this is schematically represented in Fig. 4. The d -axis stator flux linkage, λ_{sd}^r is represented by (25), λ_{sd}^{r+} is the d -axis flux linkage when positive d -axis current step, ΔI_{sd}^r , is applied (26), while λ_{sd}^{r-} is the d -axis flux linkage when negative d -axis current step, $-\Delta I_{sd}^r$, is applied (27). The stator flux linkages, λ_{sd}^r , λ_{sd}^{r+} and λ_{sd}^{r-} are not obtained using (25)–(27), instead, they are estimated by the Gopinath type flux observer shown in the previous subsection. $\hat{\lambda}_{pm}^+$ and $\hat{\lambda}_{pm}^-$ are

estimated from (28) and (29), respectively. $\hat{\lambda}_{pm}$ (PM flux linkage when no applying ΔI_{sd}^r) is finally obtained as the average of $\hat{\lambda}_{pm}^+$ and $\hat{\lambda}_{pm}^-$, (30).

$$\lambda_{sd}^r = \lambda_{pm} + L_d \cdot I_{sd}^r \quad (25)$$

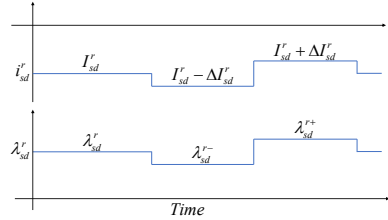
$$\lambda_{sd}^{r+} = \lambda_{pm}^+ + L_d \cdot (I_{sd}^r + \Delta I_{sd}^r) \quad (26)$$

$$\lambda_{sd}^{r-} = \lambda_{pm}^- + L_d \cdot (I_{sd}^r - \Delta I_{sd}^r) \quad (27)$$

$$\hat{\lambda}_{pm}^+ = \frac{1}{\Delta I_{sd}^r} \left[I_{sd}^r \hat{\lambda}_{sd}^{r+} - (I_{sd}^r + \Delta I_{sd}^r) \hat{\lambda}_{sd}^r \right] \quad (28)$$

$$\hat{\lambda}_{pm}^- = \frac{1}{\Delta I_{sd}^r} \left[(I_{sd}^r - \Delta I_{sd}^r) \hat{\lambda}_{sd}^r - I_{sd}^r \hat{\lambda}_{sd}^{r-} \right] \quad (29)$$

$$\hat{\lambda}_{pm} = \frac{\hat{\lambda}_{pm}^+ + \hat{\lambda}_{pm}^-}{2} \quad (30)$$

Fig. 4 – Schematic representation of the injected stator d -axis current, fundamental and small-amplitude, low frequency, squarewave currents, (i_{sd}^r) and resulting stator d -axis flux (λ_{sd}^r).

IV. FEA ANALYSIS OF THE METHOD

Simulation results of the proposed method by means of FEA are provided in this section. Fig. 5 shows the schematic representation of the test machine that will be used for simulation verification. The parameters of the VLF-PMSM test machine are shown in Table II.

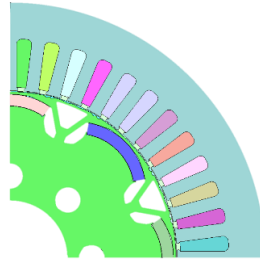


Fig. 5 – Schematic representation of the test machine.

TABLE II. MACHINE PARAMETERS

P_{Rated} [kW]	110
I_{Rated} [A]	640
ω_r [rpm]	10000
T_{Rated} [Nm]	250
Poles	8

Simulations are performed at 500 rpm (low speed) in order to test the proposed method performance in the speed region where the current model dominates the flux observer estimation and the parameter sensitivity is higher. A pulsating HF current signal with $I_{HF} = 0.05pu$ is injected to estimate HF inductances and resistance following the method described in Section IV.

A. Cross-coupling inductance effect

The obtained d and q -axes HF inductances are compared with the DC inductances in Fig. 6a and 6b, respectively. The obtained HF and DC values are not matching, this is produced by the relatively high cross-coupling inductance present in VLF-PMSMs. In Section III, the cross-coupling inductance effect is not taken into account. Modifying the HF model (5) to include this effect, the new HF model is shown in (31).

$$\begin{bmatrix} v_{sdHF}^r \\ v_{sqHF}^r \end{bmatrix} = \begin{bmatrix} R_{dHF} & 0 \\ 0 & R_{qHF} \end{bmatrix} \begin{bmatrix} i_{sdHF}^r \\ i_{sqHF}^r \end{bmatrix} + p \begin{bmatrix} L_{dHF} & L_{qdHF} \\ L_{dqHF} & L_{qHF} \end{bmatrix} \begin{bmatrix} i_{sdHF}^r \\ i_{sqHF}^r \end{bmatrix} + \begin{bmatrix} -\omega_r L_{dqHF} & -\omega_r L_{qHF} \\ \omega_r L_{dHF} & \omega_r L_{qdHF} \end{bmatrix} \begin{bmatrix} i_{sdHF}^r \\ i_{sqHF}^r \end{bmatrix} \quad (31)$$

■ DC inductance ■ FEA HF inductance

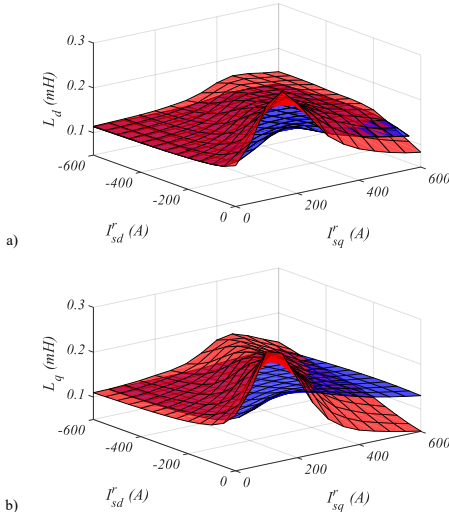


Fig. 6 - a) d -axis HF and DC inductance vs. stator current and b) q -axis HF and DC inductance vs. stator current. $I_{HF}=0.05 pu$, $\omega_{HF}=2*\pi*500 rad/s$, $\omega_r=500 rpm$ and $T_r=20^\circ C$.

Following the procedure described in Section III with the new HF model, the estimated HF inductances in (13) and (19) becomes (32) and (33), respectively. It is observed from (32) and (33) that actual d and q -axis HF inductances can be obtained by subtracting the cross-coupling (L_{qdHF} and L_{dqHF}) inductances

from estimated values. The cross-coupling inductances are defined in (34) and (35), being $L_{qdHF} = L_{dqHF}$.

$$\hat{L}_{dHF} = \Im[Z_{dHF}] / \omega_{HF} = L_{dHF} + L_{qdHF} \quad (32)$$

$$\hat{L}_{qHF} = \Im[Z_{qHF}] / \omega_{HF} = L_{qHF} + L_{dqHF} \quad (33)$$

$$L_{qdHF} = \frac{\partial \lambda_{sd}}{\partial i_{sq}^r} \quad (34)$$

$$L_{dqHF} = \frac{\partial \lambda_{sq}}{\partial i_{sd}^r} \quad (35)$$

In order to compensate for the cross-coupling inductance effect, cross-coupling inductance value must be known. It is possible to estimate the cross-coupling inductance using the q -axis stator flux response to the squarewave, small-amplitude, low frequency current signal already used in Section III. In Section III, only d -axis stator flux estimation from flux observer was used to estimate PM flux linkage; for cross-coupling inductance estimation, only q -axis stator flux estimation from flux observer will be used. The cross-coupling inductance is obtained in (36), being λ_{sq}^{r+} the q -axis flux linkage when positive d -axis current step, ΔI_{sd}^{r+} , is applied, while λ_{sq}^{r-} is the q -axis flux linkage when negative d -axis current step, $-\Delta I_{sd}^{r-}$, is applied.

$$L_{qdHF} = L_{dqHF} = \frac{\partial \lambda_{sq}}{\partial i_{sd}^r} \approx \frac{\Delta \lambda_{sq}}{\Delta i_{sd}^r} = \frac{\lambda_{sq}^{r+} - \lambda_{sq}^{r-}}{2 \Delta I_{sd}^r} \quad (36)$$

B. DC inductance estimation from HF inductance

Another reason for the mismatch between estimated HF inductance and DC inductance is the magnetic saturation of the machine. While the DC inductance is defined as the linearized or apparent inductance from the origin to the operating point, the HF (or dynamic) inductance is defined as the variation of the flux respect the current (37) i.e. the slope of the flux-current curve around the operating point [27]. This is schematically shown in Fig. 7.

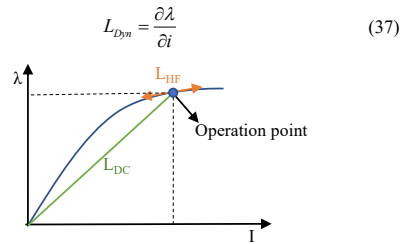


Fig. 7 – Schematic representation of DC or linearized inductance and HF or incremental inductance.

In order to obtain the DC inductances from the HF results, the HF inductance can be integrated along the current trajectory of the machine. This technique will provide instantaneous DC

inductance estimation in d and q -axis using the estimated HF inductance, as shown in (38) and (39).

$$L_{dDC} = \frac{\int L_{dDyn}(I_{sd}^r, I_{sq}^r) \partial I_{sd}^r - \lambda_{pm}(I_{sd}^r, I_{sq}^r)}{I_{sd}^r} \quad (38)$$

$$L_{qDC} = \frac{\int L_{qDyn}(I_{sd}^r, I_{sq}^r) \partial I_{sq}^r}{I_{sq}^r} \quad (39)$$

C. Simulation results

HF inductances are calculated using (32) and (33) to take into account the cross-coupling inductance. The cross-coupling inductance is obtained from (36) using the q -axis flux observer output estimation. Fig. 8a and 8b show the estimated d and q -axis HF inductances considering the cross-coupling inductance, respectively. For the sake of comparison, Fig. 8a and 8b, also show the dynamic inductances theoretically calculated from FEA data using (37) for both d and q -axis. It is observed that HF and dynamic inductances are matching as it was expected.

■ Dyn inductance ■ FEA HF inductance

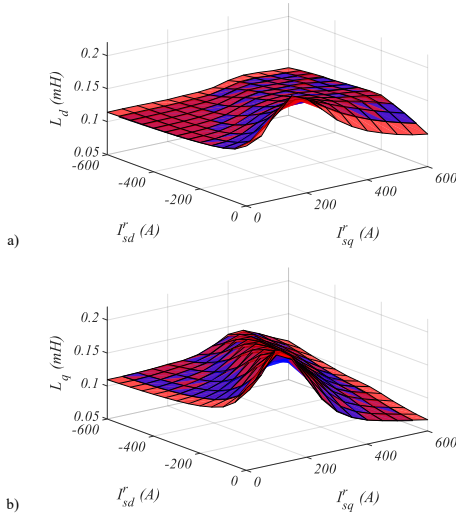


Fig. 8 - a) d -axis HF and Dynamic inductance vs. stator current and b) q -axis HF and Dynamic inductance vs. stator current. $I_{HF}=0.05$ pu, $\omega_{HF}=2*\pi*500$ rad/s, $\omega_s=500$ rpm and $T_s=20^\circ\text{C}$.

In order to further enhance the stator flux observer estimation, instead of introducing the HF inductances into the flux observer, the DC inductance values are estimated using (38) and (39). Fig. 9a and 9b show the estimated d and q -axis DC inductances, respectively, and actual d and q -axis DC inductances are also shown for comparison. It is observed that estimated and actual DC inductances are matching as it was expected.

■ DC inductance ■ FEA estimated DC inductance

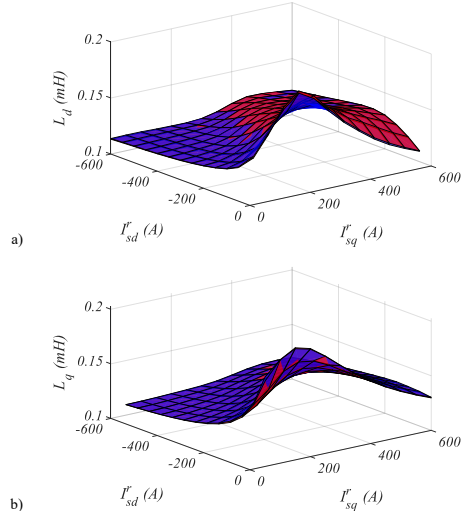


Fig. 9 - a) d -axis estimated and actual DC inductance vs. stator current and b) q -axis estimated and actual DC inductance vs. stator current. $I_{HF}=0.05$ pu, $\omega_{HF}=2*\pi*500$ rad/s, $\omega_s=500$ rpm and $T_s=20^\circ\text{C}$.

After the stator inductances are estimated, using the procedure described in Section III, the stator resistance is estimated and represented in Fig. 2c.

The last parameter to be estimated is the PM flux linkage, it is estimated using a square-wave current signal with $\pm \Delta I_{sd}^r=0$, as described in Section III. Fig. 2d shows the estimated PM flux linkage using this procedure.

The estimated parameters and PM flux linkage are used in the Gopinath type flux observer. Estimated d and q -axis stator flux are shown in Fig. 10a and 10b, respectively, and actual machine flux from FEA data is also represented for comparison. The stator flux observer provides an accurate estimation as it was expected. Finally, the torque is estimated using (2) and it is represented vs. stator current in Fig. 11a and the estimation error is calculated as (40) and shown in Fig. 11b, being \hat{T} the torque estimated by proposed method and T_{FEA} the actually produced torque extracted from FEA results. It is observed from Fig. 10 that the method provides good accuracy in the whole stator current region. The largest error is produced at high load and deep flux weakening current region, where the machine is not likely to be operated. Furthermore, the maximum error magnitude is around 1 Nm, which is 0.4% of rated torque.

$$error = \hat{T} - T_{FEA} \quad (40)$$

V. CONCLUSIONS

This paper proposes a torque estimation method for VLF-PMSMs based on the stator flux linkage. Stator flux linkage is estimated using a flux observer. d and q -axis inductances and stator resistance are estimated online from the response of the machine to a pulsating HF current signal which is injected on top of the fundamental excitation. PM flux linkage is estimated from the response to a low-frequency, low-magnitude square-wave current which is also injected on top of the fundamental excitation. Cross-coupling inductance effect is compensated and DC inductance is obtained from HF values and used in the stator flux observer. Accurate stator flux estimation is obtained from flux observer using estimated parameters, leading to accurate torque estimation. Simulation results have been provided to demonstrate the validity of the proposed technique.

REFERENCES

- [1] V. Ostovic, "Memory motors", IEEE Ind. Appl. Mag., 9(1): 52–61, Jan. 2003.
- [2] T. Kato, M. Minowa, H. Hijikata, K. Akatsu, and R. D. Lorenz, "Design Methodology for Variable Leakage Flux IPM for Automobile Traction Drives", IEEE Trans. Ind. Appl., 51(5): 3811–3821, Sep. 2015.
- [3] A. Athavale, T. Fukushige, T. Kato, C. Yu, and R. D. Lorenz, "Variable Leakage Flux IPMSMs for Reduced Losses Over a Driving Cycle While Maintaining Suitable Attributes for High-Frequency Injection-Based Rotor Position Self-Sensing", IEEE Trans. Ind. Appl., 52(1): 234–241, Jan. 2016.
- [4] Jang-Mok Kim and Seung-Ki Sul, "Speed control of interior permanent magnet synchronous motor drive for the flux weakening operation", IEEE Trans. Ind. Appl., 33(1): 43–48, Jan. 1997.
- [5] C. Lin, S. Liang, J. Chen, and X. Gao, "A Multi-Objective Optimal Torque Distribution Strategy for Four In-Wheel-Motor Drive Electric Vehicles", IEEE Access, 7: 64627–64640, 2019.
- [6] D. O. Neacsu and K. Rajashekara, "Comparative analysis of torque-controlled IM drives with applications in electric and hybrid vehicles", IEEE Trans. Power Electron., 16(2): 240–247, Mar. 2001.
- [7] Z. Zhang, R. Ma, L. Wang, and J. Zhang, "Novel PMSM Control for Anti-Lock Braking Considering Transmission Properties of the Electric Vehicle", IEEE Trans. Veh. Technol., 67(11): 10378–10386, Nov. 2018.
- [8] P. Sue, D. Wilson, L. Farr, and A. Kretschmar, "High precision torque measurement on a rotating load coupling for power generation operations", in IEEE Int. Instrum. Meas. Technol. Conf. Proc., pp: 518–523, May 2012.
- [9] K. C. Yeo, G. Heins, and F. De Boer, "Comparison of torque estimators for PMSM", in Australas. Univ. Power Eng. Conf., pp: 1–6, Dec. 2008.
- [10] B. Cheng and T. R. Tesch, "Torque Feedforward Control Technique for Permanent-Magnet Synchronous Motors", IEEE Trans. Ind. Electron., 57(3): 969–974, Mar. 2010.
- [11] M. Martinez, D. Reigosa, D. Fernández, J. M. Guerrero, and F. Briz, "PMSMs Torque Estimation Using Pulsating HF Current Injection", in 2018 IEEE 9th Int. Symp. Sensorless Control Electr. Drives SLED, pp: 96–101, Sep. 2018.
- [12] F. Jukic, D. Sumina, and I. Erceg, "Comparison of torque estimation methods for interior permanent magnet wind power generator", in Int. Conf. Electr. Drives Power Electron. EDPE, pp: 291–296, Oct. 2017.
- [13] J. X. Xu, S. K. Panda, Y. J. Pan, T. H. Lee, and B. H. Lam, "Improved PMSM pulsating torque minimization with iterative learning and sliding mode observer", in IEEE Int. Conf. Ind. Electron. Control Instrum., Nagoya, Japan, 3, pp: 1931–1936, 2000.

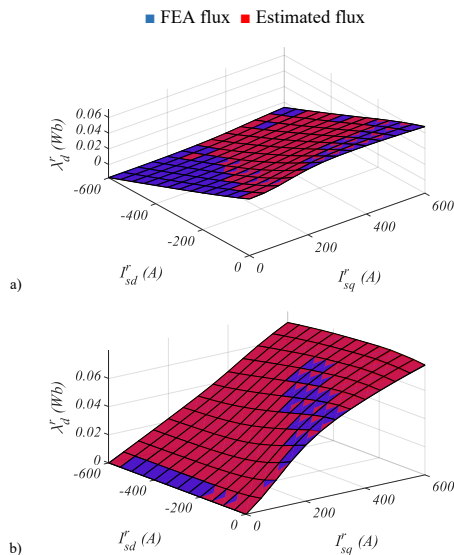


Fig. 10 - a) estimated and actual d -axis flux vs. stator current and b) estimated and actual q -axis flux vs. stator current. $I_{HF}=0.05$ pu, $\omega_{HF}=2*\pi*500$ rad/s, $\omega_r=500$ rpm and $T_r=20^\circ\text{C}$.

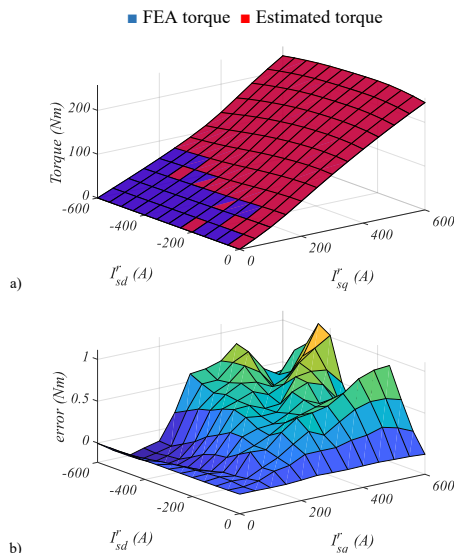


Fig. 11 - a) estimated and FEA output torque, and b) estimation error. $I_{HF}=0.05$ pu, $\omega_{HF}=2*\pi*500$ rad/s, $\omega_r=500$ rpm and $T_r=20^\circ\text{C}$.

- [14] Weizhe Qian, S. K. Panda, and Jian-Xin Xu, "Torque ripple minimization in PM synchronous motors using iterative learning control", *IEEE Trans. Power Electron.*, 19(2): 272–279, Mar. 2004.
- [15] Se-Kyo Chung, Hyun-Soo Kim, Chang-Gyun Kim, and Myung-Joong Youn, "A new instantaneous torque control of PM synchronous motor for high-performance direct-drive applications", *IEEE Trans. Power Electron.*, 13(3): 388–400, May 1998.
- [16] X. Dong, W. Tianmiao, and W. Hongxing, "Comparison between model reference observer and reduced order observer of PMSM torque", in *IEEE Conf. Ind. Electron. Appl.*, pp: 663–667, Jun. 2011.
- [17] Q. Liu and K. Hameyer, "High-Performance Adaptive Torque Control for an IPMSM With Real-Time MTPA Operation", *IEEE Trans. Energy Convers.*, 32(2): 571–581, Jun. 2017.
- [18] Y. A.-R. I. Mohamed and T. K. Lee, "Adaptive self-tuning MTPA vector controller for IPMSM drive system", *IEEE Trans. Energy Convers.*, 21(3): 636–644, Sep. 2006.
- [19] W. F. Traoré and R. McCann, "Torque measurements in synchronous generators using giant magnetoresistive sensor arrays via the Maxwell stress tensor", in *2013 IEEE Power Energy Soc. Gen. Meet.*, pp: 1–5, Jul. 2013.
- [20] Z. Lin, D. S. Reay, B. W. Williams, and X. He, "Online Modeling for Switched Reluctance Motors Using B-Spline Neural Networks", *IEEE Trans. Ind. Electron.*, 54(6): 3317–3322, Dec. 2007.
- [21] J. F. Gieras, *Permanent magnet motor technology: design and applications*. CRC press, 2009.
- [22] H.-S. Jung, D. Park, H. Kim, S.-K. Sul, and D. J. Berry, "Non-Invasive Magnet Temperature Estimation of IPMSM Based on High-Frequency Inductance With a Pulsating High-Frequency Voltage Signal Injection", *IEEE Trans. Ind. Appl.*, 55(3): 3076–3086, May 2019.
- [23] D. Reigosa, D. Fernández, M. Martínez, J. M. Guerrero, A. B. Diez, and F. Briz, "Magnet Temperature Estimation in Permanent Magnet Synchronous Machines Using the High Frequency Inductance", *IEEE Trans. Ind. Appl.*, 55(3): 2750–2757, May 2019.
- [24] J. S. Lee, C.-H. Choi, J.-K. Seok, and R. D. Lorenz, "Deadbeat-Direct Torque and Flux Control of Interior Permanent Magnet Synchronous Machines With Discrete Time Stator Current and Stator Flux Linkage Observer", *IEEE Trans. Ind. Appl.*, 47(4): 1749–1758, Jul. 2011.
- [25] P. L. Jansen and R. D. Lorenz, "A physically insightful approach to the design and accuracy assessment of flux observers for field oriented induction machine drives", *IEEE Trans. Ind. Appl.*, 30(1): 101–110, Jan. 1994.
- [26] T. Kato, T. Matsuura, K. Sasaki, and T. Tanimoto, "Principle of variable leakage flux IPMSM using arc-shaped magnet considering variable motor parameter characteristics depending on load current", in *Proc IEEE Energy Convers Congr Expo*, pp: 5803–5810, Oct. 2017.
- [27] W. Xu and R. D. Lorenz, "High-Frequency Injection-Based Stator Flux Linkage and Torque Estimation for DB-DTFC Implementation on IPMSMs Considering Cross-Saturation Effects," *IEEE Trans. Ind. Appl.*, 50(6): 3805-3815, Nov.-Dec. 2014.

B.2.3 Online PI Current Controller Tuning Based on Machine High-Frequency Parameters

Online PI Current Controller Tuning Based on Machine High-Frequency Parameters

Diego F. Laborda
University of Oviedo
Dept. of Elect., Computer &
System Engineering
Gijón, Spain
dflaborda@uniovi.es

Juan Manuel Guerrero
University of Oviedo
Dept. of Elect., Computer &
System Engineering
Gijón, Spain
guerrero@uniovi.es

Marcos Orviz Zapico
University of Oviedo
Dept. of Elect., Computer &
System Engineering
Gijón, Spain
orvizmarcos@uniovi.es

Daniel Fernández
University of Oviedo
Dept. of Elect., Computer &
System Engineering
Gijón, Spain
fernandezaldaniel@uniovi.es

David Díaz Reigosa
University of Oviedo
Dept. of Elect., Computer &
System Engineering
Gijón, Spain
diazdavid@uniovi.es

Fernando Briz
University of Oviedo
Dept. of Elect., Computer &
System Engineering
Gijón, Spain
fernando@isa.uniovi.es

Abstract— Synchronous PI current regulators are the preferred option for the current control of ac electric drives. The controller tuning requires knowledge of machine parameters that can change during normal operation, e.g. due to saturation and temperature variations, leading to changes in the current regulator dynamic response. This paper proposes the use of high-frequency signal injection (HFI) for parameter identification. This will enable online adaptation of the current regulator gains, eventually making their response robust against parameter variations.

Keywords— PI Current Regulator, PI Current Controller, Tuning, High-Frequency Injection, HFI, Online Parameter Adaptation.

I. INTRODUCTION

Field-oriented control (FOC) normally uses Proportional Integral (PI) current controllers, as they guarantee zero steady-state error at the fundamental excitation frequency as well as a good dynamic response [1]. Controller tuning requires knowledge of the machine parameters [2], which are subjected to variations due to temperature and saturation. This can result in a degradation of the control performance. This can be avoided through robust control designs, e.g. sliding mode control [3], linear parameter varying [4], or internal mode control [5]. Alternatively, machine parameters can be estimated to adapt the controller gains. High-frequency injection (HFI) [6]–[12],

extended Kalman filter (EKF) [13], model reference adaptive systems (MRAS) [14], neural networks (NNs) [15] or recursive least square (RLS) [16] have been reported in the literature. Table I summarizes their main characteristics.

HFI is a reliable method to estimate machine parameters [6]–[12]. The use of an HF signal for machine parameter estimation and PI controller tuning has been proposed in [10]; the method relies on spatial inductance mapping and does not allow online tuning (i.e. during normal operation of the machine) of the PI controllers.

This paper proposes an online tuning method for synchronous PI current controllers using a pulsating HF current signal superimposed to the fundamental excitation at 45° between d - and q -axes. Machine parameters will be estimated from its response to the HF signal. The proposed method can be used with any synchronous machine design, including interior permanent magnet synchronous machines (IPMSMs) and surface permanent magnet synchronous machines (SPMSMs), wound-rotor synchronous machines (WRSMs), and synchronous reluctance machines (SynRMs). This paper will focus on the IPMSMs case.

The paper is organized as follows: in Section II the fundamental model of PMSMs is shown; in Section III the PI current controller tuning method is explained; in Section IV the

TABLE I – ADVANTAGES AND DISADVANTAGES OF PARAMETER ESTIMATION METHODS

	Need of additional signals	Parameter sensitivity	No commissioning	Computational burden
HFI [6]–[12]	✗	✓	✓	✓
EKF [13]	✓	✓	✗	✗
MRAS [14]	✓	✗	✓	✓
NNs [15]	✓	✓	✗	✗
RLS [16]	✓	✓	✗	✗

This work was supported in part by the Research, Technological Development and Innovation Programs of the Spanish Ministry of Science and Innovation, under grant PID2019-106057RB-I00

HF inductance and resistance estimation are shown; in Sections V and VI simulation and experimental results are provided, respectively. Finally, conclusions are provided in Section VII.

II. FUNDAMENTAL MODEL OF PMSMS

The fundamental model of a PMSM in a reference frame synchronous with the rotor is given by (1) [17], where p stands for the time derivative, R_d , R_q , L_d , and L_q are the d - and q -axis resistances and apparent (dc) d - and q -axis inductances respectively, ω_r is the rotor speed and λ_{pm} is the PM flux linkage. The d -axis is aligned with the PM flux.

$$\begin{bmatrix} v_{sd}^r \\ v_{sq}^r \end{bmatrix} = \begin{bmatrix} R_d & -\omega_r L_q \\ \omega_r L_d & R_q \end{bmatrix} \begin{bmatrix} i_{sd}^r \\ i_{sq}^r \end{bmatrix} + p \begin{bmatrix} L_d & 0 \\ 0 & L_q \end{bmatrix} \begin{bmatrix} i_{sd}^r \\ i_{sq}^r \end{bmatrix} + \begin{bmatrix} 0 \\ \lambda_{pm} \omega_r \end{bmatrix} \quad (1)$$

Inductances in (1) are commonly considered as constant values, therefore not being affected by the derivative operator [17]. However, in practice machine inductances vary due to saturation and temperature. Saturation can be modeled as shown in (2), which can be further reorganized as (3) by applying the chain rule for derivatives to (2). Finally, (4) is obtained, dynamic inductances being defined in (5). It is concluded that dynamic inductance should be used for current controller tuning if the magnetic saturation effect is to be considered. Temperature effects are not explicitly shown in the model, but its effects will be compensated by means of the parameter estimation method.

$$\begin{bmatrix} v_{sd}^r \\ v_{sq}^r \end{bmatrix} = \begin{bmatrix} R_d & -\omega_r L_q \\ \omega_r L_d & R_q \end{bmatrix} \begin{bmatrix} i_{sd}^r \\ i_{sq}^r \end{bmatrix} + p \left(\begin{bmatrix} L_d & 0 \\ 0 & L_q \end{bmatrix} \begin{bmatrix} i_{sd}^r \\ i_{sq}^r \end{bmatrix} + \begin{bmatrix} L_d & 0 \\ 0 & L_q \end{bmatrix} p \left(\begin{bmatrix} i_{sd}^r \\ i_{sq}^r \end{bmatrix} + \begin{bmatrix} 0 \\ \lambda_{pm} \omega_r \end{bmatrix} \right) \right) \quad (2)$$

$$\begin{bmatrix} v_{sd}^r \\ v_{sq}^r \end{bmatrix} = \begin{bmatrix} R_d & -\omega_r L_q \\ \omega_r L_d & R_q \end{bmatrix} \begin{bmatrix} i_{sd}^r \\ i_{sq}^r \end{bmatrix} + \begin{bmatrix} \frac{\partial L_d}{\partial i_{sd}^r} & 0 \\ 0 & \frac{\partial L_q}{\partial i_{sq}^r} \end{bmatrix} p \left(\begin{bmatrix} i_{sd}^r \\ i_{sq}^r \end{bmatrix} \right) \begin{bmatrix} i_{sd}^r \\ i_{sq}^r \end{bmatrix} + \begin{bmatrix} L_d & 0 \\ 0 & L_q \end{bmatrix} p \left(\begin{bmatrix} i_{sd}^r \\ i_{sq}^r \end{bmatrix} \right) + \begin{bmatrix} 0 \\ \lambda_{pm} \omega_r \end{bmatrix} \quad (3)$$

$$\begin{bmatrix} v_{sd}^r \\ v_{sq}^r \end{bmatrix} = \begin{bmatrix} R_d & -\omega_r L_q \\ \omega_r L_d & R_q \end{bmatrix} \begin{bmatrix} i_{sd}^r \\ i_{sq}^r \end{bmatrix} + \begin{bmatrix} L_{dDyn} & 0 \\ 0 & L_{qDyn} \end{bmatrix} p \begin{bmatrix} i_{sd}^r \\ i_{sq}^r \end{bmatrix} + \begin{bmatrix} 0 \\ \lambda_{pm} \omega_r \end{bmatrix} \quad (4)$$

$$\begin{bmatrix} L_{dDyn} & 0 \\ 0 & L_{qDyn} \end{bmatrix} = \begin{bmatrix} \frac{\partial L_d}{\partial i_{sd}^r} i_{sd}^r + L_d & 0 \\ 0 & \frac{\partial L_q}{\partial i_{sq}^r} i_{sq}^r + L_q \end{bmatrix} \quad (5)$$

III. PI CURRENT CONTROLLER TUNING

A. Synchronous PI current controller with cross-coupling decoupling

This section discusses PI current controller tuning using dynamic inductance and resistance. Zero-pole cancellation (ZPC) will be used. Fig. 1 schematically shows the current control scheme in the rotor synchronous reference frame. It is assumed that the back-EMF and cross-coupling terms of (1) are perfectly canceled [18].

The plant becomes (6) where the subscript x stands for d - or q -axis. (7) shows the PI current controller transfer function. PI controller parameters k_p and k_i are obtained from (8) and (9), where ω_{bw} is the desired bandwidth.

Fig. 2a shows the root locus of the control system shown in Fig. 1 in the case of an ideal ZPC. In the case of q -axis saturation due to q -axis current (positive or negative) injection, q -axis inductance will decrease; the resulting root locus being shown in Fig. 2b. An analogous effect will result from a stator resistance increase due to a stator temperature increase. In both cases, the resulting system settling time will be increased. In the case of negative d -axis current injection (i.e. flux weakening current), d -axis inductance will increase, the resulting root locus being shown in Fig. 2c. In this case, the resulting system settling time could be increased or create an undamped response, depending on the current controller gains.

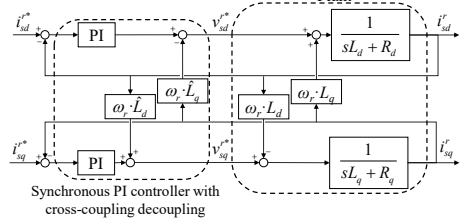


Fig. 1 - IPMSM control system scheme.

$$G(s) = \frac{1}{sL_x + R_x} \quad (6) \quad C(s) = k_p + \frac{k_i}{s} \quad (7)$$

$$k_p = \omega_{bw} \hat{L}_x \quad (8) \quad k_i = \omega_{bw} \hat{R}_x \quad (9)$$

Additionally, inductance variations affect the cross-coupling decoupling performance typically used with synchronous PI controllers, leading to larger settling time and undamped responses when the machine speed approaches the current control bandwidth. To overcome this issue an improved synchronous PI controller structure for machines with magnetic reluctance ($L_d \neq L_q$), generalized from the complex-vector PI current regulators [18] is described in this paper along with the tuning procedure.

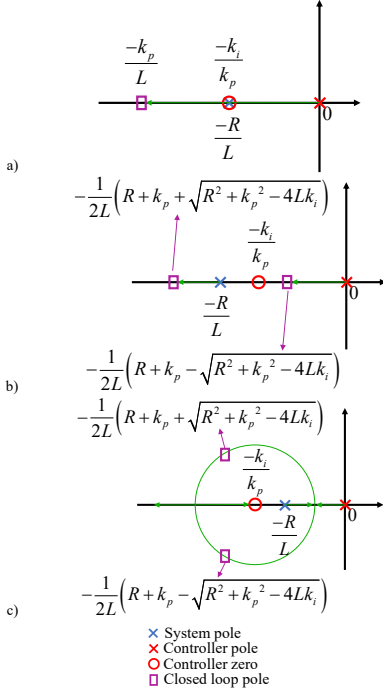


Fig. 2 – Root locus obtained by zero-pole cancellation. a) ideal, b) inductance decreased or resistance increased, and c) inductance increased.

B. Matrix synchronous PI current controller

A similar controller structure to that of (7) can be used with k_p and k_i being matrices defined in (10) and (11), where ω_{bw} is the desired bandwidth. This gain selection achieves ZPC in the cross-coupled system, similarly to the complex vector PI current controller for machines without reluctance ($L_d = L_q$) machines [18] and being analogous to the internal mode control (IMC) regulator presented in [19].

The block diagram of this controller is shown in Fig. 3. It is observed that the implementation is similar to the synchronous PI current controller with the addition of the cross-coupling branches.

$$k_i = k_p \begin{bmatrix} \hat{R}_d & \omega_r \hat{L}_q \\ \hat{L}_d & -\hat{L}_d \\ \omega_r \hat{L}_d & \hat{R}_q \\ \hat{L}_q & \hat{L}_q \end{bmatrix} \quad (10)$$

$$k_p = \begin{bmatrix} \omega_{bw} \hat{L}_d & 0 \\ 0 & \omega_{bw} \hat{L}_q \end{bmatrix} \quad (11)$$

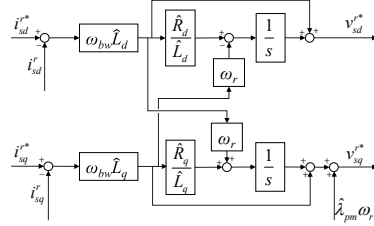


Fig. 3 – Matrix synchronous PI current controller structure.

Regardless of the structure or tuning technique used, accurate parameter (dynamic inductance and resistance) estimation is needed to guarantee both precise cross-coupling decoupling and the desired dynamic performance during machine normal operation.

IV. DYNAMIC INDUCTANCE AND RESISTANCE ESTIMATION USING AN HF SIGNAL INJECTION

A. Dynamic inductance and HF inductance

The dynamic inductances are defined as the slope of the machine flux vs. current, around the operating point, and they can be obtained from (12) and (13). The injection of an HF current signal on top of the fundamental excitation creates small variations in machine flux, and voltages, around the operating point, HF inductances being possible to be calculated. If the HF current magnitude is small, the HF inductance values can be assumed to match with the dynamic inductances (5) [21], [22]. This is schematically shown in Fig. 4 for both d - and q -axes.

$$L_{dHF} \approx L_{dDyn} = \frac{\partial \lambda_{sd}^r}{\partial i_{sd}^r} = \frac{\partial (i_{sd}^r L_d + \lambda_{pm})}{\partial i_{sd}^r} = \frac{\partial L_d}{\partial i_{sd}^r} i_{sd}^r + L_d \quad (12)$$

$$L_{qHF} \approx L_{qDyn} = \frac{\partial \lambda_{sq}^r}{\partial i_{sq}^r} = \frac{\partial (i_{sq}^r L_q)}{\partial i_{sq}^r} = \frac{\partial L_q}{\partial i_{sq}^r} i_{sq}^r + L_q \quad (13)$$

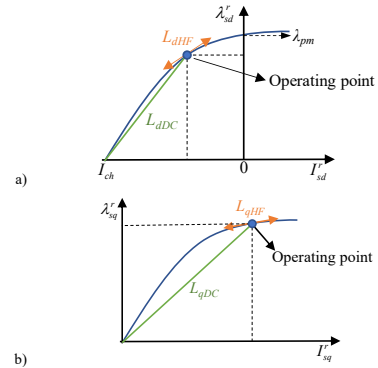


Fig. 4 - Schematic representation of dc (apparent) inductance and HF (dynamic) inductance for a) d -axis and b) q -axis.

B. HF inductance and resistance estimation

The HF model of a PMSM in a reference frame synchronous with the rotor is given by (14) [6], [20], where R_{dHF} , R_{qHF} , L_{dHF} , and L_{qHF} are the d - and q -axis HF resistances and inductances, respectively, i_{sdHF}^r and i_{sqHF}^r are the d - and q -axis HF currents and v_{sdHF}^r and v_{sqHF}^r are the d - and q -axis HF voltages.

$$\begin{bmatrix} v_{sdHF}^r \\ v_{sqHF}^r \end{bmatrix} = \begin{bmatrix} R_{dHF} & -\omega_r L_{qHF} \\ \omega_r L_{dHF} & R_{qHF} \end{bmatrix} \begin{bmatrix} i_{sdHF}^r \\ i_{sqHF}^r \end{bmatrix} + p \begin{bmatrix} L_{dHF} & 0 \\ 0 & L_{qHF} \end{bmatrix} \begin{bmatrix} i_{sdHF}^r \\ i_{sqHF}^r \end{bmatrix} \quad (14)$$

A pulsating HF current signal injected at 45° from the d -axis (15) can be used to estimate d - and q -axis HF stator resistances and inductances [6], where I_{HF}^* is the magnitude and ω_{HF} is the frequency of the injected signal. To inject the pulsating HF current signal on top of the fundamental excitation, a resonant controller in the synchronous reference frame is used as shown in Fig. 5. The d - and q -axis HF impedance are obtained from (16) and (17), respectively. The d - and q -axis HF inductances are obtained from (18) and (19), while the d - and q -axis HF resistances are obtained from (20) and (21) [6]. These equations are computed in the parameter estimation block shown in Fig. 5. The PI gains are then obtained using (8) and (9).

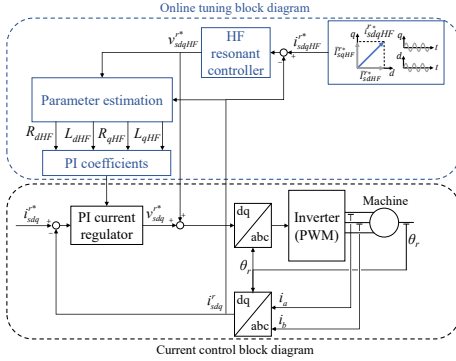


Fig. 5 - Proposed online PI current controller tuning based on HFI and current controller.

$$i_{sdqHF}^* = \begin{bmatrix} \bar{I}_{sdHF}^* \\ \bar{I}_{sqHF}^* \end{bmatrix} = \begin{bmatrix} I_{HF}^* \cos(\omega_{HF} t) \\ I_{HF}^* \cos(\omega_{HF} t) \end{bmatrix} \quad (15)$$

$$Z_{dHF} = \frac{\bar{V}_{sdHF}^*}{\bar{I}_{sdHF}^*} = R_{dHF} - \omega_r L_{qHF} + j\omega_{HF} L_{dHF} \quad (16)$$

$$Z_{qHF} = \frac{\bar{V}_{sqHF}^*}{\bar{I}_{sqHF}^*} = R_{qHF} + \omega_r L_{dHF} + j\omega_{HF} L_{qHF} \quad (17)$$

$$L_{dHF} = \Im[Z_{dHF}] / \omega_{HF} \quad (18)$$

$$L_{qHF} = \Im[Z_{qHF}] / \omega_{HF} \quad (19)$$

$$R_{dHF} = \Re[Z_{dHF}] + \omega_r L_{qHF} \quad (20)$$

$$R_{qHF} = \Re[Z_{qHF}] - \omega_r L_{dHF} \quad (21)$$

V. SIMULATION RESULTS

Finite element analysis (FEA) model of the IPMSM under test is shown in Fig. 6. The motor parameters are shown in Table II.

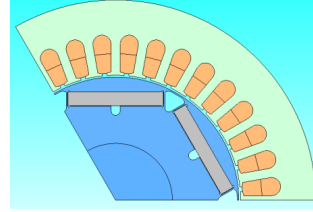


Fig. 6 - FEA model of tested IPMSM.

TABLE II- IPMSM PARAMETERS

Rated Current	14 A
Rated Voltage	350 V
Rated Power	4 kW
Rated Speed	1000 r/min
Pole Pairs	3
Stator Resistance	1.2 Ω
d -axis inductance	4.2 mH
q -axis inductance	15 mH

In this section, the proposed method to adapt the controller gains is used for both synchronous PI current controller with cross-coupling decoupling (see Section III.A) and matrix synchronous PI current controller (see Section III.B). Their performance is tested by means of step reference tracking capabilities in both d - and q -axes. Their dynamic responses are compared with non-adaptive controllers and an ideal first-order response.

Non-adaptive current controllers are tuned with the nominal machine parameters (see Table II), while the adaptive current controllers obtain the machine parameters from HFI (see Section IV) at the operating point prior to the current step command. The HF current signal is injected at 45° between d - and q -axes with a magnitude of 0.05 p.u. and 1kHz of frequency. The selected bandwidth for tuning of all the tested controllers is 150 Hz. Relatively low bandwidths (150 Hz and 50 Hz) are used in this paper to emphasize the performance differences among current controller structures.

The operating point for the d -axis current step response test is $I_{sd}^* = -1$ p.u., $I_{sq}^* = 0$ p.u., and the d -axis inductance is increased to 9.4 mH (+124%) by the FEA results. In a similar way, the operating point for the q -axis current step response test is $I_{sd}^* = 0$ p.u., $I_{sq}^* = 0.9$ p.u., with a decrease of the q -axis inductance to 14 mH (-7%) by the FEA results. In both tests, the current step command value is +0.1 p.u.

Fig. 7 shows the d -axis current regulator response to a d -axis current step command. Fig. 7a shows the simulation results at zero speed condition providing an intrinsic decoupling between d - and q -axes, while Fig. 7b shows the simulation results at 300 r/min. Both non-adaptive controller responses are overlapped

and show larger settling time and overshoot due to inductance variation, while both adaptive controllers maintain the desired settling time (also overlapping in the figure). There are no significant differences in the dynamic response between controller types or between different speed conditions exhibiting a correct decoupling between axes.

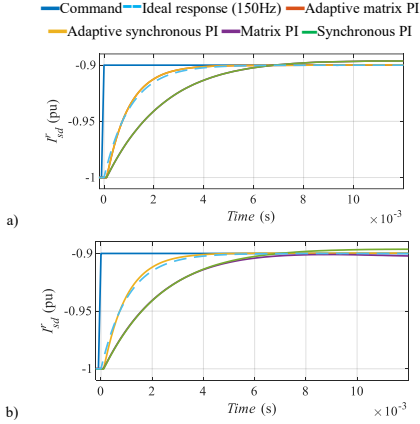


Fig. 7 - Simulation results. 0.1 p.u. d -axis step current response (L_d increased to 9.4mH, +124%) a) at zero speed and b) at $\omega_r = 300\text{r/min}$. $\omega_{bm} = 2\pi \cdot 150$ rad/s. HFI: $I_{HF} = 0.05$ p.u., 1 kHz. Sampled at 10 kHz.

Fig. 8 shows an analogous experiment to Fig. 7 but for a q -axis current step command. In this case, the differences between the adaptive PI controllers and non-adaptive PI controllers are negligible (responses are overlapped in the figure) due to the smaller inductance variation in the q -axis at this operating point.

From these simulation results, it can be concluded that the adaptation of controller gains based on HF estimated parameters allow to maintain the desired bandwidth even when the machine inductance or resistance vary due to magnetic saturation or temperature variations.

The HF parameter estimation errors in simulations have shown to be around 3%, while the estimation error in experimental results is expected to be larger due to inverter nonlinearities and noise. The quantification of estimation errors in experimental results is still ongoing research.

The estimation accuracy might affect the performance of adaptive controllers, therefore an estimation error of -20% in the d -axis inductance is artificially introduced in the next simulation results to test the impact of estimation errors in the performance of the method. Fig. 9 shows the d -axis current regulator response to a d -axis step command for adaptive matrix PI and adaptive synchronous PI current regulators when a -20% inductance estimation error is artificially introduced. The controller bandwidth has been lowered to $2\pi 50$ rad/s to amplify the effects of cross-coupling. It can be seen that inductance estimation errors have a larger effect when using the synchronous PI with

cross-coupling decoupling (Section III.A) than matrix PI (Section III.B), as expected.

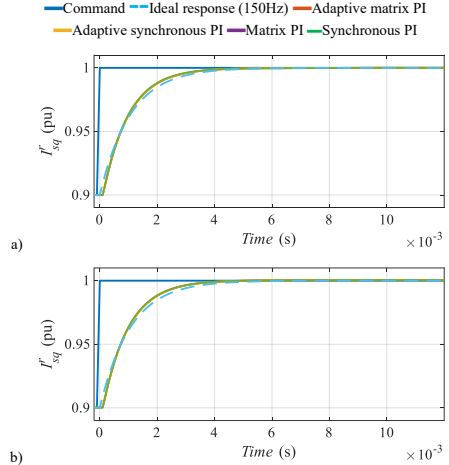


Fig. 8 - Simulation results. 0.1 p.u. q -axis step current response (L_q decreased to 14mH, -7%) a) at zero speed and b) at $\omega_r = 300\text{r/min}$. $\omega_{bm} = 2\pi \cdot 150$ rad/s. HFI: $I_{HF} = 0.05$ p.u., 1 kHz. Sampled at 10 kHz.

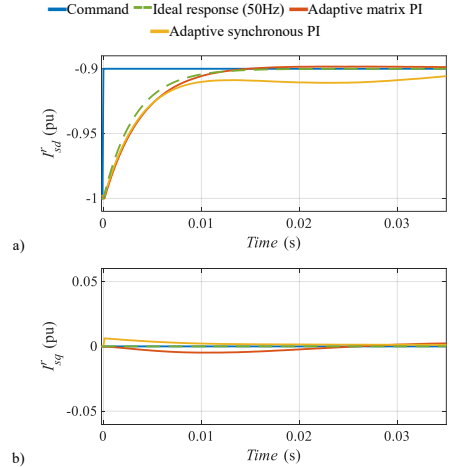


Fig. 9 - Simulation results. 0.1 p.u. d -axis step current response a) d -axis current response and b) q -axis current response with a -20% L_d estimation error, at $\omega_r = 300\text{r/min}$. $\omega_{bm} = 2\pi \cdot 50$ rad/s. HFI: $I_{HF} = 0.05$ p.u., 1 kHz. Sampled at 10 kHz.

VI. PRELIMINARY EXPERIMENTAL RESULTS

This section shows some preliminary experimental results of the proposed method. The IPMSM shown in Fig. 10 will be used

for the experimental verification of the method, its parameters can be seen in Table II.

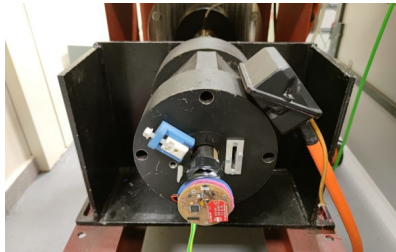


Fig. 10 – IPMSM used for experimental verification of the method.

Non-adaptive current controllers are tuned at the operating point: $I_{sd}^* = -0.1$ p.u., $I_{sq}^* = 0$ p.u. with a bandwidth of 150 Hz and their current step dynamic response is shown in Fig. 11. At this operating point, non-adaptive controllers have the desired dynamic response and both matrix and synchronous PI have overlapped responses.

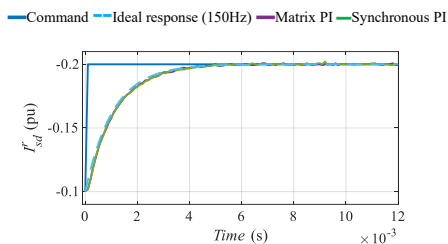


Fig. 11 – Experimental Results. -0.1 p.u. d -axis step current response, at zero speed. $\omega_{bm} = 2\pi \cdot 150$ rad/s. Sampled at 10 kHz by the DSP.

The tuned non-adaptive controllers are used and compared with adaptive controllers at a different operating point ($I_{sd}^* = -1$ p.u., $I_{sq}^* = 0$ p.u.) where the magnetic saturation is lower (inductance is increased). First, an HF current signal of 0.05 p.u. and 1 kHz is injected between d - and q -axes to estimate both axis dynamic inductances and resistances at the operating point. After the machine parameters are estimated, a 0.1 p.u. step is applied to the d -axis current command. The results are compared in Fig. 12 with non-adaptive PI current controllers tuned at low current operating point ($I_{sd}^* = -0.1$ p.u., $I_{sq}^* = 0$ p.u.) and the first-order system ideal response. Both adaptive controllers meet the desired bandwidth and dynamic response, while non-adaptive controllers show a larger settling time and overshoot, as expected. The non-adaptive controllers show faster dynamics compared with simulation results due to differences between FEA machine model and the actual machine parameters at the tested operating point. Nevertheless, the effect of the increased d -axis inductance is in good agreement with simulation results.

VII. CONCLUSIONS

A method for online tuning of PI current controllers based on HFI is proposed in this paper. It is demonstrated that dynamic inductances are responsible for machine dynamics. Simulation and preliminary experimental results have been presented to demonstrate the performance of the proposed method.

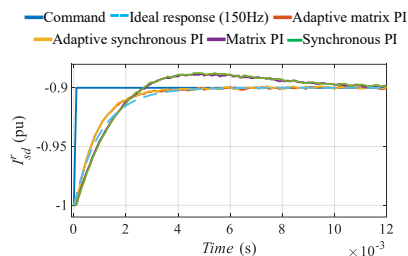


Fig. 12 – Experimental Results. 0.1 p.u. d -axis step current response, at zero speed. $\omega_{bm} = 2\pi \cdot 150$ rad/s. HFI: $I_{HF} = 0.05$ p.u., 1 kHz. Sampled at 10 kHz by the DSP.

REFERENCES

- [1] T. M. Rowan and R. J. Kerkman, "A New Synchronous Current Regulator and an Analysis of Current-Regulated PWM Inverters," in *IEEE Trans. Ind. Appl.*, vol. IA-22, no. 4, pp. 678–690, Jul. 1986, doi: 10.1109/TIA.1986.4504778.
- [2] A. G. Yepes, A. Vidal, J. Malvar, O. López, and J. Doval-Gandoy, "Tuning Method Aimed at Optimized Settling Time and Overshoot for Synchronous Proportional-Integral Current Control in Electric Machines," in *IEEE Trans. Power Electron.*, vol. 29, no. 6, pp. 3041–3054, Jun. 2014, doi: 10.1109/TPEL.2013.2276059.
- [3] V. I. Utkin, "Sliding mode control design principles and applications to electric drives," in *IEEE Trans. Ind. Electron.*, vol. 40, no. 1, pp. 23–36, Feb. 1993, doi: 10.1109/41.184818.
- [4] F. Amato, *Robust Control of Linear Systems Subject to Uncertain Time-Varying Parameters*. Berlin Heidelberg: Springer-Verlag, 2006.
- [5] L. Harnefors and H.-Nee, "Robust current control of AC machines using the internal model control method," in *IAS '95. Conference Record of the 1995 IEEE Industry Applications Conference Thirtieth IAS Annual Meeting*, Oct. 1995, vol. 1, pp. 303–309 vol.1, doi: 10.1109/IAS.1995.530315.
- [6] D. F. Laborda, D. D. Reigosa, D. Fernández, K. Sasaki, T. Kato, and F. Briz, "Enhanced Torque Estimation in Variable Leakage Flux PMSM Combining High and Low Frequency Signal Injection," in *2020 IEEE Energy Conversion Congress and Exposition (ECCE)*, Oct. 2020, pp. 1764–1771, doi: 10.1109/ECCE44975.2020.9235869.
- [7] D. Raca, P. Garcia, D. Reigosa, F. Briz, and R. Lorenz, "A comparative analysis of pulsating vs. rotating vector carrier signal injection-based sensorless control," in *2008 Twenty-Third Annual IEEE Applied Power Electronics Conference and Exposition*, Feb. 2008, pp. 879–885, doi: 10.1109/APEC.2008.4522824.
- [8] Y. G. Kang, D. Reigosa, B. Sarlioglu, and R. D. Lorenz, " D - and Q -Axis Inductance Estimation and Self-Sensing Condition Monitoring Using 45° Angle High-Frequency Injection," in *IEEE Trans. Ind. Appl.*, vol. 57, no. 1, pp. 506–515, Jan. 2021, doi: 10.1109/TIA.2020.3029993.
- [9] M. Martínez, D. Reigosa, D. Fernández, J. M. Guerrero, and F. Briz, "Enhancement of Permanent-Magnet Synchronous Machines Torque Estimation Using Pulsating High-Frequency Current Injection," in *IEEE Trans. Ind. Appl.*, vol. 56, no. 1, pp. 358–366, Jan. 2020, doi: 10.1109/TIA.2019.2954297.
- [10] F. Erturk and B. Akin, "Spatial Inductance Estimation for Current Loop Auto-Tuning in IPMSM Self-Commissioning," in *IEEE Trans. Ind.*

- Electron.*, vol. 67, no. 5, pp. 3911–3920, May 2020, doi: 10.1109/TIE.2019.2914640.
- [11] D. Reigosa, Y. g Kang, M. Martínez, D. Fernández, J. M. Guerrero, and F. Briz, “SPMSMs Sensorless Torque Estimation Using High-Frequency Signal Injection,” in *IEEE Trans. Ind. Appl.*, vol. 56, no. 3, pp. 2700–2708, May 2020, doi: 10.1109/TIA.2020.2975757.
- [12] M. Martínez, D. F. Laborda, D. Reigosa, D. Fernández, J. M. Guerrero, and F. Briz, “SynRM Sensorless Torque Estimation Using High Frequency Signal Injection,” in *2019 IEEE 10th International Symposium on Sensorless Control for Electrical Drives (SLED)*, Sep. 2019, pp. 1–5, doi: 10.1109/SLED.2019.8896220.
- [13] T. Boileau, N. Leboeuf, B. Nahid-Mobarakkeh, and F. Meibody-Tabar, “Online Identification of PMSM Parameters: Parameter Identifiability and Estimator Comparative Study,” in *IEEE Trans. Ind. Appl.*, vol. 47, no. 4, pp. 1944–1957, Jul. 2011, doi: 10.1109/TIA.2011.2155010.
- [14] O. C. Kivanc and S. B. Ozturk, “Sensorless PMSM Drive Based on Stator Feedforward Voltage Estimation Improved With MRAS Multiparameter Estimation,” in *IEEE ASME Trans. Mechatron.*, vol. 23, no. 3, pp. 1326–1337, Jun. 2018, doi: 10.1109/TMECH.2018.2817246.
- [15] Yang Yi, D. M. Vilathgamuwa, and M. A. Rahman, “Implementation of an artificial-neural-network-based real-time adaptive controller for an interior permanent-magnet motor drive,” in *IEEE Trans. Ind. Appl.*, vol. 39, no. 1, pp. 96–104, Jan. 2003, doi: 10.1109/TIA.2002.807233.
- [16] S. J. Underwood and I. Husain, “Online Parameter Estimation and Adaptive Control of Permanent-Magnet Synchronous Machines,” in *IEEE Trans. Ind. Electron.*, vol. 57, no. 7, pp. 2435–2443, Jul. 2010, doi: 10.1109/TIE.2009.2036029.
- [17] J. F. Gieras, *Permanent magnet motor technology: design and applications*. CRC press, 2009.
- [18] F. Briz, M. W. Degner and R. D. Lorenz, “Analysis and design of current regulators using complex vectors,” in *IEEE Trans. Ind. Appl.*, vol. 36, no. 3, pp. 817–825, May–June 2000, doi: 10.1109/28.845057.
- [19] L. Harnefors and H. -P. Nee, “Model-based current control of AC machines using the internal model control method,” in *IEEE Trans. Ind. Appl.*, vol. 34, no. 1, pp. 133–141, Jan.–Feb. 1998, doi: 10.1109/28.658735.
- [20] W. Xu and R. D. Lorenz, “High-Frequency Injection-Based Stator Flux Linkage and Torque Estimation for DB-DTFC Implementation on IPMSMs Considering Cross-Saturation Effects,” in *IEEE Trans. Ind. Appl.*, vol. 50, no. 6, pp. 3805–3815, Nov. 2014, doi: 10.1109/TIA.2014.2322134.
- [21] M. Ganchev, C. Kral, and T. M. Wolbank, “Compensation of Speed Dependence in Sensorless Rotor Temperature Estimation for Permanent-Magnet Synchronous Motor,” in *IEEE Trans. Ind. Appl.*, vol. 49, no. 6, pp. 2487–2495, Nov. 2013, doi: 10.1109/TIA.2013.2263211.
- [22] M. Martínez, D. Reigosa, D. Fernández, J. M. Guerrero and F. Briz, “Enhancement of Permanent-Magnet Synchronous Machines Torque Estimation Using Pulsating High-Frequency Current Injection,” in *IEEE Trans. Ind. Appl.*, vol. 56, no. 1, pp. 358–366, Jan.–Feb. 2020, doi: 10.1109/TIA.2019.2954297.

B.2.4 Comparative Analysis of Torque Pulsations Measurement Methods for PMSM Drives

Comparative Analysis of Torque Pulsations Measurement Methods for PMSM Drives

Maria Martinez

Dept. Electrical Engineering
University of Oviedo
Gijón, Spain
martinezm@uniovi.es

Diego F. Laborda

Dept. Electrical Engineering
University of Oviedo
Gijón, Spain
dflaborda@uniovi.es

David Reigosa

Dept. Electrical Engineering
University of Oviedo
Gijón, Spain
diazdavid@uniovi.es

Fernando Briz

Dept. Electrical Engineering
University of Oviedo
Gijón, Spain
fernando@isa.uniovi.es

Abstract—Torque pulsations in permanent magnet synchronous machines are a main concern in many applications. Accurate measurement of torque pulsations can be needed for different purposes, e.g. to validate the effectiveness of machine designs or to develop control strategies for their mitigation. This paper discusses the performance of three torque pulsations measurement methods, using: torque transducers, rotor position sensors, and shaft-mounted accelerometers. The analysis will consider hardware complexity, accuracy, speed range and cost. Simulation and experimental results are presented.

Index Terms—Permanent Magnet Synchronous Machines, torque ripple measurement.

I. INTRODUCTION

Permanent magnet synchronous motors (PMSMs) have received much attention in high performance applications such as automotive, robotics, military, aerospace, etc. due to their inherent advantages such high efficiency, high-power density, and high dynamic response [1], [2]. Depending on the machine design, smooth torque production (i.e. minimization of torque pulsations) can be difficult to achieve [3]–[6]. Torque pulsations in PMSM can be due to several reasons, including a) interaction between PMs and the stator slot opening, i.e. cogging torque; b) non-sinusoidal distribution of the stator windings, c) non-sinusoidal current waveform or d) non-sinusoidal back-EMF [7]–[12], i.e. electromagnetic torque ripple. Smooth torque production can be achieved by proper machine design [8]–[11], by means of improved control strategies [7], [12], or both. Independent of the approach being followed, experimental validation is required. Torque measurement methods can be roughly separated in three groups:

- Rotatory torque transducers strain gauges-based systems are the most common option [13], [14]. However, they are expensive, bulky, and introduce flexible elements in the shaft, reducing the torsional resonant frequency and eventually the measuring frequency range of the whole system [15]. Additionally, they are scaled to measure the average torque (i.e.: dc component of the torque) what reduces the resolution for measuring torque pulsations (i.e. torque pulsations are relatively small compared to DC component of the torque). As an attempt to eliminate the additional coupling required by traditional rotatory torque transducer, a wireless transmission of the

strain gauge sensor signals by means of telemetry and wireless power supply was reported in [16], [17]. This method is directly attached to the rotor shaft resulting in lighter and smaller sensors. However, these sensors are also scaled to measure the average torque and have a reduced bandwidth, what compromises their capability to measure the torque ripple at high rotational speeds.

- Accelerometer based systems proposed in [14], [18], [19] are based on the relationship between torque and angular acceleration, therefore knowledge of shaft inertia is needed to estimate the torque pulsations [18]. However, these methods are independent of the average torque, increasing the accuracy of the measurements and are independent of the rotational speed. In [14], a piezoelectric accelerometer is mounted in an aluminum disk attached to the rotor shaft. The need of mechanical couplings has similar concerns as the mentioned for the rotatory torque transducer. However, wireless accelerometer system proposed in [19] is directly mounted on the shaft to measure the tangential acceleration using one microelectromechanical system (MEMS) accelerometer, eliminating therefore the need of additional mechanical couplings.
- Rotatory encoders can be used to estimate the angular acceleration as proposed in [14], [20]. This method involves a double differentiation from the measured angular position. However, as most of the PMSMs control strategies require accurate rotor position measurement, estimating torque ripple from position sensors would be especially advantageous for commercial applications.

The first two sensors require the use of slip rings or contactless signal transmission from rotor to stator side. Slip rings increase maintenance costs and decrease system lifetime. Piezoelectric accelerometer system proposed in [14] use contactless analog signal transmission what involves modulation at the rotor and demodulation at stator side, furthermore, it is supplied via contactless power transfer (e.g. rotary transformer). This makes the implementation difficult. However, wireless

accelerometer system proposed in [15] is supplied from a battery and the acceleration signals are digitally transferred via wireless communication, making the implementation simpler.

The main target of this paper is to perform a comprehensive analysis of torque pulsation measurement based on rotary torque transducers [15], rotor position sensors [14] and shaft mounted accelerometers [19].

The paper is organized as follows: working principles of the three methods being considered are presented in Section II; simulation results are shown in Section III; the test rig to be used for experimental verification is described in Section IV; conclusions are finally provided in Section V.

II. TORQUE PULSATIONS MEASUREMENT SYSTEM

This section describes the methods being considered.

1) *Rotary torque transducer*: They measure the torsion of the shaft, which is assumed to be proportional to the applied torque [14]. This type of sensors can achieve high accuracy, with an error lower than 0.1% of the nominal torque [13]. However, some considerations must be made regarding their use for torque pulsations measurement:

- The measurement range and the subsequent signal acquisition system must be scaled according to the maximum torque, which will be normally much higher than the torque pulsations [15]. The quantization error, Q , (1) in the discretization of the analog signal provided by the sensor can be critical in this regard. From (1), it is seen that quantization error is directly proportional to the sensor measurement range and inversely proportional to the number of bits of the discretization.
- High precision commercial sensors have a bandwidth up to 1.2kHz [13], [16]. Since the torque harmonics in PMSMs occur at multiples of the fundamental frequency, torque pulsations at high speeds could be beyond the bandwidth of the sensor.
- Torque transducer increases the shaft length and add flexible couplings to machine's shaft. This will decrease the system resonant frequency and limit the frequency range of the sensor due to the interference/overlap of the torque pulsations and system resonances [15].

$$Q = \frac{\text{Range}/2^{\text{bits}}}{2} \quad (1)$$

2) *Shaft-mounted accelerometers* [19]: They rely on the centripetal (2) and tangential accelerations (3) of the shaft measured using accelerometers [19], where r is the radius from the sensor to the center of the shaft, ω_r is the mechanical angular frequency, g is the Earth's gravity, a_{ch} is the magnitude of the h_{th} harmonic component of the centripetal acceleration, a_{th} is the magnitude of the h_{th} harmonic component of the tangential acceleration, h is the harmonic order of the h_{th} harmonic component, φ_{ch} is the phase of the h_{th} harmonic component of the centripetal acceleration and φ_{th} is the phase of the h_{th} harmonic component of the tangential acceleration.

The relationship between torque τ and angular acceleration α_r is given by (4), where J is the moment of inertia.

$$a_c = r\omega_r^2 + g \cos(\omega_r t) + \sum_{h=1}^{inf} a_{ch} \cos(h\omega_r t + \varphi_{ch}) \quad (2)$$

$$a_t = g \sin(\omega_r t) + \sum_{h=1}^{inf} a_{th} \cos(h\omega_r t + \varphi_{th}) \quad (3)$$

$$\tau = J \alpha_r = m r^2 \alpha_r = m r a_t \quad (4)$$

It is observed from (2) that the centripetal acceleration includes the effect of machine's speed ($r\omega_r^2$), while tangential acceleration (3) contains the gravity, g , effect. Estimation of the torque pulsations from the measured tangential acceleration requires knowledge of the rotational inertia (4).

The bandwidth of the system will depend on the sampling frequency of the analog-to-digital converter, the sensor mechanical resonant frequency and filters used in the acquisition system, values in the range of one full order of magnitude above the rotary transducer can be achieved (up to 12.8 kHz [19]). This method does not increase the shaft length and does not require couplings either, still the response depends on system inertia.

3) *Rotor position sensor*: Use of encoder signals, often present for position feedback, to measure torque pulsations was proposed in [14], [20]. Since torque pulsations are proportional to acceleration, obtaining torque pulsations from encoder signals requires a double differentiation, which is problematic due to noise. In addition, since the position corresponds to the second integral of acceleration, the magnitude of the oscillation in the position is attenuated by a factor of $(h\omega_r)^2$ as shown in (6), which places significant sensitivity concerns if the frequency of the vibration is high.

$$\omega_r(t) = \int \alpha_r(t) dt = \int \frac{a_{th} \sin(h\omega_r t)}{r} dt = \frac{-a_{th} \cos(h\omega_r t)}{r h \omega_r} \quad (5)$$

$$\begin{aligned} \theta_r(t) &= \int \omega_r(t) dt = \frac{1}{r h \omega_r} \int -a_{th} \cos(h\omega_r t) dt \\ &= \frac{-a_{th} \sin(h\omega_r t)}{r (h\omega_r)^2} \end{aligned} \quad (6)$$

III. SIMULATION RESULTS

Fig. 1 shows a schematic representation of the simulation model that will be used to evaluate the performance of the three methods being considered. Its main blocks are:

- System model: A predefined torque pulsation (ΔT_{eHF}) of frequency, ω_{HF} , is applied to the shaft, from which acceleration, speed and position are obtained using (4) and (5)-(6).
- "Torque transducer" block emulates a rotary torque transducer. Torque is acquired using a sample and hold (SH) and analogue to Digital Converter (ADC) circuit.
- "Accelerometer based-method" estimates the torque pulsations from the measured angular acceleration. It also includes SH and ADC circuits.

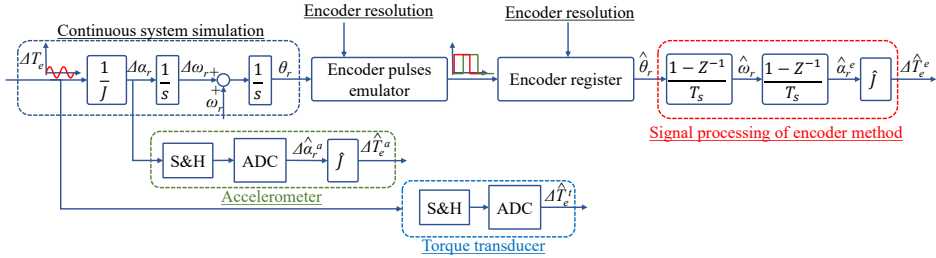


Fig. 1. Simulation model scheme.

- Encoder pulses feed an “Encoder register” block that emulates the dedicated encoder; rotor speed ($\hat{\omega}_r$) and acceleration ($\hat{\alpha}_r^a$) are obtained using Euler approach (7)–(8); the estimated system torque pulsations are obtained using the estimated system inertia (\hat{J}).

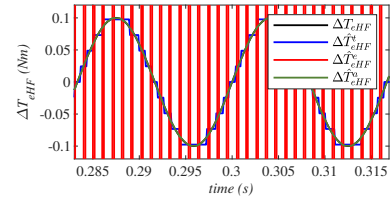
$$\hat{\omega}_r = \frac{\hat{\theta}_r(k) - \hat{\theta}_r(k-1)}{T_s} \quad (7)$$

$$\hat{\alpha}_r = \frac{\hat{\omega}_r(k) - \hat{\omega}_r(k-1)}{T_s} \quad (8)$$

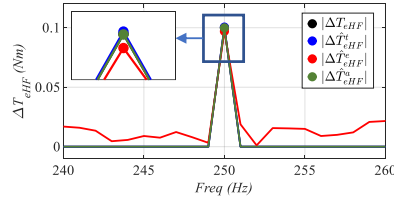
Fig. 2(a) and Fig. 2(b) show the torque pulsation estimated by the three methods and the corresponding frequency spectrum zoomed around the frequency of interest ($\omega_{HF} \approx 250$ Hz), when the torque pulsation described in the caption of the figure is applied. Torque transducer and accelerometer are seen to produce an accurate measurement of torque ripple. On the contrary, the torque pulsations estimated from encoder signals shows a large amount of noise due to the combined effect of quantization error and the double differentiation, which results in undesired frequency components observed in Fig. 2(b).

Fig. 3 shows the error in the estimated torque (9) for the three analyzed methods as a function of torque pulsation magnitude and frequency. It can be seen from Fig. 3(a) that the error using the torque transducer increases inversely proportional to the magnitude of the torque pulsation, due to the resolution of the acquisition system. For the shaft-mounted accelerometer based-method, see Fig. 3(b), error is independent of the load and injected frequency. It is noted that a precise estimate of the inertia is needed, see Fig. 3(b). Fig. 3(c) and 3(d) show the results for two different encoder resolutions. Torque oscillations estimated from encoder are seen to show a rather random behavior, which would be explained by the random nature of quantization noise (1) which is intrinsic to encoder pulses sampling. As expected, the magnitude of the error decreases as the resolution of the encoder increases.

$$e = |\Delta T_{eHF}| - |\Delta \hat{T}_{eHF}^x| \quad (9)$$



(a)



(b)

Fig. 2. Estimated torque pulsations simulation results: (a) Estimated torque pulsations. $\omega_r = 600$ rpm, $\Delta T_{eHF} = 0.1$ Nm, $\omega_{HF} = 250$ Hz, $f_s = 10$ kHz, encoder = 1024 ppr, accelerometer resolution = 14 bits and range = $\pm 4g$, torque transducer resolution = 12 bits and range = 100 Nm. Superindex t , a and e stand for torque transducer, encoder and accelerometer respectively.

IV. EXPERIMENTAL VERIFICATION

A. Implementation and experimental setup

Experimental results have been conducted using a 7.5 kW IPMSM shown in Fig. 5, its main characteristics being shown in Table I. The IPMSM is equipped with a rotor acceleration measurement system [15], see Table II, an encoder of 1024 ppr and a torque transducer [see Table III]. The speed of the test machine is fixed using the load machine, which is a commercial 40-kW PMSM [21]. The speed control loop has a bandwidth of 5 Hz. The moment of inertia, J , of the mechanical system has been estimated from the measured rotor

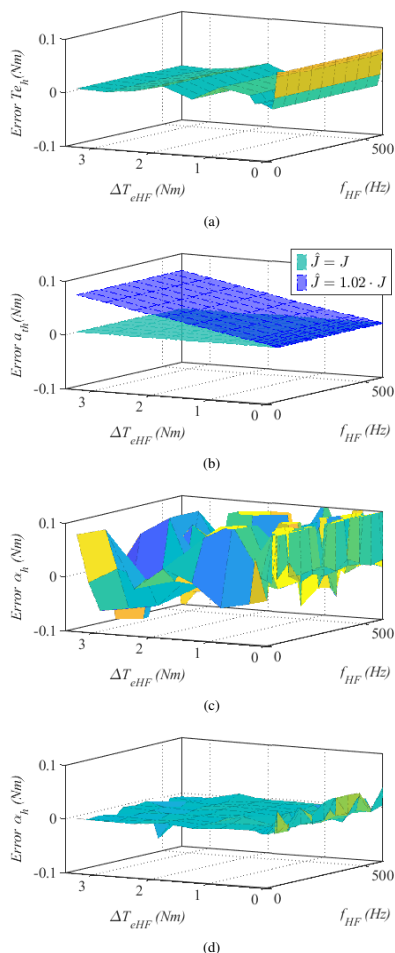


Fig. 3. Simulations results: (a) Torque transducer pulsations measurement error, Range=100 Nm, Resolution=11 bits; (b) Shaft-mounted accelerometer based-method error. Range=8g, Resolution=11 bits; (c) Encoder based-method error. Resolution=1024 ppr, (d) Encoder based-method error. kHz, Resolution=16384 ppr. $f_s=10$ kHz in all cases

shaft acceleration when applying a step-like change in the q -axis current. The moment of inertia of the mechanical system was estimated to be 250 kgcm^2 .

As discussed in the previous section, performance of the three sensors is analysed from the response to a predefined

TABLE I
IPMSM PARAMETERS

Rated power	P_{rated}	7.5 kW
Rated voltage	V_{rated}	350 V
Rated speed	n_{rated}	1800 rpm
Rated current	I_{rated}	14 A_{rms}
PM flux	λ_{PM}	0.63 Wb
Poles pairs	P	3

TABLE II
MAIN CHARACTERISTICS OF SHAFT MOUNTED ACCELEROMETER

LSB	0.488 mg
Measurement range	$\pm 4g$
Bandwidth	12.8 kHz
Sensors number	1 (3-axis)
Output noise	1.3 $mm/s^2/\sqrt{Hz}$
Distance to the shaft center (r)	24.6 mm

TABLE III
MAIN CHARACTERISTICS OF TORQUE TRANSDUCER

Range	100 Nm
Resolution	12 bits
Bandwidth	1 kHz

torque pulsation (ΔT_{eHF}). A pulsating q -axis HF current (10) of magnitude I_{sqHF}^r and frequency ω_{HF} has been injected in the test machine using a resonant controller (11); K_p is the proportional gain of the controller, T_i is the integral time and ω_{HF} is the resonant frequency. The PR controller has been tuned to inject the torque ripple at different frequencies, emulating torque ripple produced in an IPMSM. Fig. 4 shows the implementation of the method.

$$\vec{i}_{sdqHF}^{r*} = \begin{bmatrix} i_{sdHF}^{r*} \\ i_{sqHF}^{r*} \end{bmatrix} = \begin{bmatrix} 0 \\ I_{sqHF}^{r*} \sin(2\pi f_{HF} t) \end{bmatrix} \quad (10)$$

$$PR(s) = K_p \frac{s^2 + s/T_i + \omega_{HF}^2}{s^2 + \omega_{HF}^2} \quad (11)$$

Overall electromagnetic torque of a IPMSM is represented by (12), while torque ripple due to the HF signal can be expressed as (13), where P is the number of pole pairs.

$$T_c = \frac{3}{2} P (\lambda_{PM} i_{sq}^r + (L_d - L_q) i_{sd}^r i_{sq}^r) \quad (12)$$

$$\Delta T_{eHF} = \frac{3}{2} P (\lambda_{PM} i_{sqHF}^r) \quad (13)$$

B. Experimental results

Fig 6 shows experimental results when the magnitude of the pulsating q -axis HF current, I_{sqHF}^r is equal to 5A and the HF signal was injected at 50Hz. Fig. 6(a) and Fig. 6(b) shows the injected dq -axes HF current and the corresponding FFT. No fundamental current has been applied. Fig. 6(c), Fig. 6(e) and 6(g) show the torque pulsation measured by the three methods

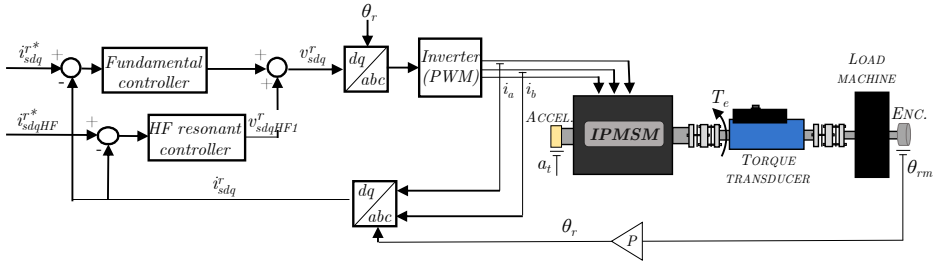


Fig. 4. Block diagram of a IPMSM including fundamental control and HF signal injection for creating known torque pulsations.

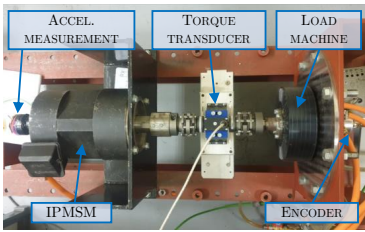


Fig. 5. Experimental set-up: Picture of the test bench.

and Fig. 6(d), 6(f) and 6(h) shows the corresponding frequency spectrums. Consistently with the simulation results, torque transducer and accelerometer are seen to provide a rather clean signal, accurately estimating the magnitude of the torque ripple. On the contrary, the torque pulsations estimated from encoder signals shows large amount of undesired frequency components.

Fig. 7 shows experimental results when the magnitude of the q -axis HF pulsating current changes from 0 to 5A for different values of the HF frequency, f_{HF} , and with the rotor speed command set to 0rpm. No fundamental current was being injected in the machine. Fig. 7(a), Fig. 7(b) and Fig. 7(c) show the torque pulsation measurement using the accelerometer, torque sensor and encoder, respectively. The expected torque pulsations (13), T_{est} , is included for comparison purposes. It can be seen from Fig.7(a) that the torque pulsations measurement using the accelerometer-based method is independent of the load and the frequency of the torque pulsations. On the contrary, it can be seen from Fig. 7(b) that the error using the torque transducer is negligible for low frequency torque pulsations, but becomes more relevant as the frequency increases. Torque oscillations measured error using the encoder (see Fig. 7(c)) are seen to be negligible for larger torque pulsations and low frequency of injection but becomes more relevant as the torque pulsations decrease and

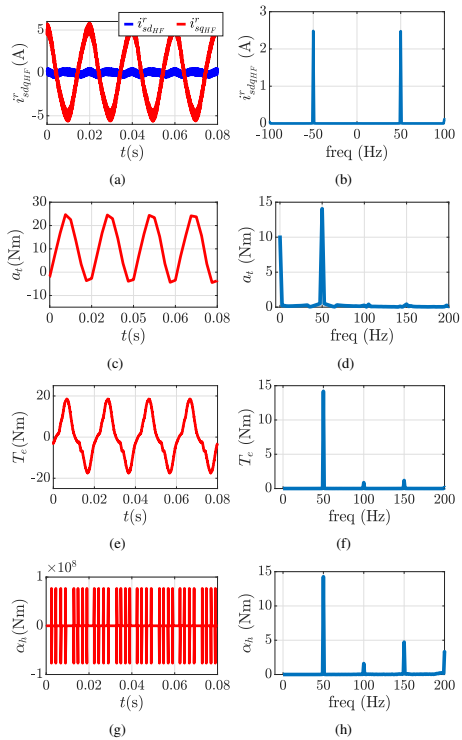


Fig. 6. Experimental results: (a) Injected HF current, i_{sdqHF}^{r*} ; (b) FFT of i_{sdqHF}^{r*} ; (c) measured tangential acceleration from the shaft-mounted accelerometer, a_t ; (d) FFT of a_t ; (e) measured output torque, T_c ; (f) FFT of T_c ; (g) measured angular acceleration from the encoder, α_h ; (h) FFT of α_h .

the frequency increases.

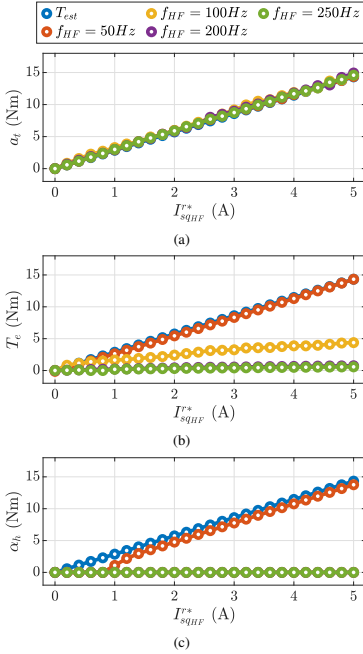


Fig. 7. Experimental results: (a) Measured tangential acceleration from the shaft-mounted accelerometer, a_t , Range=4g, Resolution=14 bits; (b) Measured output torque, T_e , Range= ± 100 Nm, Resolution=12 bits; (c) measured angular acceleration from the encoder, α_h , Resolution=1024 ppr. $\omega_r=0$ rpm, $f_s=10$ kHz in all cases

Similarly to Fig. 7, Fig. 8 shows the measured torque ripple at a rotational speed of 100rpm. It can be observed comparing Fig. 7(a) with Fig. 8(a) and Fig. 7(b) with Fig. 8(b) that the torque pulsation measurement using the accelerometer-based method and the torque transducer do not change significantly with rotor speed. On the contrary, the encoder is able to measure higher-order harmonics (see Fig. 8(c)). This suggests that encoder pulses generated due to low rotational speeds has a similar effect as dithering the encoder signal, masking the noisy harmonics generated from quantization distortion.

The increase of the torque pulsations error with the injected frequency seen in Fig. 7(b) and Fig. 8(b) compared with the simulation results in Fig. 3(a), suggests that the error using the torque transducer could be caused due to the friction torque, which was not considered in the simulation results. Non ideal behaviour of mechanical couplings (e.g. vibration models) are another likely source. A similar effect is observed in the torque ripple measured from the encoder-based method when the

machine is rotating at low speeds (see Fig. 8(c)). This is a subject of ongoing research.

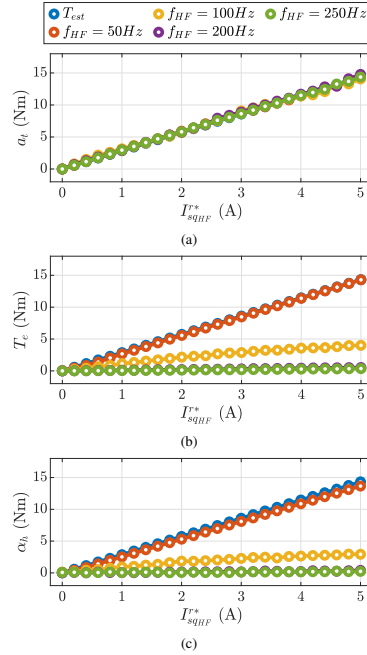


Fig. 8. Experimental results: (a) Measured tangential acceleration from the shaft-mounted accelerometer, a_t , $f_s=10$ kHz, Range=4g, Resolution=14 bits; (b) Measured output torque, T_e , $f_s=10$ kHz, Range= ± 100 Nm, Resolution=12 bits; (c) measured angular acceleration from the encoder, α_h , $f_s=10$ kHz, Resolution=1024 ppr. $\omega_r=100$ rpm, $f_s=10$ kHz in all cases

Frequency analysis has been used so far for the evaluation of the methods. This analysis is useful for off-line implementations and under the assumption that the machine operates in steady state, as it allows very precise isolation of the frequency components of interest. However, its use for real time implementation is not advisable, simpler forms of filtering must be used in this case, e.g. band-pass filters. Such filters will suffer from a reduced capability to remove frequency components close to the target frequency. The Total Harmonic Distortion (THD) of the signals (see Fig. 9) is in this case an useful metric to assess the accuracy for each measurement method that could be expected in a real implementation. It is seen from Fig. 9(a) and Fig. 9(b) that the THD of both signals is $< 15\%$. However, for the encoder-based method, inadmissible high values of the THD are observed. This places serious concerns on the effectiveness of on-line signal processing methods to extract the acceleration ripple from the encoder signals.

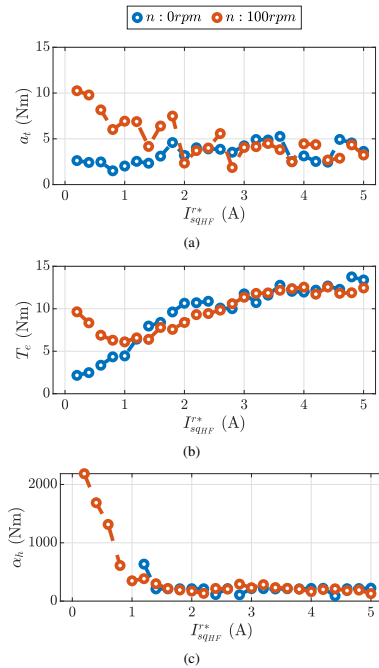


Fig. 9. Experimental results: (a) THD of the measured tangential acceleration from the shaft-mounted accelerometer, a_t , $f_s=10$ kHz, Range=4g, Resolution=14 bits; (b) THD of the measured output torque, T_c , $f_s=10$ kHz, Range= ± 100 Nm, Resolution=12 bits; (c) THD of the measured angular acceleration from the encoder, α_b , $f_s=10$ kHz, Resolution=1024 ppr. $I_{sqHF}^*=5A$, $f_{HF}=50Hz$, $f_s=10$ kHz in all cases

V. CONCLUSIONS

Precise measurement of torque pulsations produced by PMSM can be required in several scenarios, including due to application requirements, or to validate the performance of machine designs and/or control strategies. Torque pulsations can be measured by using torque transducers or estimated from encoder signals or shaft-mounted accelerometers. The proposed paper discusses the performance of the three aforementioned methods. Encoder based methods do not involve additional hardware but provide the lowest performance. Shaft mounted accelerometers have been shown to provide the most accurate result. However, it requires knowledge of mechanical inertia. Finally, torque transducers have been shown to have an unexpected error dependency with the frequency of the torque pulsations. Simulations results and experimental have been provided to support the analysis presented in this paper.

REFERENCES

- [1] D. W. Novotny and T. A. Lipo, *Vector Control and Dynamics of AC Drives*. Clarendon Press, 1996, google-Books-ID: 5FAHb_z4eAQC.
- [2] D. C. Hanselman, *Brushless Permanent-magnet Motor Design*, Feb. 1994.
- [3] B. P. Saunders, G. Heins, F. D. Boer, and M. Thiele, "Cogging Torque Estimation for Sensorless PMSM," in *Proceedings 2012 XXth International Conference on Electrical Machines*. IEEE, Institute of Electrical and Electronics Engineers, 2012, pp. 2949–2954. [Online]. Available: <https://researchers.cdu.edu.au/en/publications/cogging-torque-estimation-for-sensorless-pmsm>
- [4] M. Piccoli and M. Yim, "Cogging Torque Ripple Minimization via Position Based Characterization," Jul. 2014.
- [5] "Advanced measurement of rotor vibration in electric drives | IEEE Journals & Magazine | IEEE Xplore." [Online]. Available: <https://ieeexplore.ieee.org/document/673738>
- [6] Z. Azar, Z. Zhu, and G. Ombach, "Influence of Electric Loading and Magnetic Saturation on Cogging Torque, Back-EMF and Torque Ripple of PM Machines," *IEEE Transactions on Magnetics*, vol. 48, pp. 2650–2658, Oct. 2012.
- [7] S. Rojas, M. A. Pérez, J. Rodríguez, and H. Zelaya, "Torque ripple modeling of a permanent magnet synchronous motor," in *2010 IEEE International Conference on Industrial Technology*, Mar. 2010, pp. 433–438.
- [8] N. Bianchi and S. Bolognani, "Design techniques for reducing the cogging torque in surface-mounted PM motors," *IEEE Transactions on Industry Applications*, vol. 38, no. 5, pp. 1259–1265, Sep. 2002.
- [9] Z. Zhu and D. Howe, "Influence of design parameters on cogging torque in permanent magnet machines," *IEEE Transactions on Energy Conversion*, vol. 15, no. 4, pp. 407–412, Dec. 2000.
- [10] L. Dosiek and P. Pillay, "Cogging Torque Reduction in Permanent Magnet Machines," *IEEE Transactions on Industry Applications*, vol. 43, no. 6, pp. 1565–1571, Nov. 2007.
- [11] C. Studer, A. Keyhani, T. Sebastian, and S. Murthy, "Study of cogging torque in permanent magnet machines," in *IAS '97. Conference Record of the 1997 IEEE Industry Applications Conference Thirty-Second IAS Annual Meeting*, vol. 1, Oct. 1997, pp. 42–49 vol.1, iSSN: 0197-2618.
- [12] H. Le-Huy, R. Perret, and R. Feuillet, "Minimization of Torque Ripple in Brushless DC Motor Drives," *IEEE Transactions on Industry Applications*, vol. IA-22, no. 4, pp. 748–755, Jul. 1986.
- [13] "Torque Sensors and Torque Transducers Archives - Interface Force Measurements." [Online]. Available: <https://interfaceforce.co.uk/category/products/torque-sensors-and-transducers/>
- [14] A. Schramm, E. Sworowski, and J. Roth-Stielow, "Methods for measuring torque ripples in electrical machines," in *2017 IEEE International Electric Machines and Drives Conference (IEMDC)*, May 2017, pp. 1–8.
- [15] G. Heins, M. Thiele, and T. Brown, "Accurate Torque Ripple Measurement for PMSM," *IEEE Transactions on Instrumentation and Measurement*, vol. 60, no. 12, pp. 3868–3874, Dec. 2011.
- [16] "Wireless Torque Sensor for Rotary Torque Measurement | Binsfeld." [Online]. Available: <https://binsfeld.com/torquetrak/temporary-torque-measurement/torquetrak-10k/>
- [17] "TELI-PCM-FLEX-IND - Extremely flat & flexible transmitter - KMT Telemetry." [Online]. Available: <https://www.kmt-telemetry.com/telemetry/1-channel-telemetry/tel1-pcm-flex-ind/>
- [18] K. Liu and Z. Zhu, "Fast Determination of Moment of Inertia of Permanent Magnet Synchronous Machine Drives for Design of Speed Loop Regulator," *IEEE Transactions on Control Systems Technology*, vol. 25, no. 5, pp. 1816–1824, Sep. 2017.
- [19] M. Martinez, D. Fernandez, D. Reigosa, J. M. Guerrero, and F. Briz, "Wireless Torque Pulsations Measurement System for PMSMs," *IEEE Transactions on Industry Applications*, vol. 56, no. 6, pp. 6467–6476, Nov. 2020.
- [20] X. Liu, D. Liang, J. Du, Y. Yu, and X. Yang, "A torque measuring method based on encoder for permanent magnet synchronous machine," in *2014 17th International Conference on Electrical Machines and Systems (ICEMS)*, Oct. 2014, pp. 1510–1514.
- [21] "Emrax e-motors, "standard motors: Emrax 228,"." [Online]. Available: <https://emrax.com/products/emrax-228>

B.2.5 Use HF Signal Injection for Simultaneous Rotor Angle, Torque and Temperature Estimation in PMSMs

Use HF Signal Injection for Simultaneous Rotor Angle, Torque and Temperature Estimation in PMSMs

Marcos Orviz Zapico
University of Oviedo. Dept of Elect.
Computer & System Engineering, Gijón,
33204, Spain
orvizmarcos@uniovi.es

María Martínez Gómez
University of Oviedo. Dept of Elect.
Computer & System Engineering, Gijón,
33204, Spain
martinezgmaria@uniovi.es

David Díaz Reigosa
University of Oviedo. Dept of Elect.
Computer & System Engineering, Gijón,
33204, Spain
diazdavid@uniovi.es

Juan Manuel Guerrero Muñoz
University of Oviedo. Dept of Elect.
Computer & System Engineering, Gijón,
33204, Spain
guerrero@uniovi.es

Diego Fernández Laborda
University of Oviedo. Dept of Elect.
Computer & System Engineering, Gijón,
33204, Spain
dflaborda@uniovi.es

Fernando Briz del Blanco
University of Oviedo. Dept of Elect.
Computer & System Engineering, Gijón,
33204, Spain
fernando@isa.uniovi.es

Abstract— Use of high frequency (HF) signal injection-based methods with PMSMs has been widely investigated for several purposes including rotor angle/speed estimation, permanent magnet (PM) temperature estimation and torque estimation. This paper analyses the opportunities of multi-estimation. The physics behind these methods are analyzed, from which the number and characteristics of the HF signals to be injected can be deduced. Based on this, injection of a pulsating HF current 45° shifted from the d -axis and a rotating HF current in the stationary reference frame is found to be a suitable solution for simultaneous rotor angle, torque and magnet temperature estimation.¹

Keywords— Permanent Magnet Synchronous Machine (PMSM), high frequency signal injection, sensorless control, torque estimation, temperature estimation

I. INTRODUCTION

The use of PMSMs has increased during the last decades in a large variety of applications thanks to their improved performance in terms of torque/power density, efficiency, and controllability compared to other types of electric machines. Torque and motion control of PMSMs drives requires knowledge of the rotor angle, which can be measured or estimated. In addition, knowledge of machine torque and magnet temperature can be highly desirable for control and reliability purposes.

Optical encoders and resolvers, are the preferred solution in the industry for rotor angle feedback [1]-[2], though other alternatives are available [3]-[5]. Cost of the position sensor and the associated cabling and interfaces can account for a significant portion of the overall drive cost, especially in low-power applications. In addition, the sensor itself and the associated cabling and connectors can be a source of failures, reducing the drive reliability. Elimination of the position/speed sensor is therefore desirable. Sensorless methods are an alternative to the

use of position sensors [6]-[20]. Sensorless methods can be broadly classified into methods based on the fundamental excitation [6], and saliency tracking based techniques [7]-[20].

Fundamental excitation-based methods are effective when the back electromotive force (BEMF) signal is sufficiently large, i.e., at medium and high speeds; operation at low speed or standstill not being possible. Saliency tracking based techniques were proposed to overcome the limitations of BEMF based methods in the low-speed range, since they allow rotor angle estimation at low and zero speed.

Precise knowledge of the torque produced by the machine is also a highly appealing feature in many applications [21]. Torque measurement can be done using strain gauges [22], other methods like those based on torsional displacements being less extended [23]. Independently of the method, torque measurement is costly and requires additional cabling and room. Hence, torque estimation is preferred in most applications. Torque estimation methods include equation based methods [24]-[28], indirect estimation methods [29] and neural networks [30]. All these methods require knowledge of certain machine parameters (e.g., magnet flux, inductances, and resistances) which often can vary with machine operating conditions (e.g., temperature, saturation, or speed). Injection of a HF signal into the stator terminals of the machine has been reported as a viable option for real time adaption of machine parameters needed by torque estimation methods, eventually enhancing their accuracy [27].

Finally, the performance and reliability of the drive also depends on the PMSM temperature, especially PMSMs' temperature. Magnet temperature can be measured by means of contact type sensors (e.g., PTC thermistors, thermocouples, etc.) or non-contact type sensors (e.g., IR sensors) [31]. However, PM temperature measurement is not easy in practice as it implies modifications of the machine design, which can affect to its

Table I. Estimation information from the machine's response to the HF

	Rotor angle Estimation		Temperature Estimation		Torque Estimation	
	Asymmetric	Symmetric	Asymmetric	Symmetric	Asymmetric	Symmetric
Resistance	✓ [20]	✗	✗	✓ [35]	✗	✗
Inductance	✓ [7]	✗	✗	✓ [37]	✓ [24]	✓ [27]

✓ means "already published", ✗ means "not published"

¹ This work was supported in part by the Research, Technological Development and Innovation Programs of the Spanish Ministry of Science and Innovation, under grant PID2019-106057RB-I00.

Table II: HF Signal Injection Possibilities for Rotor Angle Estimation

Injection reference frame	HF signal type (Periodic)								
	Rotating Signal (Sinusoidal)		Pulsating Signal (Sinusoidal)				Rotating Signal (Square-Wave)	Pulsating Signal (Square-Wave)	
	Voltage	Current	<i>d</i> -axis		<i>q</i> -axis		Voltage	<i>d</i> -axis	<i>q</i> -axis
			Voltage	Current	Voltage	Current		Voltage	Voltage
Stationary (<i>d</i> -axis aligned with phase A)	✓ [7], [8]	✓ [9]	✓ [11]	✗	✓ [11]	✗	✓ [16]	✗	✓ [18]
Synchronous (<i>d</i> -axis aligned with PM)	✓ [10]	✗	✓ [8]	✓ [15]	✓ [14]	✓ [15]	✗	✓ [17]	✓ [19]
Used signal	Negative sequence HF current	Negative sequence HF voltage	<i>q</i> -axis HF current	<i>q</i> -axis HF voltage	<i>d</i> -axis HF current	<i>d</i> -axis HF voltage	Reconstructed current	<i>q</i> -axis HF current	Induced HF current
Frequency Range	250 – 1000 Hz	200 – 910 Hz	330 – 2000 Hz	500 – 1000 Hz	330 – 2000 Hz	1000 Hz	1500 Hz	625 – 5000 Hz	800 Hz

reliability and increase its cost. Hence, PM temperature estimation is preferred. PM temperature estimation methods include thermal model based [32], BEMF based [33], and HF signal injection based [34]-[37] methods. Thermal models require previous knowledge of the machine geometry, materials, and cooling system. BEMF based methods do not work at standstill or low speeds. Appealing properties of HF signal injection based methods include the capability of operating in the whole speed range and the reduced sensitivity with respect to machine's geometry.

The response of the machine to the injected HF signal can be modelled as an RL load, which in a general case will consist of an average value and a differential value. The information of interest can be embedded in the resistive and/or inductive part, of either the symmetric or asymmetric components, as shown in Table I. Main facts observed from Table I are:

- Temperature estimation methods mostly rely on the symmetric behaviour of the machine, use of both inductive and resistive parts being feasible.

- Torque estimation relies on either the symmetric or asymmetric behaviour of the inductive part.
- Rotor angle estimation methods usually rely on the asymmetric part of the inductive component.

A critical aspect in the implementation of HF signal injection methods is the selection of the frequency. Generally speaking, lower frequencies will be advantageous when the information of interest is embedded in a resistive component, while higher frequencies will be preferred when the information of interest is embedded in an inductive component.

The following conclusions can be reached from the previous discussion and Table I:

- Simultaneous estimation of position, temperature, and torque, from the machine response to a HF signal seems possible.
- The fact that rotor angle estimation and temperature estimation rely on the asymmetric and symmetric parts respectively suggest that the challenges for simultaneous estimation of these two variables should be moderate.

Table III: HF Injection Possibilities for Torque Estimation

Injection Reference Frame	HF signal type (Periodic)				
	Rotating Signal	Pulsating Signal			
	Voltage	Voltage		Current	
		<i>d</i> - and <i>q</i> - axis	45° from <i>d</i> - axis	<i>d</i> - and <i>q</i> - axis	45° from <i>d</i> - axis
Stationary (<i>d</i> -axis aligned with phase A)	✓ [24]	✗	-	✗	-
Synchronous (<i>d</i> -axis aligned with PM)	✓ [25]	✗	✓ [26]	✓ [27]	✓ [28]
Injected signals	1	-	1	2	1
Used signal	Positive and negative HF current	-	<i>d</i> - and <i>q</i> -axes HF current	<i>d</i> - and <i>q</i> -axes HF voltage	<i>d</i> - and <i>q</i> -axes HF voltage
Estimated parameters	L_d, L_q, λ_{PM} [24] L_d, L_q [25]	-	L_d, L_q	L_d, L_q, λ_{PM}	L_d, L_q, λ_{PM}
Frequency Range	500 Hz	-	250 Hz	500 – 1000Hz	500 Hz

- means "not possible" or "no sense"

- The fact that torque estimation can be performed using either the symmetric or asymmetric parts of the machine reveals a well-known fact: load level can produce severe disturbances to both rotor angle estimation and temperature estimation methods.
- Selection of the HF signals (number of signals, signals type and frequency) will be critical to minimize the risk of interference between rotor angle, temperature and torque estimations.

This paper deals with the simultaneous estimation of rotor angle, temperature and torque in PMSM using HF signal injection. The paper is organized as follows. Section II reviews the existing literature on the estimation of these three quantities. Opportunities and challenges for simultaneous estimation are presented in Section III. Implementation of the proposed method for simultaneous estimation is presented in Section IV. Simulations results are provided in Section V. Finally, conclusions are presented in Section VI.

II. REVIEW OF HF SIGNAL INJECTION BASED ROTOR ANGLE, TEMPERATURE AND TORQUE ESTIMATION

In this section, the existing literature on the independent estimation of rotor angle, torque and PM temperature estimation will be reviewed.

A. HF Signal Injection Based Rotor Angle Estimation

Rotor angle of PMSMs can be estimated by injecting a HF signal superimposed on top of the fundamental excitation [7]. Different alternatives depending on the type of HF signal and injection reference frame have been proposed, see Table II. Although all these forms of HF excitation respond to the same physical principles and can potentially provide the same performance, some differences exist in their practical implementation. Existing methods can be classified following multiple criteria: rotating vs. pulsating; sine-wave or square-wave; voltage vs. current; injection in the stationary reference frame vs. synchronous reference frame. Furthermore, pulsating HF signal injection in the synchronous reference frame allows selection of the angle of injection, e.g., d -axis, q -axis or in between d - and q -axis (45° from d -axis); only d - or q -axis injection has been reported for rotor angle estimation.

$$T = \frac{3P}{2} [\lambda_{PM} i_{qs}^r + (L_d - L_q) i_{ds}^r i_{qs}^r] \quad (1)$$

B. HF Signal Injection Based Torque Estimation

On-line estimation of the machine parameters involved in the general torque equation (GTE) (1), i.e., d - and q -axes inductance (L_d and L_q) and the PM flux linkage (λ_{PM}), through HF signal injection has been recently proposed [24]-[28]. Different alternatives can be distinguished depending on the number of injected signals, magnitude (voltage or current), shape (pulsating, rotating, etc.) and injection reference frame, see Table III. Injection of a rotating voltage (whether in synchronous or stationary reference frame) or pulsating current/voltage signal at 45° from the d -axis allow both electromagnetic and reluctance torque estimation using a unique signal. Injection of a pulsating current in the d -axis of the synchronous reference frame does not allow reluctance torque estimation, as no information about the q -axis inductance is obtained. Hence, pulsating HF signal injection in both the d - and q -axes is required in saliency machines, e.g., IPMSMs, that produce reluctance torque. For SPMSMs, pulsating signal injection in the d -axis would be enough.

C. HF Signal Injection Based PM Temperature Estimation

HF signal injection based PM temperature estimation methods rely on the variation of the stator-reflected magnet HF electrical resistance [34]-[35] or the stator d -axis HF inductance [37] with PM temperature. Depending on the type of HF signal and the injection reference frame, different alternatives have been proposed, see Table IV. Estimation of the d -axis resistance through a rotating HF voltage requires the frequency of the injected signal to be considerably higher than the fundamental one ($\omega_{HF} \gg \omega_r$); this assumption is realistic for SPMSMs but not for IPMSMs. Injection of a pulsating voltage or current signal in the d -axis (synchronous reference frame) allows estimation of the d -axis HF resistance and inductance, and therefore temperature.

III. COMBINED ROTOR ANGLE, TORQUE AND TEMPERATURE ESTIMATION BASED ON THE INJECTION OF A HF SIGNAL

This section analyses simultaneous estimation of rotor angle, torque, and rotor temperature using HF signal injection. Table V shows the available options, using a single HF signal (first column), or two HF signals (right column). Drawbacks of injecting more than one HF signals are the increased complexity of the signal processing as well as the increased losses.

Injection Reference Frame	HF signal type			
	Periodic (Frequency-Based)			Non-Periodic (Time-Based)
	Rotating Signal	Pulsating Signal		Pulse Signal
	Voltage	Current (d -axis)	Voltage (d -axis)	Voltage (d -axis)
Stationary (d -axis aligned with phase A)	✓ [34] *	✗	✗	✗
Synchronous (d -axis aligned with PM)	✗	✓ [35], [37]	✓ [35]	✓ [36]
Used signal	HF positive sequence current	d -axis HF voltage	d -axis HF current	d -axis transient current
Estimated parameters	R_{dqHF}	R_{dHF} [35] L_{dHF} [37]	R_{dHF}	L_{dHF}
Frequency Range	250 Hz	250 – 2500 Hz	250 Hz	-

*Only valid for SPMSMs

Table V: HF Injection Options for Rotor Angle, Torque and Temperature Estimation		
Estimated parameter	Number of injected HF signals	
	Options injecting one HF signal	Options injecting two HF signals
Rotor angle	1. Rotating Voltage/Current (Stationary) 2. Pulsating Voltage/Current (d -sync)	-
Torque	1. Rotating Voltage (Stationary) 2. Rotating Voltage (Sync) 3. Pulsating Voltage/Current (d -sync) * 4. Pulsating Voltage/Current (45° from d -sync.)	1. Pulsating Voltage/Current (d -sync) + Pulsating Voltage/Current (q -sync)
Magnet temperature	1. Rotating Voltage (Stationary) * 2. Pulsating Voltage (d -sync) 3. Pulsating Voltage/Current (d -sync) 4. Pulsating Voltage/Current (45° from d -sync.)	-
Rotor angle and torque	1. Rotating Voltage (Stationary) 2. Pulsating Voltage/Current (d -sync) *	1. Pulsating Voltage/Current (d -sync) + Pulsating Voltage/Current (q -sync)
Rotor angle and magnet temperature	1. Rotating Voltage (Stationary) * 2. Pulsating Voltage/Current (d -sync)	1. Pulsating Voltage/Current (d -sync) + Rotating Voltage/Current (Stationary)
Magnet temperature and torque	1. Rotating Voltage (Stationary) * 2. Pulsating Voltage/Current (d -sync) * 3. Pulsating Current (45° from d -sync)	1. Pulsating Voltage/Current (d -sync) + Pulsating Voltage/Current (q -sync)
Rotor angle, magnet temperature and torque	1. Rotating Voltage (Stationary) * 2. Pulsating Voltage/Current (d -sync) *	1. Pulsating Voltage/Current (d -sync) + Pulsating Current (q -sync) 2. Pulsating Voltage/Current (d -sync) + Rotating Voltage/Current (Stationary) 3. Pulsating Voltage/Current (45° from d -sync) + Pulsating Voltage/Current (d -sync) 4. Pulsating Voltage/Current (45° from d -sync) + Rotating Voltage/Current (Stationary)

*Only valid for SPMSMs

For each case, Table I shows which behaviour of the machine (symmetric/asymmetric, inductive/resistive) is to be used. Focusing on simultaneous rotor angle, torque, and magnet temperature estimation, it can be seen that the available possibilities injecting a single HF signal are limited to SPMSMs. The injection of two different HF signals opens more possibilities which are not limited to SPMSMs (i.e. can be used in any PMSM type): (i) injection of a pulsating voltage/current in the d -axis of the synchronous reference frame for rotor angle [8], [15] and temperature estimation [35], [37] which can be combined with a pulsating current in the q -axis for torque estimation [27]; (ii)

injection of a rotating voltage in the stationary reference frame for rotor angle [7], [8] and torque estimation [24], which can be combined with a pulsating voltage/current in the d -axis for magnet temperature estimation [35], [37], (iii) injection of a pulsating HF current at 45° from the d -axis for temperature [35] and torque estimation [28] which can be combined with a rotating HF voltage/current in the stationary reference frame for rotor position estimation [7]-[9] and (iv) injection of a pulsating voltage/current in the d -axis of the synchronous reference frame for rotor angle estimation [8], [15] which can be combined with

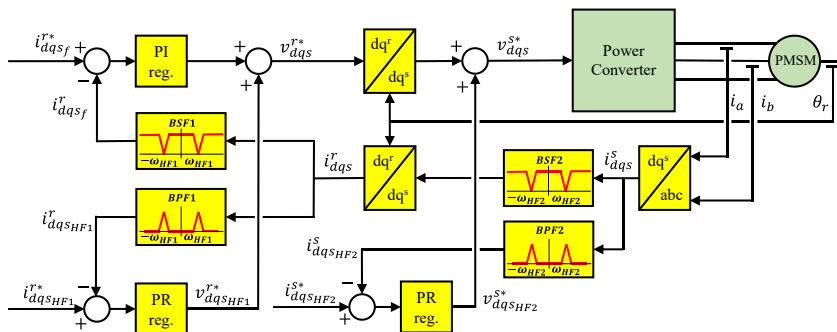


Fig. 1: Control scheme for simultaneous rotor angle, torque and magnet temperature estimation combining a pulsating HF current 45° shifted from the d -axis (HF₁) and a rotating HF current in the stationary reference frame (HF₂).

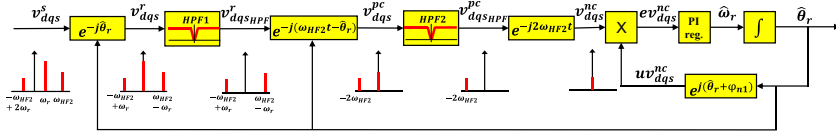


Fig. 2: Rotor position estimation control block diagram (PLL).

the same signals as in (iii) for torque and magnet temperature estimation.

Following the preceding discussion, the combined use of a pulsating HF current 45° shifted from the d -axis and a rotating HF current in the stationary reference frame has been chosen. This option is advantageous in terms of injection frequency selection: lower frequencies will be used for the pulsating current as it is preferable for dq -axes resistance, R_{dqHF} (for magnet temperature estimation) and inductance, L_{dqHF} (for torque estimation) estimation, while higher frequencies for the rotating HF current are preferable for rotor angle estimation. In addition, it can be observed that this option does not require to combine parameters estimated with different HF signals, i.e., both rotor angle, torque as well as magnet temperature are independently estimated through a single HF signal.

IV. IMPLEMENTATION

This section discusses the implementation of the selected method. Fig. 1 shows the corresponding block diagram. A pulsating HF current 45° shifted from the d -axis (HF₁) and a rotating HF current in the stationary reference frame (HF₂) are injected. Two band-stop filters (BSF1 and BSF2) are used to remove both HF components (ω_{HF1} and ω_{HF2}) in the fundamental current feedback. Proportional resonant (PR) controllers are used to control the injected HF currents, band-pass filters (BPF1 and BPF2) being used to isolate each HF component in the corresponding HF current feedback, i.e., ω_{HF1} for the pulsating HF current feedback, and ω_{HF2} for the rotating HF current feedback.

A. Rotor Angle Estimation Using Rotating HF Current Injection in the Stationary Reference Frame

If a sinusoidal rotary HF current signal (2) is injected into the stator terminals of a PMSM, the resulting HF voltages are represented by (3) assuming a pure inductive behaviour of the PMSM, where $\sum L_s$ (4) and ΔL_s (5) are the mean and differential inductances respectively. (3) can be also expressed as (6), where V_{pc} (7) is the magnitude of the positive sequence component and V_{nc} (8) the magnitude of the negative sequence component. It can be observed from (6) that the resulting stator HF voltage can be decomposed into a positive sequence component, that does not provide any information about the rotor position, and a negative sequence component, with rotor position information [7].

$$i_{dqHF2}^s = I_{HF2} \begin{bmatrix} \cos(\omega_{HF2}t) \\ \sin(\omega_{HF2}t) \end{bmatrix} \quad (2)$$

$$v_{dqHF2}^s = j\omega_{HF2} \sum L_s i_{dqHF2}^s \cdot \begin{bmatrix} \sum L_s + \Delta L_s \cos(2\theta_r) & -\Delta L_s \sin(2\theta_r) \\ -\Delta L_s \sin(2\theta_r) & \sum L_s - \Delta L_s \cos(2\theta_r) \end{bmatrix} \quad (3)$$

$$\sum L_s = \frac{L_{ds} + L_{qs}}{2} \quad (4) \quad \Delta L_s = \frac{L_{qs} - L_{ds}}{2} \quad (5)$$

$$v_{dqHF2}^s = v_{dqHF2pc}^s + v_{dqHF2nc}^s = jV_{pc} e^{j\omega_{HF2}t} + V_{nc} e^{-j(\omega_{HF2}t - 2\theta_r)} \quad (6)$$

$$V_{pc} = \omega_{HF2} I_{HF2} \sum L_s \quad (7) \quad V_{nc} = \omega_{HF2} I_{HF2} \Delta L \quad (8)$$

Fig. 2 shows the control block diagram for rotor position estimation when using a rotating HF current injection. The input of the control block diagram is the stator voltage in the stator reference frame, v_{dq}^s which is first transformed to a reference frame synchronous with the estimated rotor position, v_{dq}^r .

Two high-pass filters (HPF) are used to remove the fundamental voltage (HPF1), v_{dqHF1}^r being obtained, and the positive sequence of the HF voltage (HPF2), v_{dqHF1}^{pc} being obtained; the resulting voltage consisting therefore only of the negative sequence component, see v_{dq}^s , v_{dq}^r will feed a PLL used to estimate the rotor position [9].

B. Torque and Temperature Estimation through Pulsating HF Signal Injection at 45° from the d -axis

Simultaneous rotor temperature, T_r and torque, T estimation can be achieved through the injection of a pulsating HF signal at 45° from the d -axis. A resonant controller can be used to inject the HF current, i_{dqHF1}^r (9), the HF voltage, v_{dqHF1}^r , (10) being thus commanded. Estimation of the d -axis HF resistance, R_{dHF1} , and inductance, L_{dHF1} , can be done through the measured d -axis HF current, i_{dqHF1}^r , (11), and the commanded d -axis HF voltage, v_{dqHF1}^r , (12). Both (11) and (12) can be decomposed into a positive ($i_{dqHF1pc}^r$ and $v_{dqHF1pc}^r$) and negative sequence component ($i_{dqHF1nc}^r$ and $v_{dqHF1nc}^r$), see (13) and (14). The d -axis HF impedance, Z_d can be obtained either from the positive or the negative sequence component, as shown in (15). Taking the real part of (15) the d -axis HF resistance, R_{dHF1} is obtained (16). Taking the imaginary part of (15) the d -axis HF inductance, L_{dHF1} is obtained (17). Following an analogous process, but using the q -axis voltage and current (18)-(22), the q -axis HF inductance, L_{qHF1} can be also obtained (23).

$$i_{dqHF1}^r = \begin{bmatrix} i_{dsHF1}^r \\ i_{qsHF1}^r \end{bmatrix} = \begin{bmatrix} I_{HF1} \cos(\omega_{HF1}t) \\ I_{HF1} \sin(\omega_{HF1}t) \end{bmatrix} \quad (9)$$

$$v_{dqHF1}^r = \begin{bmatrix} v_{dsHF1}^r \\ v_{qsHF1}^r \end{bmatrix} = \begin{bmatrix} (R_{dHF1} + j\omega_{HF1}L_{dHF1})\vec{i}_{dsHF1}^r - \omega_r L_{qHF1}\vec{i}_{qsHF1}^r \\ (R_{qHF1} + j\omega_{HF1}L_{qHF1})\vec{i}_{qsHF1}^r + \omega_r L_{dHF1}\vec{i}_{dsHF1}^r \end{bmatrix} \quad (10)$$

$$i_{dqHF1}^r = \begin{bmatrix} i_{dsHF1}^r \\ 0 \end{bmatrix} = \begin{bmatrix} I_{HF1} \cos(\omega_{HF1}t) \\ 0 \end{bmatrix} \quad (11)$$

$$v_{dqHF1}^r = \begin{bmatrix} v_{dsHF1}^r \\ 0 \end{bmatrix} = \begin{bmatrix} (R_{dHF1} + j\omega_{HF1}L_{dHF1})\vec{i}_{dsHF1}^r - \omega_r L_{qHF1}\vec{i}_{qsHF1}^r \\ 0 \end{bmatrix} \quad (12)$$

$$i_{dqSHF1}^{r'} = \frac{|i_{dqSHF1}^{r'}|}{2} e^{j\omega_{HF1}t} + \frac{|i_{dqSHF1}^{r'}|}{2} e^{-j\omega_{HF1}t} = \quad (13)$$

$$= i_{dqSHF1pc}^{r'} + i_{dqSHF1nc}^{r'}$$

$$v_{dqSHF1}^{r'} = \frac{|v_{dqSHF1}^{r'}|}{2} e^{j(\omega_{HF1}t - \varphi_{Zd})} \quad (14)$$

$$+ \frac{|v_{dqSHF1}^{r'}|}{2} e^{j(-\omega_{HF1}t + \varphi_{Zd})}$$

$$= v_{dqSHF1pc}^{r'} + v_{dqSHF1nc}^{r'}$$

$$Z_d = R_{dHF1} - \omega_r L_{qHF1} + j\omega_{HF1} L_{dHF1} = \quad (15)$$

$$= \frac{v_{dqSHF1pc}^{r'}}{i_{dqSHF1pc}^{r'}} = \frac{v_{dqSHF1nc}^{r'}}{i_{dqSHF1nc}^{r'}}$$

$$R_{dHF1} = \Re[Z_{dHF1}] / \omega_{HF1} \quad (16)$$

$$L_{dHF1} = \Im[Z_{dHF1}] / \omega_{HF1} \quad (17)$$

$$i_{dqSHF1}^{r*} = \begin{bmatrix} 0 \\ i_{qsHF1}^{r*} \end{bmatrix} = \begin{bmatrix} 0 \\ I_{HF1} \cos(\omega_{HF1}t) \end{bmatrix} \quad (18)$$

$$v_{dqSHF1}^{r''} = \begin{bmatrix} 0 \\ (R_{dHF1} + j\omega_{HF1} L_{qHF1}) \vec{i}_{qsHF1}^{r''} + \omega_r L_{dHF1} \vec{i}_{dsHF1}^{r''} \end{bmatrix} \quad (19)$$

$$i_{dqSHF1}^{r''*} = \frac{|i_{dqSHF1}^{r''*}|}{2} e^{j\omega_{HF1}t} + \frac{|i_{dqSHF1}^{r''*}|}{2} e^{-j\omega_{HF1}t} \quad (20)$$

$$= i_{dqSHF1pc}^{r''*} + i_{dqSHF1nc}^{r''*}$$

$$v_{dqSHF1}^{r''} = \frac{|v_{dqSHF1}^{r''}|}{2} e^{j(\omega_{HF1}t - \varphi_{Zd})} \quad (21)$$

$$+ \frac{|v_{dqSHF1}^{r''}|}{2} e^{j(-\omega_{HF1}t + \varphi_{Zd})}$$

$$= v_{dqSHF1pc}^{r''} + v_{dqSHF1nc}^{r''}$$

$$Z_q = R_{qHF1} - \omega_r L_{dHF1} + j\omega_{HF1} L_{qHF1} = \quad (22)$$

$$\frac{v_{dqSHF1pc}^{r''}}{i_{dqSHF1pc}^{r''}} = \frac{v_{dqSHF1nc}^{r''}}{i_{dqSHF1nc}^{r''}}$$

$$L_{qHF1} = \Im[Z_{qHF1}] / \omega_{HF1} \quad (23)$$

According to [27], λ_{PM} variation with the d -axis inductance is given by (24) where λ_{PM0} and L_{d0} are the PM flux and d -axis inductance at the room temperature (T_{r0}) and when no dq -axis fundamental current is injected respectively, L_{dHF1} is the d -axis inductance when the magnet temperature is T_r and when dq -axis fundamental current is injected (17) and K_{BEMF} is the coefficient linking the d -axis HF inductance with the PM flux.

$$\lambda_{PM} = \left(\lambda_{PM0} + k_{BEMF} \frac{L_{dHF1} - L_{d0}}{L_{d0}} \right) \quad (24)$$

Then, substituting (17), (23) and (24) in the GTE (1), the output torque, T , can be finally estimated.

PM temperature can be estimated through d -axis HF resistance (25) [35], being T_s and T_r the stator and rotor temperatures respectively, T_0 the room temperature, R_{dsHF1} and R_{drHF1} the stator and rotor contributions to the d -axis HF resistance, and α_{cu} and α_{mag} the copper and magnet thermal resistive coefficients respectively.

$$R_{dHF1(T_s, T_r)} = R_{dsHF1(T_s)} + R_{drHF1(T_r)} = \quad (25)$$

$$= R_{dsHF1(T_0)}(1 + \alpha_{cu}(T_s - T_0))$$

$$+ R_{drHF1(T_0)}(1 + \alpha_{mag}(T_r - T_0))$$

Fig. 3 shows the signal processing block diagram for simultaneous torque estimation (GTE) and rotor temperature estimation (d -axis HF resistance).

V. SIMULATION RESULTS

This section presents simulation results showing simultaneous rotor angle, torque, and temperature estimation. Rotor temperature is assumed to increase proportionally to the squared stator current due to joule losses; an unrealistically low value of the thermal constant has been used to reduce the simulation time. It is noted that

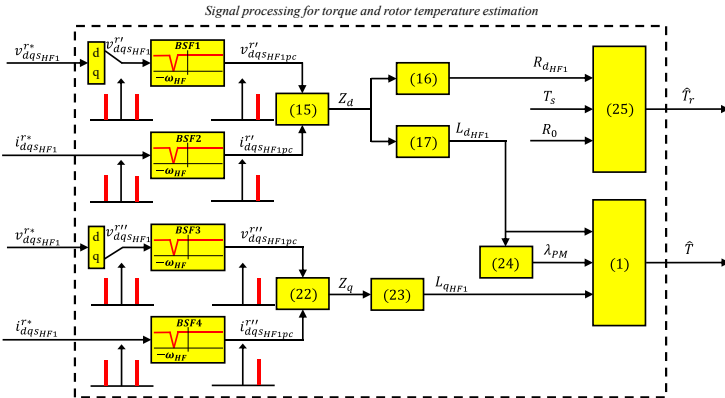


Fig. 3: Torque and rotor temperature estimation control block diagram.

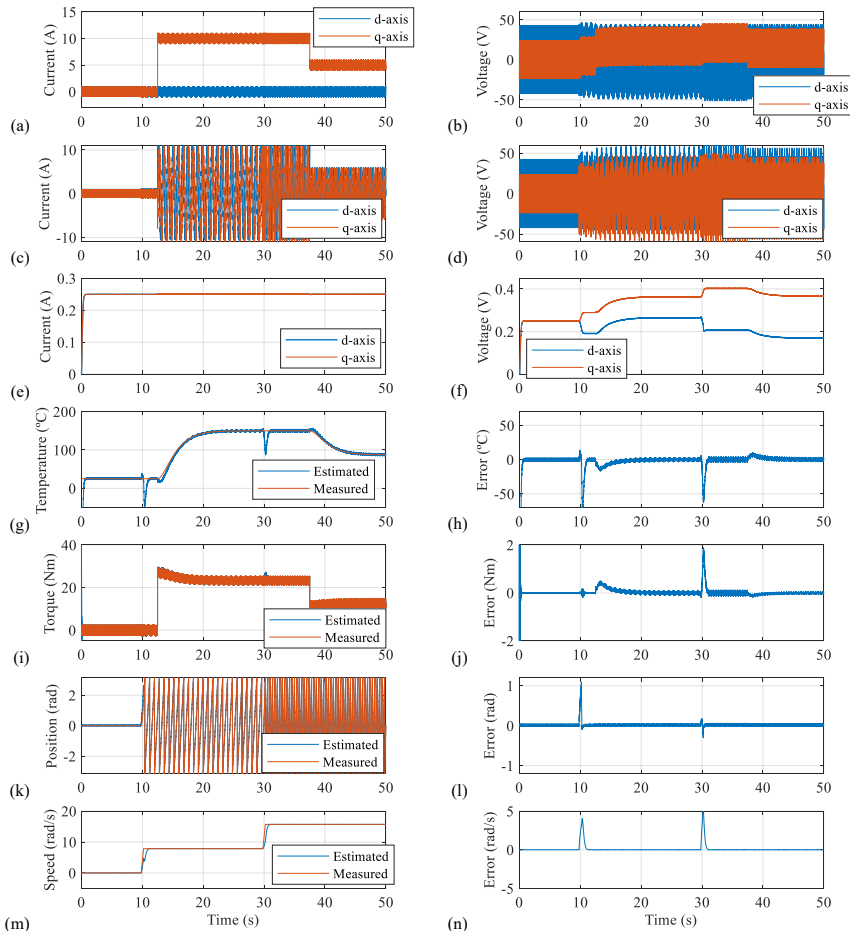


Fig. 4: (a) dq -axes current and (b) voltage in the synchronous reference frame, (c) pulsating HF current (HF_i), (f) resulting stator HF voltage, (g) measured and estimated temperature, (h) temperature estimation error, (i) measured and estimated torque, (j) torque estimation error, (k) measured and estimated rotor angle, (l) rotor angle estimation error, (m) measured and estimated speed and (n) speed estimation error. $\omega_{HF} = 2\pi \cdot 250$ rad/s, $I_{HF} = 0.05$ pu, $\omega_{HF} = 2\pi \cdot 500$ rad/s and $I_{HF} = 0.05$ pu.

this has no further effects on the results. Fig. 4 (a) and (b) show the dq - axes currents and voltages in the synchronous reference frame respectively, (c) and (d) show the dq - axes currents and voltages in the stationary reference frame, (e) shows the injected pulsating HF current (HF_i), (f) shows the resulting stator HF voltage, (g) and (h) show both the measured and estimated temperature and the corresponding temperature estimation error, (i) and (j) show both the measured and estimated torque and the corresponding torque error, (k) and (l) show both the measured and estimated rotor position and the resulting rotor position

estimation error, finally (m) and (n) show the measured and estimated speed and the resulting speed estimation error. Steady state estimation errors are seen to be $< 5^\circ\text{C}$ for magnet temperature (Fig. 4h), < 0.12 Nm (0.4%) for torque (Fig. 4j) and < 0.07 rad (Fig. 4l) for rotor angle, respectively.

VI. CONCLUSIONS

This paper proposes the use of HF signal injection for simultaneous rotor angle, torque, and magnet temperature estimation in PMSMs. Available options in terms of

number and types of signals that could be injected have been discussed. Simultaneous rotor angle, torque and magnet temperature estimation using a single HF signal has been shown to be only feasible for SPMSMs, the use of at least two HF signals being required for IPMSMs.

Combination of a rotating HF current in the stationary reference frame (rotor angle estimation) and a pulsating HF current in the synchronous reference frame (torque and magnet temperature estimation) has been chosen as the preferred solution. Simulation results have been provided to demonstrate the viability of the proposed method. Experimental verification of the proposed method is ongoing.

REFERENCES

- [1] Maxonmotorsa.com, "maxon sensor - Key information," Sep. 20, 2020. [Online]. Available: <http://www.maxonmotorsa.com/>
- [2] Figueiredo, "Resolver models for manufacturing," *IEEE Trans. Ind. Electron.*, 58(8): 3693-3700, Aug. 2011
- [3] R. M. Kennel and S. Basler, "New developments in capacitive encoders for servo drives," 2008 International Symposium on Power Electronics, Electrical Drives, Automation and Motion, Ischia, 2008, pp. 190-195, doi: 10.1109/SPEEDHAM.2008.4581311.
- [4] B. S. Nauduri and G. Shaga, "A novel approach of using a planar inductive position sensor for the Permanent magnet synchronous motor control application," 2018 IEEE Sensors Applications Symposium (SAS), Seoul, 2018, pp. 1-5, doi: 10.1109/SAS.2018.8336708.
- [5] P. Kejik, S. Reymond, and R. S. Popovic, "Purely CMOS angular position sensor based on a new Hall microchip," in Proc. 34th Annu. Conf. IEEE Ind. Electron., Nov. 10-13, 2008, pp. 1777-1781.
- [6] L. A. de S. Ribeiro, M. C. Harke, and R. D. Lorenz, "Dynamic properties of back-EMF based sensorless drives," in Conf. Rec. IEEE IAS Meeting, Oct. 2006, vol. 4, pp. 2026-2033
- [7] M. W. Degner and R. D. Lorenz, "Using multiple saliencies for the estimation of flux, position, and velocity in AC machines," in *IEEE Transactions on Industry Applications*, vol. 34, no. 5, pp. 1097-1104, Sept.-Oct. 1998, doi: 10.1109/28.720450.
- [8] Y. Joang, R. D. Lorenz, T. M. Jahns, and S.-K. Sul, "Initial rotor position estimation of an interior permanent-magnet synchronous machine using carrier-frequency injection methods," *IEEE Trans. Ind. Appl.*, vol. 41, no. 1, pp. 38-45, Jan./Feb. 2005.
- [9] L.A.S. Ribeiro, M.W. Degner, F. Briz y R.D. Lorenz. Comparison of carrier signal voltage and current injection for the estimation of flux angle or rotor position. En IEEE Industry Applications Society Annual Meeting. IAS'98, tomo 1, páginas 452-459. St. Louis, MO, USA, 1998.
- [10] C. Caruana, G. M. Asher, K. J. Bradley and M. Woolfson, "Flux position estimation in cage induction machines using synchronous HF injection and Kalman filtering," in *IEEE Transactions on Industry Applications*, vol. 39, no. 5, pp. 1372-1378, Sept.-Oct. 2003, doi: 10.1109/TIA.2003.2293000.
- [11] J. M. Liu and Z. Q. Zhu, "Novel Sensorless Control Strategy With Injection of High-Frequency Pulsating Carrier Signal Into Stationary Reference Frame," in *IEEE Transactions on Industry Applications*, vol. 50, no. 4, pp. 2574-2583, July-Aug. 2014, doi: 10.1109/TIA.2013.2293000.
- [12] M. Linke, R. Kennel, and J. Holtz, "Sensorless speed and position control of synchronous machines using alternating carrier injection," in Proc. IEEE IEMDC, 2003, vol. 2, pp. 1211-1217.
- [13] G. Foo and M. F. Rahman, "Sensorless Sliding-Mode MTPA Control of an IPM Synchronous Motor Drive Using a Sliding-Mode Observer and HF Signal Injection," in *IEEE Transactions on Industrial Electronics*, vol. 57, no. 4, pp. 1270-1278, April 2010, doi: 10.1109/TIE.2009.2030820
- [14] M. J. Corley and R. D. Lorenz, "Rotor position and velocity estimation for a salient-pole permanent magnet synchronous machine at standstill and high speed," *IEEE Trans. Ind. Appl.*, vol. 34, no. 4, pp. 784-789, Jul./Aug. 1998
- [15] M. Selmeier, A. Boehm, I. Hahn and B. Piepenbreier, "Identification of time-variant high frequency parameters for sensorless control of PMSM using an internal model principle based high frequency current control," 2012, 20th International Conference on Electrical Machines, Marseille, 2012, pp. 987-993, doi: 10.1109/ICEMach.2012.6349996.
- [16] G. Wang, D. Xiao, G. Zhang, C. Li, X. Zhang and D. Xu, "Sensorless Control Scheme of IPMSMs Using HF Orthogonal Square-Wave Voltage Injection Into a Stationary Reference Frame," in *IEEE Transactions on Power Electronics*, vol. 34, no. 3, pp. 2573-2584, March 2019, doi: 10.1109/TPEL.2018.2844347.
- [17] S. Yang, "Saliency-Based Position Estimation of Permanent-Magnet Synchronous Machines Using Square-Wave Voltage Injection With a Single Current Sensor," in *IEEE Transactions on Industry Applications*, vol. 51, no. 2, pp. 1561-1571, March-April 2015, doi: 10.1109/TIA.2014.2358796.
- [18] J. Zhao, S. Nalakath and A. Emdadi, "A High Frequency Injection Technique With Modified Current Reconstruction for Low-Speed Sensorless Control of IPMSMs With a Single DC-Link Current Sensor," in *IEEE Access*, vol. 7, pp. 136137-136147, 2019, doi: 10.1109/ACCESS.2019.2942148.
- [19] Y. Yoon and S. Sul, "Sensorless Control for Induction Machines Based on Square-Wave Voltage Injection," in *IEEE Transactions on Power Electronics*, vol. 29, no. 7, pp. 3637-3645, July 2014, doi: 10.1109/TPEL.2013.2278103.
- [20] P. Garcia, F. Briz, D. Reigosa, C. Blanco and J. M. Guerrero, "On the use of high frequency inductance vs. high frequency resistance for sensorless control of AC machines," 2011 Symposium on Sensorless Control for Electrical Drives, Birmingham, 2011, pp. 90-95, doi: 10.1109/SLED.2011.6051550.
- [21] C. Lin, S. Liang, J. Chen, and X. Gao, "A Multi-Objective Optimal Torque Distribution Strategy for Four In-Wheel-Motor Drive Electric Vehicles", *IEEE Access*, 7: 64627-64640, 2019.
- [22] [Online]. Available: <http://www.interfacetorque.co.uk>. Accessed on: Sep. 20, 2020.
- [23] P. Sue, D. Wilson, L. Farr, and A. Kretschmar, "High precision torque measurement on a rotating load coupling for power generation operations," in *IEEE Int. Instrum. Meas. Technol. Conf. Proc.*, pp. 518-523, May 2012.
- [24] W. Xu and R. D. Lorenz, "High-Frequency Injection-Based Stator Flux Linkage and Torque Estimation for DB-DTFC Implementation on IPMSMs Considering Cross-Saturation Effects," in *IEEE Transactions on Industry Applications*, vol. 50, no. 6, pp. 3805-3815, Nov.-Dec. 2014, doi: 10.1109/TIA.2014.2322134.
- [25] M. Martínez, D. F. Laborda, D. Reigosa, D. Fernández, J. M. Guerrero and F. Briz, "SynRM Sensorless Torque Estimation Using High Frequency Signal Injection," 2019 IEEE 10th International Symposium on Sensorless Control for Electrical Drives (SLED), Turin, Italy, 2019, pp. 1-5, doi: 10.1109/SLED.2019.8896220.
- [26] D. Reigosa, Y. g. Kang, M. Martínez, D. Fernández, J. M. Guerrero and F. Briz, "SPMSMs Sensorless Torque Estimation Using High-Frequency Signal Injection," in *IEEE Transactions on Industry Applications*, vol. 56, no. 3, pp. 2700-2708, May-June 2020, doi: 10.1109/TIA.2020.2975757.
- [27] M. Martínez, D. Reigosa, D. Fernández, J. M. Guerrero, and F. Briz, "PMSMs Torque Estimation Using Pulsating HF Current Injection," in 2018 IEEE 9th Int. Symp. Sensorless Control Electr. Drives SLED, pp: 96-101, Sep. 2018.
- [28] D. F. Laborda, D. Diaz Reigosa, D. Fernández, K. Sasaki, T. Kato and F. Briz, "Enhanced Torque Estimation in Variable Leakage Flux PMSM Combining High and Low Frequency Signal Injection," 2020 IEEE Energy Conversion Congress and Exposition (ECCE), Detroit, MI, USA, 2020, pp. 1764-1771, doi: 10.1109/ECCE44975.2020.9235869
- [29] F. Jukic, D. Sumina, and J. Erege, "Comparison of torque estimation methods for interior permanent magnet wind power generator", in Int. Conf. Electr. Drives Power Electron. EDPE, pp: 291-296, Oct. 2017.
- [30] Z. Lin, D. S. Reay, B. W. Williams, and X. He, "Online Modeling for Switched Reluctance Motors Using B-Spline Neural Networks", *IEEE Trans. Ind. Electron.*, 54(6): 3317-3322, Dec. 2007.
- [31] Miguel A. Perez. Instrumentación electrónica, volume 1 of 1. Paraninfo, The address. 1 edition, 1 2014. Spanish.
- [32] M. Kamiya, Y. Kawase, Y. Kosuda, and N. Matsui, "Temperature distribution analysis of permanent magnet in interior permanent magnet synchronous motor considering PWM carrier harmonics," in Proc. IEEEICEMS, Oct. 2007, pp. 2023-2027.
- [33] K. Liu and Z. Q. Zhu, "Online estimation of the rotor flux linkage and voltage source inverter nonlinearity in permanent magnet synchronous machine drives," *IEEE Trans. Power. Electron.*, vol. 29, no. 1, pp. 418-427, Jan. 2014.
- [34] D. Reigosa, F. Briz, P. Garcia, J. M. Guerrero, and M.W. Degner, "Magnet temperature estimation in surface PM machines using high frequency signal injection," *IEEE Trans. Ind. Appl.*, vol. 46, no. 4, pp. 1468-1475, Jul./Aug. 2010.
- [35] D. Reigosa, D. Fernandez, M. Yoshida, T. Kato, and F. Briz, "Permanent magnet temperature estimation in PMSMs using pulsating high frequency current injection," *IEEE Trans. Ind. Appl.*, vol. 51, no. 4, pp. 3159-3168, Jul./Aug. 2015.
- [36] M. Ganchev, C. Kral, and T. Wolbank, "Compensation of speed dependency in sensorless rotor temperature estimation for permanent-magnet synchronous motors," *IEEE Trans. Ind. Appl.*, vol. 49, no. 6, pp. 2487-2495, Nov./Dec. 2013.
- [37] D. Reigosa, D. Fernández, M. Martínez, J. M. Guerrero, A. B. Diez and F. Briz, "Magnet Temperature Estimation in Permanent Magnet Synchronous Machines Using the High Frequency Inductance," in *IEEE Transactions on Industry Applications*, vol. 55, no. 3, pp. 2750-2757, May-June 2019, doi: 10.1109/TIA.2019.2895557.

B.2.6 Comparison Of Anti-Windup Alternatives For Parallel Controllers

Comparison Of Anti-Windup Alternatives For Parallel Controllers

Cristina González Moral
R&D department
Elinsa - Amper
Oviedo, Spain
cgonzalez@elinsa.org

Diego Fernández Laborda
Dept. of Electrical Engineering
University of Oviedo
Gijón, Spain
dflaborda@uniovi.es

Juan M. Guerrero Muñoz
Dept. of Electrical Engineering
University of Oviedo
Gijón, Spain
guerrero@uniovi.es

Carlos Rivas
R&D department
Elinsa - Amper
La Coruña, Spain
crivas@elinsa.org

David Díaz Reigosa
Dept. of Electrical Engineering
University of Oviedo
Gijón, Spain
diazdavid@uniovi.es

Abstract—Parallel controller structures are broadly used for controlling electrical variables in distorted grids and other applications such as electric drives. Each controller in the structure ideally regulates a single harmonic component. In the event of controller output saturation, some anti-windup strategy must be implemented to ensure a correct operation of the controller and a fast and smooth transition from saturated to non-saturated state. The anti-windup techniques proposed for single controller structures can be applied to parallel structures. However, two options exist: 1) Consider the controllers in the parallel structure as independent units during saturation; 2) Consider the parallel controller structure as a whole. The first one is broadly used while the second one has been recently proposed. This paper analyzes the implementation differences and the performance of both solutions in different scenarios: grid-forming and grid-feeding applications.

Index Terms—Realizable references, grid feeding, grid forming.

I. INTRODUCTION

A high percentage of non-linear loads are present in grids and micro-grids. They inject a significant amount of current harmonic content that can eventually distort the grid voltage, increasing the Total Harmonic Distortion (THD) above the admissible values given by regulations and standards [1]–[3]. Harmonic compensation can be implemented using dedicated devices, as passive filters or centralized Active Power Filters (APF) [4], [5]. Since the interface of Distributed Power Generation Systems (DPGSs) is generally based on power converters, this also has opened opportunities for harmonic compensation both in grid forming [6], [7] and grid feeding [3], [8]–[10] converters.

Parallel controller structures are often used for controlling different harmonic components in voltage or current controllers. The discussion will be focused on complex vector current controllers within this paper, although the results can

be later extended to both voltage and single-phase controllers. The operation of the parallel controller structures under saturation must be correctly addressed to minimize either the voltage/current THD or the decrease of the fundamental component magnitude. When output saturation is detected in the controller, a two-stage process is needed, as seen in Fig. 1 for a single current controller: a) Saturation: to decide the output voltage vector ($u_s[z]$) within the voltage limits to replace the actual controller output ($u[z]$); b) Anti-windup: to properly saturate the controller to prevent it from working with nonlinear states. For the sake of simplicity, no special notation is given to the complex vector variables.

The hexagon with radius $\frac{2}{3}V_{dc}$ and apothem $\frac{V_{dc}}{\sqrt{3}}$ in Fig. 2 represents the maximum allowable voltage range when using a three-phase inverter, where V_{dc} is the dc-link voltage. Any voltage command (u) that gets outside the voltage hexagon limits (e.g. u_1) must be limited in amplitude and/or distorted in phase. While the hexagon limitation maximizes the inverter voltage utilization, it brings several drawbacks, as implementation complexity, reference frame dependence, and the injection of additional harmonics when the voltage moves along the hexagon sides. An alternative often selected as the limit is using the hexagon inscribed circle seen in Fig. 2. To achieve those limits either Sinusoidal PWM (SPWM) with

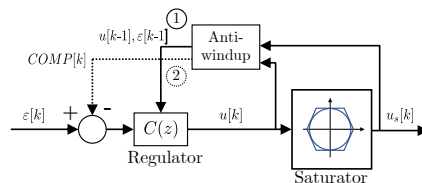


Fig. 1. Saturation and anti-windup conceptual representation for a single controller structure. Two anti-windup alternatives are shown: ① Realizable reference, ② Back-tracking calculation.

This work was supported in part by the Research, Technological Development and Innovation Programs of the Spanish Ministry of Science and Innovation, under grant PID2019-106057RB-I00

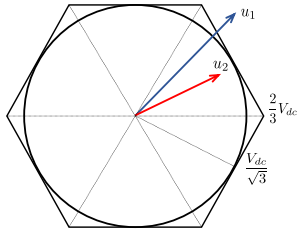


Fig. 2. Complex vector voltage limits, hexagon and circle saturation.

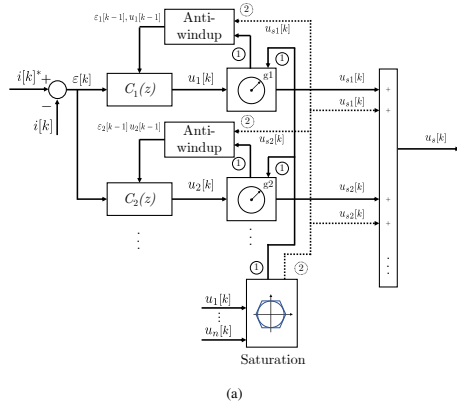
third harmonic injection or Space Vector Modulation (SVM) can be used [11].

The selection of the different saturation methods will depend on the application (grid feeding, APFs, grid forming...), and it is mainly determined by the current/voltage THD or the current/voltage fundamental component magnitude error [3], [5], [7]–[10].

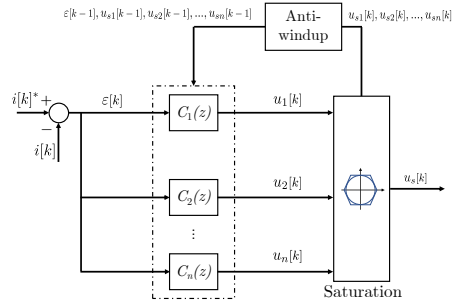
In grid-feeding applications, the goal is to inject an undistorted current into the grid in the presence of grid voltage harmonics. Different alternatives have been proposed, as trajectory analyzers [3], [9], [12], [13] to limit the controller output in case of saturation and avoid harmonic injection, back-tracking schemes that remove low priority harmonics from the compensation [8] or instantaneous methods which estimate trajectories at every time step to avoid overmodulation [10], [14]. APFs need to inject current harmonics into a nonlinear load to remove them from the grid current. In [5], three different instantaneous saturation strategies for APFs are analyzed and compared. Both grid-feeding and APFs applications are mainly oriented to obtain a low THD in the current. In grid-forming applications, both fundamental and harmonic current components need to be injected to obtain a low THD and a low magnitude error in the synthesized voltage. Therefore, the saturation strategies must be different in this case [7].

In addition to the selection of the saturated voltage, some anti-windup technique is needed to allow the controller to operate as in linear region during saturation in order to achieve a fast and bump-less transition from saturated to non-saturated operation [15]. Different strategies have been proposed for single controller systems [15], as the calculation of the realizable reference error, ① in Fig. 1, error compensation under saturation (back-tracking), ② (dotted line) in Fig. 1, controller output clamping, integrator clamping, etc.

These anti-windup strategies can be applied to parallel controller structures using any of the two alternatives proposed in the literature that will be described in the next section. This paper will focus on the comparison of both alternatives in different scenarios, as grid forming and grid feeding. This will help to better understand the performance of the existing alternatives which has not been addressed so far. The paper is organized as follows: the alternative methods are described



(a)



(b)

Fig. 3. Different parallel controllers structures treatment in realizable references anti-windup schemes. a) LAW; b) GAW.

is Section II, simulation results for a grid feeding application and a grid forming application are shown in Section III, and conclusions are presented in Section IV.

II. ANTI-WINDUP IMPLEMENTATION IN PARALLEL CONTROLLERS

Fig. 3 shows the two alternatives for anti-windup implementation in parallel controller structures. The most often used is shown in Fig. 3(a), that will be herein called “Local anti-windup (LAW)”. The output of each individual controller in the structure is compared with their own voltage limit, assigned by some global saturation strategy. If the output surpasses the limit, it is saturated and some anti-windup algorithm as described in Fig. 1 is implemented, as for instance realizable reference as shown in Fig. 3(a). Different saturation alternatives have been proposed belonging to this group. The most simple but inefficient uses pre-defined values for the controller limits (g_1, g_2, \dots, g_n) [16]. Others examine the global output vector [5], [8], [17] and recalculate the voltage limits

of each controller [see ① in Fig. 3(a)] at every control step. Finally, other methods assign the saturated output for each controller at every control step [5], [10], marked as ② in Fig. 3(a). In any case, the anti-windup is locally applied to each controller. This means that under saturation, each controller in the parallel structure will have a different past-error value. This seems contradictory to the fact that all of them receive the same error at the beginning of each control step, but the impact of this has not been studied so far. It is noted that, in addition to the described anti-windup strategy, some researchers have also proposed to modify the current reference to force the voltage trajectory to avoid saturation in steady-state [3], [9], [10]. However, the analysis made here will be still valid for those methods during the tracking of the optimal trajectory and during load and command transients.

Another alternative shown in Fig. 3(b) has been recently proposed [7], called here “Global anti-windup (GAW)”. In this case, the saturated output is also obtained following some strategy and the individual controller saturated outputs are calculated. This is similar to the last type of the aforementioned methods. However, the anti-windup strategy is completely different, since a common past-error is calculated for all the controllers in the parallel structure. This seems more consistent with the fact that the same error is shared among all the controllers. However, any possible improvement of this solution still needs to be proved. The next section shows results of their performance under the same operating conditions in grid feeding and grid forming applications.

III. METHOD COMPARISON

As explained in Section I, in grid-forming applications the goal is to generate an undistorted grid voltage in the presence of current harmonics generated by the consumption of the loads. On the contrary, in grid-feeding applications, the goal is to inject an undistorted current into the grid in the presence of voltage harmonics. In the first case, the desired grid voltage will be the output of the converter. In the second case, the minimum voltage generated by the inverter (considering only active power, i.e., injection in phase with the grid) would be the grid voltage. This means that this voltage must be increased in order to generate a voltage difference that (and taking into account the impedance of the filter at the grid's frequency) would generate a current injection into the grid. Both applications are analyzed in the following subsections.

A. Grid forming application

This section contains simulation results for a grid-forming application. Fig. 4 shows a three-phase inverter with an output LC filter, an unbalanced three-phase linear load, and a non-linear load. The main system parameters can be found in Table I. The goal is to obtain a balanced three-phase voltage at the filter output. The THD and fundamental component of this voltage will be used to benchmark the anti-windup schemes.

Since voltage controllers could affect the analysis of the two anti-windup strategies, pre-calculated current commands to ideally achieve a balanced three-phase voltage ($400 V_{rms}$,

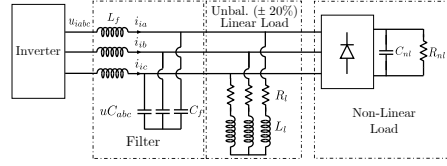


Fig. 4. Test system: Grid forming scenario including unbalanced and non-linear loads.

TABLE I
SYSTEM PARAMETERS FOR A GRID FORMING APPLICATION

Rated voltage	V_r	400 V _{rms}	Linear load	L_l	6.6 mH
Rated current	I_r	144 A _{rms}	Linear load	Unbalance	$\pm 20\%$
Filter	L	260 μ H	Non-linear load	C_{nl}	1 mF
Filter	C	270 μ F	Non-linear load	R_{nl}	8.35 Ω
Linear load	R_l	3.36 Ω	Switching Frequency	f_s	10 kHz

50 Hz) at the capacitor will be commanded to the current regulators [7]. This current command is obtained by replacing the inverter and the filter inductor L_f in Fig. 4 by an ideal three-phase voltage source and obtaining the resulting current. In order to track the current command, a parallel vector controller structure composed of seven complex vector PI controllers is implemented in stationary reference frame for the fundamental, negative sequence, and the five largest harmonic components (-250, 350, -550, 650, and 950 Hz), as in Fig. 4. A 700 V dc-link voltage ensures a non-saturated operation of the controller obtaining a 1.23% voltage THD and 0% magnitude error in the capacitor voltage.

Fig. 5 shows the inverter voltage trajectory (in blue) for the current command under the non-linear load conditions. The hexagons in red represents different dc-link voltages: 700 V (non-saturated state), 600, 570 and 540 V (saturated states).

The realizable reference anti-windup technique is implemented for both LAW (Fig. 3a, option ①) and GAW (Fig. 3b). In both cases, the saturated error (ε_{sat}) is calculated using (1) [7], where $\varepsilon[k]$ is the unsaturated error, u_{sat} is the saturated output of the regulator (coming from the saturation strategy) and $u[k]$ is the unsaturated output of the regulator. In the GAW strategy, b_0 is the sum of the first z-transform numerator coefficient of all the controllers in the parallel

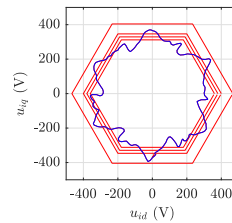


Fig. 5. Grid forming application. Non-saturated inverter voltage trajectory (blue) and hexagon voltage limits (700, 600, 570, 540 V, red).

structure $[C_1, C_2 \dots C_n]$ in Fig. 3], while in the LAW strategy the equation is applied individually for each regulator, so b_0 represents just the first z-transform numerator coefficient of the controller.

$$\varepsilon_{\text{sat}} = \varepsilon[k] + \frac{1}{b_0} (u_{\text{sat}} - u[k]) \quad (1)$$

Both GAW and LAW strategies have been tested with three different saturation alternatives. The first one is termed ‘‘Global’’ (Fig. 6a), in which the output voltage is reduced keeping the original angle (reducing equally all the vector components) [7]. In this method, the magnitudes (i.e. not considering the angle) of the voltage vector components from the current controller are added and then compared with the voltage limit. The last technique is called ‘‘Group’’ (Fig. 6b) and corresponds with Method 2 in [5]. In this case, the fundamental component is favored over the rest of the harmonics, to which the ‘‘Global’’ technique is applied. Hexagon or circle voltage limits were considered as indicated in Table II. As explained in Section I, the hexagon limit provides the best voltage utilization at the cost of a higher computational burden. On the other hand, the circle limit provides higher simplicity but worse voltage utilization.

Fig. 7 (LAW) and Fig. 8 (GAW) compare the voltage and current tracking when both methods use the ‘‘Global’’ saturation method during 570 V (0.81 p.u.) dc-link voltage operation and the hexagon voltage limit. Subfigure (a) shows the actual output voltage and the ideal one (dotted line), while (b) shows the actual phase currents and their commands (dotted line), for both Figs. 7 and 8 (GAW). A more accurate current tracking during saturation is seen in the GAW alternative (Fig. 8) also obtaining less grid-formed voltage distortion compared with

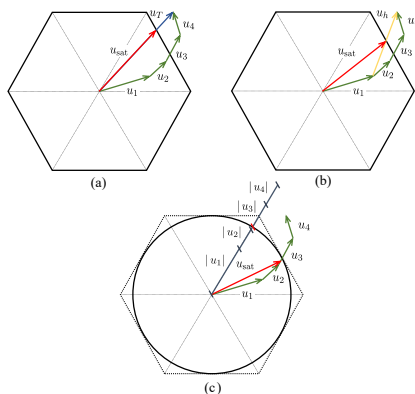


Fig. 6. Saturation methods. (a) ‘‘Global’’. (b) ‘‘Group’’. (c) ‘‘Magnitude’’.

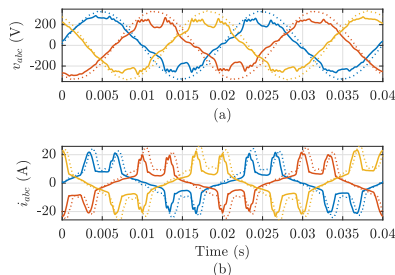


Fig. 7. Grid-formed voltage (a) and phase current tracking (b) during saturation (570 V dc-link) using the ‘‘Global (hexagon)’’ saturation method with LAW. Dotted: current commands. Continuous: Actual currents.

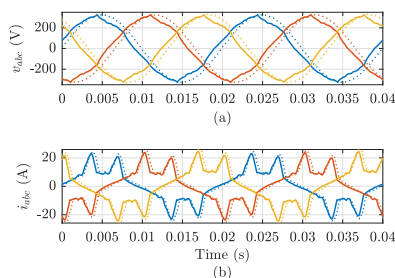


Fig. 8. Grid-formed voltage (a) and phase current tracking (b) during saturation (570 V dc-link) using the ‘‘Global (hexagon)’’ saturation method with GAW. Dotted: current commands. Continuous: Actual currents.

the LAW alternative (Fig. 7).

A similar experiment has been repeated for the different cases summarized in Table II for 3 different saturation levels (600, 570 and 540 V), showing both the THD of the voltage at the filter capacitor and the magnitude error of the fundamental component using 3 saturation strategies. In the case of the ‘‘Magnitude’’ technique, only the circle saturation is considered to make it simpler. These results show that the GAW strategy outperforms the LAW one regardless of the saturation strategy in terms of THD (with the only exception being the ‘‘Global’’ (circle) at deep saturation, i.e. 540 V). The ‘‘Group’’ strategy produces a high distortion if combined with LAW, which is especially noticeable at low saturation levels. The magnitude error is also smaller for the GAW strategy except in case the ‘‘Group’’ strategy is adopted. However, the penalty in THD for the LAW strategy is evident in that case. Therefore, it would be advisable to adopt the GAW strategy in most cases regarding grid forming applications.

B. Grid feeding application

This section contains simulation results for a grid-feeding application. Fig. 9 shows a three-phase inverter with an output L filter, connected to an unbalanced grid. The main system parameters can be found in Table III. The goal is to inject a

TABLE II
GRID FORMING APPLICATION: CAPACITOR VOLTAGE DISTORTION USING DIFFERENT SATURATION STRATEGIES FOR THE DIFFERENT ANTI-WINDUP APPROACHES

Method	600 V		570 V		540 V	
	THD (%)	Mag. Error (%)	THD (%)	Mag. Error (%)	THD (%)	Mag. Error (%)
Global (circle) GAW	2.96	5.20	5.68	9.17	18.59	15.60
Global (circle) LAW	5.48	15.65	8.96	22.34	10.24	27.50
Global (hexagon) GAW	2.80	4.89	4.55	7.83	6.93	10.25
Global (hexagon) LAW	5.46	15.56	8.99	22.35	10.35	28.00
Magnitude (circle) GAW	4.13	15.16	5.59	19.29	7.50	23.13
Magnitude (circle) LAW	10.88	28.86	14.13	34.88	17.63	40.12
Group (circle) GAW	2.63	3.42	3.87	6.85	4.77	10.22
Group (circle) LAW	6.65	1.40	4.85	2.23	5.13	6.49
Group (hexagon) GAW	2.63	3.24	3.82	6.42	4.94	9.56
Group (hexagon) LAW	11.24	0.76	7.80	1.28	6.72	0.12

TABLE III
SYSTEM PARAMETERS FOR A GRID FEEDING APPLICATION

Rated voltage	V_r	400 V _{rms}	Voltage THD	THD _v	≈ 8%
Rated current	I_r	200 A _{rms}	-1^{st} harmonic	h_n	3%
Filter	L	260 μH	-5^{th} harmonic	h_5	5%
Nominal dc-link	V_{dc}	700 V	7^{th} harmonic	h_7	5%
Switching frequency	f_s	10 kHz			

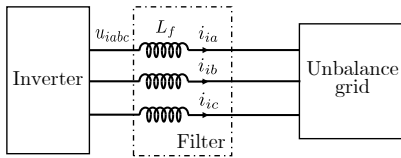


Fig. 9. Test system: Grid feeding scenario with an unbalanced grid.

balanced three-phase current to the grid, despite the voltage distortion. The THD and fundamental component of this current will be used to benchmark the anti-windup schemes.

According to the IEEE standard 519-2014 [2], the maximum voltage THD in a grid should not exceed an 8%, while each individual harmonic should remain below a 5%. Due to this, simulations are carried out with around an 8% of grid voltage THD, which would be the worst-case scenario, and 3 different harmonics: -50, -250 and 350 Hz.

In order to track the current command injected to the grid, a parallel current controller structure composed of six complex vector PI controllers is implemented in stationary reference frame for the fundamental, negative sequence, and the most significant first four harmonic components (-250, 350, -550 and 650 Hz). A 700 V dc-link voltage and 200 A peak current reference ensures a non-saturated operation of the controller obtaining a 2% THD and 0% magnitude error in the current through the output inductor.

Fig. 10 shows the inverter voltage trajectory (in blue) for the current command under the distorted grid conditions (in black). The hexagons in red represents different dc-link voltages: 700 V (non-saturated state), 670, 650 and 640 V (saturated states). The particular characteristics of this application results in saturation with a higher voltage in the dc-link compared to the grid forming case.

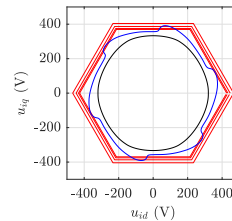


Fig. 10. Grid feeding application. Non-saturated inverter voltage trajectory (blue), hexagon voltage limits (700, 670, 650, 640 V, red) and grid voltage (black).

The realizable reference anti-windup technique is implemented for both LAW (Fig. 3a, option ①) and GAW (Fig. 3b). In addition, both have been tested with two different saturation alternatives: “Global” (Fig. 6a) and “Group” (Fig. 6c). The “Magnitude” strategy (Fig. 6b) was discarded due to its significantly worse results compared to the other strategies, which causes the algorithm to enter into saturation even at 700 V. This is due to the addition of the magnitude of all the harmonics for the saturation analysis.

Fig. 11 compares the current tracking between the two methods using the “Global” saturation method during 640 V (0.91 p.u.) dc-link voltage operation (hexagon limit). Fig. 11(a) shows the grid voltage with its distortion. Fig. 11(b) and (c) show the current command vs the actual current command for the GAW and the LAW cases, respectively. A more accurate current tracking during saturation is seen in the GAW alternative, also obtaining less inductor current distortion (1.71% vs 2.26% THD).

A similar experiment has been repeated for the different cases summarized in Table IV for 3 different saturation levels (670, 650 and 640 V), showing both the THD of the inverter’s current output and the magnitude error of the fundamental current component using two saturation strategies. These results show that the GAW method outperforms the LAW one in the case of the “Global” strategy in terms of THD and current magnitude error. In the case of the “Group” strategy the LAW method behaves better than the GAW method for higher saturation levels but worse for lower saturation levels. In general, both of them behave far worse than the “Global”

TABLE IV
GRID FEEDING APPLICATION: INDUCTOR CURRENT DISTORTION USING DIFFERENT SATURATION STRATEGIES FOR THE DIFFERENT ANTI-WINDUP APPROACHES

Method	670 V		650 V		640 V	
	THD (%)	Mag. Error (%)	THD (%)	Mag. Error (%)	THD (%)	Mag. Error (%)
Global (circle) GAW	1.97	0.23	1.74	1.96	1.70	3.00
Global (circle) LAW	2.13	2.37	1.67	2.93	2.38	18.34
Global (hexagon) GAW	1.96	0.1	1.65	1.03	1.71	2.08
Global (hexagon) LAW	1.99	0.28	2.13	2.89	2.26	6.23
Group (circle) GAW	1.75	0.06	5.34	24.93	7.17	41.39
Group (circle) LAW	2.14	2.38	2.21	12.17	2.38	18.31
Group (hexagon) GAW	1.96	0.04	1.84	0.09	2.10	0.34
Group (hexagon) LAW	1.88	0.00	2.14	0.01	2.46	0.00

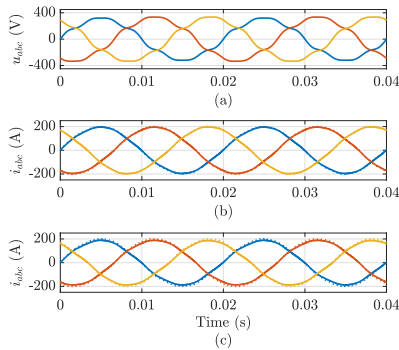


Fig. 11. Grid feeding application. Inverter output voltage and phase current tracking during saturation (640 V dc-link voltage) using the "Global (hexagon)" saturation method. (a) Grid voltage. (b) GAW case. (c) LAW case. Dotted: current commands. Continuous: Actual currents.

strategy. Due to this, the GAW method together with the "Global" strategy would be advisable in the case of grid feeding converters.

IV. CONCLUSION

This paper explores the different performance between local and global anti-windup in parallel controllers under the same operating conditions. Results show a better performance of the GAW approach in terms of output voltage distortion in grid forming converters for all the saturation techniques analyzed.

Regarding grid feeding converters, results are not so straightforward, and the analysis depends on the saturation levels and saturation method employed. In general, results are better with the GAW approach using the "Global" saturation technique. Regarding the "Group" method, results are better with the LAW method, but the performance of the method is worse in general compared to the "Global" case, since this method was proposed for grid forming applications.

REFERENCES

- [1] F. Blaabjerg, R. Teodorescu, M. Liserre, and A. V. Timbus, "Overview of Control and Grid Synchronization for Distributed Power Generation Systems," *IEEE Transactions on Industrial Electronics*, vol. 53, no. 5, pp. 1398–1409, Oct. 2006.

- [2] "IEEE Recommended Practice and Requirements for Harmonic Control in Electric Power Systems," *IEEE Std 519-2014 (Revision of IEEE Std 519-1992)*, pp. 1–29, Jun. 2014.
- [3] M. Rizo, M. Liserre, E. J. Bueno, F. J. Rodríguez, and A. Rodríguez, "Distortion-Free Saturators for Power Converters Under Unbalanced Conditions," *IEEE Transactions on Power Electronics*, vol. 30, no. 6, pp. 3364–3375, Jun. 2015.
- [4] M. El-Habrouk, M. Darwish, and P. Mehta, "Active power filters: a review," *IEE Proceedings - Electric Power Applications*, vol. 147, no. 5, pp. 403–413, Sep. 2000.
- [5] A. Amerise, M. Mengoni, G. Rizzoli, L. Zari, A. Tani, and D. Casadei, "Comparison of three voltage saturation algorithms in shunt active power filters with selective harmonic control," *IEEE Transactions on Industry Applications*, vol. 56, no. 3, pp. 2762–2772, May 2020.
- [6] R. H. Lassetter, Z. Chen, and D. Pattabiraman, "Grid-forming inverters: A critical asset for the power grid," *IEEE Journal of Emerging and Selected Topics in Power Electronics*, vol. 8, no. 2, pp. 925–935, 2020.
- [7] C. G. Moral, J. M. Guerrero, D. Fernández, D. Reigosa, C. Rivas, and F. Briz, "Realizable reference anti-windup implementation for parallel controller structures," *IEEE Journal of Emerging and Selected Topics in Power Electronics (early access)*, pp. 1–1, 2020.
- [8] L. Harnefors, A. G. Yepes, A. Vidal, and J. Doval-Gandoy, "Reduction of saturation-induced distortion and antiwindup in multifrequency current control," *European Conference on Power Electronics and Applications (EPE)*, pp. 1–7, Sep. 2015.
- [9] —, "Multifrequency Current Control With Distortion-Free Saturation," *IEEE Journal of Emerging and Selected Topics in Power Electronics*, vol. 4, no. 1, pp. 37–43, Mar. 2016.
- [10] J. Moriano, M. Rizo, E. Bueno, J. R. Sendra, and R. Mateos, "Distortion-Free Instantaneous Multifrequency Saturator for THD Current Reduction," *IEEE Transactions on Industrial Electronics*, vol. 66, no. 7, pp. 5310–5320, Jul. 2019.
- [11] D. G. Holmes and T. A. Lipo, "Pulse Width Modulation For Power Converters," 1st edition. Wiley-IEEE Press, 2003.
- [12] A. G. Yepes, J. Doval-Gandoy, and H. A. Toliyat, "Multifrequency Current Control Including Distortion-Free Saturation and Antiwindup With Enhanced Dynamics," *IEEE Transactions on Power Electronics*, vol. 33, no. 9, pp. 7309–7313, Sep. 2018.
- [13] A. G. Yepes and J. Doval-Gandoy, "Effective current limitation for multifrequency current control with distortion-free voltage saturation and antiwindup," *IEEE Transactions on Power Electronics*, vol. 35, no. 12, pp. 13 697–13 713, May 2020.
- [14] J. Serrano, J. Moriano, M. Rizo, and F. J. Dongil, "Enhanced current reference calculation to avoid harmonic active power oscillations," *Energies*, vol. 12, no. 21, Oct. 2019.
- [15] Youbin Peng, D. Vranic, and R. Hanus, "Anti-windup, bumpless, and conditioned transfer techniques for PID controllers," *IEEE Control Systems Magazine*, vol. 16, no. 4, pp. 48–57, Aug. 1996.
- [16] P. Mattavelli, "Synchronous-frame harmonic control for high-performance AC power supplies," *IEEE Transactions on Industry Applications*, vol. 37, no. 3, pp. 864–872, May/Jun. 2001.
- [17] T. C. Y. Wang and X. Yuan, "Design of multiple-reference-frame PI controller for power converters," in *2004 IEEE 35th Annual Power Electronics Specialists Conference (IEEE Cat. No.04CH37551)*, vol. 5, pp. 3331–3335, Jun. 2004.

B.2.7 Magnetic Resolver Using Hall-Effect Sensors

Magnetic Resolver Using Hall-Effect Sensors

Ye Gu Kang
Electrical & Electronic Dept.
University of Oviedo
 Gijón, Spain
 email address or ORCID

Diego F. Laborda
Electrical & Electronic Dept.
University of Oviedo
 Gijón, Spain
 dflaborda@uniovi.es

Daniel Fernández
Electrical & Electronic Dept.
University of Oviedo
 Gijón, Spain
 fernandezlodaniel@uniovi.es

David Reigosa
Electrical & Electronic Dept.
University of Oviedo
 Gijón, Spain
 diazdavid@uniovi.es

Fernando Briz
Electrical & Electronic Dept.
University of Oviedo
 Gijón, Spain
 fernando@isa.uniovi.es

Abstract— Control of AC electric machines requires, in many cases, accurate knowledge of rotor position. Encoders and resolvers are the most widely used option in the industry. Variable reluctance (VR) resolvers are advantageous in harsh environments due to their robustness; however, they represent a significant portion of the total drive cost. This paper presents a magnetic resolver using low-cost Hall effect sensors. Advantages with conventional encoders include compactness and reduced cost, which are achieved without penalizing the other properties of VR resolvers. The proposed sensor is fully compatible with conventional drives and supports wide carrier frequency and supply voltage variations.

Keywords—Magnetic Resolver, Hall-sensor, angular position measurement.

I. INTRODUCTION

Electric drives are used in a vast range of applications, including domestic, industrial, traction, aerospace, etc. Precise control of AC electric machines requires accurate knowledge of the rotor position. Optical encoders (optical-based angular position sensors) and resolvers (inductive-based angular position sensors), are the most used sensors in the industry [1]-[5], although many other alternatives have been reported in the literature: capacitive [2]-[3], inductive [4] or magnetic-based angular position sensors are available. Capacitive-based angular position sensors in [3], [4] provide high precision output but requires additional circuitry to be compatible with standard encoder or resolver signals. Inductive position sensors are axially planar [4], low weight, with a similar operation principle to a transformer but lack robustness. Magnetic angular position sensors are mainly based on Hall-effect or Giant Magnetoresistance (GMR) devices [16],[17]. Magnetic sensors used for automotive applications (e.g. throttle position detection, shaft position...) are also commercially available [16], [17]. The main drawbacks of these devices are the robustness decrease, inertia increase, and extra room. In addition, their accuracy depends on the offset or misalignment of the permanent magnet material that must be attached to the rotating part.

Optical encoders are likely the preferred option in general purpose applications and can provide incremental or, at a higher cost, absolute angular position. However, they often suffer from a limited range of temperature of operation and a reduced capability to withstand shock and vibration compared to resolvers.

This work was supported in part by the Research, Technological Development and Innovation Programs of the Spanish Ministry Economy and Competitiveness, under grant MINECO-17-ENE2016-80047-R and by the Government of Asturias under project IDI/2018/000188 and FEDER funds.

Resolvers inherently detect the absolute position and exhibit high vibration and shock withstand capability, a wide range of temperature of operation, and high rotational speed. Resolvers can be brushless [8], brushed (in disuse), or variable reluctance (VR) [9]-[10]. A brushless resolver is a rotatory transformer excited by AC voltage to the rotor winding [8]. An AC voltage is induced in the output winding (stator), which is modulated by the rotor position. VR resolvers do not have rotor windings and bearings and have both the output and the excitation windings in the stator; no brushes or rotating transformer is therefore required. They can be easily made frameless mounted, integrated into the motor without the need of a coupling device, and without adding friction to the system [7], what makes them appealing in traction applications (i.e. electric vehicles and hybrid electric vehicles), [7], [8]. Their main drawback, however, is the cost [6],[11].

This paper proposes an alternative design of a magnetic resolver using field sensors (i.e. Hall-effect) and a magnetized moving part made of non-laminated electrical steel and permanent magnets. Compared to VR resolver, the proposed design is simpler, more compact, cheaper, and easier manufacturability: it does not require stator/rotor laminations nor windings. Its power consumption is very low, and it can provide more than one independent output for a redundant mode of operation. It can be easily scalable in size, or the number of poles to meet the requirements of a specific application. Still, it will retain the main properties of VR resolver, and is fully compatible, meaning that no modification in the cabling or electronics of the drive is required.

The paper is organized as follows: principles of operation are discussed in Section II, design optimization is discussed in section III, and the validation of the model using FEA is presented in Section IV. Section V shows an assembly of the proposed prototype, and experimental results and conclusions are presented in sections VI and VII, respectively.

II. PRINCIPLE OF OPERATION OF OPERATION

A brief description of conventional resolvers aimed to establish the basis for the assessment of the proposed concept is presented following.

Resolvers can be classified into brushless wound field (WF) and variable reluctance (VR). Both are a special type

of rotary transformer that couples a primary winding (Excitation see Fig. 1) with two secondary windings (Output 1 & 2) that are 90 electrical degrees phase shifted. Excitation signal, i.e. $v_E(t)$ in Fig. 1, is generally a sine wave (1) (see Fig. 2a), of magnitude and angular frequency E_0 and ω_s , respectively. The output signals of the resolver are $v_S(t)$ **Error! Reference source not found.** and $v_C(t)$ **Error! Reference source not found.** (see Figs. 2b and 2c), where k is the equivalent turns ratio of the magnetic coupling, θ_r is the rotor position, X is a multiplication factor for the angle **Error! Reference source not found.**

$$v_E(t) = E_0 \sin(\omega_s t) \quad (1)$$

$$v_S(t) = E_0 \sin(\omega_s t) k \sin(X\theta_r) \quad (2)$$

$$v_C(t) = E_0 \sin(\omega_s t) k \cos(X\theta_r) \quad (3)$$

$$\dot{v}_S(t) = k \sin(X\dot{\theta}_r) \quad (4)$$

$$\dot{v}_C(t) = k \cos(X\dot{\theta}_r) \quad (5)$$

Voltages $v_S(t)$ and $v_C(t)$ are the input to a resolver-to-digital (R/D) converter, which typically includes a demodulation stage to subtract the excitation signal; **Error! Reference source not found.** and **Error! Reference source not found.** being obtained after the demodulation. A large variety of methods have been reported to obtain the rotor position, θ_r , from **Error! Reference source not found.** and **Error! Reference source not found.** [15].

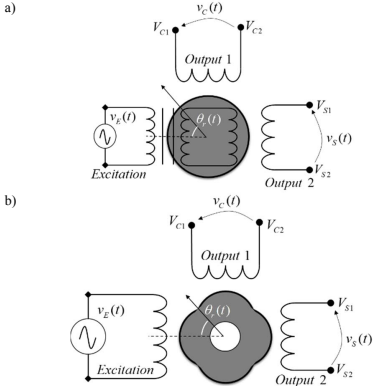


Fig. 1. Resolvers, a) WF and b) VR.

Rotor winding of WF resolvers is excited by an AC voltage, which can be produced by means of a magnetic coupling (i.e. brushless WF, see Fig. 1a). Voltages in the stator windings are a *sine* and *cosine* signal, which is modulated by the rotor angle θ_r . In VR resolvers, excitation winding is also placed in the stator (see Fig. 1b), avoiding the use of brushes or slip rings. In addition, they can be in-shaft installed. An AC voltage/current signal is injected into the excitation winding, the resulting voltages in the two stator windings being a *sine* and *cosine* signals whose angle is modulated by the rotor angle as for the WF case. VR

resolvers have a wider temperature range of operation and, with simple and robust construction, are less sensitive to noise and allow longer transmission cables **Error! Reference source not found.** **Error! Reference source not found.**

A. Principle of Operation of the proposed magnetic resolver

The proposed magnetic resolver is schematically shown in Fig.3. It consists of a rotor and a stator: the rotor is made of a non-laminated ferromagnetic core and permanent magnets (PMs in Fig.3); the stator consists of two Hall-effect sensors 90 electrical degrees phase shifted. Linear Hall-effect integrated circuit (IC) sensors will be used for the assembly of the proposed magnetic resolver. These types of ICs allow current control through the Hall element without integrated electronics.

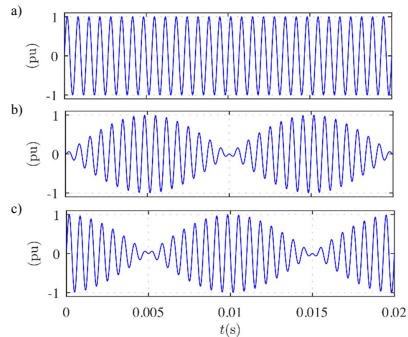


Fig. 2. Resolver signals, a) excitation, $v_E(t)$, b) Output 1 of the resolver, $v_S(t)$ (i.e. *cosine*), c) Output 2 of the resolver, $v_C(t)$ (i.e. *sine*). $\omega_s = 2 \cdot \pi \cdot 500$ rad/s, $\omega_r = 2 \cdot \pi \cdot 50$ rad/s

Hall-effect sensors are usually fed using DC voltage (6) or current, see Fig. 4a. The output voltage (Hall voltage) of the Hall-effect sensors $v_{HS}(t)$ and $v_{HC}(t)$ (see Fig. 3) for the case of a constant rotor speed are (7)-(8), (see Fig. 4b and Fig. 4c). While these signals are modulated by the rotor position, they differ from the signals provided by conventional resolvers, where the position information signals produce an amplitude modulation of a carrier signal (see Fig. 2). Alternatively, the Hall-effect sensors can be fed with and AC voltage (or current). The output voltages depending on the rotor speed will be in this case (11)-(12) (see Fig. 4d and Fig. 4f), which are equal to the signals provided by conventional resolvers. For every pair of poles (p) in the rotor, four Hall-effect sensors can be installed in the rotor providing duplicated signals for applications where redundancy is required.

It must be remarked that (11)-(12) results from a sinusoidal flux distribution in the rotor surface. Rotor design to achieve this target is described following.

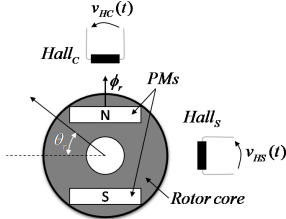


Fig. 3. Schematic representation of the proposed magnetic resolver and position of the Hall-effect sensors.

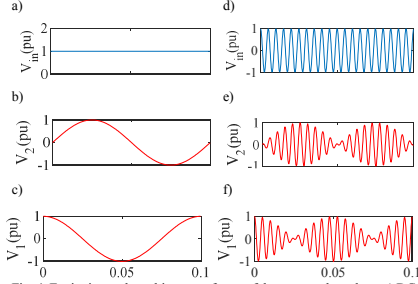


Fig. 4. Excitation and resulting waveforms of the proposed resolver: a) DC excitation, b) Sin output for DC excitation, c) Cos output for DC excitation, d) AC excitation, e) sin output for AC excitation and f) cos output for AC excitation.

$$v_E(t) = E_0 \quad (6)$$

$$v_{HS}(t) = k \sin(\theta_r) \quad (7)$$

$$v_{HC}(t) = k \cos(\theta_r) \quad (8)$$

$$\dot{v}_{Hall}(t) = k i(t) B(t) \quad (9)$$

$$v_E(t) = E_0 \sin(\omega_r t) \quad (10)$$

$$v_{HS}(t) = E_0 \sin(\omega_r t) k \sin(\theta_r) \quad (11)$$

$$v_{HC}(t) = E_0 \sin(\omega_r t) k \cos(\theta_r) \quad (12)$$

$$MO = Penalty + \sum_{n=1}^3 O_n w_n \quad (13)$$

III. ROTOR DESIGN OPTIMIZATION OF THE PROPOSED MAGNETIC RESOLVER

The optimization technique applied to the proposed magnetic resolver is explained in this section. The rotor geometry is evaluated to achieve three main targets: reduced use of magnetic materials, high fundamental flux amplitude and low harmonic distortion on the flux density waveform.

Differential evolution optimization technique [13] was used to find the optimum solution in the design space using 2D finite element analysis (FEA). Rotor parameters are shown in Fig. 4 and Table. II.

The desired properties of the hall effect sensor based resolver are included in the objective function variable, O_n , in the multi-objective (MO) in (13): the magnitude of the airgap flux density, Q_z , Total harmonic distortion (THD) of the flux density, Q_s , and the volume of the permanent magnet (PM), Q_v . The fundamental component of the airgap flux density will decide the sensitivity of the proposed resolver, where the level of THD indicates the quality of the signal for the rotor position estimation. The PM volume is included in the objective function to result in a low-cost, high accuracy resolver. The goal for the multi-objective optimization is to find a minimum cost of the MO in (13), where w_n is the weighting factor of each objective variable. More details about the variable used in the multi-objective optimization is in Table I. The penalty is used for eliminating designs that violate the geometric constraints set for the geometrical parameters shown in Table II.

TABLE I. PARAMETERS OF THE MULTY-OBJECTIVE FUNCTION

Symbol	Function	Definition
O_s	THD	Harmonic distortion of flux in %
O_z	$(B_{fund} - 0.08)^2$	Fundamental flux amplitude in Tesla with a target amplitude of 0.08
O_v	PM Volume	Magnet volume in mm^3
w_1	20	Weighting factor of O_s
w_2	20000	Weighting factor of O_z
w_3	10	Weighting factor of O_v
Penalty	0 if within the boundary 100 if outside boundary	Penalty is given when the input variables are outside the minimum and maximum range.

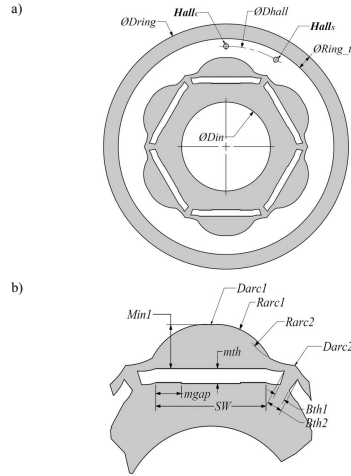


Fig. 4. Dimensions of the magnetic resolver a), general view and b), detailed view.

The resulting optimized resolver design, therefore, will be high sensitivity, low distortion, low-cost given the pre-defined boundary conditions. Three different types of

permanent magnet materials have been evaluated: Ferrite, sintered NdFeB, and bonded NdFeB magnets. Table III summarizes the optimization results.

TABLE II. GEOMETRIC PARAMETERS DESCRIPTION

Symbol	Definition
$Darc1$	Rotor d-axis outer diameter
$Darc2$	Rotor q-axis outer diameter
$\phi Dhall$	Hall sensor distance from center
ϕDin	Rotor inner diameter
$\phi Dring$	Ring outer diameter
$Ring_{th}$	Ring thickness
$Rarc1$	Rotor d-axis outer arc
$Rarc2$	Rotor q-axis outer arc
mth	Magnet thickness
$Min1$	Magnet distance from $\phi Darc1$
$mgap$	Magnet gap in slot
SW	Slot width
$Bth1$	Outer bridge thickness
$Bth2$	Inner bridge thickness

Fig. 5 shows an example of the flux distribution when using the selected geometry for the three permanent magnet materials, main properties of each case being shown in Table III. As expected, the maximum peak flux density in the airgap is obtained with the prototype equipped with sintered NdFeB magnets, see Table III. This will allow better use of the measuring range of the Hall-effect sensor, eventually improving the signal to noise ratio. Obtaining a similar peak flux density, bonded NdFeB magnets requires almost twice of magnetic material, see Table III. Ferrite magnets provide, as expected, the smallest flux density, with a peak value in around half of that obtained with NdFeB magnets. The Ferrite vs. NdFeB volume to achieve the same peak flux density is around 2.5, see Table III. Even in this case, the ferrite-based solution is expected to be cheaper.

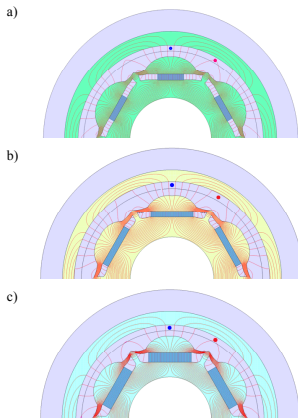


Fig. 5. Flux lines distribution for the optimized magnetic resolver design equipping a) Sintered NdFeB magnets, b) Bonded NdFeB magnets, and c) Ferrite magnets. Blue (•) and red (•) spots represent the Hall_s and Hall_r sensors.

TABLE III. OPTIMIZATION RESULTS OF THE MAGNETIC RESOLVER

	PM Material		
	Ferrite	Sintered NdFeB	Bonded NdFeB
THD (%)	1.55	0.27	0.84
Fundamental flux amplitude (mT)	36.23	95.81	86.68
PM volume (mm ³)	97.33	37.16	60.65

^a Results obtained from FEA simulation

IV. VALIDATION OF THE RESOLVER USING FEA

This section shows FEA results for the three optimized prototypes using sintered NdFeB, bonded NdFeB, and Ferrite, respectively.

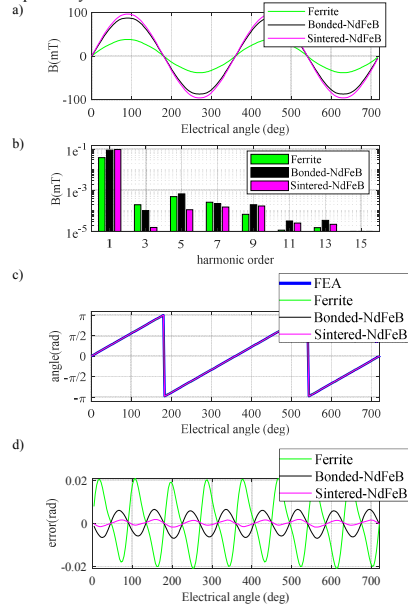


Fig. 6. Performance of the three types of resolvers, a) \sin output of the hall effect sensors, b) FFT of \sin output (in a)), c) resulting position angle and d) resulting angle error.

Fig. 6a shows the magnetic flux density at the position of “Hall_s” sensor (see Fig. 3 and 5) for one rotor revolution for the three cases. Fig. 6b shows the corresponding FFTs, from which the THDs in Table III are obtained. It can be observed that the THD in all cases is <1.55%, all harmonics being at least two orders of magnitude smaller than the fundamental component. It is noted that these results might be influenced by the bandwidth of the Hall-Effect sensors, which is typically >250kHz [12]; i.e., the bandwidth of the Hall-effect sensors will have virtually no influence in standard machines used in traction applications [14]. Fig. 6c shows the measured position for the three different rotor designs and the real position (i.e. FEA). Fig. 6d shows the error in the measured position, which is due to the harmonics in the flux waveform shown in Fig. 6b and does not account for errors due to assembling tolerances, circuitry, noise, misalignments, etc.

It can be observed in Fig. 6d that the lower error is obtained for the sintered NdFeB magnet, ferrite magnets showing the worst behavior. Measurement errors are $\pm 1.1^\circ$ (Ferrite based), $\pm 0.35^\circ$ (bonded NdFeB based), and $\pm 0.09^\circ$ (sintered NdFeB based). Position error of commercially available resolvers is in the range of ± 0.5 - 1.0° for VR resolvers [11] and around $\pm 0.16^\circ$ for brushless resolvers, meaning that the accuracy is comparable with commercially available resolvers.

V. ASSEMBLY OF THE PROPOSED PROTOTYPE

The proposed prototype can be assembled in two different configurations: in-shaft mounting and shaft-type for connections through flexible couplings. In any case, the necessary circuitry is the same, both allowing redundant configuration (i.e. providing duplicated signals). Fig. 7a shows the laser cutout of the optimized designs for the prototypes equipping Ferrite magnets and sintered NdFeB magnets, the PM samples being shown in Fig. 7b. The same laser cutout and magnets will be used for both the in-shaft and shaft-type resolvers.

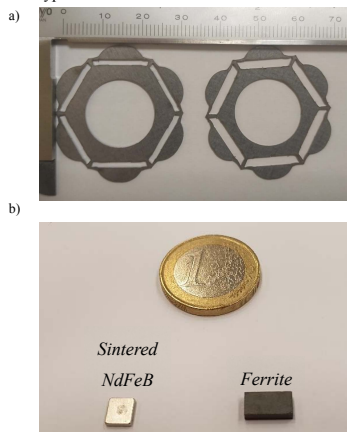


Fig. 7. a) Lamination of the optimized geometries for the magnetic resolver design equipping: sintered NdFeB (left) and Ferrite (right). Scale in mm, and b) NdFeB and Ferrite magnets for the designs in Fig. 7a.

A. Shaft-type assembly

The shaft-type magnetic resolver is shown in Fig. 8. It is equipped with the rotor cutout and PMs shown in Fig. 7. It was designed with a $\varnothing 8$ mm shaft, the diameter of the body and axial dimensions being $\varnothing 52$ mm and 17 mm respectively. This design is suitable for the connection through flexible couplings. It can be observed that the PCB integrates four Hall-effect sensors (i.e. two $Hall_c$ and two $Hall_s$), i.e. it provides redundant output signals. The design also includes two bearings: front and rear cover hosts.

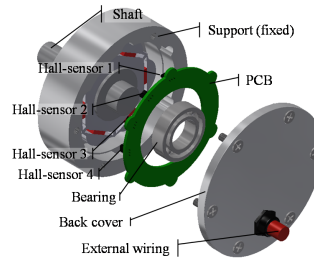


Fig. 8. Disassemble view of the Shaft-type magnetic resolver

B. In-shaft mount assembly

The in-shaft type magnetic resolver is shown in Fig. 9. It is equipped with the rotor cutout and PMs shown in Fig. 7. The rotor of the sensor is directly connected to the machine shaft and fixed by a nut. The axial length of the sensor exploding bolts is 5 mm, and the diameter of the sensor is $\varnothing 70$ mm. In this case, the PCB integrates only two Hall-effect sensors (i.e. $Hall_c$ and $Hall_s$), although this design also allows redundant configuration. This design requires no bearings..

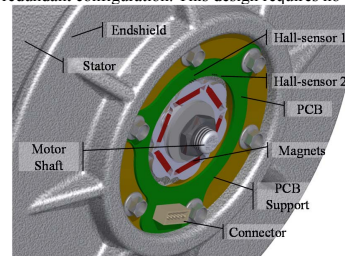


Fig.9 In-shaft type magnetic resolver inserted in an endshield of a machine.

C. Electronic circuitry

A conditioning system is required for the proposed prototype to achieve full compatibility with commercial drives in terms of power supply and output voltage levels. Its objective is twofold: provide supply voltages for the Hall elements and the additional ICs, and adapt output voltage levels within the range of commercial drives.

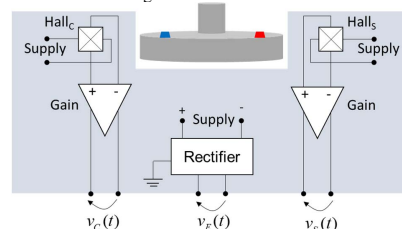


Fig. 10. Simplified representation of the electronic circuitry.

Fig. 8 shows a simplified representation of the electronic circuit needed for the proposed sensor. The excitation signal,

which will be provided by the drive (i.e. standard resolver excitation), is rectified to provide symmetrical voltage supply to the circuit, as demanded by the operational amplifiers. Hall elements (i.e. $Hall_C$ and $Hall_S$) are fed using constant voltage what produces a constant current through the hall elements since hall elements are resistors from an electrical point of view. Note that a temperature variation of the hall element will have a direct impact on the current through the hall element. However, this will not affect the position measurement since the rotor position information is included the phase of the current waveforms but not in the amplitude (see Fig. 2).

The total power consumption of the proposed system is in the range of the power consumption of the Hall-elements: 12.5 mW per sensor. The power consumption of the rectification stage can be negligible (i.e., conduction losses of a rectifier diode). The power consumption of the gain stages can also be negligible since ultra-low power differential operational amplifiers are used.

The circuit in Fig. 8 provides differential output signals to enhance noise immunity in the transmission wire.

VI. EXPERIMENTAL RESULTS

A prototype of the shaft-type sensor is shown in Fig. 11, corresponding to the drawing in Fig. 8. In this design, the fixed parts of the sensor (i.e. shaft, stator and cover) have been 3D printed using polyacid material (PLA). The moving parts (i.e., magnets and rotor) are made of Sintered NdFeB magnets and the laser-cut silicon steel 50H350, see Fig. 7. The prototype integrates two pairs of Hall-effect sensors (i.e. $Hall_C$ and $Hall_S$) for a redundant output, the simplified power and conditioning stages for each pair of sensors being shown in Fig. 10.

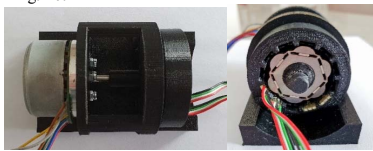


Fig. 11. 3D printed position sensor (right) and testbench (left)

The sensor is attached to a brushless PMS motor in a testbench, see Fig. 11. Fig. 12 shows the output waveforms provided by a pair of Hall-effect sensors (i.e. $Hall_C$ and $Hall_S$) when they are fed with a sinusoidal waveform of 7V_{RMS} at 10 kHz. It can be observed that the peak amplitude of the magnetic flux density waveform in Fig. 13 is around 100mT, what matches the optimization results in Table III for sintered NdFeB magnets.

Fig. 12 shows the simplified signal processing used for speed and position estimation. Measured flux densities by $Hall_C$ and $Hall_S$ are multiplied by the excitation signal at the demodulation stage. The phase of the resulting complex vector signals, V_{α} , V_{β} are normalized (14) and \vec{V}_{dq}^r (15)-(16), is obtained using a synchronous reference frame phase-locked loop (SRF-PLL), which provides the estimated rotor speed and position [18].

The signal processing scheme in Fig. 12 is applied to the signals in Fig. 13. Rotor speed and position are obtained from the waveforms in Fig. 13 after the demodulation process, that are later normalized in amplitude (see Fig. 14) in order to feed a the SRF-PLL in Fig. 12.

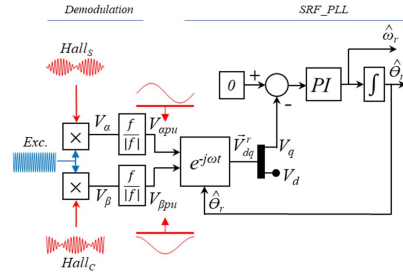


Fig. 12 Schematic representation of the signal processing used for speed and position estimation

$$V_{\alpha pu} = \frac{V_{\alpha}}{|V_{\alpha}|}; \quad V_{\beta pu} = \frac{V_{\beta}}{|V_{\beta}|} \quad (14)$$

$$\vec{V}_{\alpha\beta pu}^s = V_{\alpha pu} + jV_{\beta pu} \quad (15)$$

$$\vec{V}_{dq}^r = \vec{V}_{\alpha\beta pu}^s e^{-j\theta_r} \quad (16)$$

Fig. 15 shows the estimated speed obtained from the proposed sensor during the startup of the brushless machine in open loop. The machine is stopped until 2.75 s, and at $t=2.75$ s the speed increases up to 20 rad/s. Fig. 16 shows the estimated absolute angular position. An aluminum design of the system with more accurate tolerances and higher stiffness is currently under development.

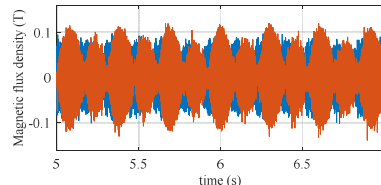


Fig. 13. Magnetic resolver signals: Hallc signal (blue), Vc(t) (i.e. cosine) and Halls signal (red), Vs(t) (i.e. sine). $\omega_s = 2 \cdot \pi \cdot 10000$ rad/s, $\omega_r = 2 \cdot \pi \cdot 1.1$ rad/s

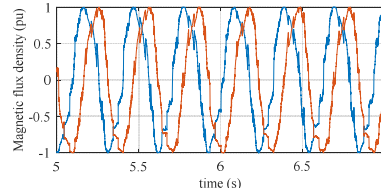


Fig. 14. Normalized magnetic resolver signals: Hallc signal (blue), Vc(t) (i.e. cosine) and Halls signal (red), Vs(t) (i.e. sine) $\omega_s = 2 \cdot \pi \cdot 10000$ rad/s, $\omega_r = 2 \cdot \pi \cdot 1.1$ rad/s

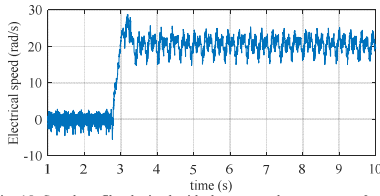


Fig. 15. Speed profile obtained with the proposed sensor. $\omega_s = 2 \cdot \pi \cdot 10000$ rad/s, $\omega_r = 2 \cdot \pi \cdot 1.1$ rad/s

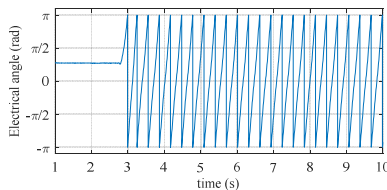


Fig. 16. Angular position profile obtained with the proposed sensor. $\omega_s = 2 \cdot \pi \cdot 10000$ rad/s, $\omega_r = 2 \cdot \pi \cdot 1.1$ rad/s

VII. CONCLUSIONS

A magnetic resolver using hall effect sensors is proposed in this paper. Compared to available resolvers, it provides similar accuracy, with a simpler and cheaper construction. Two different designs have been proposed: shaft-type or in-shaft designs; both allowing redundant position measurement. FEA results have been provided to demonstrate the viability of the proposed system and the system has been experimentally validated.

ACKNOWLEDGMENT

Author would like to thank Bomatec AG for advising and providing magnet samples.

REFERENCES

- [1] R. M. Kennel, "Why Do Incremental Encoders Do a Reasonably Good Job in Electrical Drives with Digital Control?," Conference Record of the 2006 IEEE Industry Applications Conference Forty-First IAS Annual Meeting, Tampa, FL, 2006, pp. 925-930. doi: 10.1109/IAS.2006.256635
- [2] B. Hou, C. Li, Z. Gao, Q. Wei, B. Zhou and R. Zhang, "Design, Optimization, and Compensation of a High-Precision Single-Excitation Absolute Capacitance Angular Encoder up to $\pm 4^\circ$," in IEEE Transactions on Industrial Electronics, vol. 66, no. 10, pp. 8161-8171, Oct. 2019. doi: 10.1109/TIE.2018.2886762
- [3] H. Pu, H. Wang, X. Liu, Z. Yu and K. Peng, "A High-Precision Absolute Angular Position Sensor With Vernier Capacitive Arrays Based on Time Grating," in IEEE Sensors Journal, vol. 19, no. 19, pp. 8626-8634, 1 Oct. 1, 2019. doi: 10.1109/JSEN.2019.2921479
- [4] M. Howard, Incremental encoders, absolute encoders & pseudo-absolute encoders, Feb. 2013. Accessed on: Dec. 15, 2019. [Online]. Available: https://www.zettlex.com/wp-content/uploads/2017/08/incremental-encoders-vs.-absolute-encoders_Rev_3.1.pdf
- [5] F. Jiang, D. Lou, H. Zhang, L. Tang, S. Sun and K. Yang, "Design of a GMR-based magnetic encoder using TLE5012B," 2017 20th International Conference on Electrical Machines and Systems (ICEMS), Sydney, NSW, 2017, pp. 1-4. doi: 10.1109/ICEMS.2017.8056197
- [6] C. Jin, I. Jang, J. Bae, J. Lee and W. Kim, "Proposal of Improved Winding Method for VR Resolver," in IEEE Transactions on Magnetics, vol. 51, no. 3, pp. 1-4, March 2015, Art no. 8102404. doi: 10.1109/TMAG.2014.2348321
- [7] L. Sun, "Analysis and Improvement on the Structure of Variable Reluctance Resolvers," in IEEE Transactions on Magnetics, vol. 44, no. 8, pp. 2002-2008, Aug. 2008. doi: 10.1109/TMAG.2008.923315
- [8] J. Figueiredo, "Resolver models for manufacturing," IEEE Trans. Ind. Electron., 58(8): 3693-3700, Aug. 2011.
- [9] L. Z. Sun, J. B. Zou, and Y. P. Lu, "New variable-reluctance resolver for rotor-position sensing," in Proc. IEEE Region 10th Conf. TENCN, vol. 4, Chiang Mai, Thailand, pp. 5-8, Nov. 2004.
- [10] H. Saneie, Z. Nasiri-Gheidari and F. Tootoonchian, "Design-Oriented Modelling of Axial-Flux Variable-Reluctance Resolver Based on Magnetic Equivalent Circuits and Schwarz-Christoffel Mapping," in IEEE Transactions on Industrial Electronics, vol. 65, no. 5, pp. 4322-4330, May 2018, doi: 10.1109/TIE.2017.2760862.
- [11] T. Suzuki, K. Toyotake and Y. Yamashita, "Variable reluctance type resolver rotor and brushless motor," Japan Patent JP2010048775A, Aug. 25, 2008.
- [12] D. Fernandez et al., "Permanent Magnet Temperature Estimation in PM Synchronous Motors Using Low-Cost Hall Effect Sensors," in IEEE Transactions on Industry Applications, vol. 53, no. 5, pp. 4515-4525, Sept.-Oct. 2017. doi: 10.1109/TIA.2017.2705580
- [13] S. Das and P. N. Suganthan, "Differential Evolution: A Survey of the State-of-the-Art," in IEEE Transactions on Evolutionary Computation, vol. 15, no. 1, pp. 4-31, Feb. 2011. doi: 10.1109/TEVC.2010.2059031
- [14] M. Minowa, H. Hijikata, K. Akatsu and T. Kato, "Variable leakage flux interior permanent magnet synchronous machine for improving efficiency on duty cycle," 2014 International Power Electronics Conference (IPEC-Hiroshima 2014 - ECCE ASIA), Hiroshima, 2014, pp. 3828-3833. doi: 10.1109/IPEC.2014.6870049
- [15] L. Peely, R. Schindeler, D. Cleveland and K. Hashtudi-Zaad, "High-Precision Resolver-to-Velocity Converter," in IEEE Transactions on Instrumentation and Measurement, vol. 66, no. 11, pp. 2917-2928, Nov. 2017. doi: 10.1109/TIM.2017.2714378
- [16] P. Kejik, S. Reymond and R. S. Popovic, "Circular Hall Transducer for Angular Position Sensing," TRANSDUCERS 2007 - 2007 International Solid-State Sensors, Actuators and Microsystems Conference, Lyon, 2007, pp. 2593-2596. doi: 10.1109/SENSOR.2007.4300702
- [17] K. Bienczyk, "Angle measurement using a miniature hall effect position sensor," 2009 2nd International Students Conference on Electrodynamic and Mechatronics, Silesia, 2009, pp. 21-22. doi: 10.1109/ISCON.2009.5156096
- [18] D. Reigosa, D. Fernandez, C. González, S. B. Lee and F. Briz, "Permanent Magnet Synchronous Machine Drive Control Using Analog Hall-Effect Sensors," in IEEE Transactions on Industry Applications, vol. 54, no. 3, pp. 2358-2369, May-June 2018, doi: 10.1109/TIA.2018.2802950.

